Micromechanics of hydrogen embrittlement of aluminum alloys

Leonel Stermann

Université Claude Bernard Lyon 1

N° d'ordre NNT: 2021LYSE1026

THÈSE de DOCTORAT DE L'UNIVERSITÉ DE LYON
opérée au sein de :
l'Université Claude Bernard Lyon 1

ED 52 PHAST
École Doctorale de Physique et Astrophysique de Lyon

Spécialité de doctorat : Physique des Matériaux

Soutenue publiquement le 01/02/2021, par :

Leonel D. Stermann

Micromechanics of Hydrogen Embrittlement of Aluminum Alloys

Devant le jury composé de :

M. DIMANOV Alexandre Directeur de Recherche CNRS, École Polytechnique	**Rapporteur**
Mme. GASPÉRINI Monique Professeure, Université Sorbonne Paris Nord	**Rapporteure**
M. COLOMBANI Jean Professeur, IUT Lyon 1 / Université Lyon 1	**Examinateur**
M. MOMPIOU Frédéric Chargé de Recherche CNRS, CEMES UPR 8011	**Examinateur**
Mme. TANGUY Anne Professeure, INSA Lyon	**Présidente du jury**
M. TANGUY Döme Chargé de Recherche CNRS, Université Lyon 1	**Directeur de thèse**
M. VANEL Loïc Professeur, Université Lyon 1	**Co-Directeur de thèse**

N° d'ordre NNT: 2021LYSE1026

THÈSE de DOCTORAT DE L'UNIVERSITÉ DE LYON
opérée au sein de :
l'Université Claude Bernard Lyon 1

ED 52 PHAST
École Doctorale de Physique et Astrophysique de Lyon

Spécialité de doctorat : Physique des Matériaux

Soutenue publiquement le 01/02/2021, par :
Leonel D. Stermann

Micromécanique de la fragilisation d'alliages d'aluminium par l'hydrogène

---

Devant le jury composé de :

M. DIMANOV Alexandre Directeur de Recherche CNRS, École Polytechnique	**Rapporteur**
Mme. GASPÉRINI Monique Professeure, Université Sorbonne Paris Nord	**Rapporteure**
M. COLOMBANI Jean Professeur, IUT Lyon 1 / Université Lyon 1	**Examinateur**
M. MOMPIOU Frédéric Chargé de Recherche CNRS, CEMES UPR 8011	**Examinateur**
Mme. TANGUY Anne Professeure, INSA Lyon	**Présidente du jury**
M. TANGUY Döme Chargé de Recherche CNRS, Université Lyon 1	**Directeur de thèse**
M. VANEL Loïc Professeur, Université Lyon 1	**Co-Directeur de thèse**

Remerciements

- La République Française, l'Université de Lyon et l'Institut Lumière Matière (ILM)
- Döme Tanguy for being my mentor and sometimes like my family. It is a privilege to work with him.
- Loïc Vanel for this immense opportunity and his support.
- Nicholas Blanchard, who helped me with the SEM and for his pieces of advice.
- My ILM colleagues for their assistance and camaraderie.
- My friends, the new ones and the old ones.
- My professors, teachers, and maestros.
- My homeland, Argentina.
- My parents and my brother.
- My community and G-d.

"Life is like riding a bicycle. To keep your balance you must keep moving"
A. Einstein

Résumé de la thèse présentée à l'Université Lyon 1

La fragilisation par l'hydrogène touche de nombreux alliages métalliques, dits "de structure", quand ils sont utilisés dans un milieu susceptible de générer de l'hydrogène (hydrogène gazeux, milieu corrosif aqueux, vapeur d'eau). De nombreux secteurs industriels sont ainsi concernés: aéronautique, nucléaire civil, transports maritimes... Les ruptures de matériaux en service sont à l'origine de coûts importants liés aux arrêts pour maintenance et pour inspection, sans parler des accidents. On parle de "fragilisation" car la présence d'hydrogène dans le matériau entraîne la propagation de fissures à des niveaux de charge mécanique faibles, où il n'y a normalement pas de fissuration. Prédire les conditions d'apparition des fissures, leur vitesse de propagation et caractériser la sensibilité des matériaux à ce phénomène constitue un enjeu important pour la société. Le déploiement, dans le futur, des technologies utilisant l'hydrogène gazeux comme un moyen de stockage d'énergie (électrolyseurs - piles à combustible) pourrait constituer un nouveau secteur où les problèmes de fragilisation pourraient apparaître.

Le mémoire présente, tout d'abord, les modèles phénoménologiques qui expliquent certaines observations expérimentales à partir de mécanismes microscopiques tels que: la localisation de la déformation plastique dans des bandes intenses (HELP) qui favoriserait la rupture transgranulaire par un cisaillement intense ou intergranulaire en créant des contraintes locales importantes en avant de la pointe de fissure ; la plasticité de pointe de fissure assistée par l'hydrogène adsorbé (AIDE) qui favoriserait une rupture ductile par formation de micro cupules en avant de la pointe de la fissure ; la décohésion induite par la présence d'hydrogène au niveau des joints de grains, ou le long de certains plans cristallins (HEDE) ; et enfin, la stabilisation de lacunes par l'hydrogène qui expliquerait la perte de cohésion. Des observations récentes, post mortem, par microscopie électronique en transmission et à balayage, sont présentées qui montrent la structure en cellule des dislocations en avant de la pointe de fissure, des interactions entre dislocations et joints de grains (transmission, blocage) et la formation de micro/nano cavités. Ces observations représentent un ensemble qui soutient les mécanismes élémentaires invoqués dans les modèles phénoménologiques. Enfin, des résultats récents, spécifiques aux alliages AlZnMg étudiés dans la thèse, sont résumés. Un groupe japonais a utilisé la corrélation d'images 3D obtenues par tomographie de rayons X pour caractériser la fissuration in situ en présence d'hydrogène interne. L'angle d'ouverture de la fissure, local, le profil d'ouverture, la taille de la zone plastique sont corrélés avec le mode de rupture et la vitesse de propagation. La dépendance de la fragilisation avec le temps (plus la vitesse de sollicitation est faible,

plus la fragilisation est importante) est mise en évidence. Enfin, l'utilisation d'éléments d'alliages permettant de faire varier la quantité et la nature des précipités a permis de mettre en évidence le rôle du piégeage de l'hydrogène. Un mécanisme original est proposé où l'hydrogène est piégé de manière "irréversible" (au sens où un traitement thermique ne permet pas d'éliminer la fragilisation) pour être libéré localement dans la zone déformée plastiquement en avant de la pointe de fissure. Le mécanisme est appelé "repartitionnement". Une des limitations de ces études est la faible résolution spatiale du champ de déplacement, de l'ordre de 20µm, qui provient de la corrélation d'image 3D. Dans ce contexte, il apparaît qu'il manque des observations de fissuration in situ à une échelle fine, avec caractérisation de la déformation plastique et de la vitesse de fissuration locale. L'objectif de la thèse est la mise en place d'une telle expérience de fissuration.

Le matériau choisi pour cette étude est l'alliage d'aluminium 7108 (AlZnMg à basse teneur en Cu), sous forme d'une tôle laminée d'épaisseur 8mm. Les grains sont partiellement recristallisés et présentent une morphologie allongée dans le sens du laminage avec des dimensions entre 20 et 200µm dans cette direction. Les éprouvettes de traction sont prélevées dans le "sens court" de la tôle et sont entaillées de telle sorte que la direction de propagation soit transverse au sens de laminage. Le fond d'entaille est donc parallèle à la direction où les grains sont les plus longs pour avoir le moins de grains possibles dans l'épaisseur. L'épaisseur varie entre 1 et 0.2 mm. L'objectif est d'avoir peu de joints de grains dans l'épaisseur et de les solliciter mécaniquement selon leur normale. Cette géométrie doit permettre de mettre en évidence les variations de sensibilité à la fragilisation des différents joints, si elle existe, en fonction de leur nature cristallographique, de l'orientation des plans de glissement dans les grains adjacents. L'hydrogène est introduit dans les éprouvettes de deux manières différentes: (1) une exposition à une solution d'acide sulfurique sous polarisation cathodique, préalable à la traction, ou (2) une mise en contact du fond de fissure avec une solution d'eau de mer, à potentiel de corrosion libre, tout au long de l'essai mécanique. Dans le cas (1), il s'agit d'appliquer la contrainte sur l'éprouvette alors que l'hydrogène se trouve déjà dans la masse de l'échantillon. Il peut alors diffuser vers la pointe de la fissure au cours de la propagation. Dans le cas (2) (corrosion sous contrainte), l'hydrogène est produit sur les lèvres de fissure par des réactions de corrosion. Il doit alors diffuser vers l'avant de la fissure pour participer à la propagation. Une force est appliquée sur les éprouvettes au moyen d'une micro-platine de traction, montée sous un microscope optique permettant d'effectuer les essais, au besoin avec un milieu corrosif (cas 2). Dans ce cas, une cellule de corrosion de petite dimensions, fabriquée spécifiquement par impression 3D, est collée à l'éprouvette. Des photos de la surface sont prises au cours de la fissuration. La surface, préalablement polie, présente une attaque chimique à l'issu du chargement en hydrogène (H interne). Cette attaque crée un contraste qui permet de mesurer les champs de déplacements en surface par la méthode de corrélation d'images numériques. Une résolution spatiale de 1µm a été atteinte avec une précision de l'ordre de 10 nm. Le gradient des déplacements donne accès à la déformation qui est mesurée au plus fort grossissement, sur une grille de 1µm de côté, quand elle atteint des valeurs supérieures à 1% (déformation plastique locale). Les paramètres de l'expérience sont: le niveau de force appliqué (qui est transformé a posteriori en facteur d'intensité des contraintes, macroscopique, après que la position de la fissure ait été déterminé à partir du champ de déplacement), le temps de préchargement

en hydrogène et le niveau du potentiel cathodique appliqué (dans le cas de l'hydrogène interne), l'épaisseur de l'éprouvette. Les grandeurs mesurées sont: la déformation critique locale pour former une mono-fissure à la pointe de l'entaille, la force critique pour assurer la propagation de la fissure, le champ de déplacement en cours de la propagation. Ce dernier est exploité pour obtenir: la position de la pointe de la fissure (en surface) au cours du temps et donc la vitesse locale de fissuration, le champ de déformation local, le profil d'ouverture de la fissure. Enfin, deux types d'expériences de fissuration ont été menées: fissuration par hydrogène interne et fissuration par corrosion sous contrainte.

La fissuration liée à la présence d'hydrogène interne est étudiée en premier lieu. Une dizaine d'expériences de fissuration exploitables ont été produites. Elles ont amené à 90 mesures de données locales liées à la fissuration. Le degré de fragilisation est tout d'abord déterminé à partir de mesures globales telles que: la déformation locale à la pointe de l'entaille nécessaire à la formation d'une fissure, la vitesse moyenne de fissuration et le facteur d'intensité des contraintes pour la propagation. A la vue de ces données, il semble que le potentiel cathodique appliqué lors du préchargement soit le paramètre le plus important (les teneurs en hydrogène correspondantes n'ont pas pour l'instant été déterminées). Le temps de chargement (au-delà de 24h) et l'épaisseur de l'éprouvette jouent peu, dans les limites de ce qui a été exploré. La déformation plastique à l'amorçage à la pointe de l'entaille est toujours très élevée entre 10 et 50% et s'étend sur plusieurs grains (l'éprouvette est dans le domaine élastique loin de l'entaille). Pendant la propagation de la fissure, le déplacement des mors est maintenu constant (la force décroît). La fissure avance donc dans un matériau élastique, en générant une zone plastique limitée au voisinage de la pointe de la fissure, et ce quel que soit le degré de fragilisation. Quand les déformations hors de la surface restent faibles, des mesures locales de champ de déplacement peuvent être effectuées, ce qui donne accès aux vitesses locales et à la plasticité locale en pointe de fissure, à une échelle plus petite que la taille de grain. La carte de la déformation de Von Mises, mesurée, montre qu'il y a deux types de plasticité qui sont dénommées "plasticité primaire et secondaire". La plasticité primaire est intense et s'étend sur au moins 50 µm de part et d'autre du plan de la fissure, en formant deux lobes inclinés. La plasticité secondaire est confinée à quelques microns du part et d'autre du plan de la fissure et s'étend, en avant de la pointe de la fissure, sur 4 µm en moyenne. La déformation plastique à la pointe de la fissure est de 6% en moyenne. La déformation plastique "primaire" est caractérisée par "le taux de déformation plastique" (PDR, "plastic deformation rate", sans unité). Il est proportionnel à l'intégrale de la déformation plastique de Von Mises sur une zone qui englobe la déformation plastique liée à une avancée de la fissure (c'est la quantité de déformation plastique supplémentaire qui a été injectée dans le système lors de l'avancée de la fissure), divisé par la longueur de l'incrément de fissure. Les données montrent que la vitesse locale varie entre 20 et 500 µm/h. Le PDR varie entre 0 et 8000. La tendance est intuitive: plus la vitesse locale est élevée, plus le PDR est faible (moins il y a de plasticité accompagnant la fissure). Néanmoins, pour chaque vitesse, il existe un intervalle de PDR, i.e. qu'il existe des fissures émettant peu de plasticité mais néanmoins lentes. Par contre, la plasticité secondaire varie peu, quelle que soit la vitesse de fissuration. Par ailleurs, vitesses locales et quantité de plasticité locale ont aussi été confrontées aux différents modes de rupture. Trois modes de rupture "fragiles" sont présents sur le faciès de rupture: intergranulaire lisse, intergranulaire rugueux et

transgranulaire. La rupture transgranulaire n'est observée que dans les conditions de chargement en hydrogène donnant le plus de fragilité. Elle progresse avec une quantité de plasticité émise similaire à la rupture "intergranulaire lisse", mais avec une vitesse plus faible en moyenne. La fissuration intergranulaire "rugueuse" n'existe quand dans les conditions moins fragilisantes et est accompagnée de plus de plasticité. En complément, les profils d'ouverture de fissure ont aussi été mesurés. Les observations faites à partir du PDR se retrouvent sur ces profils. Pour finir, il n'a pas été observé de variation significative du chargement mécanique critique (K) en fonction de la vitesse locale ou de la nature de la rupture, même aux épaisseurs les plus faibles (qui comporte quand même plusieurs grains et souvent une fissure légèrement ramifiée).

Le même montage que précédemment a été utilisé dans le cas de la "corrosion sous contrainte", en fixant une cellule contenant de l'eau salée sur l'éprouvette. Là aussi la fissuration est induite par l'hydrogène présent dans le système, mais il est produit en continu sur les lèvres de la fissure par les réactions de corrosion et diffuse depuis le lieu de production vers l'avant de la fissure. Une première étape a été de mesurer l'effet de l'humidité de l'air. Moyennant un chargement mécanique plus élevé et un temps d'incubation de plusieurs semaines, une monofissure transgranulaire est initiée depuis l'entaille. La propagation est lente (3 µm/h). Elle est interrompue quand l'air humide est remplacé par de l'argon, puis reprend après quelques heures d'incubation quand le système est remis en contact avec l'air du laboratoire. En présence d'eau salée, la fissuration présente les mêmes caractéristiques qu'en présence d'hydrogène interne, mais avec des vitesses de fissuration plus élevée, entre 50 et 3000 µm/h (après un temps d'incubation d'environ deux heures). La littérature permet d'interpréter ce temps d'incubation comme le temps nécessaire pour que les réactions de corrosion de surface génèrent suffisamment d'hydrogène pour initier la fissuration (la teneur moyenne en hydrogène d'échantillon de taille comparable aux nôtres, mesurée par fusion et analyse du gaz relâché, augmente très fortement dans les deux premières heures d'exposition à la corrosion). La mesure des champs de déplacement par corrélation d'images (DIC "digital image correlation") est beaucoup plus difficile que dans le cas de l'hydrogène interne car il n'y a pas de contraste visuel lié à une attaque chimique. La face de l'éprouvette observée au microscope est telle qu'elle est produite par le polissage: elle présente un contraste dû aux précipités présents dans les grains. Ces derniers n'ont ni la taille, ni la densité nécessaire pour obtenir la résolution maximale en DIC. De plus, lorsque la déformation plastique émerge en surface, elle crée un relief qui se traduit par une "ombre" sur l'image optique. Cette ombre est d'autant plus prononcée que la quantité de plasticité est importante, ce qui est le cas au voisinage de la pointe de fissure, là où la plasticité "primaire" est la plus intense. L'impossibilité de réaliser la corrélation d'image dans cette zone rend impossible l'acquisition des profils d'ouverture dans la zone qui est la plus intéressante. Cette limitation a amené en fin de thèse au développement d'un nouveau motif de surface. Néanmoins, un cas de fissuration intermittent a pu être observé. Il montre la succession de séquences de fissuration rapide, avec un angle d'ouverture de fissure faible, alternée avec des évènements de ralentissement et d'émoussement de la pointe de la fissure. Ce cas sera intéressant à modéliser à l'avenir puisque nous avons accès au moment du ralentissement de la fissure, bien qu'avec une résolution moindre, à l'étendue de la zone plastique secondaire, à l'émoussement de la pointe de la fissure et à la déformation plastique primaire. Un modèle mécanique compor-

tant la forme de la pointe émoussée, le chargement mécanique extérieur et l'effet d'écran de la zone plastique primaire devrait permettre d'évaluer l'intensité de champ de contrainte en avant de la pointe de la fissure et de discuter de la reprise de la fissuration.

Enfin, la dernière partie du manuscrit présente une discussion et les perspectives. L'objectif de la thèse était de mettre en place une expérience qui permette de sonder la sensibilité à la fragilisation par l'hydrogène de joints de grains individuels. Le bilan des résultats obtenus montre que cet objectif n'est pas complètement atteint. Le plus surprenant est que la valeur du chargement mécanique critique K est toujours dans la gamme des valeurs macroscopiques présentes dans la littérature (8 MPa $m^{1/2}$) même lorsque l'épaisseur des éprouvettes atteint 200 µm. Par ailleurs, il n'y a pas de relation unique entre la vitesse locale et la quantité de plasticité émise depuis la pointe de fissure. En particulier, il n'est pas aisé de comprendre pourquoi une fissure fragile avec un bas niveau de plasticité, i.e. qui se propage parce que la cohésion a été suffisamment réduite, et soumise à un K élevé peut avoir n'importe quelle vitesse entre 50 et 500 µm/h. Ceci est peut-être une indication que la nature polycristalline des échantillons implique de fortes hétérogénéités de chargement mécanique le long du front de fissure. Par ailleurs, le rôle de la diffusion est discuté sur la base de calculs simples de diffusion avec un coefficient de diffusion effectif de 10^{-12} m^2/s. Il est montré que la gamme des vitesses de propagation obtenue dans le cas de l'hydrogène interne est suffisamment lente pour que la fissuration ne soit pas limitée par la diffusion. Il est aussi montré que l'hydrogène interne devrait être totalement désorbé avant la fin de l'essai de fissuration. Hors, la fragilisation est toujours observée. Des essais de chargement en hydrogène, suivi d'un maintien à haute température sensé désorber l'hydrogène, puis d'une traction, ont montré que la fragilisation est toujours présente. Il existe donc des pièges profonds qui limitent la désorption de l'hydrogène tout en assurant une fragilisation suffisamment importante, en accord avec les résultats obtenus au Japon (modèle de "repartitionnement"). Enfin, les conditions pour le dépôt de nanoparticules d'or, de taille et de densité, adaptées aux essais de fissuration sous microscope optique et à balayage ont été trouvées, grâce à l'expertise présente dans d'autres équipes de l'iLM. Cette nouvelle source de contraste en surface devrait permettre de résoudre les problèmes de résolution en corrélation d'images en corrosion sous contrainte. Elle permet aussi d'envisager de la DIC à haute résolution en microscopie électronique. Du côté des simulations, les expériences ont déjà montré un certain nombre de résultats génériques, comme les caractéristiques de la plasticité secondaire, qui se prêtent bien à la simulation par "dynamique des dislocations discrètes". Un projet a été initié dans cette direction.

Contents

1 Introduction **1**

2 Literature Review **3**
2.1 Hydrogen in metallic materials . . . 3
2.1.1 Hydrogen diffusion in metals . . . 4
2.1.2 Dislocations and hydrogen . . . 4
2.2 Hydrogen embrittlement mechanisms . . . 8
2.2.1 AIDE . . . 8
2.2.2 HEDE . . . 10
2.2.3 HELP . . . 14
2.2.4 Vacancies and nano-micro voids related mechanisms . . . 21
2.3 Hydrogen assisted cracking in 7XXX alloys . . . 25
2.3.1 Local fracture properties . . . 25
2.3.2 Time dependency and strain localization . . . 28
2.3.3 Fracture modes of AlZnMg alloys with low copper content . . . 30
2.3.4 Repartitioning based model . . . 35
2.4 Summary . . . 37

3 Materials and Methods **39**
3.1 Material and equipment . . . 39
3.2 Methods . . . 46
3.2.1 Hydrogen charging electrochemical method . . . 46
3.2.2 Digital Image Correlation . . . 47
3.2.3 Stress Intensity Factor Calculation . . . 52
3.2.4 DIC validation using finite elements analysis . . . 53
3.2.5 Crack tip localization method . . . 54

4 Internal Hydrogen Embrittlement **59**
4.1 Macroscopic description of hydrogen assisted cracking . . . 59
4.1.1 Test parameters . . . 59
4.1.2 A typical crack test . . . 60
4.1.3 Analysis of the macroscopic behaviour . . . 63
4.2 Local scale observation of crack initiation and propagation . . . 68
4.2.1 Straining the notch tip and initiation . . . 68
4.2.2 Local propagation velocities and plasticity . . . 71

4.3 Summary 94

5 Stress Corrosion Cracking **97**
5.1 The sensitivity of AlZnMg alloys to stress corrosion cracking 97
5.2 SCC test in humid air 101
5.2.1 Fractography analysis 106
5.3 Macroscopic results of SCC tests in saline water 106
5.3.1 A typical SSC crack test in saline water 106
5.3.2 Analysis of the macroscopic behavior 110
5.4 Local results of SCC tests in saline water 114
5.4.1 Local plasticity 115
5.4.2 Intermittent transgranular fracture 129
5.5 Summary 133

6 Discussion, conclusions and perspectives **135**
6.1 Hydrogen diffusion 136
6.1.1 Hydrogen diffusion and crack propagation velocity 137
6.1.2 Absorption and desorption of hydrogen 138
6.2 Plasticity - grain boundary interactions 144
6.3 Optimizing the surface pattern for DIC 147
6.4 Conclusions and perspectives 154

Bibliography **157**

Chapter 1

Introduction

Metallic materials are often sensitive to "hydrogen embrittlement". When they are put in contact with the hydrogen gas, or with an environment which contains water, atomic hydrogen can be adsorbed on the surface and can penetrate the material. Once inside, and if a mechanical load is applied, hydrogen can be responsible for the initiation of cracks or the speed up of already existing cracks. This occurs for low mechanical loads where fracture is normally not observed. This phenomenon is widely active among structural metallic alloys in all sectors of industry: airplanes submitted to humid air, marine structures, pressurized water nuclear reactors... Note that "hydrogen embrittlement" is one of the mechanisms involved in "stress corrosion cracking", and is now widely recognized as the reason of the highest velocities observed, and also in "fatigue corrosion". It is therefore a major industrial concern because of its economic cost and also for safety reasons [1, 2, 3].

A new industrial sector, potentially concerned by "hydrogen embrittlement", is emerging: the "new hydrogen economy". Hydrogen gas is a way to store energy and release it in the form of electricity without emission of CO_2. It can be produced from renewable electricity by electrolyzers, from water. The gas produced should be collected, stored and distributed to users. This is planned to be done using the already existing pipeline network for CH_4 and stored under pressure. H_2 could also be stored in the solid state in the form of hydrides (in metals like Pd of Mg, or in new nanostructured materials). Finally hydrogen should be transported to the end user that could be gas stations for ground transportation (essentially trucks for public services at the moment), or to factories and even individual houses, in the future, for electricity and heating. These are produced by the reversed electrolysis combing oxygen from the air and H_2 in a fuel cell and rejecting water. Even if there is a culture of hydrogen gas storage in the chemical industry and therefore of the management of the risk of leaks, the wide variety of new installations that need to be developed involves a risk that H comes in contact with materials that can be degraded, including metallic alloys. In the European Union's (EU) vision for a climate-neutral plan, it is projected that the share of hydrogen in Europe's energy will grow from 2% (2019) to 13-14% by 2050 [4, 5].

Aluminum alloys are susceptible to hydrogen embrittlement [6, 7]. Moreover, they are present in multiple markets [8] such as transportation, energy, aerospace, packaging, automotive industries, building and construction... They are also involved in the development of the "hydrogen economy", for hydrogen production and for storage applications

[9]. This justifies studying the hydrogen embrittlement mechanisms in these materials.

In this context, a commercial AlMgZn alloy (with a low copper content) is chosen for this thesis. The conditions are such that either hydrogen is in the material before the force is applied ("internal hydrogen embrittlement" is studied) or hydrogen is produced by corrosion on the surface and the force is applied at the same time ("stress corrosion cracking", with hydrogen produced inside the crack, is studied). The force is applied on notched samples with a micro-tensile machine under an optical microscope. Single cracks are followed, on the side surface, by digital image correlation (DIC). Local velocities and strain maps with a sub-grain scale resolution are measured. Some elements of the hydrogen embrittlement mechanisms are discussed in the light of these new experiments.

The manuscript is divided into five chapters, as follows:

- Chapter 2: Literature Review. It covers the relevant hydrogen embrittlement phenomenological models, and recent studies of internal hydrogen embrittlement in 7XXX aluminum alloys (the same family of alloys as the one tested).

- Chapter 3: Materials and Methods. It describes the material and the methodology for studying fracture in conditions of internal hydrogen and in conditions of stress corrosion cracking.

- Chapter 4: Internal Hydrogen Embrittlement (IHE). It is dedicated to studying internal hydrogen assisted cracking at the macroscale and a local scale performing DIC. The samples are H-charged in an acid solution with a cathodic potential imposed. Different levels of embrittlement are obtained by varying the charging parameters (potential and time). Stress intensity factors, crack propagation velocities, quantification of the involved plasticity, and incremental crack opening profiles are measured for cracking at different embrittlement levels.

- Chapter 5: Stress Corrosion Cracking. It starts with a brief specific bibliography dedicated to stress corrosion cracking (SCC). Then SSC in humid air and in saline water at the macroscale and a local scale with DIC are studied. Similar to internal hydrogen embrittlement, stress intensity factors, crack propagation velocities, accompanying plasticity and incremental crack opening profiles are measured for cracking in different testing conditions (e.g., samples protected with lacquer to expose less surface to corrosive medium). An interesting observed phenomenon of intermittent fracture is also presented.

- Chapter 6: Discussion, Conclusion and Perspectives. SCC and IHE results are discussed using simulations and complementary experiences. Perspectives and conclusions are presented.

Chapter 2

Literature Review

2.1 Hydrogen in metallic materials

Hydrogen in its molecular state (H_2) is too large to enter in the lattice of metals, and monoatomic hydrogen (H) has to be produced to diffuse inside the metals. Early theoretical calculations [10] also show that the H_2 molecule is unstable in electron densities typical of metals and that the isolated H atom tends to segregate to regions where the electronic density is lower than the one in interstitial position. Defects (vacancies, grain boundaries, surfaces, hydrostatic stress fields) provide such environments which are more favorable for the hydrogen atom and therefore there is a tendency of hydrogen to be trapped at such defects or regions of high hydrostatic stress. For the same reason, if hydrogen is initially in the material, i.e. in interstitial position, the energy of the system will be reduced if H can find a defect and move to it. If the initial hydrogen concentration is high, the reduction of energy might even be enough to compensate the energy cost of creating new defects. This is the thermodynamic force for creating new surfaces (decohesion) or vacancies. The latter has been experimentally proved[11], the former is supported by ab initio calculations[12]. However, there are many other interactions of hydrogen with crystalline defects, especially those involving dislocations as we shall see now.

Macroscopically, hydrogen deteriorates the mechanical properties of metallic alloys. This phenomenon is called hydrogen embrittlement. This degradation occurs whether the metal has incorporated hydrogen due to previous exposure to hydrogen or because it is in contact with an hydrogen-producing environment. There is a difference in behavior under these two conditions. Therefore, the degradation due to hydrogen is classified into two categories: internal hydrogen embrittlement (IHE) and hydrogen environment embrittlement (HEE). For instance, IHE refers to the embrittlement of a metal that has been charged with hydrogen before testing. HEE refers to environments where the hydrogen may be generated from a corrosion reaction. For instance, in stress corrosion cracking (SCC) in aqueous media, hydrogen production and penetration into the material, is often the cause of an embrittlement that will contribute to SCC (7XXX aluminum alloys are an example)[2].

Several hydrogen-induced degradation models have been proposed, with multiple variations of the same elementary mechanisms. Some of the mechanisms have been changing over time and there is no consensus about the physical causes of the hydrogen embrittle-

ment phenomenon. In this chapter, the most relevant mechanisms are introduced. Because our study focuses on a face centered cubic (fcc) metal (aluminum alloy), we will focus on fcc materials but some body centered cubic metals will also be mentioned.

In this fist section of the chapter, some general aspects of hydrogen in metallic materials are mentioned (diffusion, slip planarity, crack propagation with intensive dislocation activity), merely as an introduction to better understand the hydrogen embrittlement models that are presented later.

In the second section, hydrogen embrittlement models such as AIDE, HEDE, HELP, HESIV are presented.

In the third section, relevant recent studies in the AA7XXX series (AlMgZn alloys) will be presented because our material belongs to the AA7XXX (also called 7000 series) family of alloys.

2.1.1 Hydrogen diffusion in metals

Hydrogen atoms can be accommodated in the interstitial sites of the crystal lattice and can move into neighboring positions by diffusion. The frequency of the jumps determines the hydrogen transport properties. Fick's law is usually used to evaluate the evolution of concentration. However, the crystal lattice, in a real metal, is far from perfection. The presence of vacancies, dislocations, interfaces, precipitates, grain boundaries and other defects can create the phenomenon of hydrogen trapping. Hydrogen trapping involves the "repartitioning" (redistribution) of hydrogen between "regular" interstitial sites and into the sites belonging to the microstructural defects [13], depending on the value of trap binding energy (and the temperature). Traps are usually classified as reversible or irreversible. The irreversible traps have a high migration energy barrier for an H-atom to jump back into a normal lattice site, such that a the temperature of the study, the frequency of escape from the trap is very low. The reversible trap sites have a weak binding energy. In order to take into account this complexity, an effective diffusion coefficient is used often for the diffusion calculations using Fick's law. The term effective is used to describe the combined effects of perfect lattice diffusivity, the presence of microstructural defects, and the different traps. Another important effect is the attraction of hydrogen to regions with high hydrostatic stress, such as crack tips[14][15].

2.1.2 Dislocations and hydrogen

slip planarity

The density and the distribution of dislocations have been found to depend sensitively on the crystal structure, alloying elements, temperature, stacking fault energy (SFE). A stacking fault is an interruption of the normal stacking sequence of atomic planes in a close-packed crystal structure. These faults have an excess energy, the stacking fault energy. When dislocations are dissociated into partial dislocations, or if the core is split on different planes, the lower the stacking fault energy, the further apart the partial dislocations, the more difficult the recombination of the core in order to change glide plane (it is said that screw dislocations "cross slip"), and finally the more planar glide is. Materials can be classified into two groups (1) planar slip materials, and (2) wavy slip materials. The

dislocation structure after deformation is the basis for classifying the materials in these two categories since it clearly shows the effect of cross slip.

In wavy slip for face centered cubic structures, the dislocations are arranged in dislocation tangles, which form mainly because of an extensive cross slip. The distribution of dislocations is not homogeneous. Most dislocations are clustered in high-density zones adjacent to almost dislocation-free areas, like cells. In fcc systems where slip is planar, cross slip is difficult, and the dislocations are arranged in planar arrays. The dislocation distribution on single slip planes is more uniform. Typical examples of the two types of structure after monotonic deformation are shown in Fig.2.1a and b where Al is added to Cu to change the stacking fault energy and favour slip planarity in (b). It is also possible to see the effect in an fcc steel where the change in stacking fault energy is obtained by changing the concentration of nitrogen in the system (interstitial N is supposed to segregate to stacking faults) in Fig.2.1c and d promoting slip planarity [16]. In relation with our problem, such a slip localization due to hydrogen has been proposed for a long time, but only recently quantified in Ni. A fine characterization of the influence of H on dislocation cell structure have shown that indeed H reduces cross-slip and favors localization of slip[17, 18].

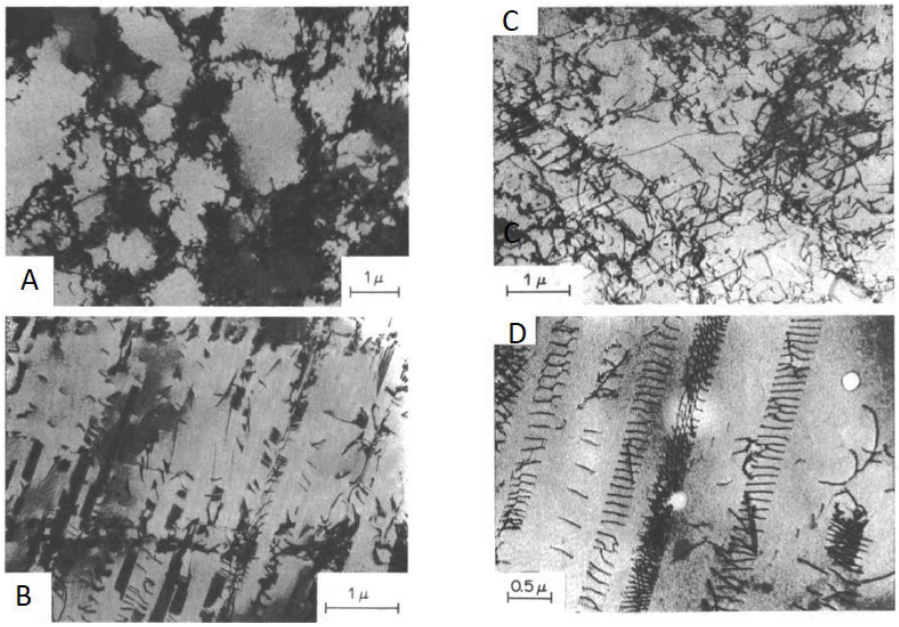

Figure 2.1: Dislocation substructure in (A) wavy case, pure copper 10% applied strain, showing a cellular arrangement of tangled dislocations, (B) planar slip case, Cu-16%Al elongated 10% showing planar dislocation arrays. The effect of nitrogen on the dislocation arrangements in 12.7% Ni stainless steel (C) 0.004N, (D) 0.12 N.[16]

Dislocation emission from the tip during crack propagation and crack tip opening displacement

Figure 2.2[19] shows a side view of a crack propagating under different partial pressures of hydrogen gas. Contrary to Al, H_2 in contact with Fe leads to a flux of atomic H in the material because a small fraction of adsorbed H_2 molecules splits and give chemisorbed atomic H on the surface. A small fraction of this enters this Fe-6%Si single crystal and leads to crack propagation. There is an intensive plastic activity at the tip which creates an opening of the crack. The angle formed changes with the partial pressure of H_2: the crack in (a) is sharper than in (b). This angle variation can be interpreted if the crack advance is a combination of some form of "decohesion" ahead of the crack tip and the contribution of the emergence of dislocations at the surface (the step formed at the surface by the dislocations is decomposed into a component with is in the direction of propagation and another one which opens the crack). This experiment illustrates the idea that "brittle fracture", due to hydrogen, occurs usually with a large amount plasticity. We will see below that the emitted dislocations "shield" the crack tip from the external load, i.e. their elastic field creates a stress singularity at the tip of sign opposite to the one created by the remote applied stress. In other words the opening stress ahead of the crack tip is decreased by the stress field of the plastic zone. Nevertheless, fracture occurs when enough hydrogen is present and the more hydrogen there is, smaller is the contribution of plasticity to the crack advance, i.e. lower is the opening angle of the crack. A good measure of the degree of embrittlement is the opening angle. It will be used (or an equivalent parameter) to characterize plasticity in our experiments.

In some interesting papers presented below in section 2.3, the authors use a similar measure which is the "crack tip opening displacement" (CTOD) [20]. It is briefly presented now. In figure 2.3a, an elliptic crack tip is represented. The procedure is the following: consider the average local propagation direction of the crack, which in this simple case is the horizontal line, and draw a 90° angle at the crack tip, oriented is such a way that the propagation direction cuts it in 2 symmetric 45° angles. Then the intersection of the two segments which define the angle with the side surfaces of the crack give two points in between which the CTOD is measured [21]. A more realistic case is shown on Fig. 2.3b.

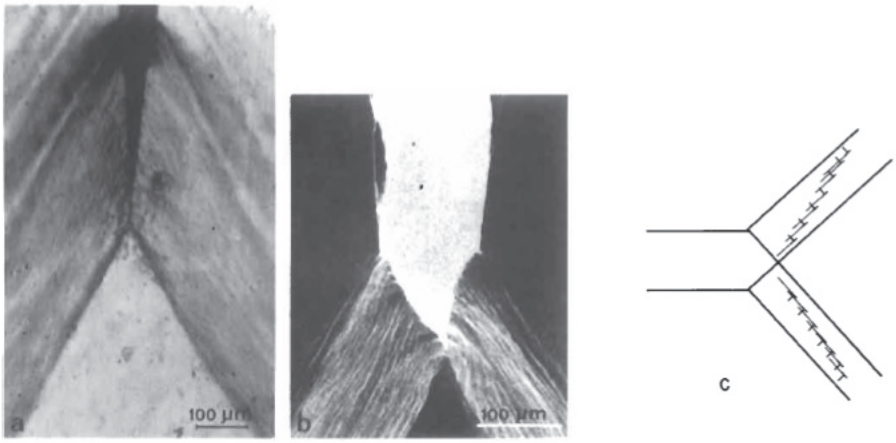

Figure 2.2: In (a) sharp crack formed in a hydrogen atmosphere in Fe-Si. In (b) the crack opens by dislocation slide-off at the crack tip. In both cases, dislocations are emitted form the crack tip, form slip bands. The angle of the wedge opening in (b) is defined by the intersection angle of the two slip planes with the crack plane. In (c) the dislocation configuration generating the crack is illustrated in terms of alternate emission of dislocations on the two complementary slip planes. [19][22]

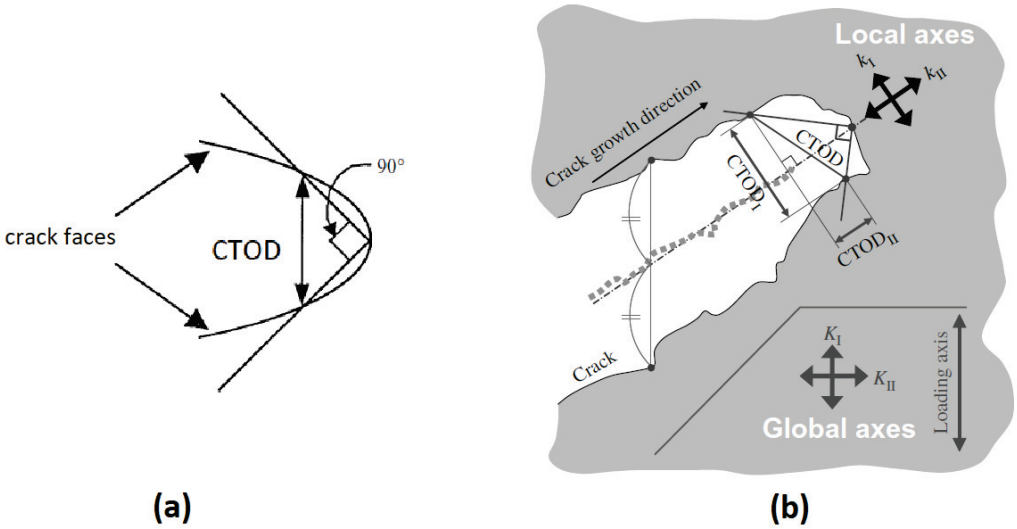

Figure 2.3: (a) CTOD definition based on a 90 degrees intercept (b) schematic illustration of the CTOD measurement in a more realistic crack configuration [21]. A tomographic slice of a cracked sample in a different position of the crack front (across the thickness) may have a different CTOD value.

2.2 Hydrogen embrittlement mechanisms

2.2.1 AIDE

Based on the similarities between internal hydrogen embrittlemnt, stress corrosion cracking, and liquid metal embrittlement, Lynch [23, 24] proposed a mechanism called adsorption-induced dislocation emission (AIDE). AIDE comprises the dislocation nucleation (facilitated by H adsorption) and the later dislocation movement away from the crack tip under the applied stress. The crack grows by the contribution of the step left by the emitted dislocation on the surface and by the nucleation and growth of microvoids (or nanovoids) ahead of crack tips. The void nucleation occurs at second phase particles and/or slip band intersections. The coalescence of the voids serves to re-sharpen crack tips and result in small crack tip opening angles. However, crack growth occurs primarily by dislocation emission from crack tips (Fig. 2.4 and 2.5A [25]) and void nucleation is not always necessary for AIDE. Note that the void nucleation, in the model, might also be facilitated by the diffusion of absorbed hydrogen and the coalescence of vacancies.

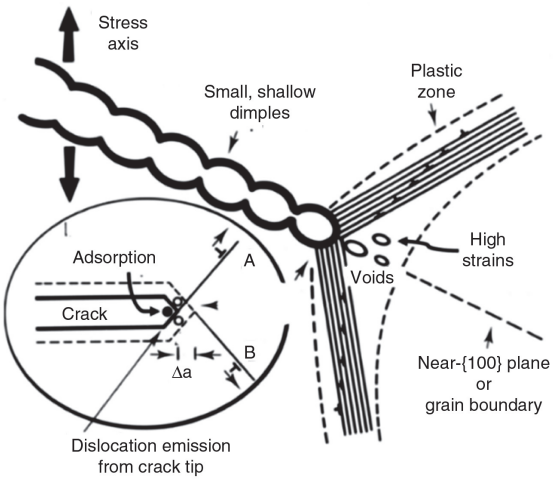

Figure 2.4: Schematic diagram illustrating the adsorption-induced dislocation emission (AIDE) mechanism, which involves crack growth by alternate-slip (for transgranular paths) from crack tips, facilitating coalescence of cracks with voids formed in the plastic zone ahead of cracks [25]

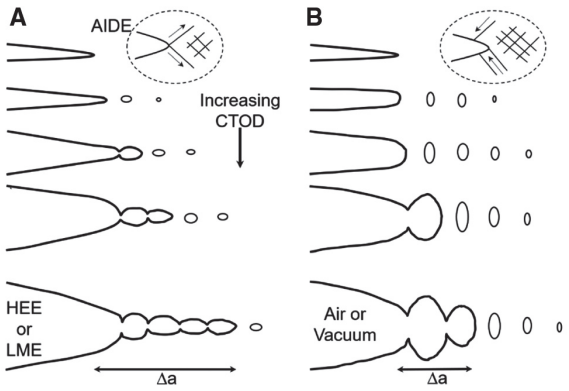

Figure 2.5: Schematic diagrams comparing crack growth from an initially sharp crack for equivalent (increasing) crack-tip-opening displacement (CTOD) (and same uniformly spaced void nuclei) for (A) crack/void growth involving AIDE at the crack tip for aggressive environment (with no significant H adsorption at voids), and (B) crack/ void growth involving egress of dislocations around cracks in inert environments. Dislocation emission from crack tips along with some general dislocation activity occurs in embrittling environments, although only general dislocation activity occurs in inert/air environments (illustrated in insets). Larger crack-growth increments, Δa, for given crack-tip-opening displacements therefore occur in embrittling environments.[25]

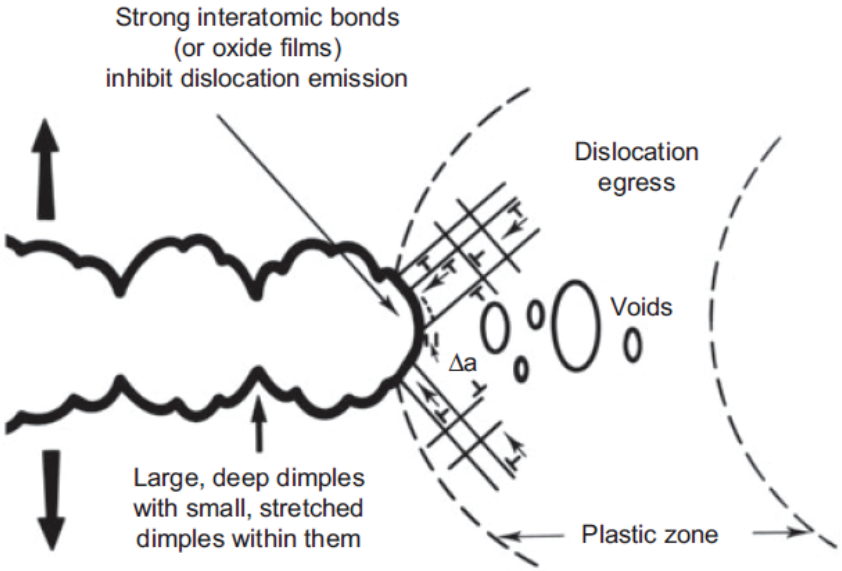

Figure 2.6: Schematic diagram illustrating fatigue ductile crack growth involving coalescence of cracks with voids by egress of dislocations nucleated from near crack tip sources [23]

In an inert environment, when dislocation egress (going out of or leaving a place) from around crack tips is predominant (Fig. 2.6) , solely a minor dislocation proportion that is emanating from near crack tip dislocation sources exactly intersect crack tips to produce crack advance. Most of the dislocations produce only blunting or contribute to the strain ahead of cracks. Therefore, large strains ahead of cracks are needed to produce crack growth by microvoid coalescence (Fig. 2.5B). Conversely, when hydrogen adsorption weakens interatomic bonds at the crack tip, it promotes dislocation emission at lower stress. A larger part of dislocation activity derives from crack growth since dislocation emission results in crack advance and crack opening (Fig. 2.5A). In this way, the coalescence of cracks with voids occurs at lower strains.

2.2.2 HEDE

The HEDE (Hydrogen-Enhanced Decohesion) model is based on hydrogen decreasing either grain boundary or cleavage plane cohesion [26, 12]. The traps lead to hydrogen segregation, for instance at grain boundaries, decreasing the cohesive strength locally between metal atoms. For example, Du [27] performed DFT calculations of hydrogen interactions at grain boundaries of FCC and BCC iron. Du stated that H accumulation at specific grain boundary structures is energetically favored. The presence of hydrogen reduces the critical strain required to fracture the material due to difference in binding energy with the hydrogen presence. The predominant experimental proof for HEDE is the observed reduction in the crack tip opening angle with increasing hydrogen content for Fe-Si [28] (Fig. 2.2). Barrera states that hydrogen embrittlement (HE) happens within the crack tip fracture process zone (FPZ), where the tensile stress is high. [29][30]. Lynch [24] states four locations where high hydrogen concentration and decohesion could be found for transgranular cracking :

- Exactly at atomically sharp crack tips due to ‘adsorbed’ hydrogen.
- Several tens of nanometres ahead of cracks where dislocation shielding effects result in a tensile-stress maximum.
- Positions of maximum hydrostatic stress (several micrometers ahead of cracks in high-strength steels).
- Particle–matrix interfaces ahead of cracks.

Lynch [24] also says that large elastic stresses might create high enough hydrogen concentrations ahead of crack tips to reach decohesion. Furthermore, such stresses could be predicted by strain-gradient plasticity models [31].

Several micromechanical models have been proposed and integrate the decohesion concept. Their derivation or justification can be found the review paper by Gangloff [26]. At the macroscopic scale, H embrittlement or stress corrosion cracking is characterized on pre-cracked compact tension samples. A typical macroscopic curve gives the crack velocity (macro) as a function of the stress intensity factor. The curve shows a threshold K_{th} below which the pre-existing crack does not propagate, then a very steep increase of the velocity in the vicinity of K_{th} and finally a "plateau velocity" or stage II velocity $\frac{da}{dt}_{II}$

where crack propagates independently of the applied K. Both quantities, K_{th} and $\frac{da}{dt}_{II}$, have been modeled.

Gerberich [32] proposes Eq.2.1. The macrosopic threshold is related to the critical local stress intensity factor for decohesion (k_{IG}). It is the Griffith stress intensity factor, calculated from atomistic quantities such as the surface excess energies and the grain boundary excess energy (for intergranular fracture). It is very low (below 1 MPa$\sqrt{m}$). The physical reason why the crack tip can withstand the very large K_{th} (about 8 MPa$\sqrt{m}$)) is the plastic zone which "shields" the stress coming from the external load. This shielding was modeled by Gerberich by a single dislocation pile up shown on Fig.2.7 and elasticity solutions for crack-discrete dislocations interactions. α' and β' are obtained from this model. Then the local hydrogen concentration C_H and the yield stress σ_{ys} are introduced empirically in the model and mean that local hydrogen decreases the Griffith stress intensity factor and that the lower the yield stress, the lower the K_{th}. Finally, the α parameter is fitted on experimental data.

$$\mathbf{K_{Ith}} = \frac{1}{\beta'} \exp \frac{(k_{IG} - \alpha C_H)^2}{\alpha' \sigma_{ys}} \tag{2.1}$$

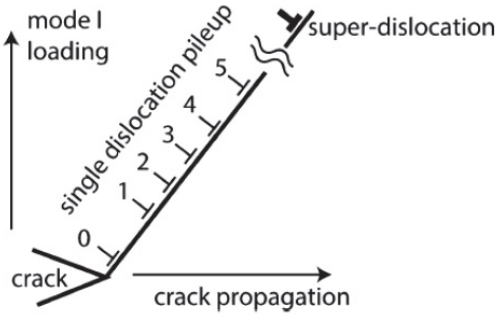

Figure 2.7: Schematic of dislocation-shielding geometry used in determination of the expression of the threshold intensity [33]

Gangloff has modelled the "plateau crack propagation velocity" [26][35][34]. His model is illustrated on Fig. 2.8. It couples the elements of crack tip H solubility, scale-dependent crack tip stress and strain, local H concentration, and a decohesion failure criterion. The crack propagation velocity $\frac{da}{dt}_{II}$ is represented by Eq 2.2:

$$(\frac{da}{dt})_{II} = \frac{4D_{eff}}{X_{crit}} \{erf^{-1}(1 - \frac{C_{H\sigma-crit}}{C_{H\sigma}})\}^2 \tag{2.2}$$

where (D_{eff}) is the effective hydrogen diffusion coefficient, X_{crit} is the distance ahead of the crack tip where the hydrostatic stress is the highest. The idea is that the plastic zone shields the external stress, i.e. eliminates the stress singularity at the tip. This moves the maximum stress at a certain distance ahead of the crack tip, where H accumulates and induces a decrease of cohesion. After a waiting time which correspond the time to reach a critical local hydrogen concentration at X_{crit}, by diffusion, fracture occurs at X_{crit} (where

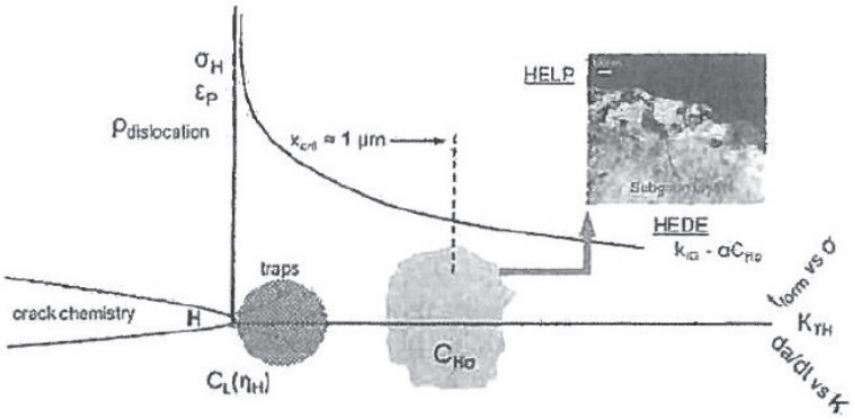

Figure 2.8: Localized crack tip chemical, mechanical and microstructure processes that interact to produce process zone H damage [34]

the stress is also the highest). This crack embryo instantaneously merges with the main crack. Crack advance is discontinuous [34]. $C_{H\sigma-crit}$ is the critical concentration of H necessary for decohesion at X_{crit} and is an inverse function of the local tensile stress, $C_{H\sigma}$ is the mobile hydrogen concentration in equilibrium with the crack tip that is enhanced by the hydrostatic stress.

The weaknesses of this model is that it is difficult to calculate X_{crit}, which requires a perfect shielding to exist. The effective diffusion coefficient is also difficult to measure or to calculate. Crack arrests markings are often found on stress corrosion cracking fracture surfaces, but they are not always in agreement with known hydrogen diffusion coefficients [36].

Effect of the stress field near the crack tip

In the model above, the distribution of the hydrostatic stress ahead of the crack tip is important because it attracts hydrogen. The stress varies with the distance from the crack tip and its magnitude near the crack tip depends on the different mechanical approach, especially the plasticity model considered to estimate the stress field. In classical plasticity, there are two main approaches: a perfectly plastic model where the stress can never be higher than the yield stress, and a plastic model that considers plastic hardening. The HRR model (Hutchinson Rice and Rosengren) describes the crack tip field (stress and strain) from the assumption that the material follows power low hardening. The HHR crack tip stress field is considered usually as "classical plasticity" for metals.

More recent plasticity models are formulated in the frame of the strain gradient plasticity (SGP) theory. The strain gradient SGP theory introduces the internal length parameter concept (l) as a material intrinsic property for solving a strain gradient problem [37]. Two important models for SGP are: Phenomenological strain gradient plasticity (Phenomenological SGP) and mechanism based strain gradient plasticity (MSG plasticity) [38]. The plasticity model chosen for describing the stress field near the crack tip can create significant differences, as can be seen in Fig. 2.9 for the Monel K500 nickel base

alloy. The stress field can raise the value of the hydrostatic stress (σ_H), close to the crack tip, more than 20 times the yield stress, depending on the applied K and the model chosen [31].

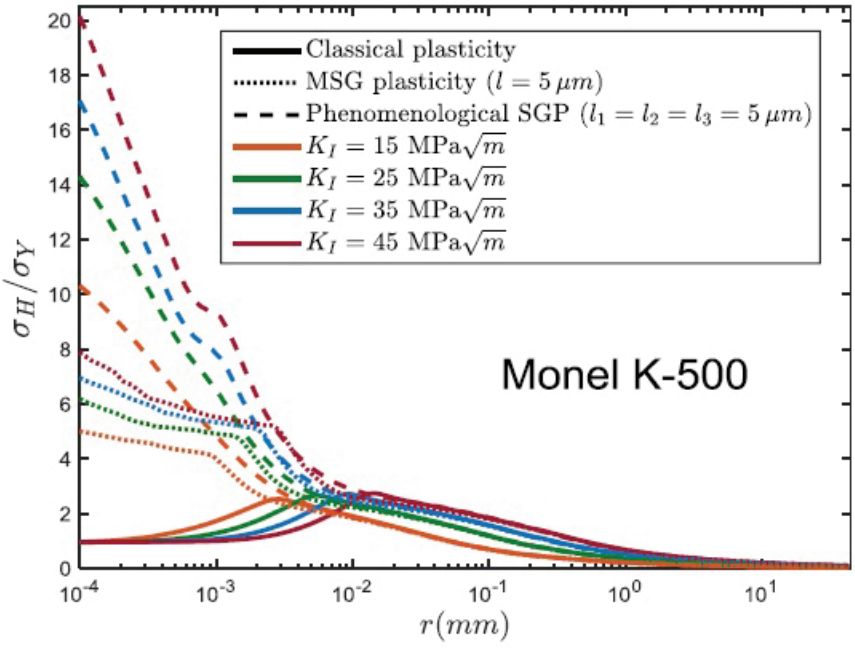

Figure 2.9: FEA calculated curves, the hydrostatic stress normalized by the yield stress versus distance ahead of a blunted crack tip with Monel K-500 material using different plasticity models [31].

The magnitude of stress close to the crack tip in SGP is particularly relevant in hydrogen assisted cracking (HAC), where the damage takes place within 1 μm to the crack tip [39]. High hydrostatic stress promotes high-trapped H concentration for crack tip damage. By using the SGP theory, the predictions of the threshold stress intensity factor and crack speed agree with experimental data for a high strength austenitic Ni-Cu super alloy[31].

2.2.3 HELP

The hydrogen-enhanced localized plasticity (HELP) theory states that hydrogen embrittlement is caused by an increase in the dislocations' mobility when hydrogen is present. This theory suggests that hydrogen has a screening effect on dislocations' elastic stress, enhancing the dislocation mobility and slip localization. The "screening"[14] of the elastic interactions comes from the segregation of hydrogen in the elastic fields: around a dislocation there are regions in tension, where the hydrogen concentration, at equilibirum, will be higher than the average and regions in compression where the H concentration will be lower than the average. As a consequence of this hydrogen distribution and due to the elastic field that it creates and which is superimposed to the one of the dislocation, the effective elastic field of the dislocation is reduced. As a consequence, hydrogen decreases the elastic interactions between dislocations and obstacles. It also enhances the rate at which dislocation sources operate. These postulates have been supported by TEM experiences in thin foils in the presence of hydrogen [40] and elastic calculations of dislocation-dislocation interactions [14]. One of the most famous is shown on Fig.2.10: the distance between dislocations in a pileup is the result of the applied stress and the repulsion between dislocations of the same sign. Introducing hydrogen in the system reduces these distances and the change is reversible when hydrogen is extracted, as is expected for the elastic theory.

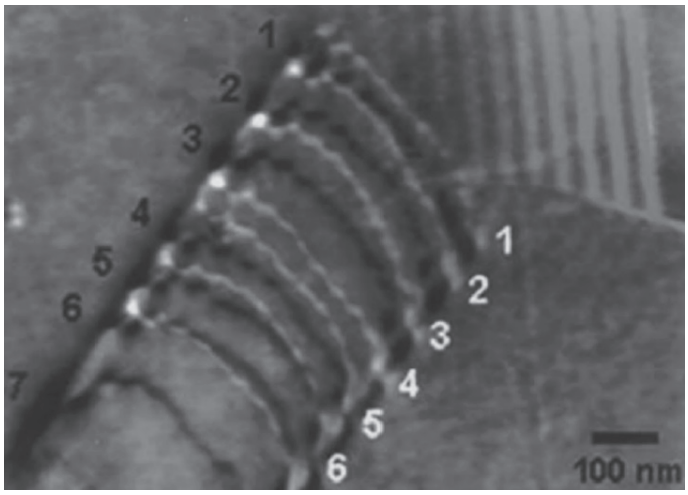

Figure 2.10: Dislocation pileup in 310 stainless steel due to solute hydrogen [40]

The reduction of the repulsive forces between dislocations by hydrogen promotes dislocation mobility, can lead to pile-up against barriers such as grain boundaries, as it is shown in Fig. 2.10. An hydrogen "atmosphere" is produced because the strain fields surrounding a dislocation attract hydrogen, resulting in lower yield strength. The hydrogen atmosphere moving with the dislocations diminishes cross-slip and increases slip planarity [29]. Hydrogen enhanced slip planarity in FCC metals [17, 18] can also be attributed to a reduction in the stacking fault energy. There is no agreement on the magnitude of the reduction in SFE [42, 29].

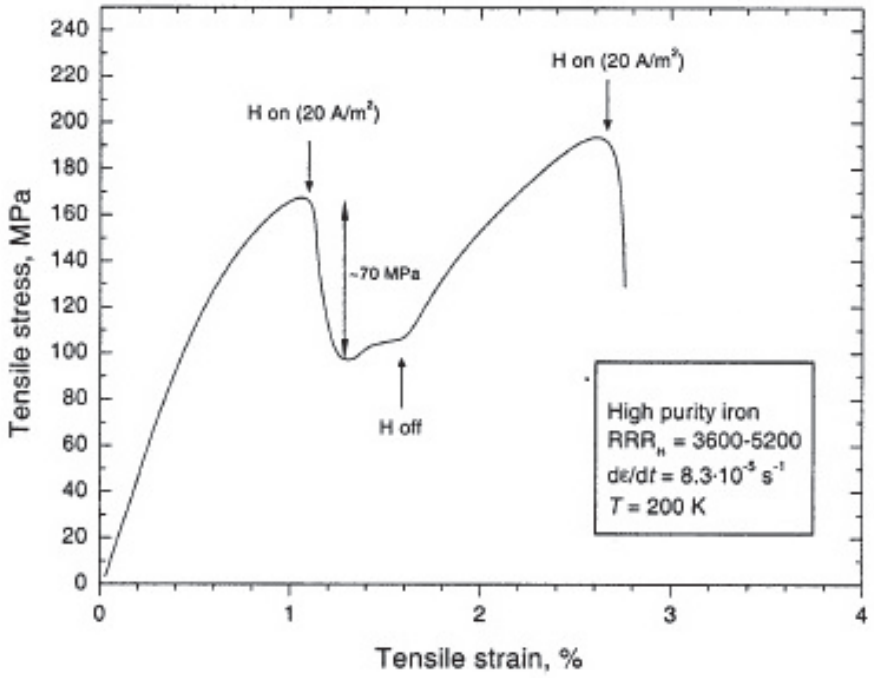

Figure 2.11: Tensile test of high purity iron with hydrogen charging (20 A/m2) in 0.1 N $CH_3OH - H_2O - H_2SO_4$ solution switched on and off. [41]

In addition, HELP is also supported by experiments at the macroscale showing softening in the presence of hydrogen. It is the case of iron in the tensile test in Fig. 2.11. The arrows indicate the hydrogen charging switching on and off. It is seen that the yield strength falls quickly from 150–170 MPa to the 70 MPa at the same moment that H is switched on (HELP results in a lower yield strength). After that switching H off, the yield strength of the iron returns to its initial value typical for the hydrogen-free material. Such reversible behavior indicates that the observed effect is not related to the formation of cracks during the hydrogen uptake under tensile stress.

Besides, based on finite elements simulations, Sofronis [43][44][45] claims that hydrogen promotes strain localization and shear bands also at the macroscale.

Enhanced dislocation mobility and fracture mechanisms

Robertson [33] establishes a link between the enhanced dislocation mobility and the fracture mechanism. It is based on a correlation between the microstructure (and the dislocation structure) formed immediately beneath the fracture surface and the hydrogen presence. For example, Martin [46] studied a Nickel 201 alloy, where hydrogen induces intergranular failure. In the presence of hydrogen, the dislocation structure found immediately beneath the intergranular crack (Fig 2.12a) is more developed than the dislocation structure that corresponds to the same level of deformation without hydrogen. The cell size and cell wall thickness of the dislocation structure, even in a large distance (a few microns) from the crack surface (Fig 2.12b), are more developed in comparison with the one found in the absence of hydrogen at 10% strain tested in the air (Fig 2.12c). Besides, hydrogen-induced intergranular cracking in Fe has similar results [47] (Fig 2.13). These two examples (Fig 2.12 and 2.13) show a dislocation structure that is more dense than the one expected in the absence of hydrogen. Robertson claims that the microstructure beneath the fracture surface is generated under stress before the failure event itself. Martin [48] [49] suggested that the modified deformation microstructure and local hydrogen concentration establish weak regions, which dictate the local crack path and the topology of the fracture surface.

Taking into account these two previous examples, it is interesting to comment about HEDE theory. It is worth to remember that HEDE uses plasticity to establish a zone of high stress ahead of the crack tip (in the fracture process zone FPZ) but does not include plasticity as a component of the fracture itself. Assuming that intergranular failure is caused by HEDE alone. In that case, prior plasticity would have no impact on the failure process, and would be unaffected by the hydrogen. However, this would be contradictory with the existence of this altered dislocation structure in the presence of hydrogen that according to Robertson[33] influences the failure mode and the crack path.

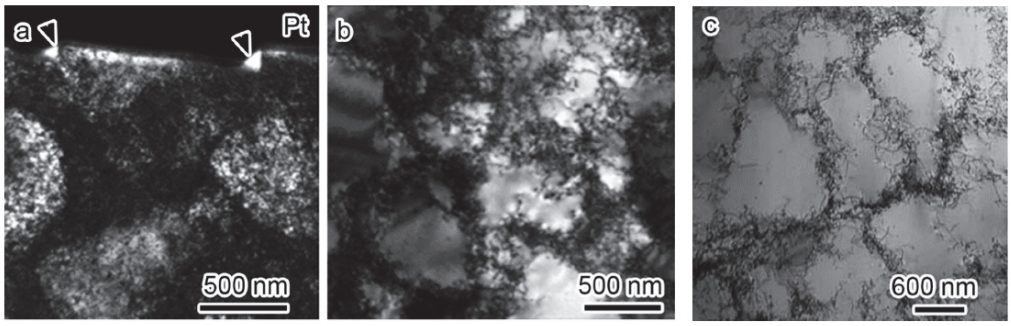

Figure 2.12: Bright-field electron images displaying the microstructure (a) immediately below an intergranular facet with hydrogen prescence, (b) 3 mm below a facet, (c) 10% strain in air. [33]

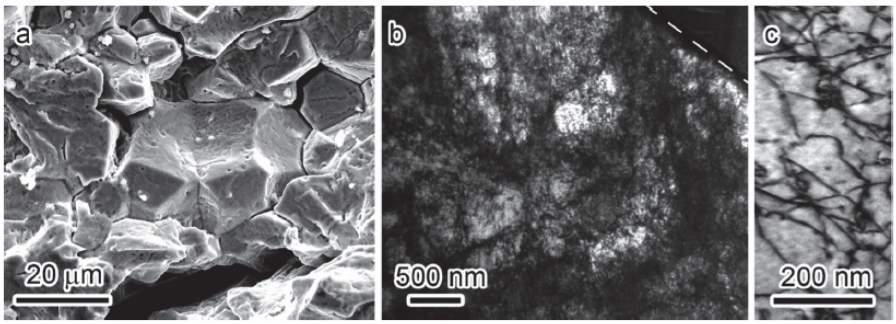

Figure 2.13: Hydrogen-induced intergranular failure of Fe following cathodic hydrogen charging during deformation: (a) low-resolution SEM image of the fracture surface; (b) bright-field electron image of the structure of the dislocations immediately beneath the facet, (c) bright-field electron image of the deformation structure for a plastic strain of 5 % in the absence of hydrogen. [47] [33]

Plasticity interaction with grain boundaries and intergranular failure

In order to better understand intergranular failure, it is helpful to present the way that dislocations interact with grain boundaries and the strain transfer across grain boundaries without hydrogen. Figure 2.14 shows images of dislocations interacting with grain boundaries [33]. Dislocations that impact a grain boundary (GB) can be accommodated in the grain boundary (Fig 2.14a). Incident dislocations can be trapped or annihilated in the grain boundary, and new dislocations can be generated and emitted from it, activating new slip systems during the emission and transferring the strain across the grain boundary [50](Fig 2.14c). It is possible that a cross-slip is produced onto the grain boundary plane, and the strain is incorporated in the GB (Fig 2.14b) and produce emission in another zone. Disruption or displacement of the GB is possible because of the interaction with dislocations (Fig 2.14d). There might be important changes in the GB structure after the interaction with the dislocations that may weaken the GB, in the presence of hydrogen.

At the the micron scale, interactions of "dislocation channels" (a localized deformation present in irradiated alloys along "channels" that were cleared from irradiation defects by the first dislocations crossing the crystal) with grain boundaries exist with similar characteristics. The dislocation channels (DC) interactions with grain boundaries can be analyzed using SEM images and also strain fields (Fig. 2.15) from DIC. Figure 2.15b shows a deformation map that shows how strain localization is blocked by a grain boundary in the case of DC2. Figure 2.15b also displays the case where the strain is transmitted across the grain boundary for DC1. The change in the direction of the deformation band after the grain boundary impact obeys a change in the slip system that is activated to enable strain transmission [51, 52, 33, 50]. The classification of grain boundary interactions with the dislocation channels (deformation bands) are summarized in Fig. 2.16. The three classifications are (a) slip blockage, (b) slip transmission and (c) slip along the grain boundary. The interactions are shown schematically, with SEM images, simulations and TEM images. Also, it is possible to show the interaction with a deformation map (Fig. 2.15b). These aspects are present in our experiments and will be discussed in the last chapter of the thesis.

Robertson [33] states that changes in the grain boundary produced by the interaction with dislocations leads to a structural modification that can alter the GB strength, playing a key role in the intergranular failure. The relative magnitudes of the compositional and structural GB alterations on its cohesive strength are unclear, especially for the hydrogen-induced intergranular cracking. Robertson has revised the fracture part of his model and now states that the HELP's role is to weaken the grain boundary, accumulate hydrogen on it, and change the local stress state, but the final fracture is produced by decohesion (while it was by an intense plastic shear parallel to the GB in the original version of his model). Martin [42] states that the mechanism of dislocation mediated decohesion is critical to establish the failure conditions and the embrittlement effect. Martin[42] also claims that HELP is a universal mechanism, based on studies performed in a variety of materials and loading conditions, regardless of the failure mode (quasi-cleavage or intergranular). Quasi-cleavage (QC) is a transgranular fracture, most likely due to intense localized plastic deformation, which appears flat in the scanning electron microscope.

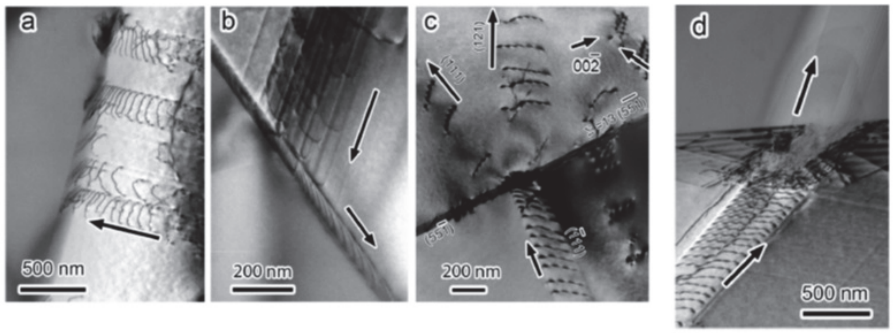

Figure 2.14: Bright-field electron images displaying possible interactions of dislocations with grain and interphase boundaries and the attendant alterations in the grain boundary structure as strain is transferred across it. (a) accommodation of lattice dislocations in a grain boundary at the point of intersections (titanium)(b) Cross slip of lattice dislocations onto a grain boundary (stainless steel). (c) Slip transfer across a grain boundary (stainless steel). (d) grain boundary structure disruption because of slip transfer [33]

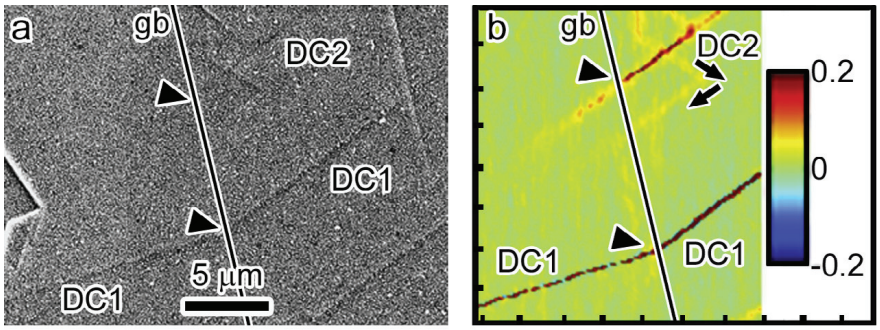

Figure 2.15: Proton-irradiated 13Cr15Ni stainless steel tensile bar. (a) SEM image showing the intersection of two dislocation channels, DC1 and DC2, with a grain boundary, with slip continuity across the grain boundary occurring for DC1 only where the strain has transmitted across the boundary. (b) Strain map determined by DIC showing the interaction region. The arrows indicate cross slip event and arrowheads the approximate interaction site with the grain boundary. The the grain boundary location is also indicated.[50] [52]

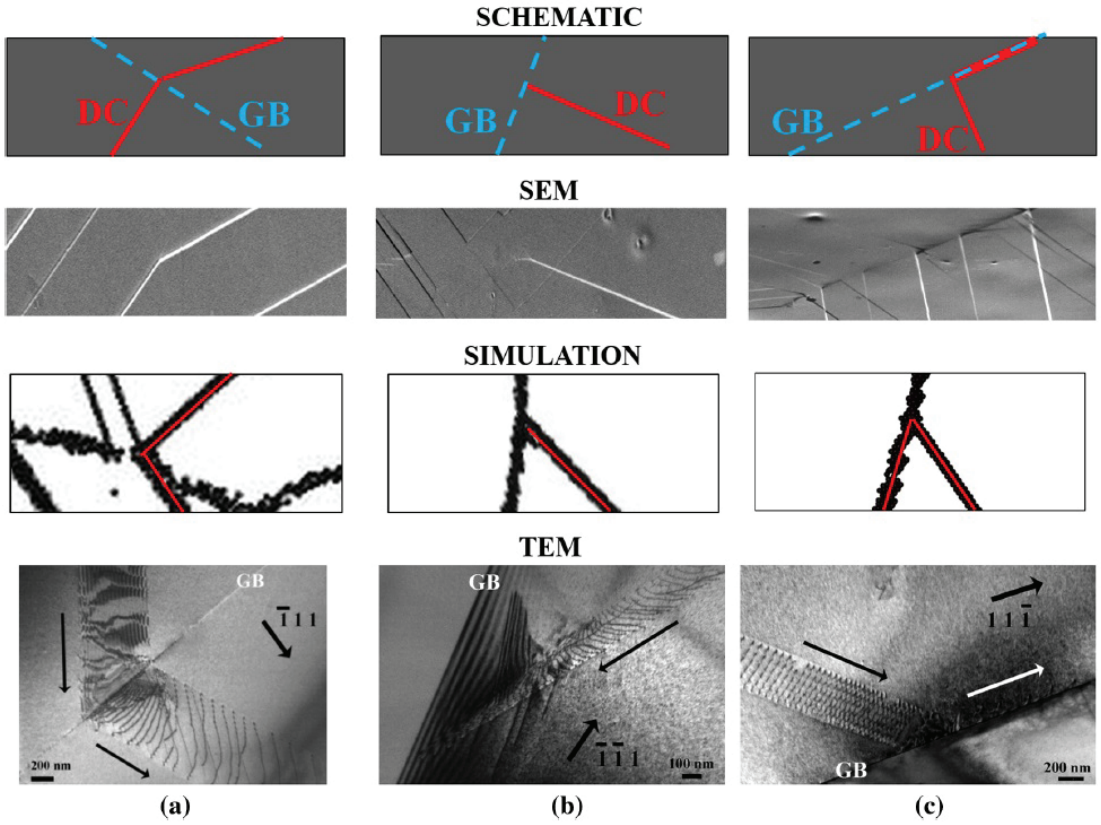

Figure 2.16: Schematic diagram, SEM, simulated example and TEM images of the DC–GB classifications; (a) slip transmission, (b) slip blockage (c) slip along the grain boundary. In the TEM images, Kr+ irradiated 304 was used in (a), and Kr+ irradiated 13Cr15Ni was used in (b) and (c). The moving directions of the dislocations are indicated by the thin arrows. Slip is highlighted in red for the simulated examples. [51]

2.2.4 Vacancies and nano-micro voids related mechanisms

The hydrogen enhanced strain induced vacancy (HESIV) formation mechanism claims that the density and clustering of vacancies are enhanced in the presence of hydrogen. The idea is that in localized strain regions, dislocations annihilate which produces vacancies. In the absence of hydrogen, these vacancies diffuse and are eliminated on kinks on dislocations or in grain boundaries. In the presence of hydrogen, they are stabilized and accumulate in the system. An important density of vacancies and their clustering has been detected at a low temperature performing thermal desorption spectroscopy and positron lifetime measurements in H embrittlement conditions. Vacancies may coalesce to form microvoids, which may combine to form larger voids leading to a decrease in ductile crack growth resistance or to damage in strain localization zone. Hydrogen related fracture modes, such as IG (intergranular) or QC (quasi-cleavage), can be produced with a HESIV contribution [53]. The HESIV phenomenon can be observed during tensile testing of hydrogen-charged samples. Nagumo originally proposed HESIV ([54] for steels and later extended by Takai [55] to iron and Inconel.

The model proposed by Nagumo ([55] [54] [56]) considers vacancy clusters rather than hydrogen itself as the primary factor of HE. Nucleation of a high density of voids enhances the localization of voids at the crack tip that leads to a reduction in ductile crack growth resistance [55]. While the observed global hydrogen content is minimal (in some steels, less than 1ppm of hydrogen can cause failure), the density of vacancies, stabilized by hydrogen, is substantial enough to cause degradation of mechanical properties.

Neeraj [57] have proposed a combination mechanism of plasticity-generation (HELP), and hydrogen enhanced vacancy formation (HESIV), to explain the fracture surface and the underneath dislocation structure of ferritic steel, which failed by ductile and quasi-brittle fracture. An important dislocation activity was found just beneath the fracture surface for both quasi-brittle and ductile failure. Neeraj [57] suggested that the interactions between hydrogen and dislocations activities in the localized deformation regions promote the nucleation of nano-voids. The linkage of these voids leads to crack initiation and propagation.

Slip bands intersections and micro-voids

Zhang [58] observed that the presence of hydrogen in nickel based alloy 718 leads to quasi cleavage. The deformation microstructure of Alloy 718 developed during slow strain rate tests is characterized by considerable slip localization and planar dislocation slip bands in the non-hydrogen charged and also in the hydrogen charged regions. In the hydrogen charged region, cracks form along the planar dislocation slip bands (Fig 2.17), leading to the formation of slip-traces like features on the fracture surface, whereas cracking along grain boundaries and twin boundaries were not observed (Fig 2.18). Underneath the fracture surface (< 200 microns beneath), likely slip planarity and localization is promoted within the framework of the HELP mechanism as suggested by Martin and Robertson [33]. Dislocations can transport hydrogen at low strain rates, and dislocations can act as trapping sites for hydrogen. Therefore, high concentrations of hydrogen agglomerate at dislocation slip bands may form after deformation (Fig. 2.19a and b), especially at their intersections (Fig. 2.19c). Consequently, extensive hydrogen-dislocation interaction at these sites leads to the formation of nano-voids. Nano-voids weaken the dislocation boundaries, and their subsequent widening and coalescence via dislocation process result in crack initiation and propagation along the dislocation boundaries (Fig. 2.19d). Koyama [59] observed slip localization and fracture surfaces in the austenitic steel, similar to Zhang's work. However, Koyama has indicated that voids tend to nucleate at the triple junctions of grain boundaries and at intersecting sites between the dislocation slip planes and grain boundaries, which was not observed in the Zhang study where slip bands intersections are predominant for crack propagation (Fig. 2.17) leading to traces in the fracture surface and characteristic features that can be related to nanovoids (Fig. 2.18).

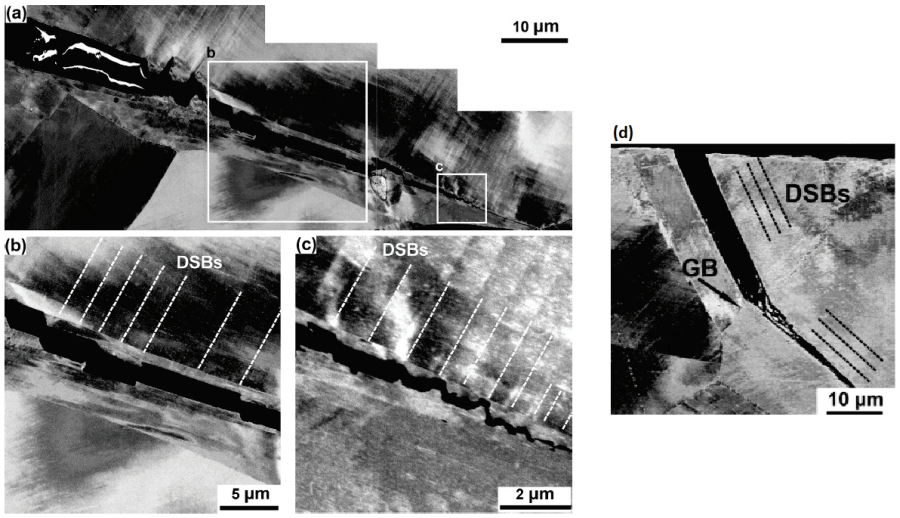

Figure 2.17: (a) an overview of the crack; (b) and (c) are magnified images showing more details about the crack in (a). Dislocation slip bands (DSBs) are indicated by dash lines. (d) crack propagation along the slip bands and crack deflection when it crosses a grain boundary [58]

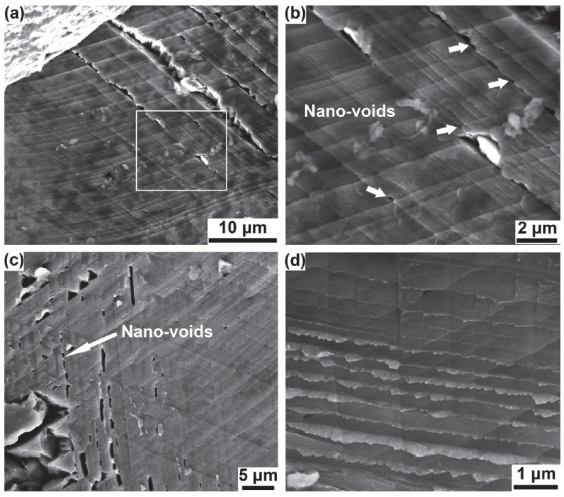

Figure 2.18: Fractographs obtained by SEM from the region with hydrogen presence: (a) image showing the Dislocation slip bands-like features on the fracture surface; (b) a magnified image from (a) showing the nano-voids formed along the traces; (c) image showing the nano-voids along the traces and potential coalescence to form cracks; (d) image showing saw-teeth shaped features along the traces. [58]

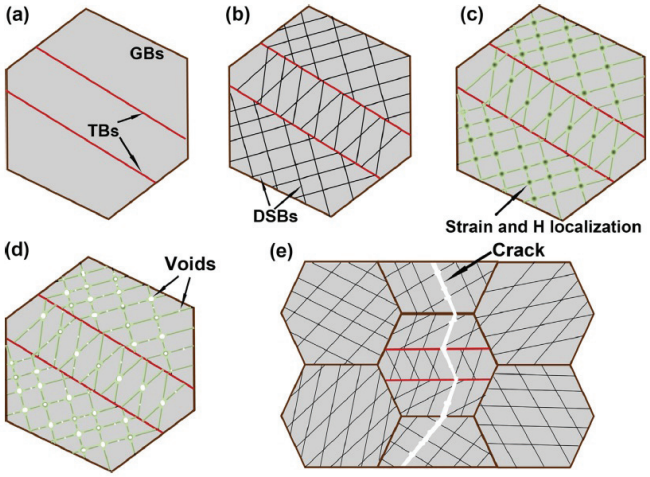

Figure 2.19: Schematic diagrams showing a possible mechanism for the hydrogen induced crack initiation and propagation in Alloy 718: (a) material prior to deformation; (b) planar dislocation slip bands (DSBs) develop during tension; (c) on the DSBs (in particular in the intersections of DSBs) slip localisation is more intensive and concentration of hydrogen is supposed to be high; (d) higher concentration hydrogen and localised slip promote the nucleation of nanoscale voids; (e) coalescence and widening of voids via dislocation process leads to crack propagation along the DSBs [58]

Simulation perspective

From the computer simulation perspective, molecular simulations were performed to evaluate the role of hydrogen–vacancy complex on nucleation and growth of nano-voids upon dislocation plasticity [60]. The simulations also help to study the interaction of dislocation and hydrogen–vacancy complex (VH_n) and their distributions (and also the vacancy distribution) especially near the slip planes and regions of dislocation plasticity. The VH_n complexes might grow larger by vacancy accumulation to form nanovoids, leading to macroscopic failure by void growth and coalescence process. On the other hand, Teranchi [61] disagrees, affirming that neither dislocations nor hydrogen plays any positive role in the formation of vacancy clusters. Moreover, large VH_n clusters by transport and trapping of vacancies is an unlikely phenomenon. Teranchi also claims that the experimentally observed presence of sustained vacancy clusters/voids on H-charged specimens' fracture surfaces must occur by some other mechanism.

2.3 Hydrogen assisted cracking in 7XXX alloys

This section focuses on the studies performed in Japan by Bhuiyan, Su, Shimizu, Toda, Tsuru and many others in recent years (mainly from 2018) on internal hydrogen embrittlement of aluminum alloys of the 7000 series. Their work combines classical macroscopic fracture tests with the local measure of the crack tip opening displacement at the micron scale[62] [63] [64] [65] [66] [67] [68] [69] [70]. These papers are based on tomography techniques allowing a 3D analysis. However the spatial resolution for estimating the strain fields is limited to 20 μm.

The section is divided in four subsections that usually follows the chronology of their work.

- The fist subsection is about local fracture toughness properties, some variables such as the CTOD (crack tip opening displacement) were measured at a local level for different fracture modes.
- The second subsection refers to time dependant nature of internal hydrogen assisted cracking and its effect in strain localization.
- The third subsection presents in more details the fracture morphologies in 3D obtained by tomography.
- The fourth subsection presents a model based on hydrogen repartition among traps that is used to explain the phenomena.

2.3.1 Local fracture properties

Bhuiyan [62] reports a correlation between the local fracture toughness and the hydrogen assisted fracture mode (Quasiclavage, Intergranular, or Dimple) in alloy AA7150 (AlZnMgCu). We recall that quasi-cleavage (QC) is a transgranular fracture, most likely due to localized plastic deformation, which appears "flat" in the scanning electron microscope (physically it is not a "cleveage"). Bhuiyan estimates the local fracture toughness by measuring the crack opening displacement (COD) profiles and the crack tip opening displacement (CTOD) via high-resolution synchrotron X-ray microtomography for two different hydrogen concentrations.

Bhuyian used a micro tensile machine with a speed of the jaws of 0.2 mm/s, applying increasing loading steps until complete failure. Two tensile samples (similar geometry to Fig. 2.20) were machined by electrical discharge machining (EDM). The samples have a fatigue pre-crack with an extension of half of the width. Hydrogen was introduced only by the EDM cutting procedure. EDM cutting introduces enough hydrogen for inducing hydrogen embrittlement [63].

One of these two samples is cycled thermally (between 350°C and 450°C in vacuum before heat treating again the sample to recover the metallurgical state), at low pressure, to remove hydrogen by desorption, obtaining low hydrogen (LH) sample. The other sample is labeled as HH (high hydrogen). The HH sample has around three times less macroscopic strain at fracture than the LH sample. The fracture surfaces are shown in Fig. 2.21 and Tab. 2.1 summarizes the percentages in the whole fracture surface of the three fracture

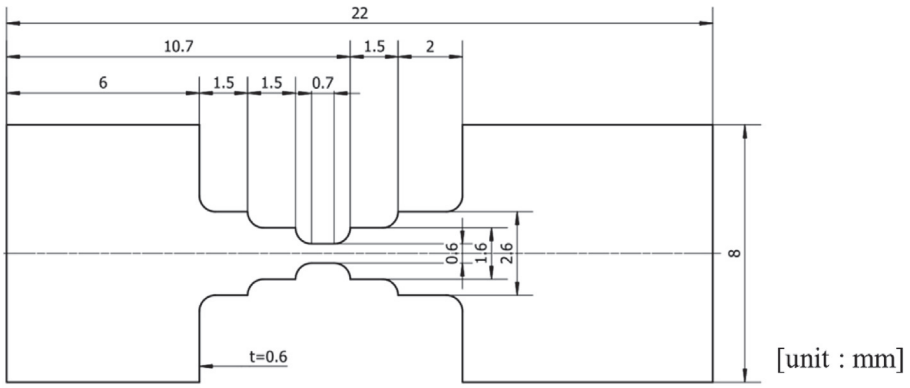

Figure 2.20: Geometrical dimensions of a tensile sample machined by EDM tested for internal hydrogen embrittlement in a micro tensile machine [62].

	QC	IG	Dimple
HH	73%	0%	0%
LH	65%	1%	3%

Table 2.1: Percentage of the fracture surface for different morphologies for a sample with high hydrogen content (HH) and low hydrogen content (LH) [62].

modes found along the crack path. Intergranular fracture is almost negligible but quasi-cleavage represents more than 60% of the fracture surface. The rest is ductile as is normally obtained in the absence of hydrogen. The difference between LH and HH is moderate which means that hydrogen was not significantly desorbed, even if the temperature used is high. Therefore, we can consider that H is "irreversibly" trapped in the system but nonetheless it induces an embrittlement. The time dependence of this embrittlement is demonstrated by Su and presented in the next subsection.

CTOD was measured in both samples in several points of along the crack front. Fig. 2.3b is a tomography slice of the thickness but the crack profile is not necessarily the same trough the entire thickness, so the CTOD is given as an average value. There is no significant difference between LH and HH in the CTOD values. The CTOD values were calculated when the crack tip is located in a specific fracture mode (QC, IG, Dimples) and reported in Table 2.2. It shows that the CTOD is dependent on the fracture mode. When

	CTOD average (μm)	CTOD min (μm)	CTOD max (μm)
QC	1.2	0.8	2
IG	6	1	15
Dimple	22	10	45

Table 2.2: crack tip opening displacement (CTOD) values for different fracture modes[62].

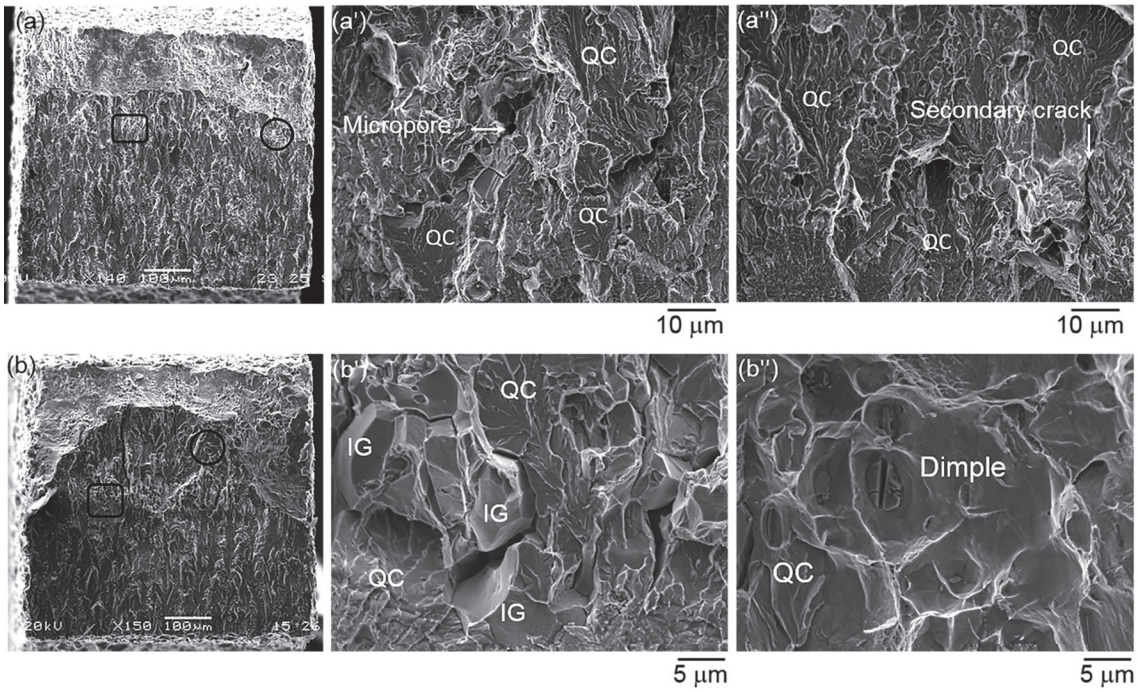

Figure 2.21: SEM fractographs showing an overview of the fracture surface for (a) material HH and (b) material LH, respectively, (a') and (b') magnified images of the part outlined by the rectangle in (a) and (b), respectively, (a") and (b") magnified images of the part outline by the circle in (a) and (b), respectively. [62]

the location of the crack tip is in the quasi-cleavage region, an average CTOD of 1.2 μm is obtained, and there is no significant difference between the HH and LH conditions. In the intergranular fracture region, compared to quasi cleavage, the average CTOD is five times higher. Finally, for the dimpled fracture mode, and even more significant increase in CTOD average is found of about 18 times higher than QC. Because the percentage of intergranular fracture is very low (about 1% of the fracture surface), the measure of the associated CTOD is not significant. A later work [68] shows that the CTOD for intergranular fracture is similar but slightly lower than the one for quasi-cleavage. The conclusion is that the local toughness associated to the two fracture modes is similar and for the two different hydrogen concentrations, it is also similar. The overall goal of this work, that will be supported by the next subsections, is that it is the "irreversibly trapped" hydrogen (in the sense that it could not get out of the sample by diffusion at high temperature) which is responsible for embrittlement. In the next subsection, the time dependence of this phenomenon is shown.

In addition, the crack opening displacement (COD) profiles measured at each loading step for LH and HH cases as represented in Fig. 2.22. It is appreciated that the cracks are more open when the step load increases. The lower COD values in the sample with a higher hydrogen content are interpreted by Bhuyian as the hydrogen effect ahead of the crack tip that reduces the crack opening displacement. However CTOD values are

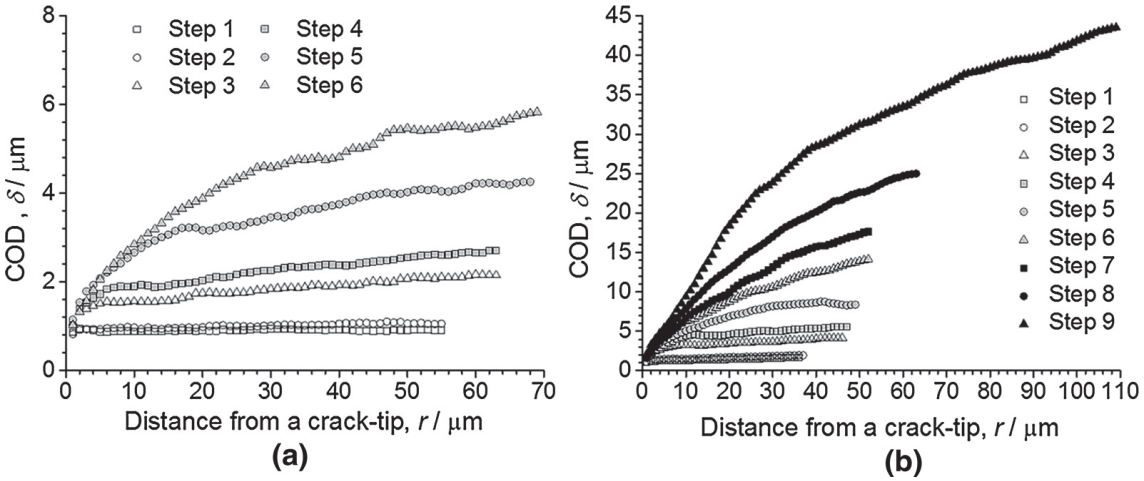

Figure 2.22: Crack opening profiles at each loading step averaged throughout the crack front line direction showing: (a) material HH and (b) material LH, respectively[62]

similar between LH and HH and seems to depend only on the fracture mode (ductile / H affected). Bhuiyad claims that a high concentration of hydrogen ahead of the crack tip increases the slip localization and reduces crack tip blunting. Also, he says that the crack grows until the tip of the crack becomes entirely blunted.

2.3.2 Time dependency and strain localization

A second and complementary paper by Su [64] characterizes the hydrogen-induced dislocation localization in terms of the microscopic strain distribution in another AlMgZnCu aluminum alloy. In this case, and in all the following cases of this chapter, the samples are not notched nor pre-cracked. Hydrogen induced strain localization was visualized in 3D using X-ray tomography and related microstructural tracking techniques. The tensile samples were machined by EDM. EDM cutting increased the H content from 0.13 ppm (before cutting) to 6.97 mass ppm H (measured by vacuum fusion method). The micro tensile test consisted of loading steps. However to study the time dependency of the hydrogen assisted cracking, a new important variable was introduced in the tensile test: a controlled constant holding time (Th) between the loading steps. One sample was tested using a holding time (Th) of roughly 50 minutes (Th=3,34 Ks) and the other of 9 minutes (Th=0.53 Ks). The tensile curve is shown in Fig 2.23a.

In Fig. 2.23a, the strain to final fracture decreased to less than half with an increase in holding time from 9 to 50 minutes. It is really important to note how drastically the ductility changes with the holding time. Figure 2.23b shows another 7XXX alloy (AlMgZn low Cu) [67] for which the same detrimental behaviour is observed with three different holding times. Decreasing the fracture strain with the increase in holding time implies that hydrogen-induced fracture is time-dependent. In the context of their previous work, exposed above, it means that H that could not diffuse at high temperature can move when the sample is strained, if the strain rate is low enough as it is the case when the holding is introduced in between strain increments. The microscopic origin of this phenomenon is

unknown but falls in the context of the HELP mechanisms as a dislocation-trap interaction.

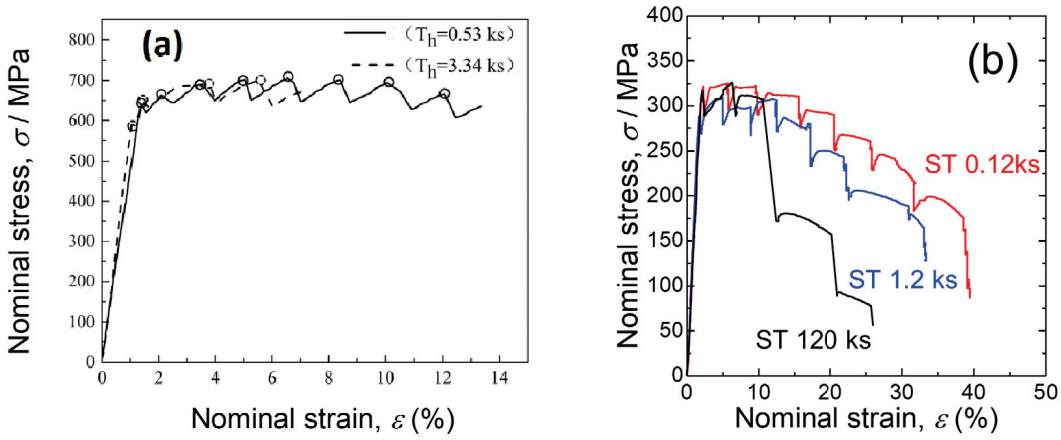

Figure 2.23: Nominal stress–strain curves obtained by in situ tensile tests at different holding times for samples charged with hydrogen by EDM (a) AlMgZnCu using two different holding times[64] (b) AlMgZn for three different holding times [68]

Moreover, Su based on DIC measurements (using microstructural tracking techniques in 3D X-ray tomography) concludes that [64][65] the strain localization is more intense with an increase in holding time at each loading step, suggesting that more internal hydrogen is partitioned to the strain localization regions with the increasing holding time.

2.3.3 Fracture modes of AlZnMg alloys with low copper content

As a continuation of this line of works, a third paper a year after by Shimizu [68] uses mainly an Al10.1Zn-1.2Mg (AlZnMg, no or low copper) alloy but also a few Al-9.9Zn-2.3Mg-1.4Cu (AlZnMgCu) samples. The high copper content alloy is tested for comparative purposes (QC cracks are more likely with copper [64]). Shimizu's study of local toughness through COD and CTOD uses similar concepts to the one of Bhuriyan. The tensile samples are similarly machined without any stress raiser and hydrogen charged by EDM. The AlZnMg (no copper) alloy produces a higher fraction of IG cracks than the alloy with copper. A new contribution in the experimental procedure is that after being machined, the samples are immersed in acetone for four days, favoring hydrogen diffusion from the surface to the center. The effective hydrogen diffusion coefficient of $2.1 \times 10^{-13} m^2 s^{-1}$ is considered. It ensures that 4 days are enough for hydrogen to diffuse into the sample. The hydrogen content measured by TDA is around 2 mass ppm.

After these four days, a tensile test of AlZnMg is carried, similarly to previous reports, for copper content [64], the increase in the holding time steps reduces the fracture strain, as shown in Fig. 2.23b. Intergranular fracture (IG), quasi-cleavage fracture (QC) and a ductile failure with dimples were reported. Intergranular cracks are present when the alloys have a low copper content.

In addition, Shimizu [68] reports that when applying a higher holding time during the tensile test, less strain is needed to initiate cracking, and the surface area of the QC and IG increases with the holding time (Fig 2.24). Besides, all the initial cracks were intergranular cracks (yellow crack in Fig. 2.24(d) through (f)), which transitioned to quasi-cleavage cracks and ductile cracks due to subsequent loading. The distinctive aspect of visualized crack growth is that the crack grew gradually in response to the given displacement rather than instantaneously advancing on one grain boundary or one facet.

According to Shimizu, the hydrogen is repartitioned during plastic deformation, inducing time-dependent fracture where localization of hydrogen is partitioned into traps near the crack tip. Hydrogen trapping at GB is considered to be responsible for IG failure. Also, intergranular and quasi-cleavage fractures modes were found with samples with a diminished hydrogen content (0.41 mass ppm). [68]

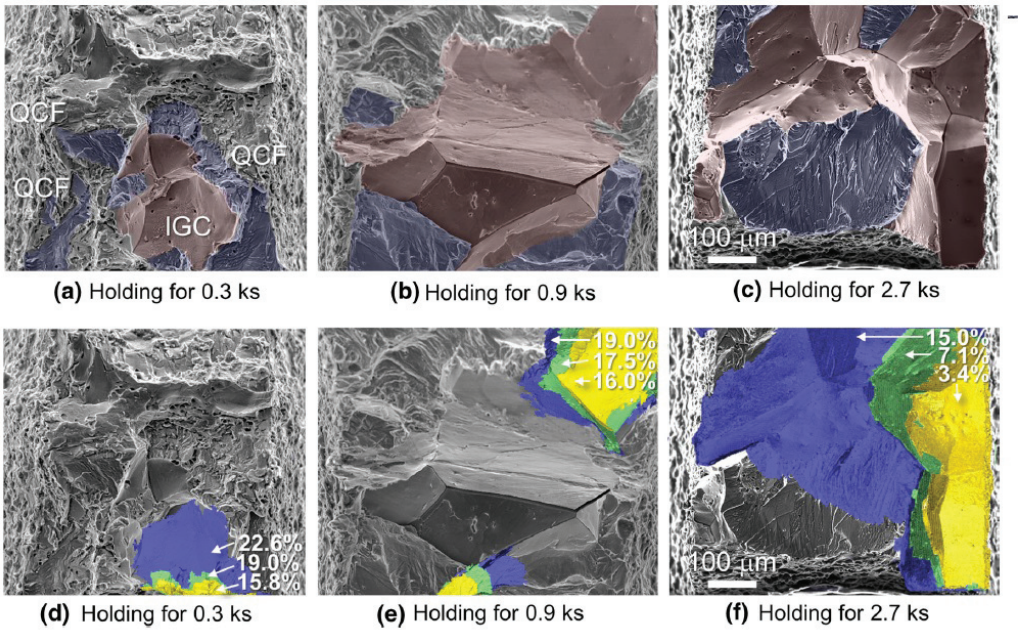

Figure 2.24: Fracture surface of tensile specimens at different holding times. In (a) through (c), intergranular and quasi-cleavage fractured regions are indicated in red and blue, respectively. In (d) through (f), cracks visualized by projection-type tomography at each strain are superimposed as yellow, green, and blue. Nominal strains are also indicated when each crack was visualized by projection-type tomography [68]

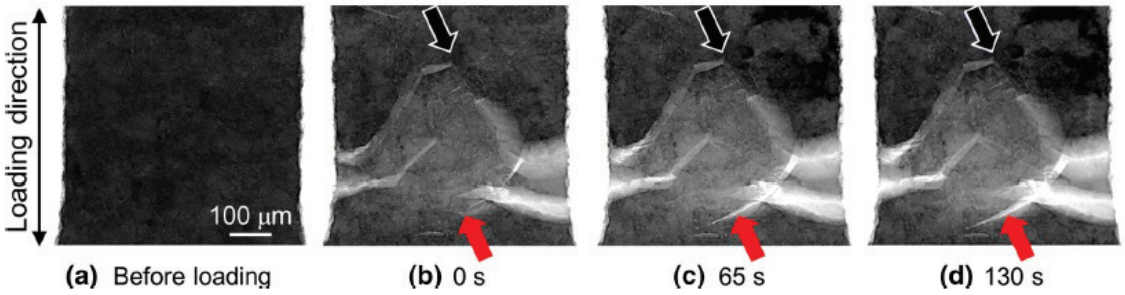

Figure 2.25: 2D projection images of specimen (a) before loading at (b) 0, (c) 65, and (d) 130 s after holding the displacement. The crack indicated by the black arrow was arrested, and the crack indicated by the red arrow grew even though the displacement was constant. [68]

The stress-strain curves in Fig. 2.23b and the crack growth behavior in Fig. 2.24 imply that intergranular and quasi-cleavage crack growths of Al-10.1Zn-1.2Mg alloy accompany plastic deformation. However, Shimizu[68] did not find such localization of plastic deformation ahead of the crack. The resolution limit of the strain field is around 20 microns due to the microstructure feature 3D tracking technique used for a DIC.

Shimizu[68] also induced a full intergranular fracture in an AlZnMg alloy with high hydrogen content. The sample was subjected to a double EDM machining for obtaining 25.4 mass ppm of hydrogen (TDA) . The intergranular crack was 2D-imaged in Fig. 2.25. The tensile load introduced multiple cracks into the specimen (applied nominal strain 4.5 %). Figures 2.25(c) and (d) show 2D projection images after 65 and 130 seconds elapsed from Figure 2.25(b) with a fixed displacement of the jaws in the micro-tensile machine. An intergranular continuous crack propagation (red arrows) is detected even when the displacement was fixed. The growth rate was approximately 1 μm/s, and the crack tip was sharp.

As a conclusion, Shimizu [68] claims that as the hydrogen content in the matrix increases, the ductile fracture transitions to a quasi-cleavage fracture. When the content increases further, intergranular fracture tends to occur.

QC and IG characterization by tomography

Shimizu [68] imaged the tips vicinity of an intergranular crack (AlZnMg) and a quasi-cleavage crack (AlZnMgCu) shown in Figures 2.26 and 2.27, respectively. The 3D image and the 2D virtual cross-section (Fig. 2.26) show that the tip of the intergranular crack is sharp and has a fracture surface that remains relatively flat compared with the quasi-cleavage crack shown in Fig. 2.27. In the intergranular failure, a crack deflection is displayed near the Fig. 2.26 (d) and (e). The deflection point corresponds to the triple junction point of the grain boundary.

The quasi-cleavage crack shown in Fig. 2.27 exhibits a tortuous morphology relative to the intergranular crack. The appearance of the crack propagating while repeatedly blunting locally and sharpening was visualized by Shimizu [68].

Finally, Fig. 2.28 (a) shows the fracture surface of AlZnMgCu alloy in SEM. Then, Fig. 2.28 (b) is an enlarged view of Fig. 2.28 (a). Also, Fig. 2.28 (b) is an image obtained by superimposing the tomographic image (Fig 2.27(a)) of the QC crack (in yellow). The rugged surface morphology of the quasi-cleavage crack shown in Fig. 2.27 coincides with the quasi-cleavage facet. Also, no void exceeding 300 nm was observed by tomographic analysis ahead of the quasi-cleavage tip that could support a void coalescence mechanism.

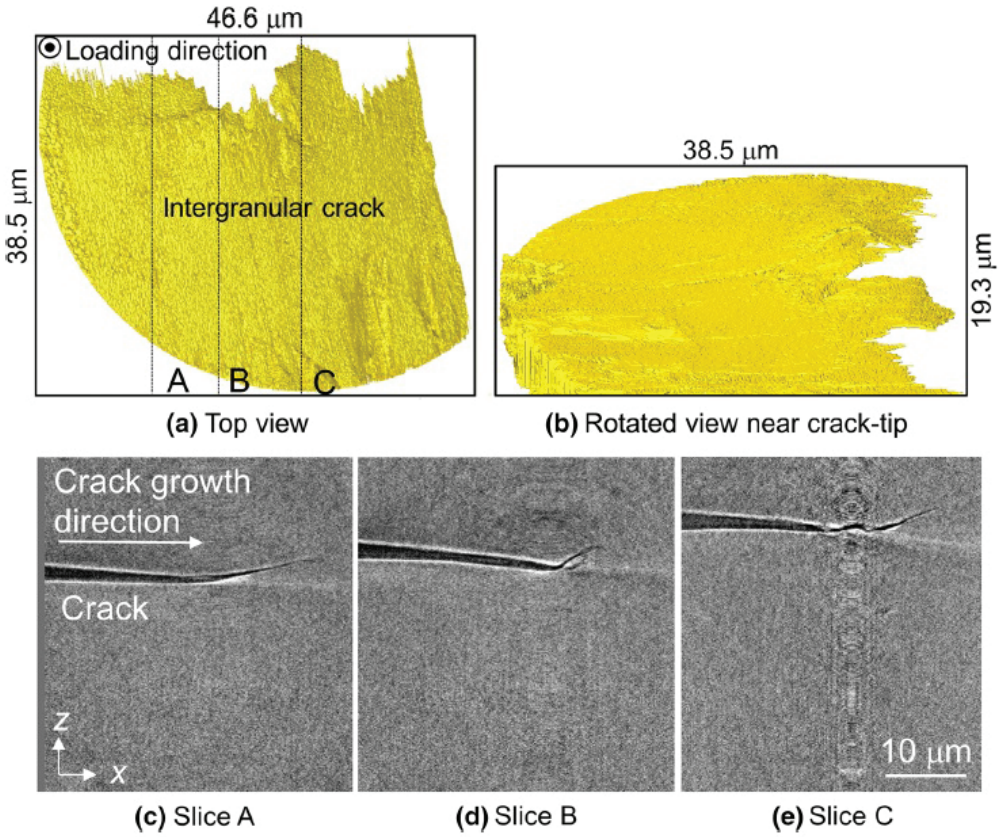

Figure 2.26: 3D tomographic images of an intergranular crack ((a) top and (b) side views). In (c) through (e), the 2D virtual cross sections of A, B, and C correspond to the dashed line in the top view [68]

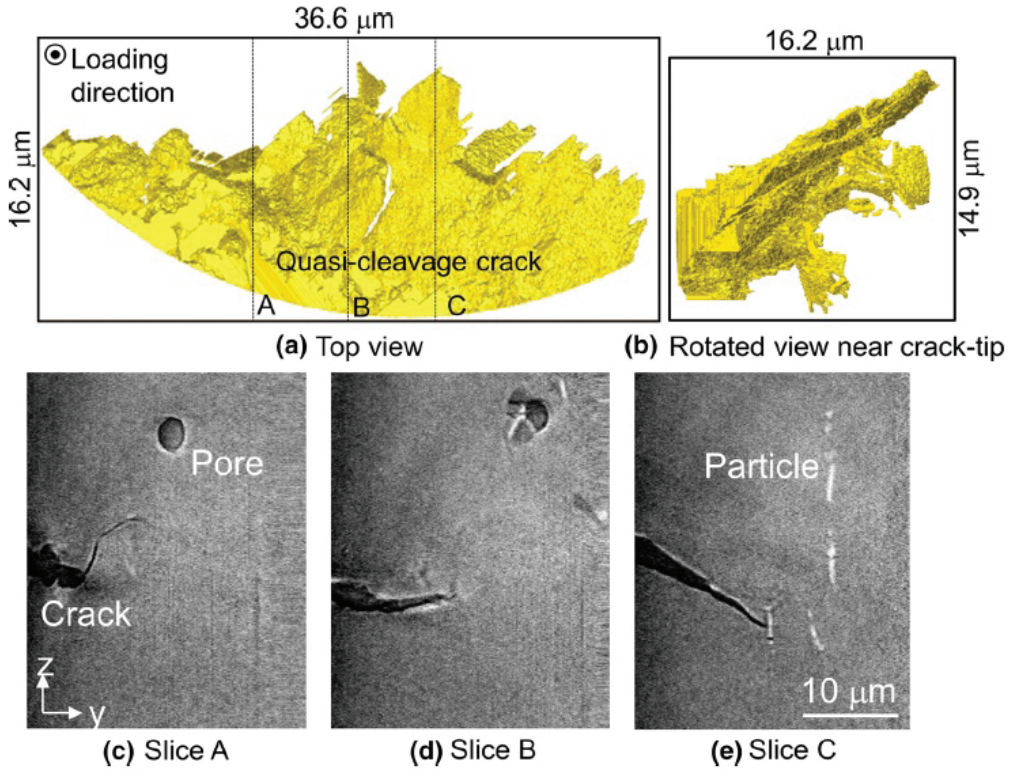

Figure 2.27: 3D tomographic images of a quasi-cleavage crack ((a) top and (b) side views). In (c) through (e), the 2D virtual cross sections of A, B, and C correspond to the dashed line in the top view [68]

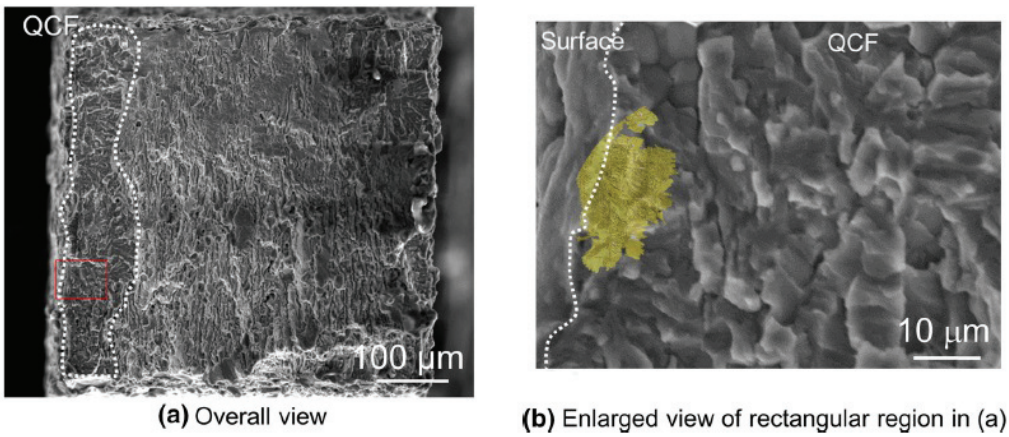

Figure 2.28: Fracture surface of Al-9.9Zn-2.3Mg-1.4Cu alloy observed by SEM. (a) The overall view of fracture surface and (b) the enlarged view of rectangular region in (a). In (b), the quasi-cleavage crack (yellow) captured by imaging-type tomography in Fig 2.27 (a) is superimposed [68]

Crack tip analysis for quasi cleavage and intergranular failure

Shimizu[68] measured the CTOD directly from the 2D virtual cross-section of the 3D crack visualized by imaging-type tomography in Fig 2.26 and 2.27. The average crack-tip-opening displacements were 0.14 and 0.23 microns for intergranular cracks and quasi-cleavage cracks, respectively. In both cases (QC, IG), the local deformation field of the crack tips were analyzed in terms of the COD profile. The COD is measured experimentally at the back of the crack tip. Continuum mechanics is used to extrapolate these measurements ahead of the crack tip. This procedure suggests that a local plastic deformation occurs in a region of 20 microns or less from the crack tip, and this plastic zone size is significantly more limited than that of a typical ductile crack. Therefore, the fracture behavior is not perfectly brittle, accompanying local deformation at the crack tip. Shimizu [68] also suggests from COD analysis that strain has already been localized before crack initiation and that sharp cracks grow along the strain-localized region.

2.3.4 Repartitioning based model

A hydrogen embrittlement model considering local thermal equilibrium among various hydrogen trap sites and related in-situ hydrogen repartitioning in the strain localization region has been proposed (Fig 2.29) [68] [64] [65].

For a higher holding time step during a tensile test, a higher concentration of hydrogen is accumulated in the strain localization region. The accumulated hydrogen is repartitioned among various trap sites such as intermetallic particles, dislocations, grain boundaries and vacancies in the strain localization region. The hydrogen partitioning has a dominant influence on both intergranular and quasi-cleavage fractures [70].

According to Shimizu [67], the initial trapped hydrogen content in grain boundaries, vacancies, and dislocations before deformation was not crucial for inducing intergranular fracture and quasi cleavage fracture. It is only because of plastic deformation that hydrogen accumulates at grain boundaries and precipitate interfaces and induces intergranular and quasi cleavage fracture, respectively.

Tsuru [70] states that despite the coherent atomic configuration, the $Al–MgZn_2$ interface is a more appealing hydrogen trap site than other defects in terms of binding energy and hydrogen partitioning. The interface's cohesivity deteriorates significantly with increasing hydrogen occupancy, while hydrogen atoms are stably trapped up to an extremely high occupancy that is equivalent to spontaneous cleavage. In other words, a high hydrogen segregation induces spontaneous fracture coupled with the formation of hydrogen molecules at the interface. The origin of this quasi-cleavage fracture involves hydrogen partitioning.

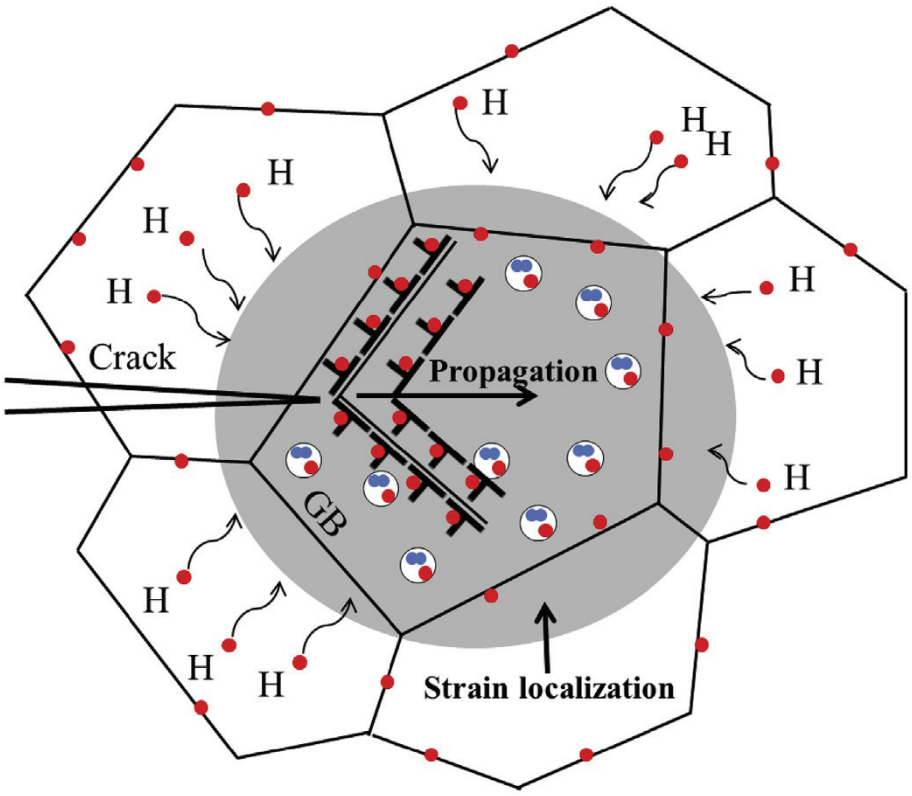

Figure 2.29: Schematic illustration of hydrogen partitioning and related crack propagation in a strain localization region. [64]

2.4 Summary

This literature review has presented an updated version of the most relevant hydrogen embrittlement mechanisms for metals, focusing on FCC materials. The main models, such as HELP, AIDE, HEDE, HESIV provide a framework for understanding the complex phenomenon of hydrogen embrittlement. Also, the possibility of the a combination of these mechanisms acting at the same time is often mentioned. Some elements involved in hydrogen embrittlement are: less cohesion in the grain boundary or a cleavage plane; the hydrogen promotes and intensifies plasticity, also the hydrogen promotes slip planarity, and this localized deformation interacts with grain boundaries perturbing the grain boundary strength; the fracture along slip bands with the assistance of micro-void coalescence.

The recent work done in Japan is a characterization of hydrogen induced embrittlement in alloys similar to ours: the 7XXX series. The authors have used a micro-tensile machine, X ray tomography and 3D digital image correlation. They show that an embrittlement can be obtained by internal hydrogen "irreversibly" trapped in the system (it could not be removed by heat treatment). Plasticity is localized near the crack tip. It was quantified by CTOD, COD measurements and continuum mechanics. This plasticity was found similar for transgranular (the so-called quasi-cleavage) and intergranular fracture based on CTOD and COD measurements but it was not directly measured experimentally ahead of the crack tip because of the low spatial resolution of the strain field measurements. Moreover, Shimizu and Su demonstrated the time dependency of the embrittlement and the major role of the traps. The hydrogen diffusion and repartitioning among traps due to plastic deformation, localized in the vicinity of the crack tip, is the reason proposed for fracture.

In this context, the goal of our work is to perform fracture experiments at a local scale, obtaining information about hydrogen assisted cracking using Digital Image Correlation (DIC) to quantify the plasticity involved. The cracks will be followed on the surface with a pattern that should increase the spatial resolution with respect to the tracking techniques used in the 3D X-ray tomography applied by Su [64][65] to perform DIC. The crack propagation velocity is another key element in the fracture process to evaluate. The correlation between the local plasticity, the fracture morphology, the hydrogen content, the crack speed and the difference between internal hydrogen assisted cracking and the stress corrosion cracking in the same alloy, and under the same testing condition, can contribute to a better understanding to this complex phenomena.

Chapter 3

Materials and Methods

3.1 Material and equipment

Our material, the aluminium based alloy AA7108, belongs to the AA7XXX series. The 7XXX alloys have applications in a wide range of industries where hydrogen embrittlement causes safety and economical issues. The alloys of the 7XXX series have zinc as the primary alloying element, but most of them include magnesium and copper as well. They harden by the formation of precipitates. They reach good mechanical properties, among Al alloys, such as high strength, toughness, ductility and resistance to fatigue.

Precipitation hardening (also called age hardening or particle hardening) is a heat treatment process used to increase the tensile strength of most structural alloys of aluminium. The heat treatments are identified using letters and numbers. The "T" designation denotes a temper. The T is followed by a number that indicates a specific sequence of basic treatments. For example[71]:

- T4: solution heat treated and naturally aged. This signifies that after solution heat treatment the mechanical properties have been stabilized by room-temperature aging.
- T6: solution heat treated and artificially aged. This means a solution heat treatment and for which mechanical properties are substantially improved by the precipitation heat treatment.

Chemical composition of our alloy

The studied material is a commercial aluminum alloy of the AA7108 series (Al-Mg-Zn with low copper). Table 3.1 shows the chemical composition presented in mass percentage.

Element	Zn	Mg	Cu
Composition (wt %)	5.0	1.2	0.16

Table 3.1: Nominal chemical composition of AA7108

Microstructure

Very often, brittle cracks propagate along grain boundaries. One difficulty, when analysing fracture, is that the grain boundary (GB) facet has an orientation which is not easily characterised when it is inclined. For this reason, we decided that tensile samples will be machined along the short transverse direction (STD) of a rolled plate (Fig. 3.1), offering a preferential intergranular path with longer grain facets perpendicular to the tensile direction. Fig. 3.2 shows an EBSD map of the rolled plate displaying the transverse direction (TD) and the short transverse direction (STD). The grain size dimension in the crack front direction (rolling direction) is at best 200 μm, and often much smaller (20 μm) in regions where the plate is partially recrystallized. With the orientation of the notch (Fig. 3.1a) and the force, the crack will propagate in the TD direction and the front is along the rolling direction.

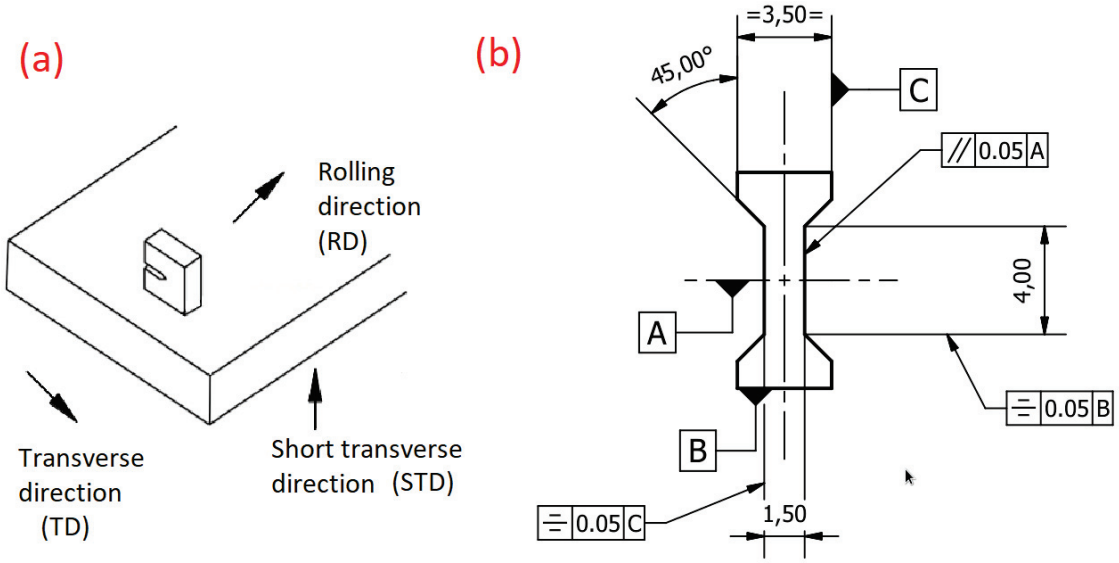

Figure 3.1: (a) Scheme of the AA7108 rolled plate and the orientation of the sample with respect to the rolling direction (RD), transverse direction (TD), and the short transverse direction (STD). (b) Geometrical dimensions of the tensile sample (mm), in the (TD,STD) plane. The total length of the sample is the thickness of the plate (8 mm).

The received plate has a non specified metallurgical state. We heat treated the tensile samples, after polishing to mirror state, at 400 °C for 1 hour, followed by a water quench and a natural aging at room temperature in order to have a T4 state, modifying its original microstructure. The heat treatment drives the precipitation process. Beginning with the solid solution (SS) at high temperature, the precipitation sequence in shown in Eq. 3.1.

$$SS \rightarrow GPZones\,(20-150°C) \rightarrow \eta'\,(100-170°C) \rightarrow \eta\,(150-300°C) \tag{3.1}$$

The precipitation sequence evolves towards stable phases η ($MgZn_2$) and the metastable phases η'. There is an early stage of precipitation called Guinier–Preston zone, or GP-zone.

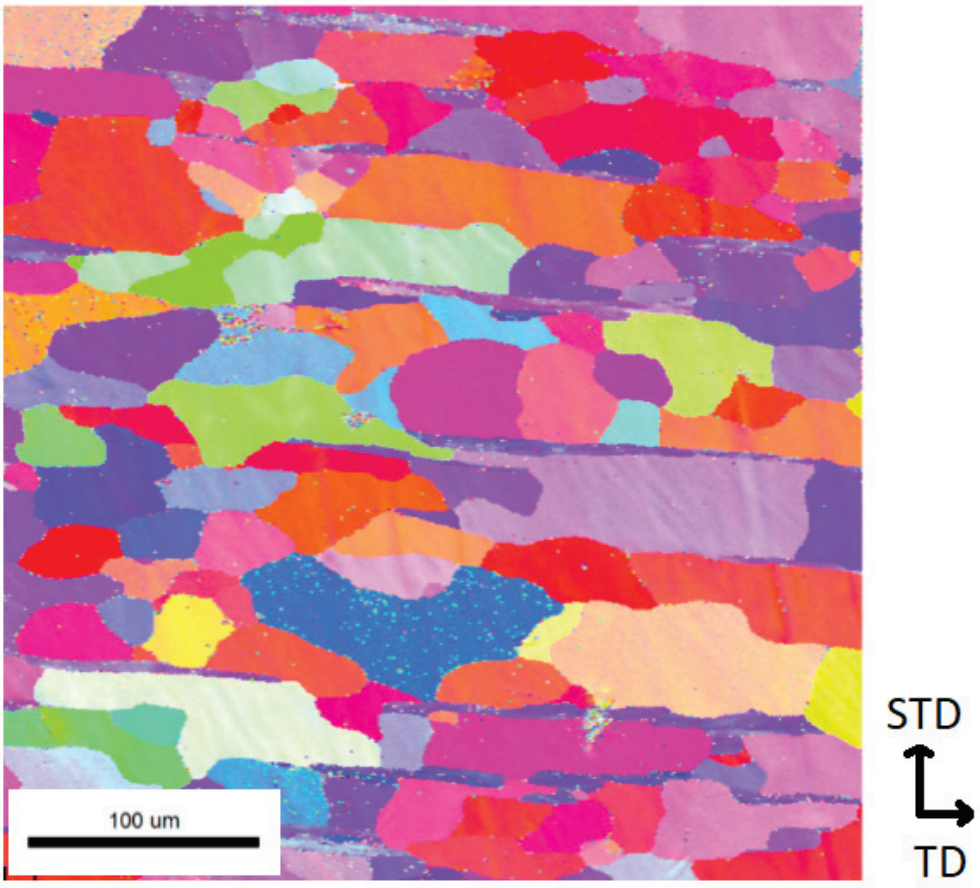

Figure 3.2: EBSD map of the rolled plate. The morphological texture is moderately elongated with some "pancake" grains and recrystallised regions.

GP zones are fine-scaled (3–10 nm) solute enriched regions, which offer obstruction to the dislocation's motion. In 7075 alloys, GP zones (Zn–Mg clusters) precede the formation of equilibrium $MgZn_2$ precipitates. Also, GP-zones are associated with the phenomenon of natural age hardening (room-temperature reactions).

AlZnMg alloys reach the maximum tensile strength by the precipitation [72] of the η' and η phases which are semi-coherent and incoherent respectively with the matrix and of chemical composition $MgZn_2$. During precipitation, there is an enhanced precipitate growth at the grain boundaries and the formation of a precipitate free zone, of a few nanometers thickness parallel to the grain boundaries [73].

In the T4 metallurgical state, the hardening comes from the precursor of η' which is the Guinier-Preston zone (a cluster of solutes on the lattice of aluminum). The material is quenched from the solid solution state and the precipitation occurs naturally at room temperature. The grain boundaries have some Mg and Zn segregation and maybe some η precipitation but at a fine scale (not visible within the SEM) [74]. This metallurgical state was chosen for the thesis because it promotes a high sensitivity to stress corrosion cracking

and hydrogen embrittlement and because the microstructure at the grain boundaries is simple (no precipitation).

The T6 state, obtained by a heat treatment at an intermediate temperature, is the peak of tensile strength with η' in the matrix, a precipitate free zone along the grain boundaries and a discontinuous intergranular precipitation of η phase [75]. The size of the precipitates are of the order of 100 nm [76]. Further heat treatment leads to a decrease in hardness and coarsening of the intergranular precipitates and a lower sensitivity to stress corrosion cracking [77].

Micro tensile test

Micro tensile samples are machined by electrical discharging machining (EDM). As mentioned above, the tensile axis is oriented in the short transverse direction of the plate to take advantage of the morphological texture. The samples have an overall length of 8 mm (plate thickness) and a gauge length of 4 mm. A single edge U-notch is machined in the middle of the gauge length with a high cutting speed rotating saw. It has a 35-50 μm radius. Its role is to favor single cracking by concentrating the stress and plastic deformation. The samples' width is 1 mm or 1.5mm, and the thicknesses are from 1 mm down to 0.2 mm. The notch depth is of the order of 300μm.

The DEBEN micro-tensile machine has a 660N load cell. The jaws displacement speed is 0.005mm/min. The gripping device is in-house designed and machined. The tensile sample, placed on the machine, is shown on Fig. 3.3. The gripping system is aligned with microscope observation assistance. The tests are performed in laboratory air under optical microscopy observation. The single crack, after initiation from the notch tip, is followed on the surface during propagation. The pictures taken during the test are analysed using digital image correlation (DIC). Scanning electron microscopy (SEM) observations of the fracture surfaces are performed after the internal hydrogen embrittlement or stress corrosion cracking test is finished.

Stress Corrosion Cracking

The embrittlement for SCC is obtained by immersing the notch in a saline solution (NaCl 30g/l). For this, the sample is mounted in contact with a micro-cell, built from a 3D printer (Fig. 3.4b). The sample itself is not fully immersed. The top surface is only exposed to air to generate the pictures used in digital image correlation (Fig. 3.4a). The tensile sample, glued to the micro cell, is placed in the gripping system of the tensile machine. This set up allows the saline water to be in contact with the notch tip (Fig. 3.4c) promoting crack initiation. The system is left at free electrochemical potential during the test.

Stress strain curve and fracture surface examination

The stress strain curve, obtained in laboratory air, for a sample in the T4 state shows an elongation to fracture of 30% (Fig.3.5). The yield stress is 150 MPa approximately, and the ultimate tensile stress is 280 MPa.

After the complete failure, the fracture surface is observed in SEM (Fig. 3.6). Most of the fracture surface displays a ductile morphology with dimples. A magnified image of this morphology is shown in Fig. 3.7a. However, on the right side of Fig. 3.6 there is a brittle

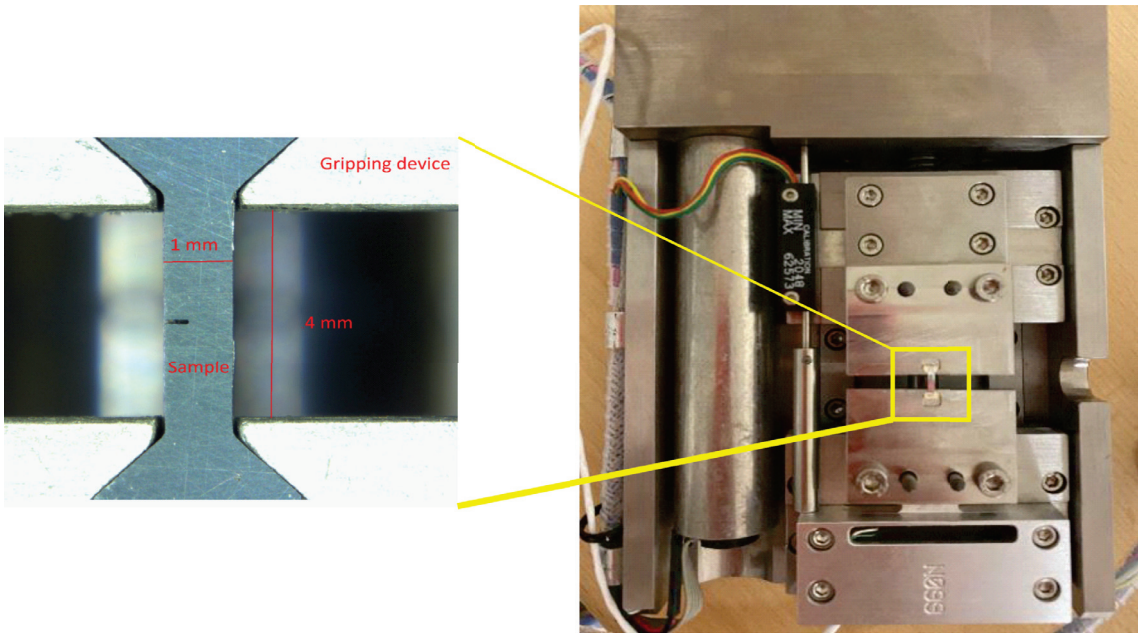

Figure 3.3: Tensile sample placed on the micro tensile machine

fracture region, with intergranular and transgranular morphologies. A magnified image of this zone is shown in Fig. 3.7b. The ductile morphology is around 76% of the total fracture surface (measured by image analysis using the "Image J" software). The brittle fracture is likely caused by internal hydrogen generated by the electrodischarge machining (EDM) because it was not present when the samples were milled in a conventional way [77]. Hydrogen-induced fracture in 7XXX alloys caused by hydrogen introduced during EDM machining has been reported in the bibliography[63][62][64][65]. Indeed, this process is a localized melting and a water flow is used to remove the products of the cutting. It is likely that it is the reaction of the freshly melted surface with water which produces hydrogen. Note that this embrittlement is limited to the side of the sample, because only a beam is machined by EDM and the samples are cut from beam by a diamond saw. Furthermore, this side is actually notched over a depth which is a little deeper than the penetration depth of the embrittlement. So the cracks studied are initiated (from the notch) in a region of the sample which is beyond the hydrogen affected zone produced by the EDM cutting.

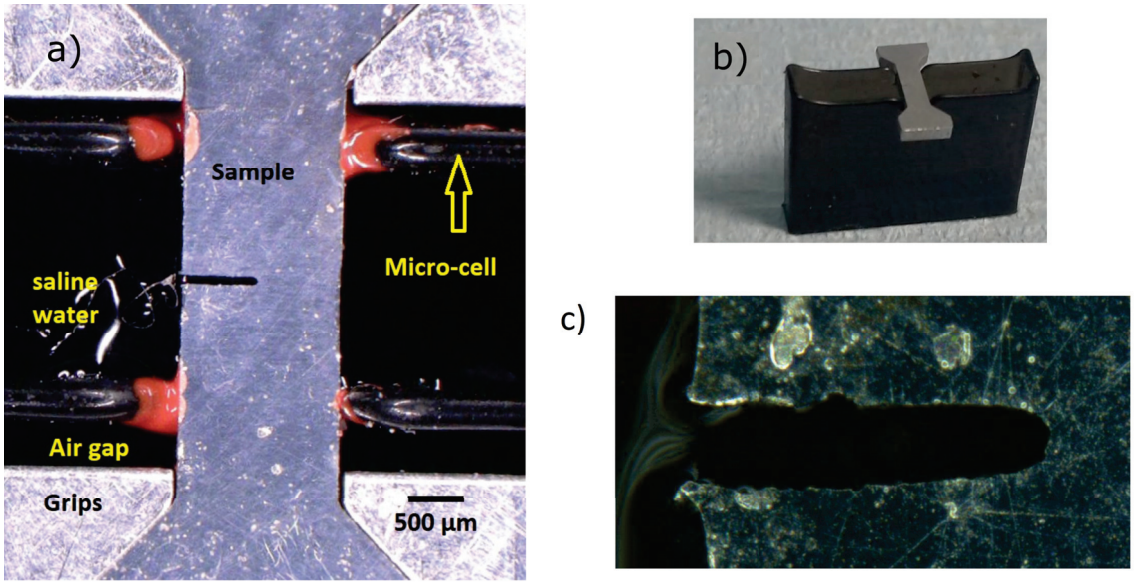

Figure 3.4: (a) Optical microscope image. The tensile sample is in contact with the saline water (bottom part and both lateral sides) contained in the 3D printed micro cell. The force is applied using the grips. The micro-cell is glued to the sample with a red joint. (b) Tensile sample is mounted in the micro-cell. (c) Optical microscope image showing the saline solution filling the notch.

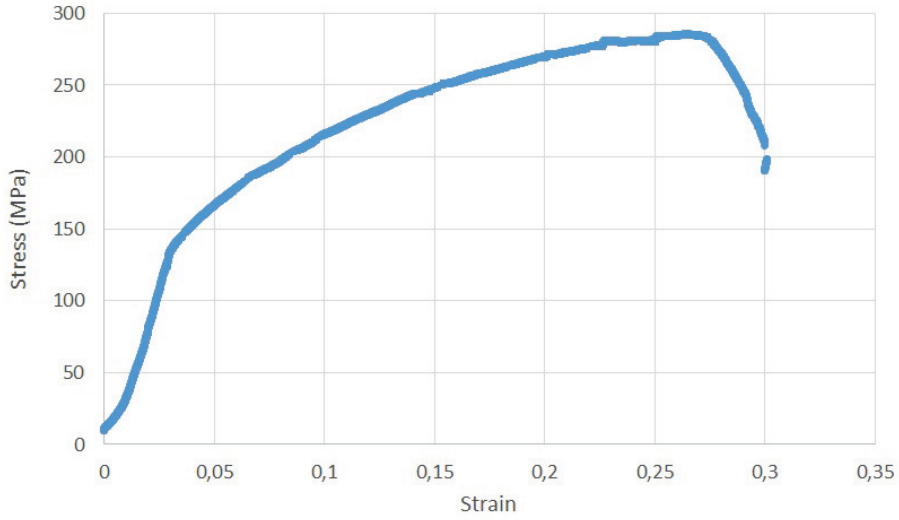

Figure 3.5: Stress strain curve until fracture in AA7108 (T4) obtained at a strain rate of $\dot{\epsilon}_0 = 2 \times 10^{-5} s^{-1}$ in laboratory air.

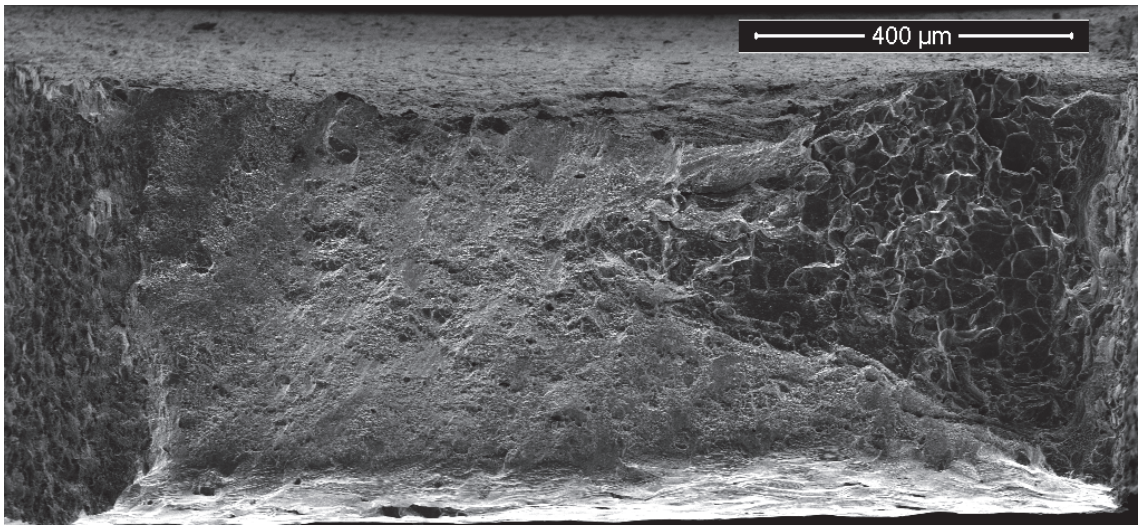

Figure 3.6: SEM image of the fracture surface of a T4 heat-treated sample machined by EDM without notch after a tensile test at a strain rate of $\dot{\epsilon}_0 = 2 \times 10^{-5} s^{-1}$.

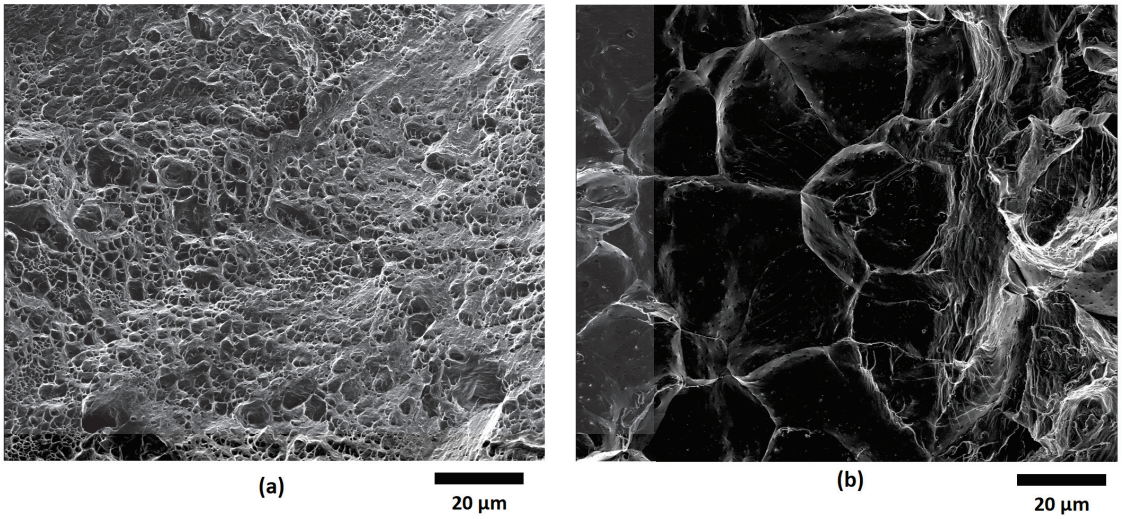

Figure 3.7: SEM image at a magnification of ×1000 (a) Ductile fracture with dimples (left side of Fig. 3.6) (b) brittle fracture intergranular and transgranular (right side of Fig. 3.6). Hydrogen introduced during manufacturing and EDM machining are reported to cause hydrogen embrittlement in the literature.

3.2 Methods

3.2.1 Hydrogen charging electrochemical method

The sample, after being polished to mirror state on one face and heat-treated to T4 state, is submitted to the electrochemical hydrogen charging procedure. The sample is immersed in a sulphuric acid solution (pH 2.0) in a 3-electrodes cell, as it is illustrated in Fig. 3.8 and a cathodic potential is imposed during a charging time. All the potentials in this text are expressed with respect to a reference which is a saturated calomel electrode (SCE). The two parameters used to control hydrogen uptake are: the imposed potential, denoted E_c, and the charging time t_c. Several combinations of potentials and charging times were tested on a set of samples.

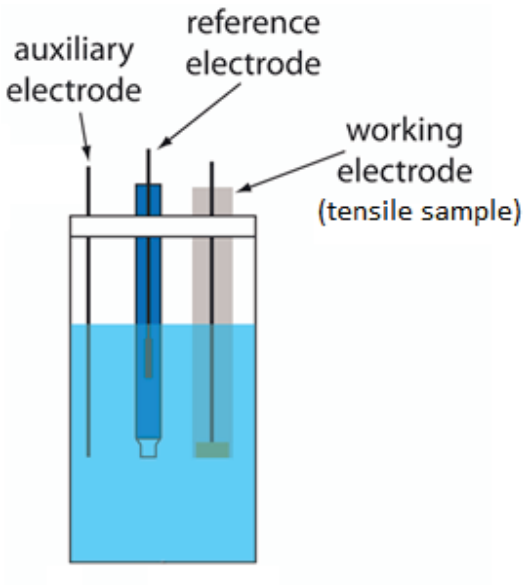

Figure 3.8: Three electrodes system set up. The solution is sulphuric acid at pH=2. The reference electrode is a saturated calomel electrode. The auxiliary electrode (or counter-electrode) is a Pt wire. The working electrode is the aluminum tensile sample (polished and heat-treated).

3.2.2 Digital Image Correlation

Digital image correlation (DIC) is used to measure the displacement field on the surface of the sample, giving the possibility to measure precisely the crack tip position and the deformation involved in the crack propagation process.

DIC is based on tracking a pattern (often called a speckle pattern) in a sequence of images. The process of a DIC experiment can be divided into three steps: (1) obtain a pattern on the sample for tracking and obtain a reference picture, (2) capture images of the sample during deformation, and (3) analyze the images to compute the sample displacements on the surface. An image of a sample during deformation can be a "reference picture" for a later image with a higher level of deformation. A diagram is shown in Fig. 3.9 for a tensile test.

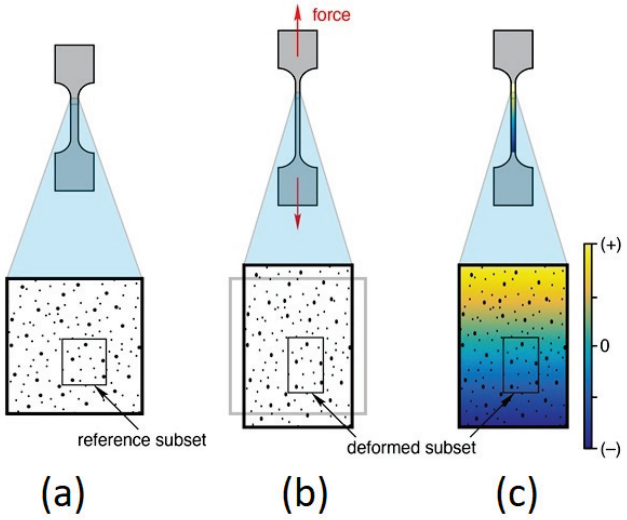

Figure 3.9: Schematic of a DIC test performed during a tensile test. The reference image, with the speckle pattern is displayed in (a). The deformed image is shown in (b), and the computed strain from the correlation is displayed in (c). [78]

A more detailed DIC analysis diagram is shown on Fig. 3.10. (a) A region (subset) of the reference image is selected for tracking, and the DIC point (redpoint) is defined in the center of the subset (where the displacement will be computed) (b) After the force is applied, the matching between the subset in the deformed image and the reference image is performed. (c) DIC calculates the relative displacement of the subset center between the two images. Fig 3.11 shows how this essential operation is extended to multiple subsets and DIC points, it has four points with displacement information, a real DIC analysis computes a field of displacements by tracking multiple subsets that can be overlapped on the reference image.

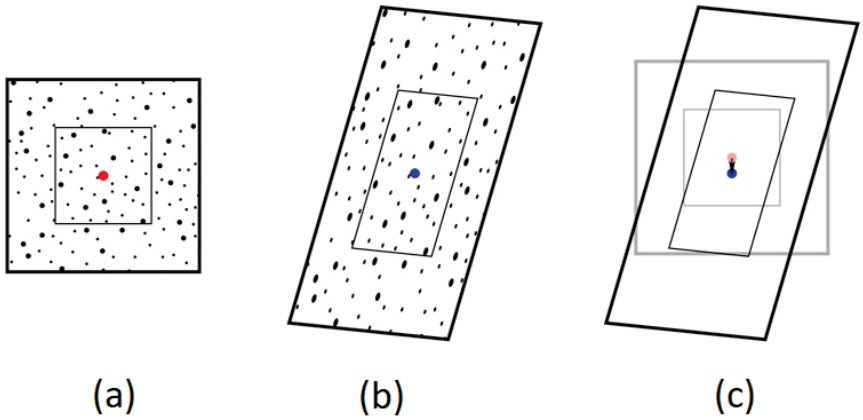

Figure 3.10: (a) speckle pattern with a single subset and a DIC point in red (b) new position of the DIC point in blue (c) calculated displacement of the DIC point [78]

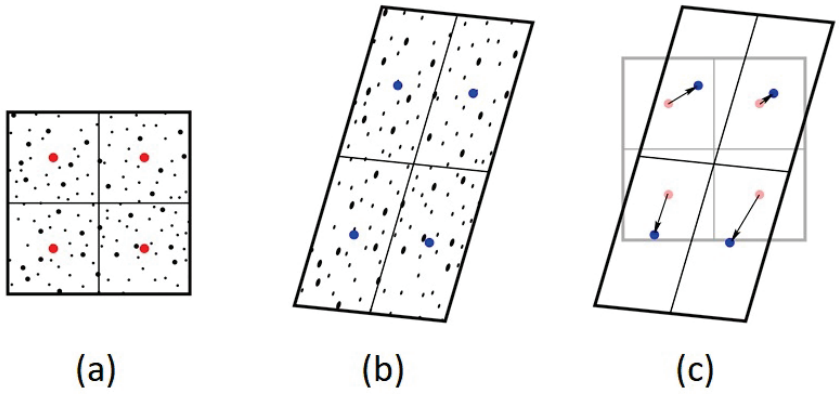

Figure 3.11: (a) reference image with multiple subsets and DIC points (b) deformed image with the new positions of the DIC points (c) computed displacement displayed with arrows. [78]

Subset and step sizes

The subset size is the length (in px) of the subset square in the reference image. The subsets can be overlapped if the subsets' centers have a distance smaller than the length of the subset size. The distance between subset centers in the reference image is denoted step size (in px). The most crucial factor for determining subset size is that each subset should contain at least three speckles [79]. There is also a delicate balance between selecting the subset size, the typical length scale of the displacement expected and the spatial resolution in the displacement field obtained at the end. A too small subset is likely to give a lot of noise. A subset too large is also not a good idea if displacement discontinuities are present (from grain boundary sliding for example)[80]. The subset must be larger than the speckle sizes and step size smaller or equal to subset size. In the example of Fig. 3.11, the subset size and the step size are the same, there is no subset overlapping. A small step size would significantly increase processing time while typically providing little to no gain because the same information is overlapped. Then, to get independent and non-repetitive data, the step size is chosen to be 1/4 of the subset's size. [79] [81]. In our work, the default step size is 10 pixels and 40 pixels is the subset size (but the influence of these parameters are tested). In other words, 10 pixels is our spatial resolution that will have different values in microns depending on the magnification of the image and the resolution of the camera.

Local and Global DIC

DIC algorithms are often classified by the pattern matching technique. In the local DIC (the one applied in this thesis), the pattern is separated into subsets that are individually matched. Conversely, for global DIC, the pattern is matched in one go using finite elements. Many of the principles mentioned before apply to local and global DIC. However, some specifics only apply to local DIC (such as subsets and step sizes). The two approaches of the algorithms are illustrated in Fig. 3.12.

However, the two algorithms are essentially different in terms of describing the underlying deformation field. In local DIC, adjacent subsets are analyzed independently without imposed continuity conditions before, resulting in separate or overlapping of deformed subsets (Fig. 3.13a). In contrast, global DIC is established based on a global description of the displacement field. As such, global DIC track the position of all the nodes (i.e., calculation points) simultaneously, therefore, evaluating the entire displacement field ensuring displacement continuity among elements (Fig. 3.13b) [83].

Pan [82] has done a comparison study between local and global DIC. He concludes that the local DIC offers better displacement precision than the global DIC method. Also, the average normal strains evaluated by local DIC are slightly better than that by global DIC in a real uniaxial tensile test. Finally, he also states that local DIC has higher computational efficiency than global DIC.

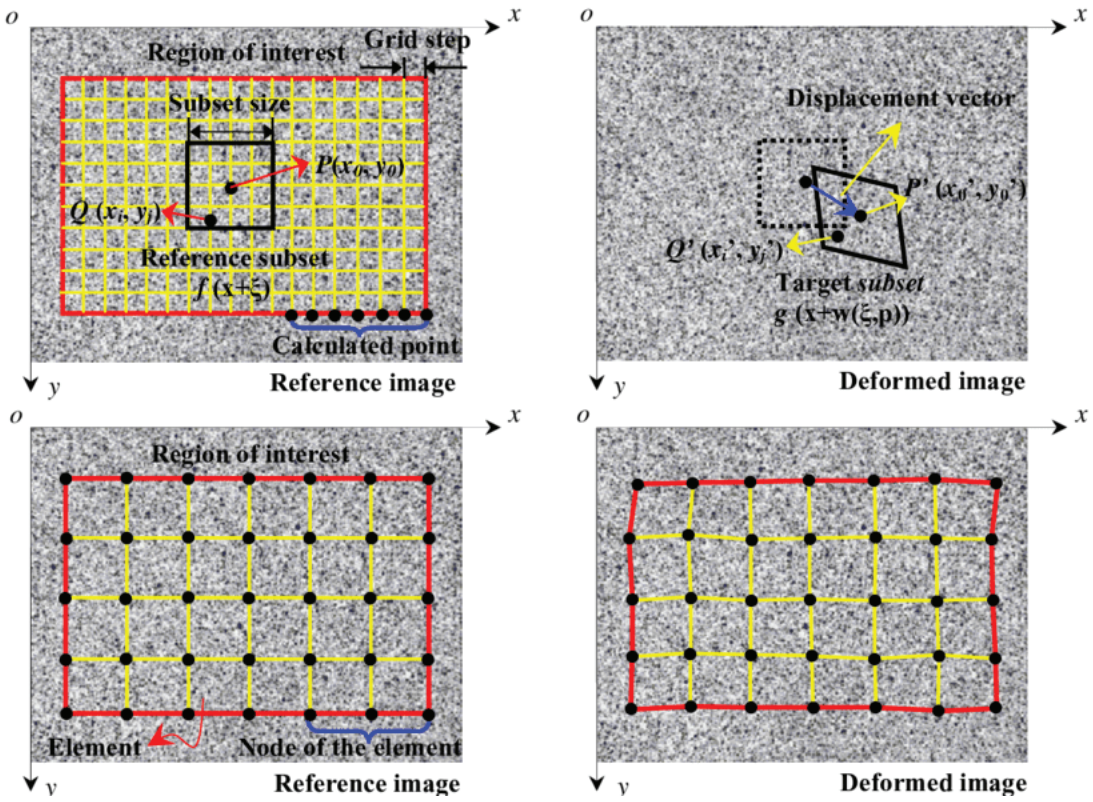

Figure 3.12: Displacement tracking strategy of (top) local DIC and (bottom) global DIC [82]

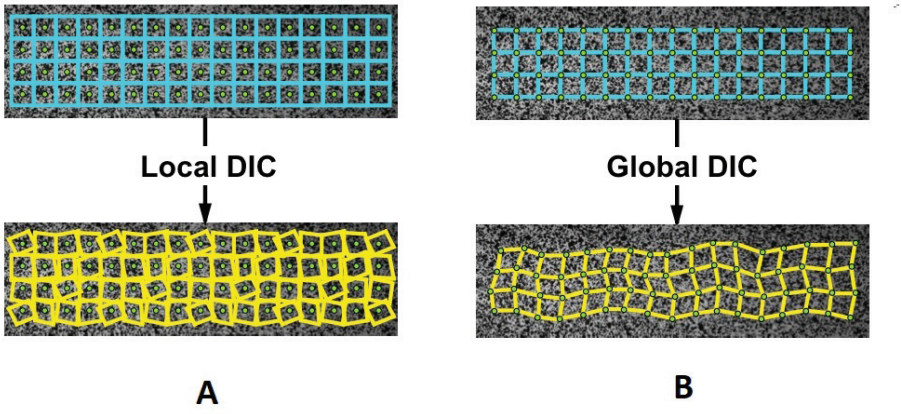

Figure 3.13: Comparison between Local Subset DIC and Global DIC[83]

DIC in python

In our study, a 2D local digital image correlation analysis is carried out using a free suite of python tools called Pydic [84], based on the library OpenCV and a local tracking method. Pydic is implemented to measure the displacement field on the sample surface from two pictures, and from this data, calculate the strain tensor. Pydic creates a correlation grid in order to find the displacement of each grid point or DIC point. The "Lucas Kanade feature tracker" from Bouguet [85] as implemented in OpenCV, is used. Rigid body translation is eliminated. Pydic has a set of numerical tools for reducing the noise of a local DIC analysis and for computing smoothed strain fields. The strain calculation involves a linear interpolation method for the displacement field and a numerical differentiation, obtaining all the strain tensor components. From the strain tensor components the Von Misses strain (also called equivalent strain) is calculated for our 2D case to create the strain maps.

Finally, 2D DIC assumes that the sample deformation is constrained to a plane that is parallel to the camera. In practice, out-of-plane motion is the main cause of additional error for 2D DIC [86]. Also, images can have distortions that introduce errors in DIC measurements. For example, camera lenses and optical microscopes generally have barrel distortions and focus problems. The experimental environment, such as fluctuating light conditions and loss of focus, is a source of errors

Speckle pattern

In order to match the reference and deformed images, DIC tracks features on the sample surface that collectively form the speckle pattern. The quality of DIC results is strongly dependent on the speckle pattern. Occasionally, a sample surface will inherently have features that suffice for a natural speckle pattern, but an artificial speckle pattern must typically be applied to the sample.

The artificial speckle pattern is obtained in our samples after the hydrogen charging procedure. It is produced by a chemical attack during the electrochemical charging in acid solution. This pattern is stable in time and also during the deformation of the sample. The pattern is influenced by the different charging times and electrochemical potentials used. Features that comprise the pattern are random in position but uniform in size and give a good grayscale contrast in the optical images.

In the SCC tests the natural pattern of the sample in polished mirror state is used. The stability of this pattern is problematic during the sample deformation. More details and insights are given in the SCC chapter and the discussion chapter.

Displacement and strain fields

The quality of the images limits the smallest possible measured displacement in the experiment. In general, DIC algorithms detect sub-pixel displacements on the order of 0.01 px. In practice, experimental variables introduce error into the measurements. The smallest displacement measurements expected from DIC, often called the noise floor or detection limit is on the order of 0.10 px. Generally, spatial strains are computed from the displacements (smoothed or not) with a spatial derivative with a filtering operator. A high interpolation in the displacement field and the filtering in the strain calculation can blur highly-localized deformations with sharp features or discontinuities. With spatial filtering

to compute the strains, the sharp features are smoothed out and can hide key phenomena like slip bands [87]. As a general rule, a larger strain filter and interpolation are necessary for a small grid size. In our study, the default grid size is 10x10 pixels. However, the grid size was changed when the speckle pattern quality was deficient, and the subset size was adjusted.

3.2.3 Stress Intensity Factor Calculation

Equation 3.2 gives the general expression of the stress intensity factor.

$$K_I = \sigma_\infty \sqrt{\pi a} f(a/W) \tag{3.2}$$

Where f(a/W) is a geometric function depending on the crack type (centered, single edge, and double edge crack) and the finite width effect correction. Stress intensity factor equations for sharp cracks in different configurations are found in Handbooks [88]. In our case, a SENT (Singled Edge Notched Test) specimen is used. where

$$f(a/W) = 1.12 - 0.23\frac{a}{W} + 10.56(\frac{a}{W})^2 - 21.74(\frac{a}{W})^3 + 30.42(\frac{a}{W})^4 \tag{3.3}$$

Numerical and finite elements methods were used to validate the solution in our specific case, taking into account the possible influence of the notch as a part of the crack, that might change the crack geometry. This formula is used to evaluate K, from the crack length measured by DIC and the force given by the load cell, in our experiments.

Notch effect

A notch causes a stress concentration effect. To know the maximum stress near a stress raiser, the stress concentration factor (theoretical) is defined as the ratio of the calculated stress peak to the nominal stress that would exist if the distribution of stress remained uniform that is

$$K_{conc} = \frac{\sigma_{nmax}}{\sigma_{nom}} \tag{3.4}$$

where σ_{nmax} is the maximum principal stress at the notch tip and σ_{nom} is the nominal stress. The stress concentration factor in Eq. 3.4 can be found tabulated [89] for different loading conditions and geometries or calculated by finite elements.

3.2.4 DIC validation using finite elements analysis

First, the DIC measurements were used as a "virtual strain gauge" to calculate the elongation in a sample and its elastic constants. The Young modulus (E) measured by DIC during elastic recovery is approximately 69 GPa, in good agreement with the literature. The Poisson's ratio is 0.3, also in agreement with the literature. Furthermore, the displacement field and the tensile deformation in the elastic range are measured in a notched sample (Fig. 3.14a and b) are in agreement with the finite elements analysis (FEA) (Fig. 3.14c) results using a commercial software called COMSOL [90]. In addition, the measured displacement by DIC during an increment in the tensile force is used as a boundary condition to the finite elements elastic model. The computed force value in the finite elements model is in agreement with the force value registered in the real sample by the load cell.

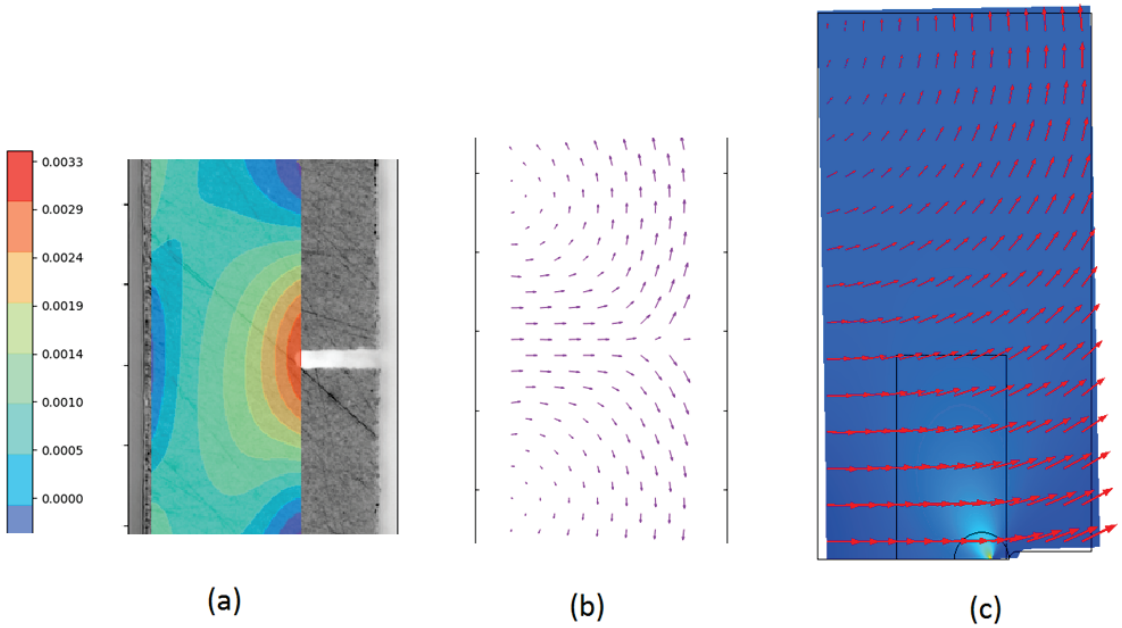

Figure 3.14: DIC measurements of the (a) tensile deformation field and (b) displacement field. (c) Displacement field computed using finite elements analysis in the elastic range with a 100 MPa applied (only half of the sample was modeled applying symmetry conditions)

Stress intensity factor measurements, validated by finite elements and DIC

In this case, the cracked sample is simulated in finite elements with the approach of a thin plate with an edge sharp crack, initiated from a U-notch tip. Determining the stress intensity factor directly from the local state at the crack tip is often problematic since the stresses are singular there in the elastic model. Because of this, more indirect energy-based methods are attractive to calculate the stress intensity factor. Consequently, K_I is

computed using the J-integral and from the energy release rate, applying a linear elasticity model.

On the experimental side, the force is recorded by the load cell during crack propagation. This force value is applied in our model to the upper horizontal edge as a force boundary condition in FEA to calculate the J-integral and the energy release rate.

Besides, a different procedure is needed to apply an experimental DIC displacement field as a boundary condition. First, an image is taken during crack propagation (first image). After that, the force is completely removed and a second picture is taken (second image). Second, a DIC analysis of these two images is performed, and the elastic displacement field is obtained. The elastic field measured by DIC is interpolated and applied as a displacement boundary condition to compute the energy release rate and the J-integral in COMSOL. The results are consistent. First, the computed K values calculated by the J-integral or by the energy release method are practically the same. Second, the K values obtained using different experimental boundary conditions, force, or displacement are very similar. Finally, the K values using FEA are in good agreement with the ones calculated applying Eq. 3.3, validating the use of this equation again even if the sample geometry is slightly different from a single edge-crack due to the presence of the notch. When the crack has grown more than 10μm from the notch tip, finite elements show that the stress is no longer influenced by the presence of the notch and the system behaves like a straight crack.

3.2.5 Crack tip localization method

The crack tip is located using the displacement field obtained by DIC between two pictures while the crack propagates in a picture sequence. Figure 3.15a shows a crack propagating, and Fig. 3.15b shows a zoom of the crack tip region where DIC is performed. Figures 3.15c and d are DIC analysis of the crack propagation in the red rectangle in Fig. 3.15b. The colored squares in Fig. 3.15c and d are 10x10 pixel size, representing the DIC grid size. On the same image, the displacement field is given by black arrows and the Von Misses strain is represented by the colors. Because in the picture sequence, the crack is opening and propagating, a discontinuity in the displacement field takes place. The displacement component aligned with the tensile force changes its sign abruptly where the crack is situated. The crack tip is the point where this discontinuity ends. The crack tip position is determined with the uncertainty of one step size (10 pixels), approximately 1 micron for the $\times$2000 magnification. If DIC can not be performed or the conditions for DIC analysis are diminished, the crack tip position is estimated from visual human inspection, for example in Fig. 3.15b the crack tip is observed (Image J is used to measure the crack length). The DIC crack tip location method and the visual human inspection are coincident when the crack is sufficiently open. Otherwise only DIC could distinguish where the crack ends.

Crack plasticity

The DIC map in Fig. 3.15c and d, shows the presence of plasticity ahead of the crack tip during crack propagation. In Fig. 3.16a and b, the DIC map of a propagating crack is shown. Two different kinds of plasticity are easily visualized. The first one is composed

of two deformation bands which expand from the tip at an angle from the crack plane, and the second one is located ahead of the crack tip and has to a few microns extension. The first one is called "primary plasticity" and the second one "secondary plasticity". In Fig. 3.16c and d, the crack tip position is found using the procedure described. The value of the Von Mises deformation at the crack tip position is designated ϵ_{tip}. The plasticity found ahead of the crack tip, over a length denoted Λ and expressed in microns, is also circled in the same figure.

Crack tip velocity determination method

The crack tip position as a function of time allows the computation of the crack propagation velocity. Measuring distances at a scale smaller than the grain size establishes a "local" crack propagation velocity on the sample surface. These velocities and their variations will be correlated with the fracture surface morphology and the accompanying plasticity quantified by some variables that will be defined in the next chapter.

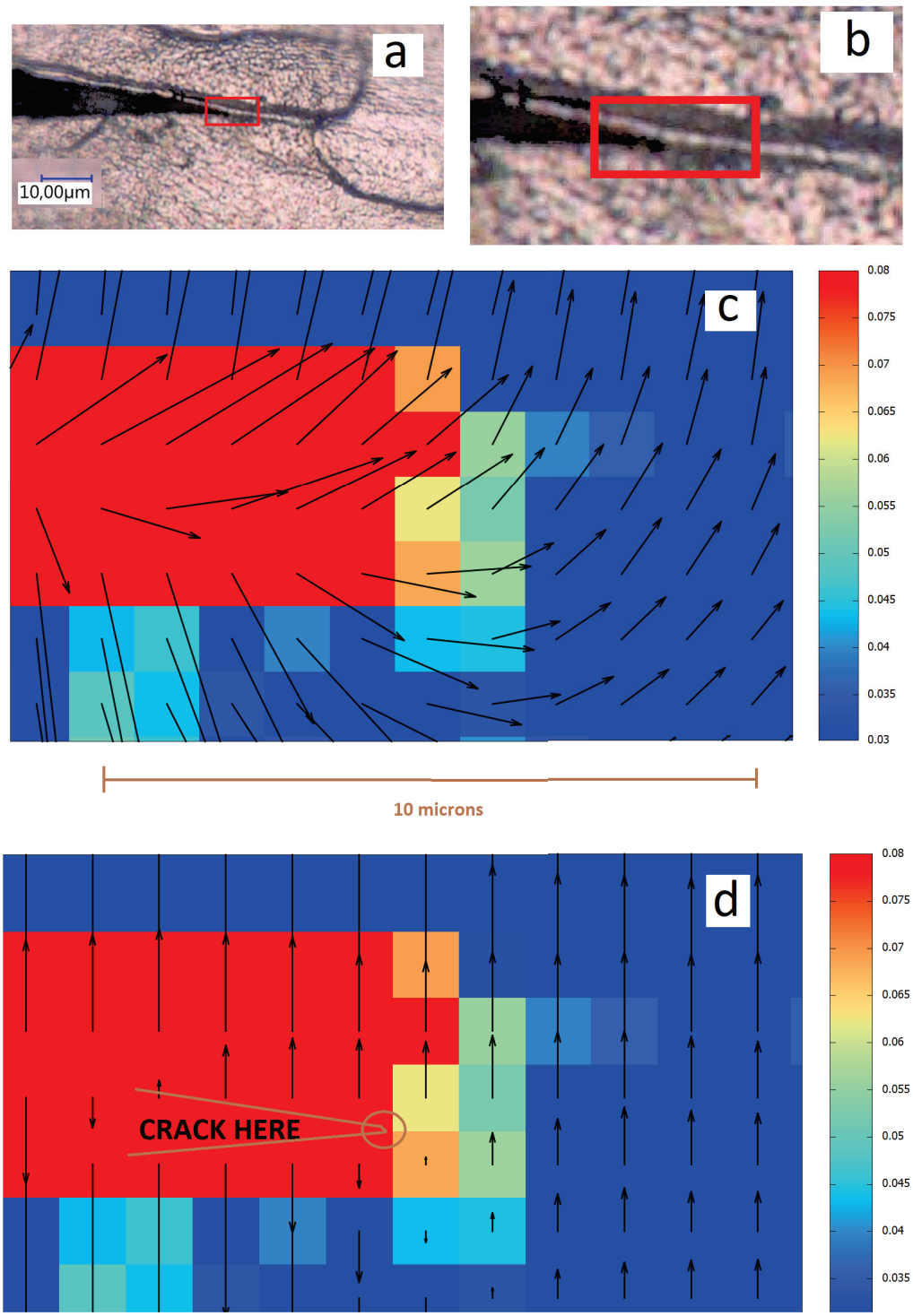

Figure 3.15: (a) Microscope image of a crack propagation during an internal hydrogen test. The all the pixels with the same color as the crack are highlighted in intense black. (b) Zoom of (a) in the crack tip region. (c) DIC analysis of the red rectangle in (a) and (b). A Von Mises strain color-map is displayed with the displacement field with black arrows. (d) A Von Mises strain color-map is displayed with only the vertical component of displacement field with black arrows. The crack tip position is marked.

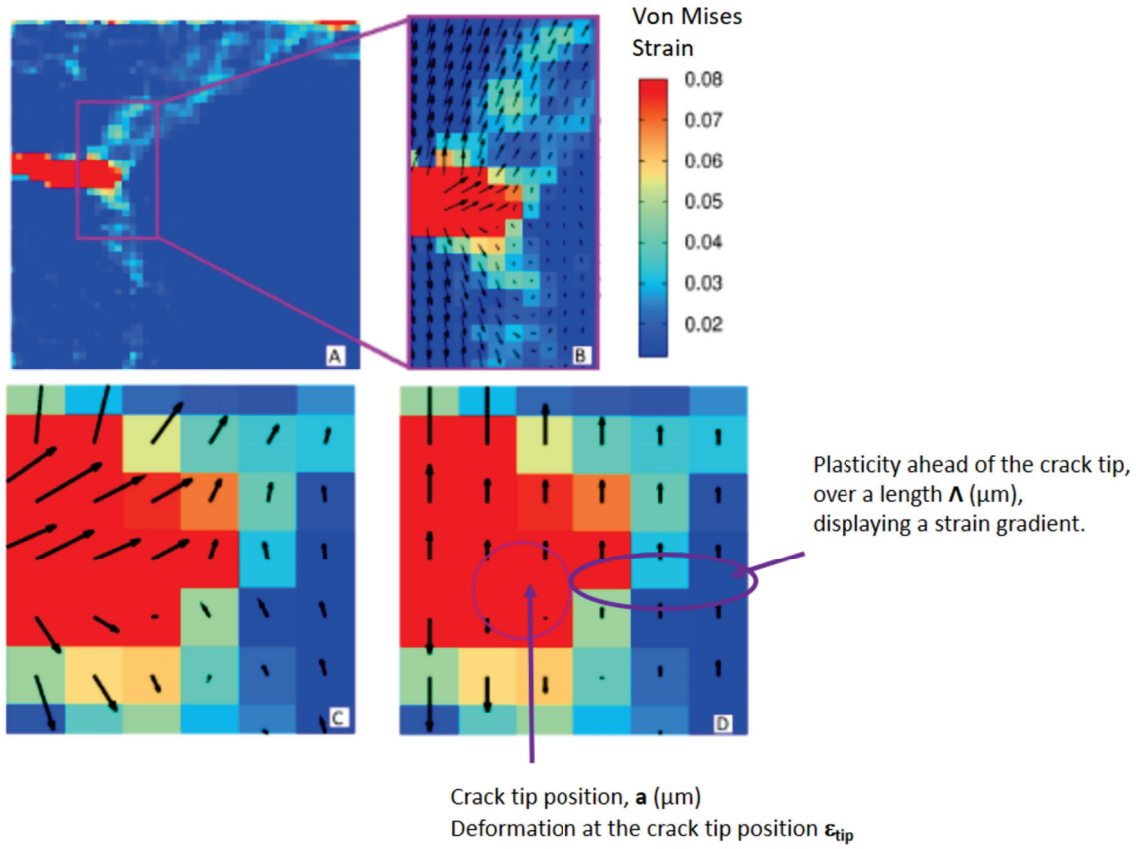

Figure 3.16: Digital image correlation analysis for crack propagation at high magnification. The square side is 1 micron approx. The displacement field (black arrows) is magnified 5 times and it is overlapped on a Von Misses strain colormap. a) full area of analysis, b) zoom of the crack tip area showing deformation bands and strain concentration, c) zoom of the crack tip opening, d) zoom of the crack tip with only one component of the displacement field, the crack tip position (a) is marked with a purple circle. The deformation at the crack tip position is evaluated ϵ_{tip}, and the extension (Λ) of the plasticity ahead of the crack tip is measured.

Chapter 4

Internal Hydrogen Embrittlement

Semi-brittle cracking due to internal hydrogen is a multiple parameter and length scale phenomenon. Our goal is to create a single crack and observe its propagation at a scale low enough to reveal crack-microstructure interactions. The overall goal is to build a physical model of cracking based on these observations. The outline of this section is the following. Cracking's general features are presented in the first section, listing the most relevant parameters (of the test itself and of the material). The fracture test is described (the force control, the initiation and propagation criterion), and finally, the macroscopic results (i.e average velocities and K levels) are given. The local scale observations, based on DIC, are presented in the second section. First, the initiation from the notch is detailed, focusing on local straining. Second, the local characteristics of single crack propagation (velocity and accompanying plasticity) are given.

4.1 Macroscopic description of hydrogen assisted cracking

A few words about the term "macroscopic". As it was stated in the methods section in the previous chapter, the tensile tests are performed in a DEBEN micro tensile machine, adapted with an in-house gripping system for the micro tensile samples. The term "macroscopic" refers to parameters that can be obtained with a traditional tensile test. However, because we use micro samples and a micro sample machine our results might differ from the ones obtained in a full macroscopic test under standard mechanical testing conditions, typical of the industry (i.e following the standards of the American Society of Testing Materials (ASTM)).

4.1.1 Test parameters

The parameters fall in three groups: hydrogen "damage" parameters, sample geometry parameters and mechanical test parameters. First, a range of hydrogen "damage" intensity is chosen. This intensity range is obtained by modifying the parameters of the electrochemical hydrogen charging procedure (E_c the cathodic electrochemical potential imposed to the sample and t_c, the duration of the exposure of the sample to E_c). Second, the geometry of the sample is also varied. The sample thickness (B) is especially important. It is expected that cracking depends on the crystallography of the grain boundaries.

Table 4.1: Characteristics of the tests done: sample name, cathodic polarization (E_c), hydrogen charging time (t_c), maximum stress (σ_{max}, force divided by the initial section not taking into account the notch), notch deformation (ϵ_{notch}), applied stress intensity factor (K), average crack velocity ($\overline{v}$), maximum local velocity (v_{max}), sample thickness (B), notch length (a_{notch}), comments on the test.

Sample	E_c mV/SCE	t_c h	σ_{max} MPa	ϵ_{notch} %	K MPa$\sqrt{m}$	$\overline{v}$ μm/h	v_{max} μm/h	B mm	a_{notch} mm
A	-1300	48	190	64	22	7	7*	0.4	0.35
B	-1400	72	158	39	10 - 11	15	96	0.5	0.35
C	-1400	24	164	53	13 - 15	25	25*	0.4	0.35
D	-1500	72	126	34	23 - 26	33	101	0.6	0.70
E	-1500	24	121	39	18 - 22	22	79	0.7	0.70
F	-1600	48	145	11	5 - 9	120	130	0.2	0.25
G	-1600	24	156	24	5 - 13	262	435	0.2	0.25
H	-1600	48	145	19	7 - 12	176	1800	0.6	0.25
I	-1600	28	162	25	8 - 14	254	528	0.6	0.25
J	-1600	24	155	18	8 - 12	65	144	0.4	0.25
K	-1600	65	155	22	7 - 12	338	480	1.0	0.25

However, the grain size is such that usually the crack front goes through many different grains. Even if the samples are taken from a rolled plate, their dimension in the crack front direction is at best of the order of 200 μm and often much smaller (20 μm) in regions where the plate is partially recrystallized. To obtain K values that are more representative of a single grain than an average on many grains, the thickness of the samples is gradually reduced. So that, the thicknesses explored range from 0.2 mm to 1 mm. The samples are notched to favor the formation of a single crack from the notch tip. The notch length (a_{notch}) is another geometrical parameter. Finally, the mechanical parameter is the force (F) applied to the sample. The control of the machine is made through F. However, the value is transformed in stress intensity factors K by using well-established equations checked by finite element calculations to get rid of the dependence on the geometrical parameters of the sample a_{notch}, width, and thickness. Table 4.1 shows the 11 tests reported, with E_c ranging from -1300 mV/SCE down to -1600 mV/SCE, t_c in between 24 h and 72 h, and thicknesses from 1 mm down to 0.2 mm. The number of successful tests was limited by the lack of reproducibility of the hydrogen charging procedure. There is more than 50% rejection due to heavy pitting during exposure to the electrochemical medium.

4.1.2 A typical crack test

H assisted cracking is strain rate dependant [26]. Therefore, it is important to define how the sample is stressed and what is the criterion to decide if the crack propagates.

The force on the sample is raised in steps at the minimum jaws velocity allowed by the machine (0.005 mm/min, $\dot{\epsilon} \approx 2 \times 10^{-5} s^{-1}$). When the target force is reached, the displacement of the jaws is fixed. There is always a small relaxation of the force (up to 1

N) over a period of time of about 5 minutes. Crack propagation under a fixed displacement of the jaws involves a force drop. In other words, the crack propagation is not only visible in microscope but also on the $F(t)$ curve, usually with a constant falling rate in the force values.

However, the crack propagation onset does not have to occur immediately, even if the force level is enough, then the force can stay on a plateau for some time before start decaying. It is, therefore, necessary to define a waiting time beyond which the crack is considered arrested in order to not increase the force unnecessarily and produce overloading.

The propagation criterion chosen is based on experience. It has evolved from the accumulation of empirical evidence in the early times of the project. The waiting time has decreased from 2 hours to about 20 minutes. A force decay, initiated after 20 minutes in fixed jaws displacement condition, has never been observed. If the waiting time is not respected and the force is increased unnecessarily, the crack will blunt or propagate under an overload with an increased plasticity level.

The typical time evolution of the force is represented in Fig. 4.1. The force is first increased in steps (Fig. 4.1(0)), with a pre-defined waiting time, until a force drop is detected and a crack length increment is visible on the side surface. This force level (Fig. 4.1(2)) defines the maximum stress $\sigma_{max} = F/S_0$, (S_0 is the section of the sample, not taking into account the existence of the notch) necessary to initiate a crack from the notch (Tab. 4.1). The force is then brought down well below the initiation value to arrest the crack (Fig. 4.1(3)), and the procedure is started again. The new crack propagation event defines the threshold stress intensity factor (K, Tab. 4.1 and Fig. 4.1(4)) for the main crack propagation. These two stress values are always similar. The crack propagation (Fig. 4.1(4)) displays an almost constant falling force rate. The crack is frequently stopped at microstructural features such as triple points or secondary cracks; it is restarted by applying force increments of the order of 0.5 N. So, the applied mechanical load changes during propagation.

Once the main crack is initiated and the mechanical load level is the minimum necessary for crack propagation, optimal conditions for local observations are looked for: flat grain boundary facets, perpendicular to the tensile axis, good focus condition for the optical microscope, and appropriate surface pattern for DIC. Pattern quality suffers fluctuations because, during hydrogen charging, the chemical attack on the surface is not homogeneous on the whole sample. If optimal observing conditions can not be achieved, pictures are taken anyway but at a lower magnification. Ideally, the crack tip is followed by displacing, manually, the field of view at the highest magnification available (x 2000), which corresponds to a maximum resolution of 110 nm per pixel.

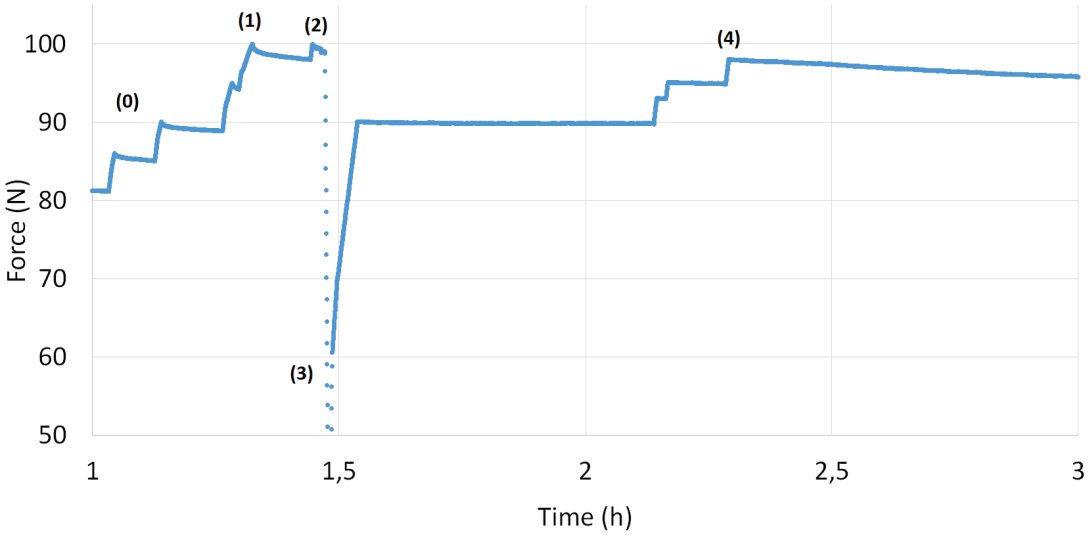

Figure 4.1: The force (F) is varied in time to obtain single crack initiation. The curve shown corresponds to the sample I of Tab. 4.1 ($E_c = -1600$ mV/SCE and $t_c = 28$ h). The force is raised in steps with a waiting time (0). When the force reaches 100 N for the first time (1), a drop of the force is obtained, but no crack advance was visible on the surface; therefore, the force is raised again up to 100 N (2), and then crack formation and propagation is observed from the tip of the notch. This force value is, therefore, the one used to calculate σ_{max}. The force is immediately dropped (3) (at time 1.5 h approx.) and then raised again in steps until the propagation conditions are met again at about 2.3 h (4). The force level is then slightly below 100 N and is the one used to define K, the threshold stress intensity factor for crack propagation.

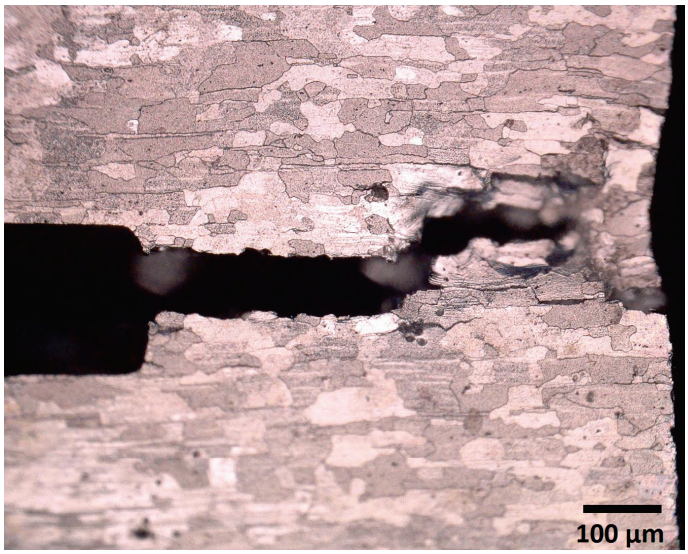

Figure 4.2: Macroscopic side view of the sample (sample G of Tab. 4.1) after the complete propagation of a crack. The H charging procedure has revealed the grains. The notch is visible on the left. The traces of the several cracks that were initiated from the notch are visible. The single, intergranular, main crack has propagated over 300 μm, perpendicular to the tensile axis. In the final stage, the crack deviates, plastic deformation is intense and multiple cracking are formed.

Complete propagation is achieved when the crack growth approaches a value of a/w (where a is the crack length and w is the width of the sample) around 0.6. At this point, a crack deflection is often produced, and multiple cracks are created all-together, as it is shown in Fig. 4.2. The crack is no longer perpendicular to the tensile force, and single crack propagation is no longer possible. In order to increase the available distance for an observable single crack propagation, the sample's width was extended from 1mm to 1.5 mm in several cases.

4.1.3 Analysis of the macroscopic behaviour

In Tab. 4.1, the H charging conditions are put in relation with different macroscopic indicators of crack initiation and propagation. Concerning the global sensitivity to hydrogen damage, it can be seen from the average velocity ($\overline{v}$, shown on the seventh column of Tab. 4.1) that the embrittlement level increases with a decreasing cathodic polarization (an increase in the absolute value). In the case A ($E_c = -1300$ mV/SCE), a crack propagation at imposed constant displacement could be obtained only on a very limited portion of the test. On the rest, the crack advance was obtained only by constantly pulling the sample. Nevertheless, an intergranular fracture was obtained, but in conditions where the sample is fully plastified during the test. A second group of tests, composed of samples B, C, D, and E, can be formed, with average velocities of the order of 25 μm/h. These correspond to $E_c = -1400$ and -1500 mV/SCE. Finally, a third one, composed of the samples H pre-charged at $E_c = -1600$mV/SCE, namely samples F, G, H, I, J, and K,

has a much higher average propagation velocity, on the order of 200 μm/h. These three groups are respectively named Group 1 (very slow propagation), Group 2 (slow propagation), and Group 3 (fast propagation). A last word on the propagation velocities. The average values are the mean of the local velocities v (see next section). The maximum value of v, v_{max}, is given in Tab. 4.1. v_{max} can apparently be as high as 1800 μm/h, but a more representative value is 500 μm/h, as discussed below. The trend with E_c is the same as the one described for $\overline{v}$.

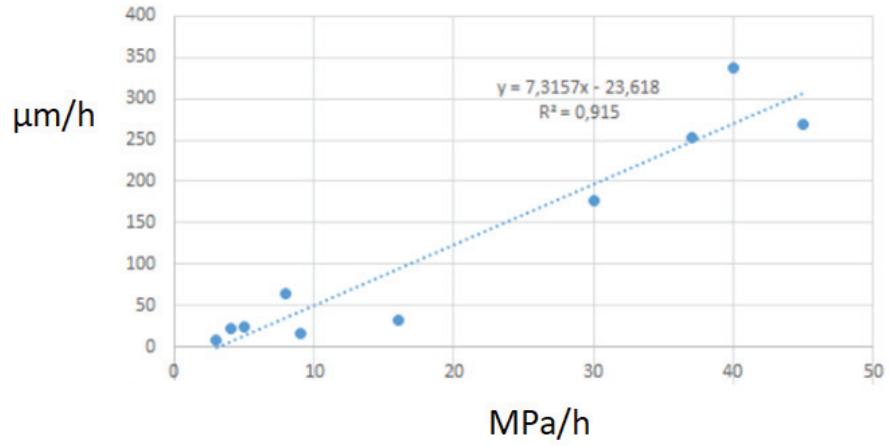

Figure 4.3: Average crack propagation velocity as a function of the average falling stress rate during crack propagation for all the tested samples

Besides, as shown in Fig. 4.1, the force is continuously decaying in time during crack propagation. The average falling stress rate of this decay is correlated with the average crack propagation velocity in Fig. 4.3. It is a plot of the average propagation velocities in Tab. 4.1, against the rate of the stress decay rate, for all the tested samples. An almost linear correlation between the two variables is visible at this macroscopic scale in Fig 4.1.

In addition, the fracture surfaces are also significantly different between the three groups. Group 1 is essentially ductile. 60% of the fracture surface is ductile covered by dimples (Tab. 4.2). The rest of the fracture shows H embrittlement. Intergranular and transgranular regions exist on the inner of the sample, while the region close to the surface is not embrittled and broke with the formation of a thin plastic lip, preventing any relevant observation of crack propagation on the side surface. A typical fracture surface affected by hydrogen of Group 2 is composed of areas that are entirely flat intergranular, intergranular with a marked roughness (Fig. 4.4). The intergranular nature of these zones will appear clearly in the next section where the fracture surface observations are enriched with an in situ side surface observation of crack propagation. It gives information on the nature of fracture, together with a fine measurement of the accompanying plasticity. On average, about 50% of the fracture surface is intergranular smooth and 20% is intergranular rough. (Tab. 4.2).

The situation is markedly different for Group 3. The propagation can also be along the grain boundaries, but the fracture path can change, even in the middle of a facet, to

a transgranular one, still parallel to the GB (Fig. 4.5). The respective percentages are present in Tab. 4.2.

Table 4.2: Percentage of the fracture surface occupied by the various mechanisms: IG smooth (intergranular brittle with no, or few, plastic features on the fractire surface), TG (transgranular brittle), IG rough (intergranular "ductile", i.e. an intergranular fracture with a plastic activity on the fracture process zone which gives a roughness on the fracture surface), ductile fracture with dimples.

Sample	% IG smooth	% TG	% IG rough	% ductile
A	20	20	-	60
B	45	-	20	35
C	50	-	20	30
D	58	-	12	30
E	37	-	17	46
G	65	21	-	14
H	54	45	-	1
I	43	56	-	1
J	45	42	-	13

The separation into three groups is also relevant concerning the mechanical aspect of fracture. First, initiation is characterized by σ_{max} and the deformation of the notch tip ϵ_{notch} at crack initiation. The later is the ratio of the notch tip opening, i.e., the ratio of initial diameter of the notch tip and its diameter at the moment of crack initiation. ϵ_{notch} is as high as 64% for Group 1, 40% for Group 2 and 22% for Group 3. The trend is again that the deformation necessary to obtain a crack decreases when E_c decreases. The strain level is high in comparison to the macroscopic strain to failure observed on the tensile curve (30%) due to the notch strain concentration effect of the notch. In the next section, DIC will help quantify the local deformation in the notch region which is necessary for initiating the crack. The σ_{max} is similar to the yield point measured in our mechanical testing conditions (150 MPa approx), so the sample is macroscopically at the beginning of the plastic regime. The stress intensity factor K, necessary for crack propagation, is an output of the test. It increases during the test because of the crack growth and the sample geometry, giving a K range. This K range is indicated in Tab. 4.1. It refers to the load at the initiation of the main crack, and the load at the end of its propagation (before deflection and final fracture). The required K level for initiation is always lower than 9 MPa$\sqrt{m}$ for Group 3. Conversely, it is always higher than 9 MPa$\sqrt{m}$ for Group 1 and 2. This division is coherent with the assumption that more H amount leads to a lower K for initiation.

The thickness has no noticeable influence on the value, at least in the experiment's current stage. It might be because of the grain size or the lack of embrittlement, which hides the GB crystallography effect on the critical mechanical load. As a comparison, the theoretical K for a brittle crack propagation, when the damage is large enough to prevent dislocation emission from the fracture process zone, is of the order of 0.5 MPa$\sqrt{m}$, from

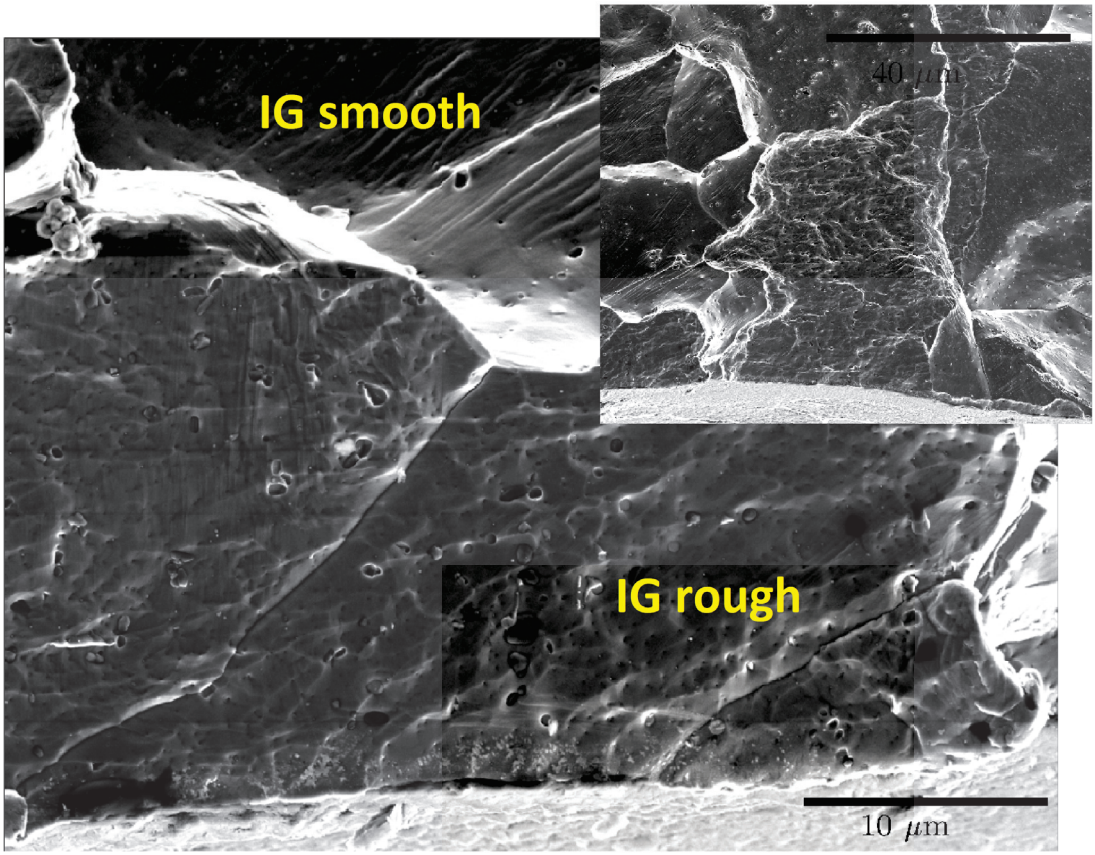

Figure 4.4: A typical zone of the fracture surface of the G2 group, obtained on sample B (Tab. 4.1). The SEM image shows a detail of an intergranular fracture with a roughness (IG rough) which is the signature of an intense plasticity accompanying fracture. The top-right picture is a more macroscopic view which shows the mixture of brittle intergranular smooth (IG smooth) fracture and this "rough" intergranular fracture.

atomistic simulations [91]. It means that crack propagation, even if intergranular, occurs with an intense emission of dislocations.

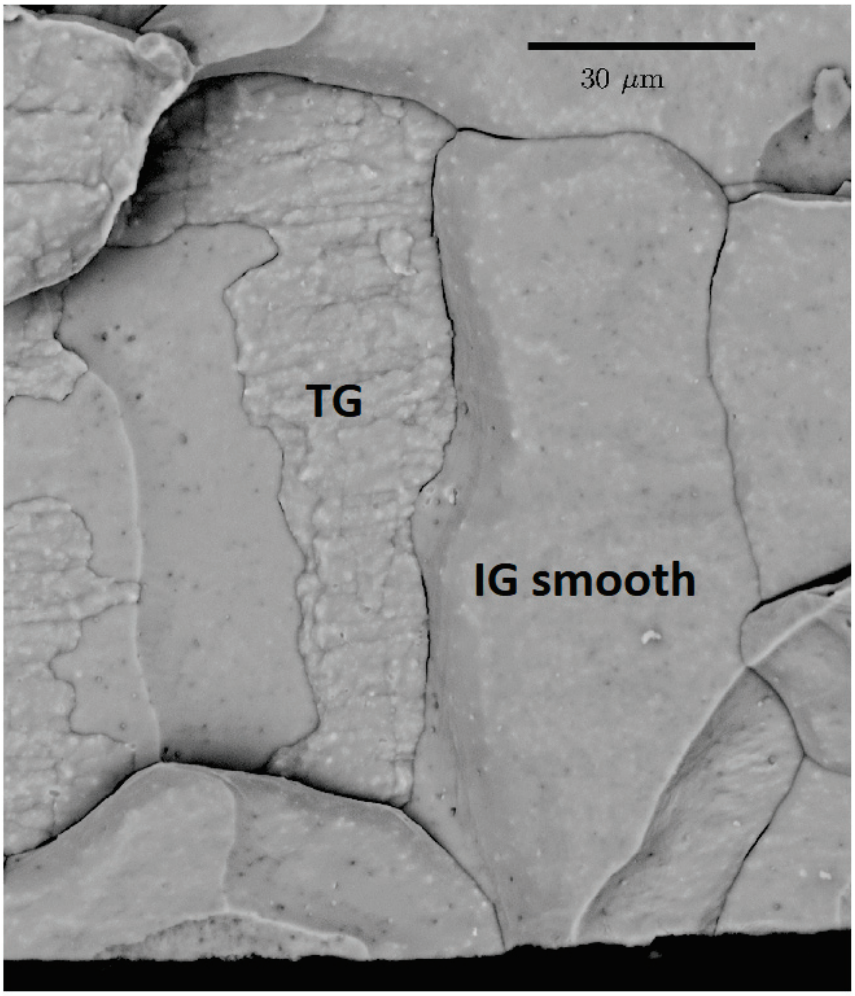

Figure 4.5: A typical zone of a fracture surface of Group 3. It was obtained on sample J (Tab. 4.1). The SEM image shows a transition between a brittle intergranular smooth fracture (IG smooth) and a transgranular fracture (TG) parallel to the grain boundary.

4.2 Local scale observation of crack initiation and propagation

The previous section showed that initiation from a notch requires a considerable strain, of at least 20%, even in the most brittle cases. Then the crack propagates at a relatively high mechanical load K$\sim$ 8 MPa$\sqrt{m}$. It seems that, at every stage, plasticity is present. In this section, the initiation and propagation stages are studied in more detail using digital image correlation to characterize the plastic deformation at initiation and during propagation. The crack tip location is precisely determined, at a scale smaller than the grain scale, which enables the measurement of the position of the crack tip and, therefore, of the local velocity. The level of plasticity, the local velocity, and the fracture details are analysed to try to establish correlations.

4.2.1 Straining the notch tip and initiation

Figure 4.6 illustrates initiation in three cases with different H charging conditions: tests D, E, and J, respectively charged at -1500 mV/SCE during 72 hours, -1500 mV/SCE during 24 hours, and -1600 mV/SCE during 24 h (table 4.1). In every case, the notch is machined with an initial radius of approximately 35 μm. The stress applied to obtain a single crack initiation σ_{max} creates a plastic opening of the notch, which is evaluated "macroscopically" (using Image J analysis) by $\epsilon_{notch} = \Delta l/l_0$ where l is the separation between the surfaces of the U notch tip after deformation and l_0 is before deformation (i.e. the initial notch diameter). ϵ_{notch} is in between 20 and 50% in the brittle cases (Tab. 4.1).

Moreover, digital image correlation (DIC) has been applied further in between the two images: the one where the notch is not stressed and the one where the stress is just below σ_{max}. The magnification and picture size is such that a pixel represents about 0.6 μm. The grid's step length for DIC is 20 pixels, giving a spatial resolution of about 12 μm for the displacement field. The strain tensor is calculated from the displacements, and the Von Mises strain is shown as colored maps on figure 4.6 b, d, and f for the three different charging conditions. The yellow color means that the deformation exceeds 10%, and black is 0% deformation. The color box range is the same for every map. The blue arrows represent the displacement vectors in pixel units. The first out of the two optical images used for DIC, the reference image (the mechanically unloaded state), is shown on the left of the figure. The DIC grid is superimposed. It is focused on the notch tip region. Note that the chemical attack during the hydrogen charging reveals the grains, especially for the long charging of 72 h (sample D, Fig. 4.6 a). The small inserts, in the superior frame part, display at which location the single cracks emerged from the notch. This location is well correlated with the maximum strain at the notch tip. Indeed, there are always two main slip bands exiting the notch tip (even if they are very branched in the D case Fig. 4.6 b). In cases D and J (Fig. 4.6 a and e), the tip of the notch is not well rounded (machining effect of the saw) and the slip bands are formed at the corners. As a result, the cracks initiate at the corners and not at the center of the notch.

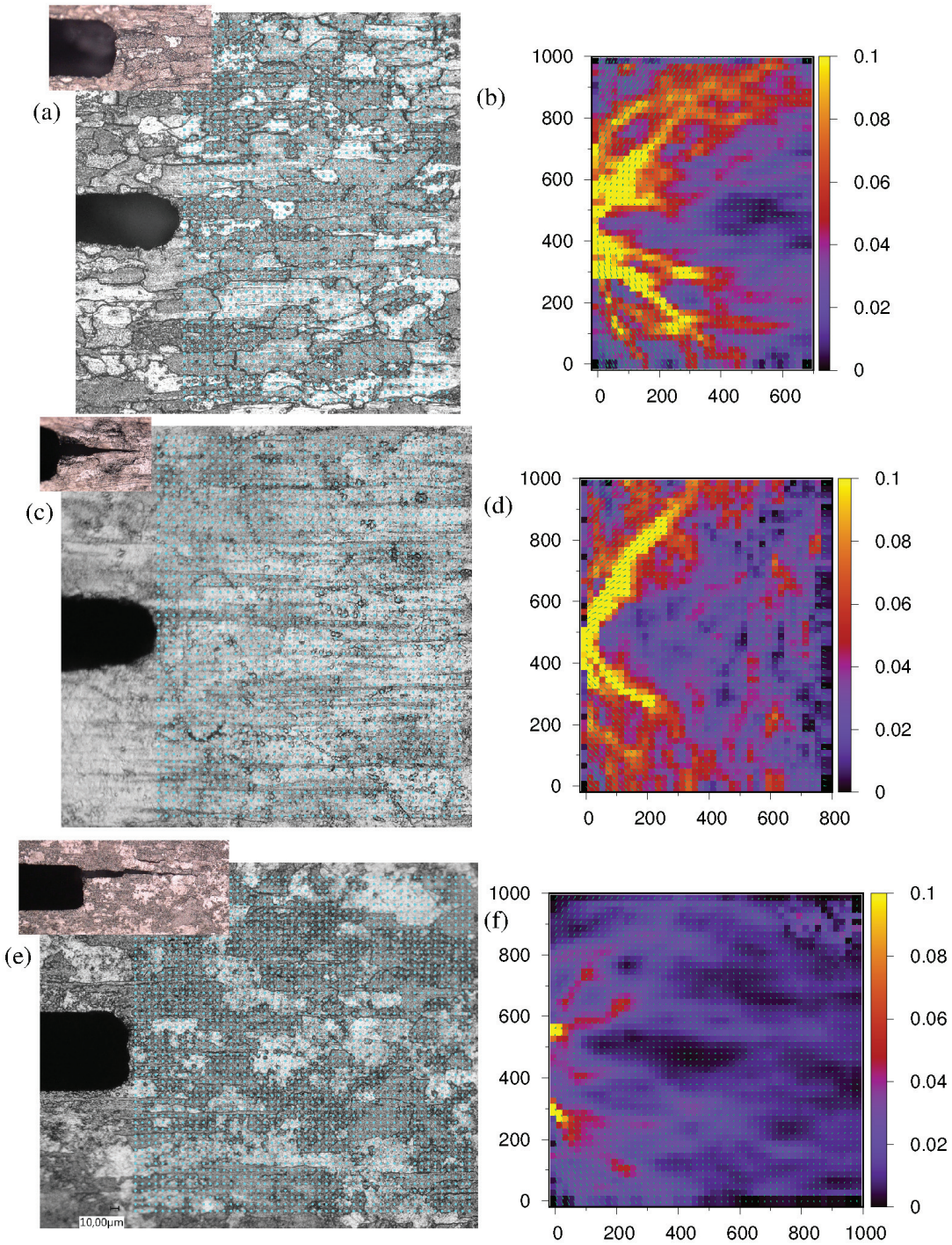

Figure 4.6: Illustration of the local strain necessary for crack initiation from a notch. Images (a,b), (c,d) and (e,f) correspond respectively to samples D, E and J (tab. 4.1), i.e. to H charging conditions (E_c=-1500 mv/SCE, t_c=72 h), (E_c=-1500 mv/SCE, t_c=24 h), (E_c=-1600 mv/SCE, t_c=24 h), respectively. Pictures on the left are optical images of the surface used for DIC. The grid is superimposed. On the right are the corresponding Von Mises deformation maps calculated from the displacement field. The axis units are in pixels (px) with 20 px = 12 μm, which is the grid step length. For example, (b) is 700 px x 1000 px = 414 μm x 593 μm.

On the contrary, in case E (Fig. 4.6 c), the notch is circular, and both bands are formed from the center of the notch. Crack initiation occurs at the center of the notch. The maximum strains measured by DIC at the initiation point are respectively 35%, 60%, and 18% for D, E, and J, which is the same ranking as the one based on ϵ_{notch}: 34%, 39%, and 18%, the right tendency is interesting because the DIC measurements are more precise and at a local scale. The inserts show the main cracks after initiation. They are all intergranular.

It is interesting to note that the region where the strain is high (typically above 10%) extends over several grains. If the notch tip radius would be smaller, it might merely blunt, as was frequently observed for cracks, and might not create a strained region large enough to promote compatibility stresses or stress concentration at pileups at the grain boundaries. We can expect that it is the resulting local stresses which are responsible for GB fracture at the initiation point. The crack passes the initiation region, which has a size limited to a few tens of microns. Note that the single crack's future path is very little pre-strained because the bands develop at an angle, and the deformation is low away from it. Therefore, apart from the necessary initiation, the notch's straining does not provide a relevant damage to the material, such as the one that can be expected from the pre-straining of 10% macroscopically in the full sample.

4.2.2 Local propagation velocities and plasticity

This subsection deals with displacement field measurements at the micron scale. It starts with the definition of the quantities derived from this field and used to characterize crack propagation. The details of the data are then presented in Tab. 4.3. Representative DIC images are shown, which illustrate the plastic deformation accompanying propagation. Then the local propagation velocities are matched with the fracture surface features. This attempts to connect velocities and the fracture mechanisms, as characterized by its appearance on the fracture surface. Finally, correlations between the local propagation velocity v and the local plasticity or between v and the three different fracture morphologies revealed by SEM are investigated.

After the initiation stage, the single crack can be followed under the optical microscope and images are collected for DIC analysis. As already presented in the previous chapter, the displacement field enables the determination of the position of the crack tip, i.e., the crack length a measured from the notch tip. DIC is crucial because it is often impossible to know where the crack tip is situated by simply inspecting the image visually. The image frequency acquisition is adjusted depending on the crack velocity on the surface. The highest frequency used is one picture taken every 20 s, which is enough to measure several crack tip locations along a single grain boundary facet. Therefore the local velocity v is measured with a spatial resolution lower than the grain size.

Besides, DIC computes the displacement field around the crack tip and, therefore, can be used to characterize the plastic deformation which follows the crack advance. Fig. 4.7 shows an example of the Von Mises strain field obtained. The strain field is overlapped with the deformed image (i.e. the second of the pair used for DIC), and the strain values between 1% and 20% are displayed. It will be shown below in details that two forms of plasticity can be differentiated. The first one is the intense plastic slip bands, which develop from the crack tip at an angle with the crack path. The second one is a deformation along the crack path, ahead of the crack tip. The first one is quantified by the plastic deformation rate (PDR), which is calculated from the plastic deformation field by integration. A few insights about the physical bases of the PDR. The Orowan formula relates the plastic deformation to the area swept by a moving dislocation, the local deformation increment $\delta\epsilon_p$ due to the crack advance Δa, assuming that every dislocation travels the same distance l (the dislocation mean free path) and that the local length of dislocation increases by δl_d, is:

$$\begin{aligned} \delta\epsilon_p &= \frac{b}{l_y}\frac{l\delta l_d}{s_0} \\ &= \delta\rho_s b l \end{aligned} \tag{4.1}$$

b is the Burgers vector, l_y is the height of the volume element, s_0 is its surface, and $\delta\rho_s$ is the increment of statistically stored dislocation density due to the crack advance at every point in the system (it is the length of dislocation per unit volume). From the DIC 2D data, the increment of dislocation length in the whole system ΔL_d is obtained by integration of $\delta\epsilon_p$. $\delta\epsilon_p$ is estimated as the Von Mises strain (ϵ_{eq}) computed during the correlation between two crack configurations. In practice, the integration is limited to the region around the crack tip defined by a lower threshold of 1% deformation, which is the noise level, and an upper value is the deformation found at the crack tip position, beyond

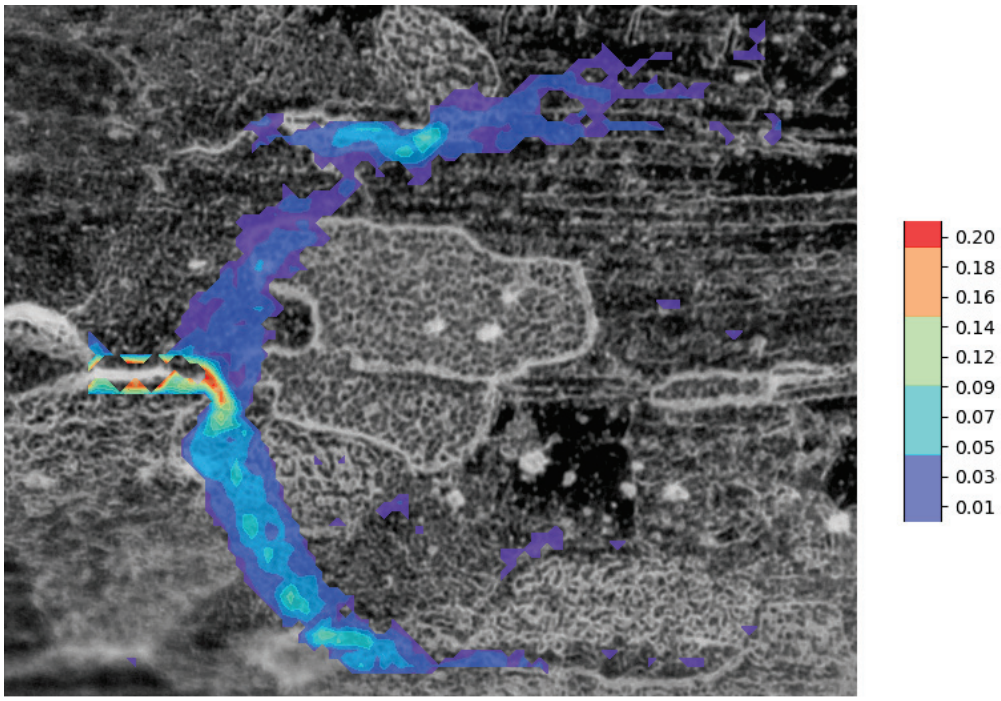

Figure 4.7: The Von Mises strain field calculated from the DIC displacement field is shown. It is overlapped with the deformed image after the crack advance. The sample is G and the final crack position is G2 in table 4.3, i.e. the crack advance is from the configuration G1 to configuration G2 and the characteristics of the plasticity increment during this increment of crack length (PDR, Λ and ϵ_{tip}) are reported on line G2 of the table.

which the deformation is not physical (inside a crack there is no material). An example of such region is given on Fig. 4.7 (colored region). The total variation of dislocation length in the system (the plasticity injected during the crack extension) is:

$$\Delta L_d = \int \delta\rho_s dV = \int \frac{\delta\epsilon_p}{bl} B dS \tag{4.2}$$

B is the thickness, which is taken as 1. The obtained value ΔL_d is divided by the crack length increment Δa. to obtain "plastic deformation rate" or PDR ($\frac{\Delta L_d}{\Delta a}$) in the Eq. 4.3).

$$PDR = \frac{\Delta L_d}{\Delta a} = \frac{1}{\Delta a\ bl} \int \epsilon_{eq} dS \tag{4.3}$$

The word "rate" does not mean a variation with time, but with the crack extension, similar to the energy release rate concept. The PDR, plastic deformation rate, is interpreted as a non-dimensional index that estimates the plasticity injected during crack growth. For example, the PDR value computed in the case of Fig. 4.7 is 2949. Finally, the plasticity just ahead of the crack tip, confined to the immediate vicinity of the crack path, is better characterized by the Von Mises deformation at the crack tip position (ϵ_{tip}), and the extension of the plasticity just ahead of the crack tip (the length Λ, defined with

more detail in the Methods chapter) limited where the deformation is at the same level as the background deformation of DIC (set to 1%).

Table 4.3 presents the measurements of these quantities for the 11 samples of Tab. 4.1. 66 pairs of images were processed by DIC. The cases of sample Ia, Ib, Ja, Jb, are different sequence of pictures for the same sample, it is because of difficulties during the test. Not all images taken were suitable for DIC because of the surface pattern's heterogeneities, or a loss of focus due to the deformation of the surface, even if the operator has optimized the quality of the image on the fly. Therefore, some crack tip positions were estimated directly on the image when the crack opening was large enough to provide a reasonable estimate of the crack tip position. These less reliable measurements are distinguished from the others by a star *. The maximum resolution has a magnification of x2000 and an image size of 1600x1200, which corresponds to 110 nm per pixel. The high-resolution DIC uses a step size of 10 pixels, i.e. gives a spatial resolution of 1.1 μm.

Table 4.3: Local measures: crack length (a), local velocity (v), force (F), stress intensity factor (K), Von Mises deformation measured at the crack tip location (ϵ_{tip}), length of the plastically deformed region just ahead of the crack tip along the future crack path (Λ), and the plastic deformation rate or PDR (the dislocation line length increment per unit crack advance $\Delta L_d/\Delta a$).

Image	a	v	F	K	ϵ_{tip}	Λ	$\Delta L_d/\Delta a$
	μm	μm/h	N	MPa$\sqrt{m}$	%	μm	
A							
1	530*	-	104.1	22.0	-	-	-
2	575*	7*	95.7	22.3	-	-	-
B							
1	500	-	111.2	11.2	-	-	-
2	503	4	106.3	10.7	7	3	5776
3	508	16	103.2	10.6	7	3	5368
4	512	16	101.9	10.5	8	3	2835
5	518	20	99.8	10.4	8	3	4738
6	523	20	98.2	10.4	8	3	4254
7	529	24	96.0	10.4	12	4	5368
9	536	24	94.0	10.4	12	4	5413
10	539*	36*	93.4	10.4	-	-	-
11	543	96*	92.7	10.4	7	6	3843*
12	548	96	91.4	10.4	7	5	2636
13	550	24	90.4	10.4	7	5	7043
14	552	24	88.8	10.4	11	4	11369
C							
1	600*	-	88.0	13.4	-	-	-
2	625*	25*	85.0	13.8	-	-	-
3	650*	25*	82.0	14.2	-	-	-
4	675*	25*	79.0	14.7	-	-	-
D							
1	920	-	101.2	25.6	-	-	-
2	929	32	98.0	25.4	10	3	2662
3	930	4	94.4	24.4	10	2	23448
4	931	4	90.9	23.7	8	4	27359
5	946	111	87.9	23.9	8	4	1805
6	952	40	86.4	23.9	8	3	3929
7	966	52	82.3	23.7	10	4	1959
E							
1	825	-	115.2	18.8	-	-	-
2	845	24	111.1	19.2	10	25	20356
3	865	48	109.0	20.0	3	20	3507
4	898	79	107.1	21.7	5	26	4675
5	918	48	105.2	21.7	3	13	2488
6	938	7	93.0	21.4	3	13	5205
7	951	16	89.2	21.3	3	13	5652

Image	a μm	v μm/h	F N	K MPa$\sqrt{m}$	ϵ_{tip} %	Λ μm	$\Delta L_d/\Delta a$
F							
1	260*	-	25.0	5.1	-	-	-
2	280*	110*	24.0	5.3	-	-	-
3	300*	-	29.0	6.9	-	-	-
4	380*	130*	27.0	8.8	-	-	-
G							
1	430*	-	22	8.2	-	-	-
2	438	185*	21.8	8.3	16	6	2949*
3	440	53	21.5	8.3	11	8	7884
4	444	53	21.0	8.3	16	8	7745
5	481	436	19.0	10.3	10	8	915
6	520*	450*	-	-	-	-	-
H							
1	321*	-	71.7	7.5	-	-	-
2	333*	144*	70.4	7.6	-	-	-
3	340	93*	68.0	7.6	8	4	849*
4	343	36	67.4	7.6	8	2	1325
5	365	132	64.4	7.9	5	2	488
6	372	60	62.3	7.9	6	2	1995
7	377*	67*	60.9	7.9	-	-	-
8	397*	400*	60.0	8.3	-	-	-
9	402	60*	58.5	8.3	6	1	302*
10	415	223	57.8	8.7	4	2	424
11	460	1800	57.0	10.3	4	3	95
12	463*	72*	56.5	10.4	-	-	-
13	472	216*	56.0	10.7	6	3	1068*
14	484	288	55.0	11.0	5	4	648
15	490	360	54.5	11.2	4	3	729
Ia							
1	290*	-	97.0	4.8	-	-	-
2	299	528*	96.6	4.9	6	2	596*
3	302	132	96.2	5.0	6	4	1856
4	304	198	95.8	5.1	6	4	1330
5	306	66	95.4	5.2	6	3	4314
6	311	330	95.0	5.3	6	4	1214
Ib							
1	415	-	78.7	10.4	6	9	-
2	428	256	77.8	10.8	6	6	658
3	443	312	76.9	11.4	6	6	1107
4	460	340	76.0	11.9	6	4	927
5	468	143	75.1	12.3	4	4	1257
6	479	227	74.2	12.7	6	4	1190
Ja							

Image	a	v	F	K	ϵ_{tip}	Λ	$\Delta L_d/\Delta a$
	μm	μm/h	N	MPa$\sqrt{m}$	%	μm	
1	418*	-	51.0	7.9	-	-	-
2	423	32	50.6	8.0	3	3	127
3	426	24	50.3	8.1	3	3	148
4	428	16	50.0	8.1	2	1	837
5	435	48	49.5	8.2	3	4	149
6	440	40	48.7	8.3	3	3	68
7	444	24	48.1	8.2	3	7	9
8	445	3	47.6	8.1	3	3	789
9	452	24	46.0	8.0	3	3	179
Jb							
1	480*	100*	42.3	8.6	-	-	-
2	486	40	41.0	8.6	10	12	6204
3	502	64	39.6	8.9	10	12	2534
4	512	40	38.8	9.3	8	10	2129
5	522	40	38.5	9.4	4	6	684
6	558	144	37.9	11.0	4	8	313
7	582	96	37.2	12.0	5	8	1200
8	586	16	37.0	12.0	5	6	2393
K							
1	300	-	143.0	7.6	-	-	-
2	324	288	139.0	8.0	8	4	1765
3	356	384	137.0	9.0	4	8	307
4	384	336	131.0	9.5	8	6	215
5	474*	480*	101.0	9.9	3	4	299*
6	481	120	98.0	10.4	5	2	2635

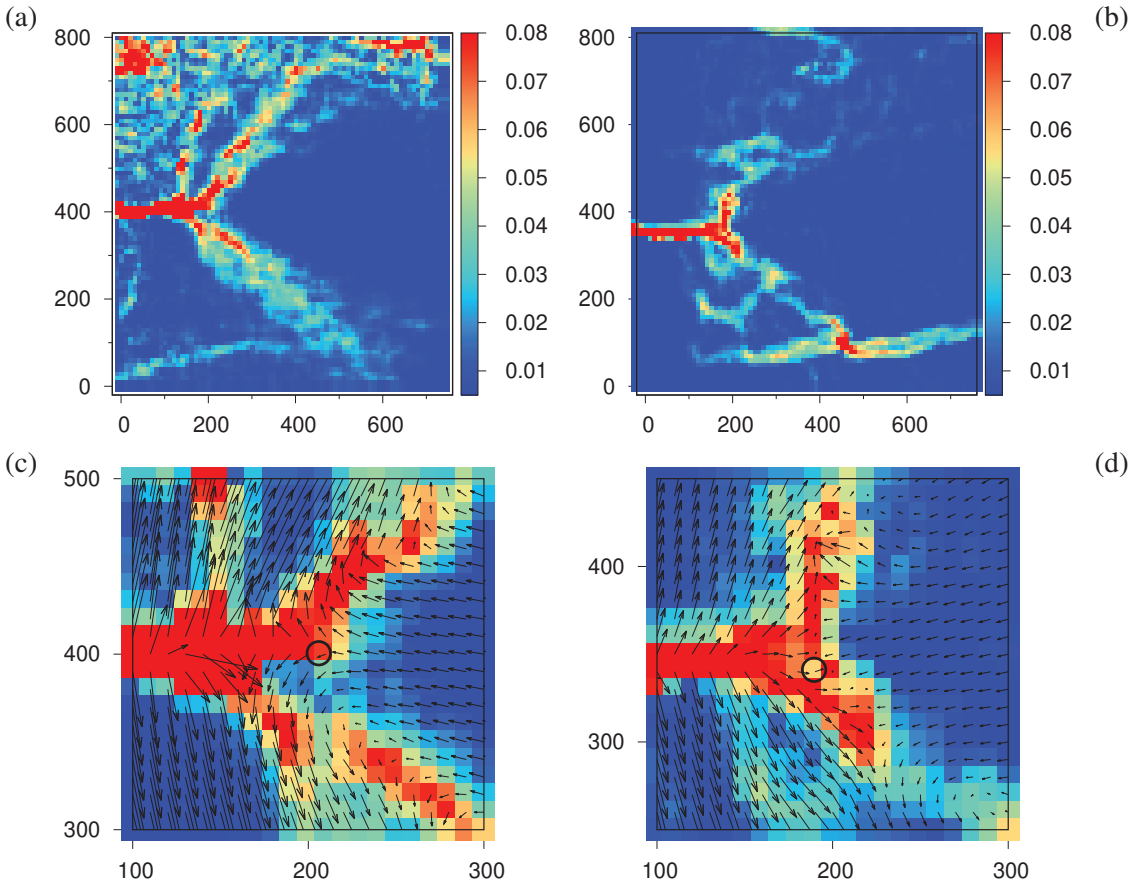

Figure 4.8: Von Mises strain maps for two crack events representative of group 2 and 3. (a) and (c) correspond to D4 and (b) and (d) to Ia5 in Tab. 4.3. (c) and (d) are details of (a) and (b) respectively. The vectors represent the displacement field magnified by a factor 5. The circles show the crack tip position. The resolution is 110 nm/px and the grid size is 10 px.

Figure 4.8 gives Von Mises strain maps for two different cracks. On the left side of Fig. 4.8, there is a strain map representative of Group 2 (Fig 4.8a), and a zoom of its crack tip area (Fig 4.8c), incorporating the displacement field with black arrows. Similarly, on the right side of Fig 4.8 b and d, there is a representative example of Group 3. More precisely, the Fig 4.8a corresponds to the fracture event D4 of Group 2, and Fig 4.8b corresponds to Ia5 of Group 3. With a simple eye inspection, it is possible to establish that the amount of plasticity involved in D4 is significantly higher than in Ia5. Quantitatively, the plastic deformation rate or PDR for D4 is 27359 and versus 4314 for Ia5 (see Tab 4.3). The PDR for Group 2 is usually above 2000 while it is generally below 2000 for Group 3. In both cases, the plastic emissions are particularly high for its respective group and they also correspond to each sample's lowest velocity point. They were selected to show a deformation map where plasticity and their differences are visibly evident. In both cases, the fracture event corresponds to a crack sequence where the velocity decreases

over a crack advance of several microns (in D4 it is almost stopped), and the injected plasticity increases before a fast crack event occur with low plasticity. The pictures show a crack tip when the plastic emission is at its maximum. This example is representative of the difference between the two groups. In 4.8a and b, the plasticity observed has a deformation band shape and spreads over at least 50 μm. It is denoted primary plasticity. The deformation bands during crack propagation are not necessarily symmetric nor have the same intensity.

There is a different kind of plasticity, denoted secondary plasticity, and located ahead of the crack tip (Fig. 4.8). In figure 4.8, there are zooms of the two crack tips to analyze the secondary plasticity, which are displayed in figures 4.8c and d. The crack tip position has to be precisely determined for the secondary plasticity observation. The displacement field, computed from DIC, contains a discontinuity behind the crack tip where the crack is open. The crack tip is at the position where this discontinuity ends, and the vertical displacement changes sign, passing trough zero (see Methods chapter). The secondary plasticity is located at the front of the crack tip and it is confined to a few microns extent with a strain gradient. The crack tip position is circled for each case to facilitate the observation on Fig. 4.8. The two variables in Table 4.3 directly related to the secondary plasticity are: the extension of the plasticity ahead of the crack tip (Λ), and the deformation value at the crack tip position (ϵ_{tip}). It is worth mentioning that in the examples of Fig. 4.8, these values are similar. In other words, the huge difference in the primary plasticity does not directly means a difference in the secondary plasticity. Fig 4.8 shows a representative example that it is confirmed by the histograms in Fig. 4.9.

Figure 4.9 displays statistical information about secondary plasticity, analyzing the secondary plasticity extent, the deformation at the crack tip location, and the secondary strain quotient. First, the secondary plasticity extent is considered (Λ). Fig 4.9a shows a histogram of the Λ measurements for Group 3. There is a predominant Λ value of 4 μm. Besides, Fig 4.9d has a similar histogram shape for Group 2 and 3 together, showing similarities in the secondary plasticity between the groups. Also, Λ is rarely higher than 8 μm. Second, the deformation at the crack tip position, ϵ_{tip}, is evaluated. The values seem to be scattered when the two groups are considered together (Fig 4.9e), and they are rarely higher than 10%. On the contrary, if only Group 3 is considered (Fig 4.9b), 6% of strain is the most frequent value. Finally, to analyze the existing strain gradient in the secondary plasticity, an oversimplification is made by calculating only a quotient. It is called the secondary strain quotient. The secondary strain quotient is defined as the strain variation of the secondary plasticity divided by the secondary plasticity extent (Λ). The strain variation ($\Delta\epsilon_{tip}$) along the extension Λ can be estimated as ϵ_{tip}-1% (1% is the background plasticity). The histograms in Fig.4.9c and d display the secondary strain quotient ($\Delta\epsilon_{tip}/\Lambda$). The values are rarely higher than 3 and the most frequent values are around 1, especially for Group 3 (Fig 4.9c).

Regardless of the important existing difference in the primary deformation between the two groups, the statistics in Fig. 4.9 show that the secondary plasticity can be similar between cases of Group 2 and 3. Moreover, Fig. 4.10 shows the relationship between the secondary (Λ and ϵ_{tip}) and the primary plasticity (PDR). It shows the primary plasticity represented by the plastic deformation rate (PDR) as a function of secondary plasticity variables. Moreover, Fig. 4.10 (a) and (b) show the PDR as a function of the crack tip

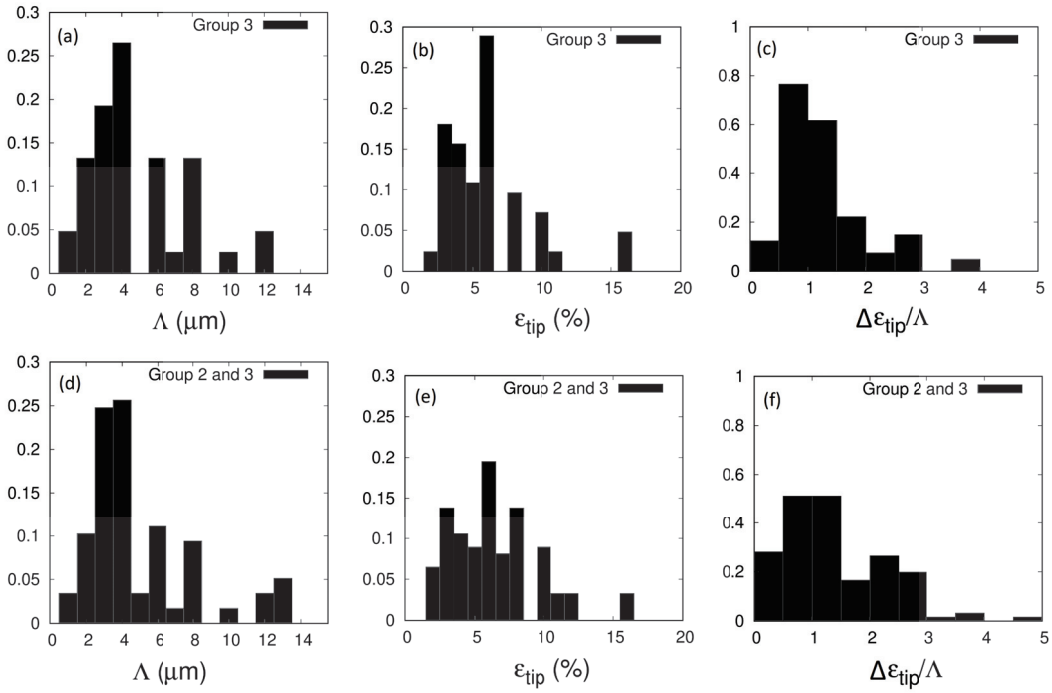

Figure 4.9: Normalized histograms of the length of the secondary plasticity area Λ (μm) for Group 3 alone (a), and for Group 2 and 3 together (d). Normalized histograms of the deformation at the tip of the crack ϵ_{tip} for Group 3 alone (b), and for Group 2 and 3 together (e). Normalized histograms of the secondary strain quotient ($\Delta\epsilon_{tip}/\Lambda$) for Group 3 alone (c) and, for Group 2 and 3 together (f).

plasticity, for Group 3 and Group 2, respectively. Similarly, Fig 4.10 (c) and (d) show the PDR as function of Λ. No simple correlation between the primary plasticity and the secondary plasticity is found, suggesting that they are independent and not related to the same origin. We could expect a relation if, for example, the secondary plasticity was the result of a stress state ahead of the tip caused by the intense slip of the primary plasticity. The graphs show that apparently it is not the case, at least by taking into account these variables for characterizing the primary and the secondary plasticity.

Matching local crack velocities with fracture surface morphology

Three different fracture morphologies, representing different fracture mechanisms, were identified on the fracture surfaces: intergranular smooth, intergranular rough and transgranular. It is tempting to establish a correlation between these mechanisms and the local velocity. In order to investigate such correlation, the local velocity at every crack tip position where it was evaluated is confronted with the details of the fracture surface at the same position on SEM pictures. This was done systematically for all the samples but only two representative examples of Group 2 and 3 are presented. In Fig. 4.11a and b is displayed the crack tip propagation along a grain facet, starting from configura-

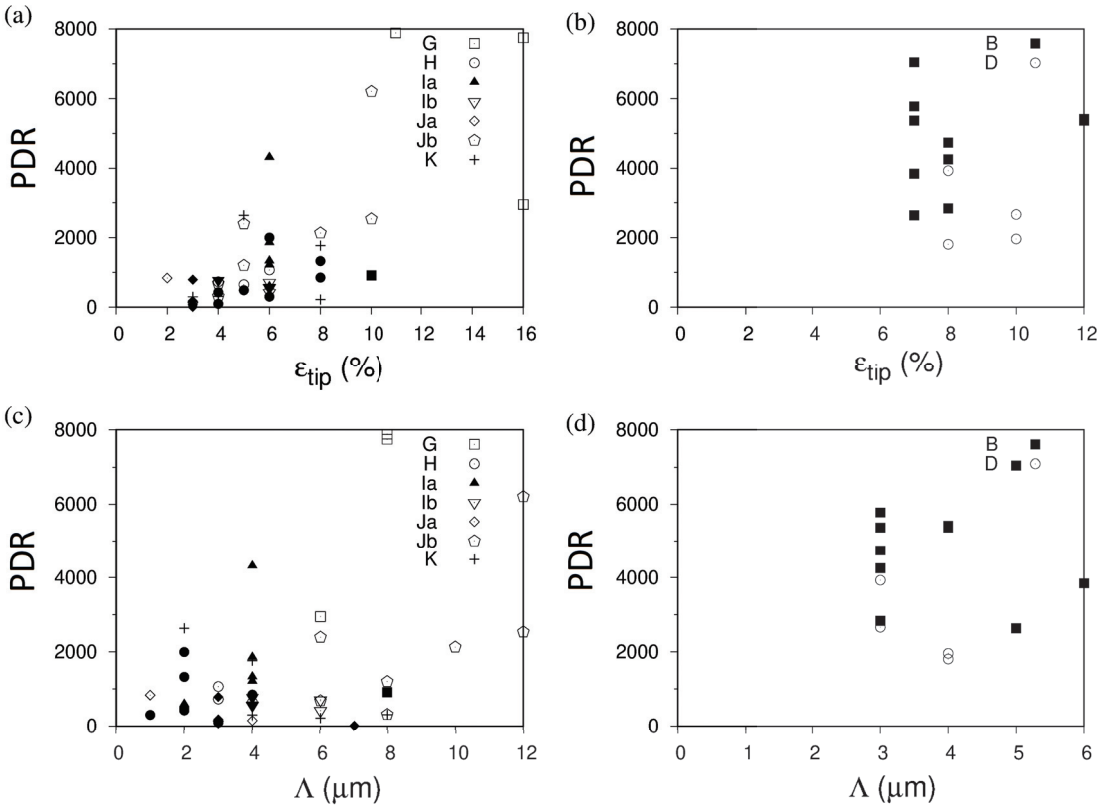

Figure 4.10: Plastic deformation rate (PDR) as a function of the deformation at the tip of the crack ϵ_{tip} for Group 3 (a) and 2 (b). PDR as a function of the length of the secondary plasticity area Λ (μm), for Group 3 (c) and 2 (d).

tion in Fig. 4.11(a) and finishing in Fig 4.11(b) (configurations Ib2 and Ib6 respectively in Tab. 4.3, Group 3). Fig 4.11 (c) is the fracture surface region corresponding to the propagation between (a) and (b). Several intermediate configurations were captured at a time interval of 1 minute. A plot of the crack velocity as a function of the crack tip position is overlapped with the fracture surface in Fig. 4.11 (c). At the beginning of the plot, the velocities are higher than 250 $\mu m/h$ reaching up to almost 350 $\mu m/h$, where the fracture morphology is intergranular smooth (IG smooth) all along this segment. The crack velocity decelerates abruptly, making a transition from IG smooth to a predominant transgranular (TG). A velocity lower than 250 $\mu m/h$ is found in the transgranular part. This suggests that transgranular fracture propagates slower than the intergranular smooth one, but statistically (Fig. 4.12), the intergranular velocities are spread but the transgranular velocities seems to have a tendency to develop slower velocities.

In addition, a Group 2 case, sample B, is shown in Fig. 4.13. The fracture morphology remains intergranular rough (IG rough) all along the sequence. In this example, the crack has a relatively constant velocity along almost all the crack path. Finally, towards the end, the crack accelerates at the same moment as it crosses the last grain boundary of the sequence. Then, the crack velocity abruptly drops when the crack gets close to a triple

point junction of three grains. This is an example of the variability of the velocity at constant fracture mechanism. Besides, deceleration or crack arrest is frequently observed, as it was shown in this case.

As a conclusion, the local velocities are largely scattered between 4 μm/h and 550 μm/h. However, at this point of the analysis, it seems to exist a weak tendency towards slow velocities for transgranular fracture.

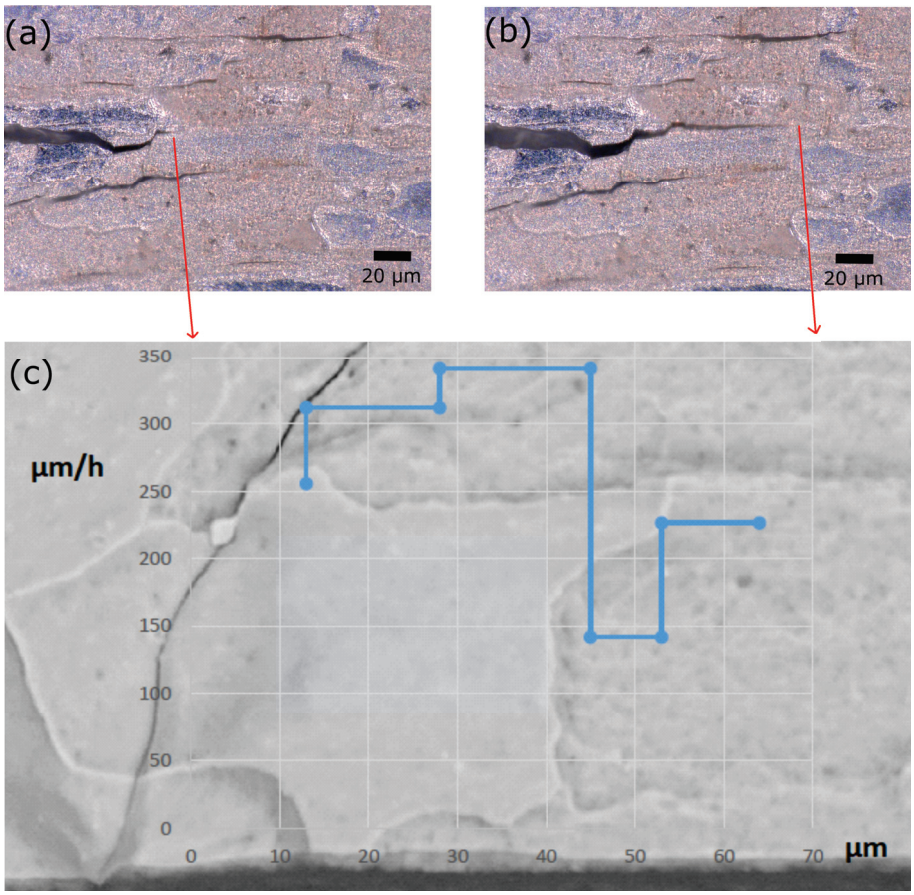

Figure 4.11: Crack propagation in sample I, sequence Ib Tab. 4.3 (a) initial crack position considered Ib2 (b) last crack tip position considered Ib6 (c) crack velocity / position plot superimposed to the fracture surface, showing all the intermediate points evaluated between (a) and (b).

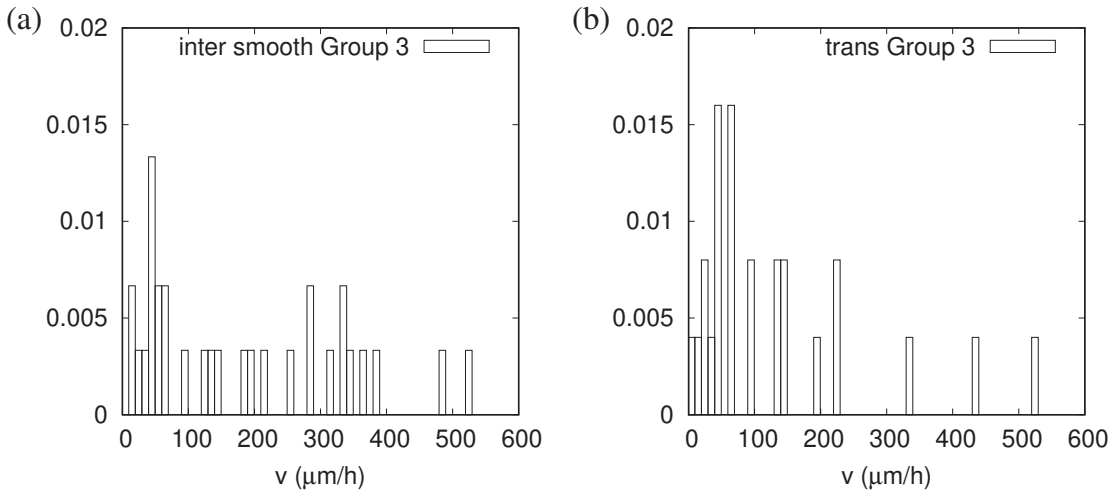

Figure 4.12: Histograms of the local velocities for all the configurations of Group 3: (a) intergranular smooth cases, (b) transgranular cases.

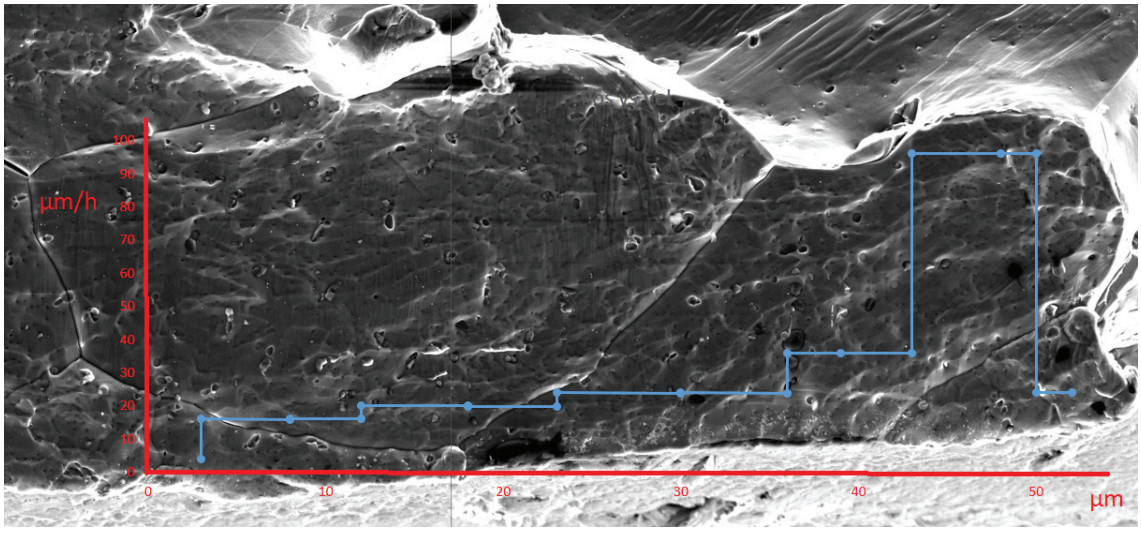

Figure 4.13: Crack velocity plot superimposed on the fracture surface of the crack path for sample B

Local propagation velocity and plasticity correlation

Another interesting correlation is the one between local velocity and plasticity, since it can be expected that a high plastic deformation will shield the applied mechanical load so that the fracture process zone (FPZ) will experience a lower tensile stress and therefore would have a slower crack propagation velocity. In order to investigate such correlation, the local velocity v and the plastic deformation rate (PDR) data are extracted from Tab. 4.3. Some points were rejected because, for example, the apparently high velocity comes from the merging of the main crack with a secondary micro-crack ahead of it. These velocities are not representative of the H affected propagation. One of such cases is H11 where the apparent crack velocity is 1800 μm/h. Another not representative case is when the crack is almost stopped (velocity below 4 $\mu m/h$) and blunts with a high plasticity. The PDR is then very high. For example, D3 and D4 are beyond 20000. After considering all theses cases, it is concluded that the acceptable velocities are limited to 600 μm/h and the acceptable PDR are below 8000. In addition, several points, marked with a star, where DIC could not be performed are also excluded (the velocity is approximately measured directly on the image and the PDR can not be evaluated).

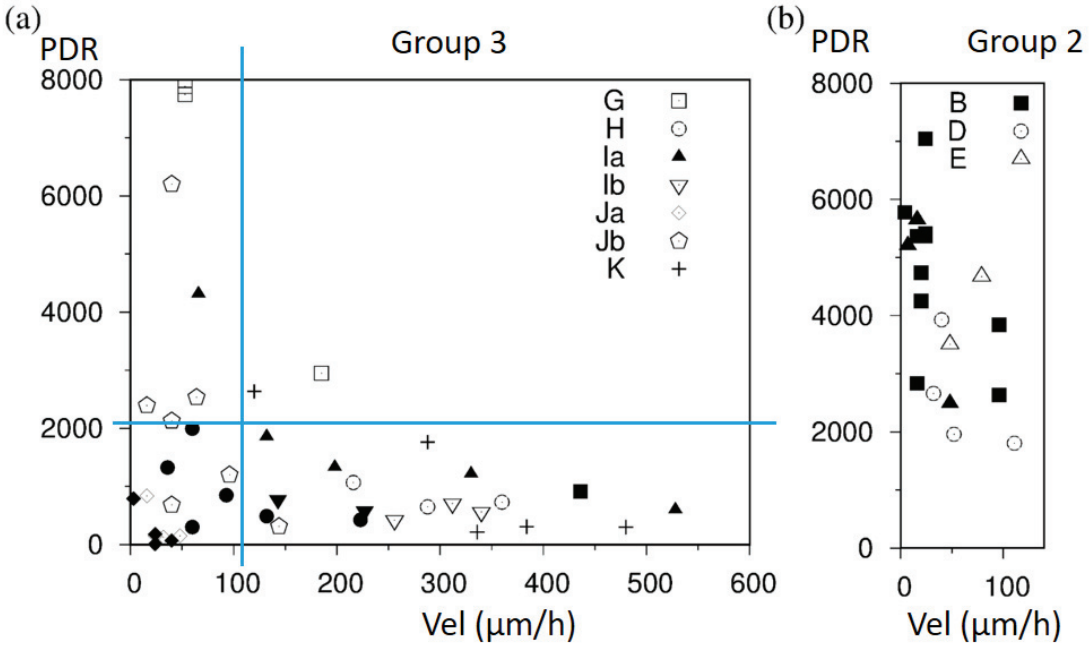

Figure 4.14: Plastic deformation rate (PDR) as a function of the local crack velocity. (a) Group 3, the filled icons indicate TG points and the empty icons (and the crosses) indicate IG smooth points. (b) Group 2, the filled coins indicate IG rough points and the empty icons indicate IG smooth points

As illustrated above during the matching of the local velocities with the fracture surface morphology, the configurations are classified according to the fracture mechanisms. They are: intergranular smooth (IG smooth), intergranular rough (IG rough) and trans-

granular (TG). By gathering all the filtered data, Fig. 4.14 is created. In the vertical axis, local plasticity quantification is represented using the PDR. In the horizontal axis, the local velocities for every sample are represented with different icons. Figure 4.14a includes the points belonging to Group 3. A filled icon represents a transgranular fracture mechanism, and an empty icon represents a smooth intergranular fracture surface. Analogously, Figure 4.14 b contains the Group 2 points. The filled icons represent a rough intergranular fracture surface, and the empty icons indicate a smooth intergranular morphology. The vertical blue line visualizes a division between "slow velocities" and "high velocities".

Similarly, the horizontal blue line in divides low and high PDR values. Figure 4.14 b shows that the samples in Group 2 have a slow velocity and high plasticity, in agreement with the weaker hydrogen embrittlement already noticed at the macroscopic scale. High plasticity involves a slow crack propagation velocity. It is also true in Group 3, where the high plasticity points are related to slow propagation velocities. However, slow crack propagation can also exist with a low plasticity level in Group 3. Velocities are scattered from 20 to 550 $\mu m/h$ in the low plasticity regime.

The fracture surface morphology seems to have a weak relation with the PDR in Group 2. Nevertheless, the rough intergranular surface points (filled Fig. 4.14 b icons) are more frequent above 4000, reaching up to more than 7000. In contrast, the intergranular smooth fracture surface has points below 2000 and does not reach 5000. It is coherent with the assumption that a rough surface has more plastic deformation than a smooth surface. Besides, in Group 3, there is a weak relation between the transgranular mechanism and the velocity. More than 80 percent of the TG points (15/18) has a velocity below 250 $\mu m/h$. This threshold velocity value is the same as in the example in Fig 4.11, where a transition of fracture mechanism is shown. In the case of IG smooth, only around 60 percent of the points are below 250 $\mu m/h$. There is also a weak relation with the plasticity; there is only one TG point with a PDR value higher than 2000. The PDR is not necessarily related to a change in fracture morphology.

Local propagation velocity and stress intensity factor

Figures 4.15a and b show the local crack velocity as a function of the applied intensity factor. Crack velocity changes, within a single experiment, occur with little modification of the stress intensity factor. The stress intensity factor does not seem to have clear influence on the local propagation velocity in the condition of this study. However, it might be inferred from Fig. 4.15 that for K level higher than 10 MPa$\sqrt{m}$, the maximum velocity found is relatively low, that could be a sign of overloading and excessive plasticity that will reduce the crack speed.

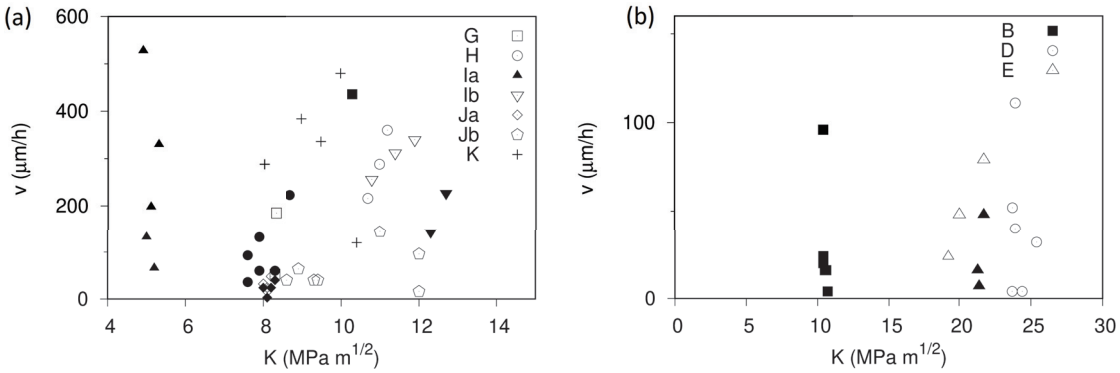

Figure 4.15: Local propagation velocity (v) for Group 3 (a) and 2 (b) as a function of the stress intensity factor (K).

Incremental crack opening displacement profiles

In this section, the incremental crack opening profiles are reported and analyzed. The opening is represented by the function $\Delta u_y(x)$. It is the difference between the tensile displacement above $u_y^+(x)$ and below $u_y^-(x)$ the crack plane at the position x, being x aligned with the crack path. Thus, a mathematical description is: $\Delta u_y(x) = u_y^+(x) - u_y^-(x)$. When plasticity accompanies crack propagation and a dislocation is emitted from the crack tip (or the fracture process zone), it creates a displacement shift between the half crystals above and below the glide plane of magnitude $\vec{b}$ (Burgers vector). This contributes to displacing the crack upward for dislocations emitted in the crack's upper part (or downward for those emitted backward) during a crack advance Δa. These elementary shifts, due to every individual dislocation, accumulate to create an opening displacement ($\Delta u_y(x)$).

Figures 4.16, 4.17 and 4.18 show representative incremental crack opening displacement (ICOD) profiles. Every profile displayed comes from the correlation between two images during propagation. In other words, the displacement profile is an increment of the opening between two crack configurations. The empty icons indicate a displacement that takes place at the back of the crack tip. Conversely, the filled dark icons indicate a displacement at the front of the crack tip (fracture process zone). The points in the profile, ahead of the tip, belong to five nearby planes, parallel to the crack plane (y=0): y= +20 px,

+10 px, 0, -10 px, -20 px. The vertical displacement of the points in these 5 planes is analysed, averaged and displayed, and they shape the profiles in Figures 4.16, 4.17 and 4.18 for different fracture events. The displacements and positions in the graphs are expressed in pixels with 1 px = 110 nm. It can be seen that the noise level is low in the profiles, especially at the back of the crack tip. Besides, the DIC algorithm allows a sub-pixel resolution. The noise level was estimated by correlating two images that were not deformed and was found of the order of 0.1 px. The crack tip position is defined, on the opening profiles, at the location where the displacement changes sign, going through zero. It means, in practice $u_y(+10) > 0.1$, $u_y(-10) < -0.1$ and $u_y(0) < 0.1$.

The profiles show that $\Delta u_y(x)$ is constant far behind the crack tip. This constant value is denoted $\Delta u_y c$. This plateau is found because of the incremental nature of the opening displacement analysis. At some distance behind the crack tip, $\Delta u_y(x)$ decreases and reaches the noise level a few microns ahead of the tip, i.e. at the end of the fracture process zone. It is often observed that the distance between the beginning of this decrease and the crack tip corresponds to the crack advance Δa. Examples shown are B2, B3 and D6, D7 on Fig. 4.16 and H13, H14 on Fig. 4.18. It means that the active dislocation sources are close to the crack plane, otherwise dislocations will emerge on the crack surface at a distance further behind the tip. A new variable is defined to estimate such plasticity emerging at the crack surface during crack growth. This new variable is a non dimensional index called "opening displacement rate" or ODR. The ODR is defined as the ratio between $\Delta u_y c$ and Δa for a crack event. As it was stated before, the $\Delta u_y c$ is measured in the constant opening displacement part of the profile, and Δa is the increment of the crack extent between the two configurations chosen for DIC. Like the PDR, in the ODR, the word "rate" refers to a crack advance dependence and not a time dependency.

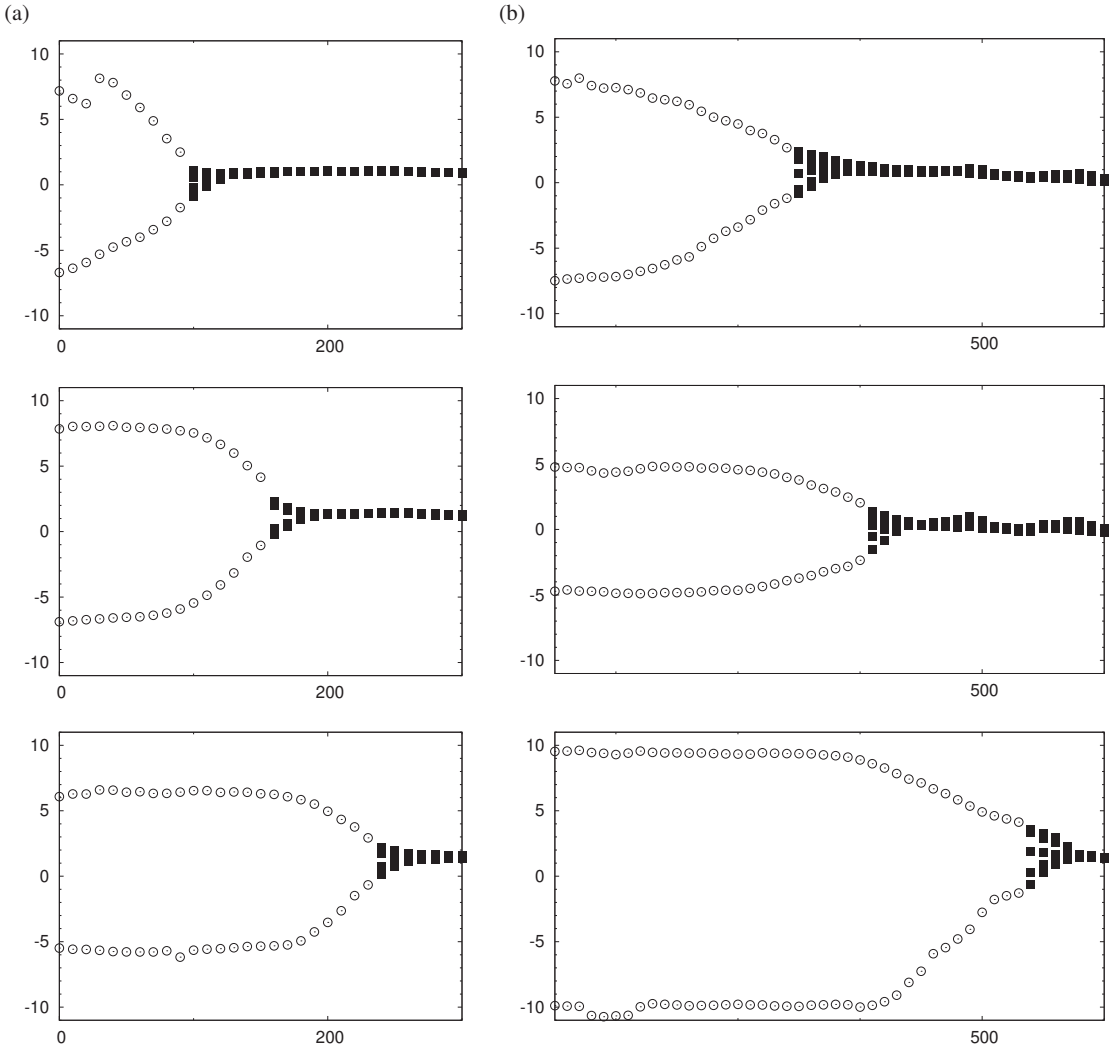

Figure 4.16: Crack opening profiles of configurations B2, B3 and B5 in (a) and D5, D6 and D7 in (b) which belong to Group 2. The x axis is the position in pixels (10 px= 1.1 μm), and the y axis is the displacement along the y direction (the tensile direction) in pixels (1 px = 110 nm). In black are the points ahead of the crack tip. The points are in between y_{tip} +/- 20 px, i.e. several planes parallel parallel to the crack plane are represented.

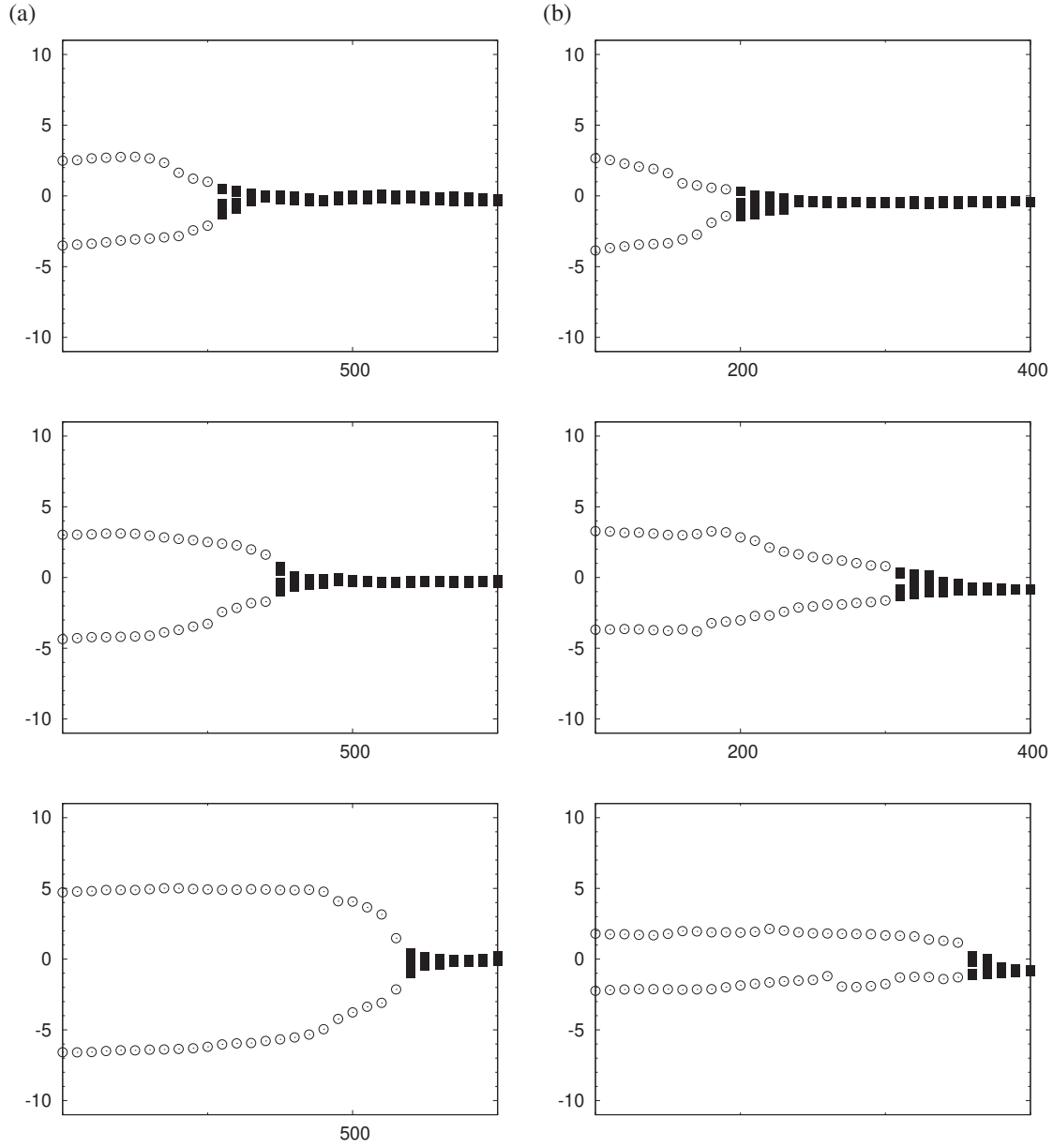

Figure 4.17: Crack opening profiles of configurations Ia2, Ia3 and Ia6 in (a) and H13, H14 and H15 in (b)) which belong to Group 3. The x axis is the position in pixels (10 px= 1.1 μm), and the y axis is the displacement along the y direction (the tensile direction) in pixels (1 px = 110 nm). In black are the points ahead of the crack tip. The points are in between y_{tip} +/- 20 px, i.e. several planes parallel parallel to the crack plane are represented.

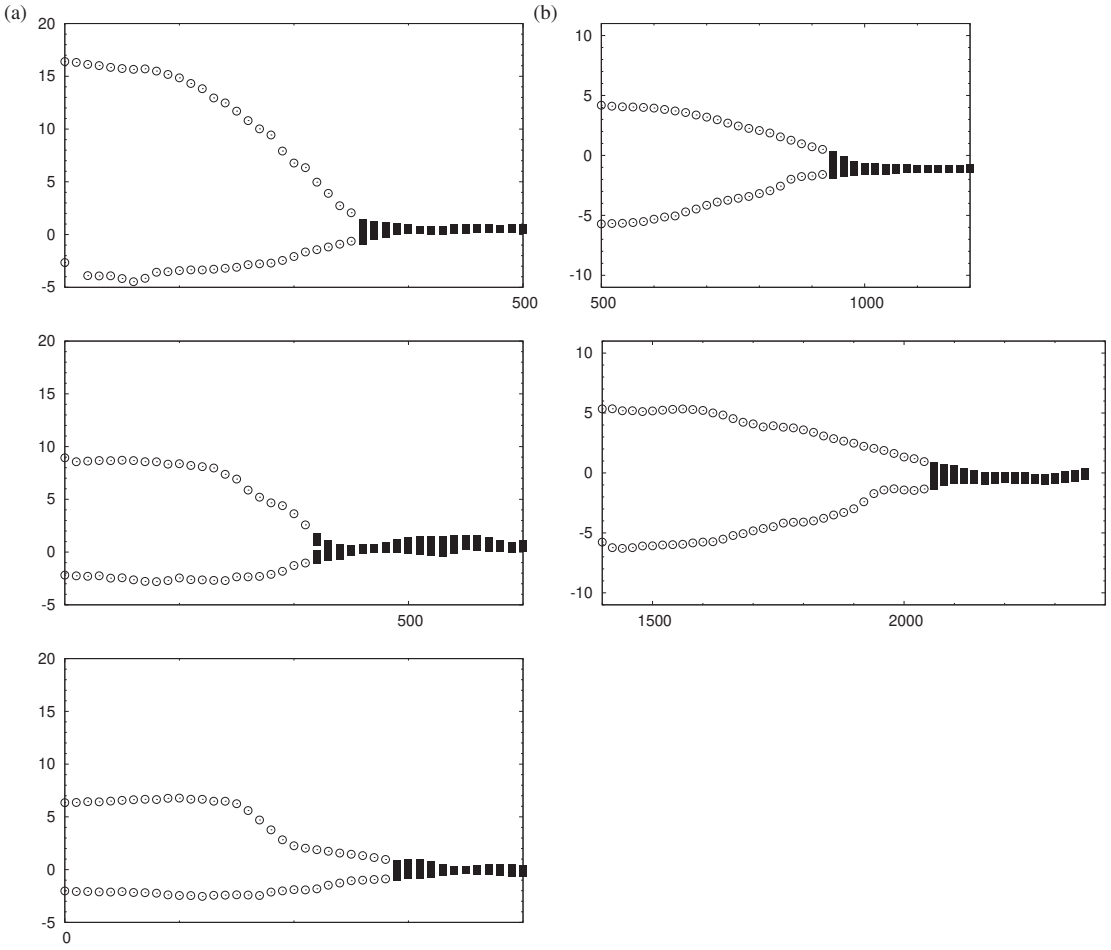

Figure 4.18: Crack opening profiles of configurations H5, H6 and H10 in (a) and K3 and K5 in (b)) which belong to Group 3. The x axis is the position in pixels (10 px= 1.1 μm), and the y axis is the displacement along the y direction (the tensile direction) in pixels (1 px = 110 nm). In black are the points ahead of the crack tip. The points are in between y_{tip} +/- 20 px, i.e. several planes parallel parallel to the crack plane are represented.

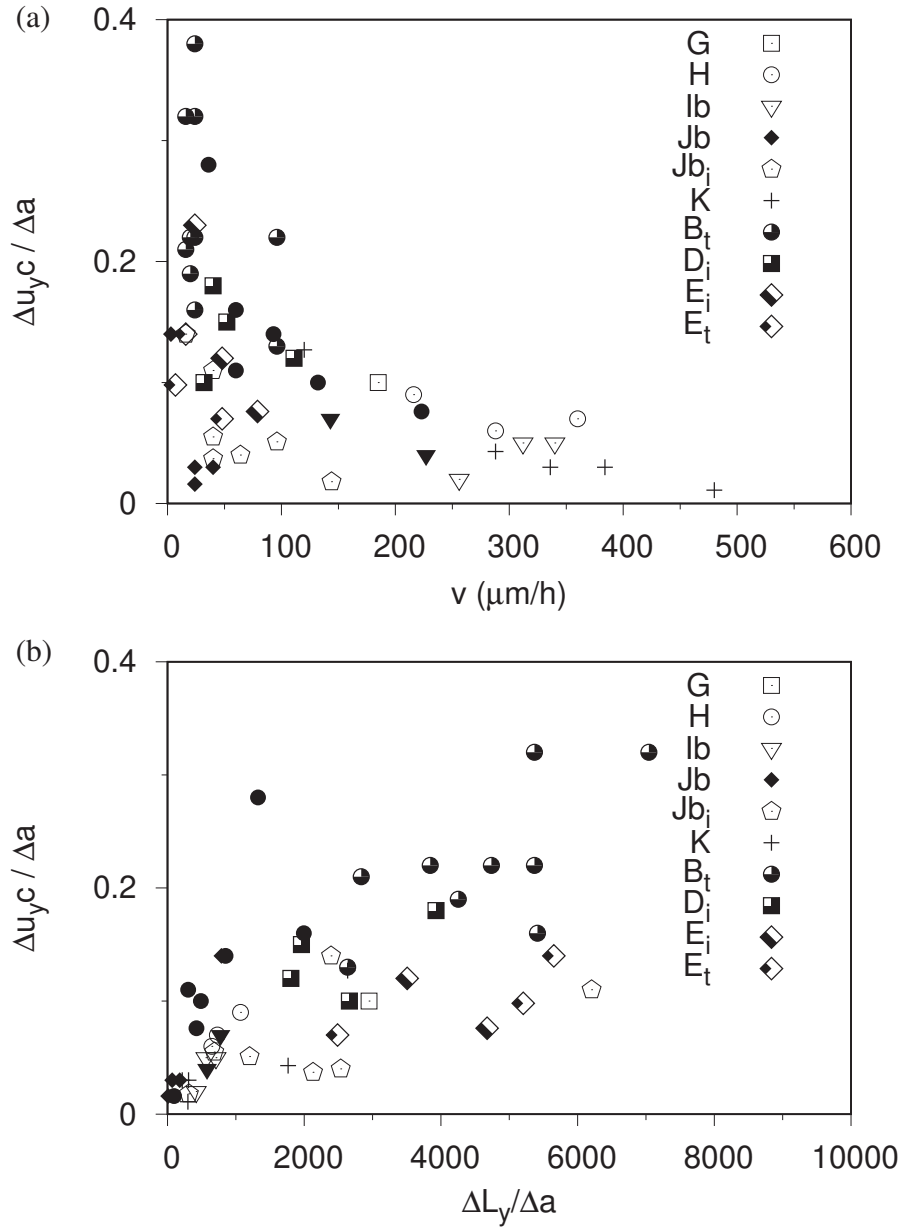

Figure 4.19: (a) Ratio $\Delta u_y c/\Delta a$, where $\Delta u_y c$ is the opening of the crack obtained during the crack advance of Δa, as a function of the local velocity. This quantity is called "opening displacement rate" (ODR) in the text. Empty symbols, and the crosses, represent intergranular smooth fracture advances, filled symbols represent transgranular fracture. For samples B, D and E (Group 2), the letter "i" in the label of the symbol means "intergranular smooth" and "t" means "intergranular rough". (b) The ODR is compared to the PDR (plastic deformation rate) which is a measure of the plasticity stored in the sample, i.e. not necessarily emerging on the surface.

In addition, Fig. 4.19a is similar to Fig. 4.14, both describing the correlation between plasticity and the local crack propagation velocity and also classifying the points according to the fracture morphology. However in Fig. 4.19a the ODR ($\Delta u_y c/\Delta a$) is used instead of the PDR ($\Delta L_d/\Delta a$). The ODR describes the plasticity that has been emitted from the crack tip or close to it, and the PDR refers to the plasticity stored in the sample. They are linearly related only for Group 3 samples (Fig.4.19b in the lower left corner), i.e. in the most brittle cases. One explanation is that when the samples are more brittle, plasticity comes essentially from the vicinity of the tip, where the stress concentration activates the dislocation sources, while in the Group 2 cases K is larger (Fig. 4.15) so the dislocation sources are activated further away and do not necessarily create an emerging plasticity. With this new measure of plasticity, the Group 2 and 3 data can now be plotted on the same graph. It is worth noting that a high velocity implies a low dislocation emission from the tip. Nevertheless, a crack with a low plasticity level can develop any speed (similar to the PDR), even a slow one. Figure 4.19a has a clear hyperbolic trend. In the ODR(v) graph it appears that above 250 μm/h, there are no transgranular points. This is because the ODR analysis enabled the exclusion of some data points.

The points discarded in Fig. 4.19 belong to two tests: Ia and G. The reason for not taking into account the Ia test relies on an anomaly that has produced a high velocity and high plasticity values of a transgranular fracture. Even if the correlation of these points is coherent with the plot's hyperbolic shape, the values are still significantly higher than the rest of the data. This high plasticity level is attributed to an overload during the tensile test. The second rejected data points are G5 and G6, also with a very high transgranular velocity (more than 430 μm/h). The fracture event in points G5 and G6 corresponds to a violent fracture through a grain after a slow intergranular fracture (even blunting), through small facets and a tortuous path. Besides, a heavily deformed unbroken ligament is visible on the side surface, behind the crack tip. It was considered that these elements created non representative conditions for crack propagation and plasticity emission.

By inspecting in detail the ICOD profiles in Figures 4.16, 4.17 and 4.18 and by crossing this information with the data available in Fig 4.19, the following statements are made for the six cases in the figures, concerning the symmetry of the profiles, the local propagation velocities, the ODR values and the fracture mechanisms.

- Figure 4.16a introduces the ICOD of the B2, B3, and B5 fracture events. The profiles are symmetric. The local propagation velocity and ODR points are located on the left side of the graph in Fig 4.19 (B_t), meaning a slow velocity and a high plasticity of this crack sequence. This sequence represents an intergranular rough fracture in Group 2.

- Figure 4.16b introduces the ICOD of the D5, D6, and D7 fracture sequence. The profiles are symmetric. Their local velocity and ODR values (v, ODR) are equal to: (111 , 0.12) , (40 , 0.18), and (52 , 0.15), respectively. These points, according to Fig 4.19, form part of a slow intergranular smooth fracture in Group 2. The velocity is slow but the ODR involved is lower than the one for a intergranular rough surface. In agreement with the concept than a rough surface will involve more plasticity, specially emitted from the crack tip, than a smooth surface with a lack of plasticity features.

- Figure 4.17a introduces the ICOD of the Ia2, Ia3, and Ia4 fracture sequence. Their (v, ODR) values are equal to: (528 , 0.07) , (132 , 0.27), and (330 , 0.25), respectively. These are the points that were rejected. They would be 2 to three times above the data represented on the graph. This crack sequence represents the "overloaded" transgranular fracture in Group 3. The profile is slightly asymmetric. This overloading is represented in the ODR values, with values higher then ones presented in the intergranular smooth but lower than the ones in the intergranular rough mechanism. The high velocity might be interpreted as also an overloading, the velocity rises because of an increment in the applied force.

- Fig 4.17b introduces the ICOD of the H13, H14, and H15 fracture sequence in Group 3. The sequence has low ODR values (lower than 0.1), and a high velocity (more than 250 μm/h). This crack sequence has an intergranular smooth fracture. The profiles show fluctuation, and changes on the slop, which are signs of modifications in the dislocation emission rate along the crack path. From the fracture surface's SEM observations, it is seen that the crack path is along inclined GB facets, i.e. tortuous.

- Fig 4.18a introduces the ICOD of the H5, H6, and H10 fracture events. Their (v, ODR) values are equal to: (132 , 0.10), (60 , 0.16) and (223 , 0.08), respectively. According to Fig 4.19, these points (dark disk icons) form part of a transgranular fracture in Group 3. The plasticity involved is relative low, in the same range as the intergranular smooth. The transgranular fracture morphology is observed in a large area of the fracture surface, estimating that the fracture mechanism is well represented in this crack sequence. The profiles are remarkably asymmetric, with less dislocation emission on the side where a grain boundary is located.

- Fig 4.18b introduces the ICOD of the K3 and K5 fracture events. This in an example of a brittle behavior, with high speed and low plasticity. The velocity is higher than 380 µm/h and the ODR lower than 0.04. These points are indicated with crosses in the Fig 4.19, and it has a "intergranular smooth" fracture morphology in agreement with the assumption of a lack of plasticity involved and a fast crack. The profiles are symmetric.

Finally, the opening displacement located in the deformed region (FPZ) ahead of the crack tip is characterized in Fig 4.20. The FPZ is approximately constant or with a low variability during the different fracture events analyzed in the same sample. In Fig 4.20, the profiles calculated and averaged are from four of the mentioned cases. They are fairly similar, with a displacement of about 1 px (110 nm) in the first micron above the crack plane. Consequently, an average deformation of approximately 10% in the tensile direction (ϵ_{yy} is estimated in the first micron ahead of the crack tip. The extension of this zone (Λ) is about 4 microns, see Tab. 4.3). In the points K3 and K5 (Fig. 4.18b), the most brittle intergranular events, the deformation in the PFZ, ϵ_{yy} is reduced to 5% (0.5 px approx.). In H5, H6, and H10 (FPZ details not displayed in the graphs), the opening at the FPZ is symmetric even if the ICOD is in general severely asymmetric. In H10, the ICOD profile has a bump, and the plastic opening is minimal. The deformation at the FPZ is also very much reduced, falling to 5%, comparable to the K cases, something that is surprising because the K cases are intergranular smooth and the H cases are transgranular.

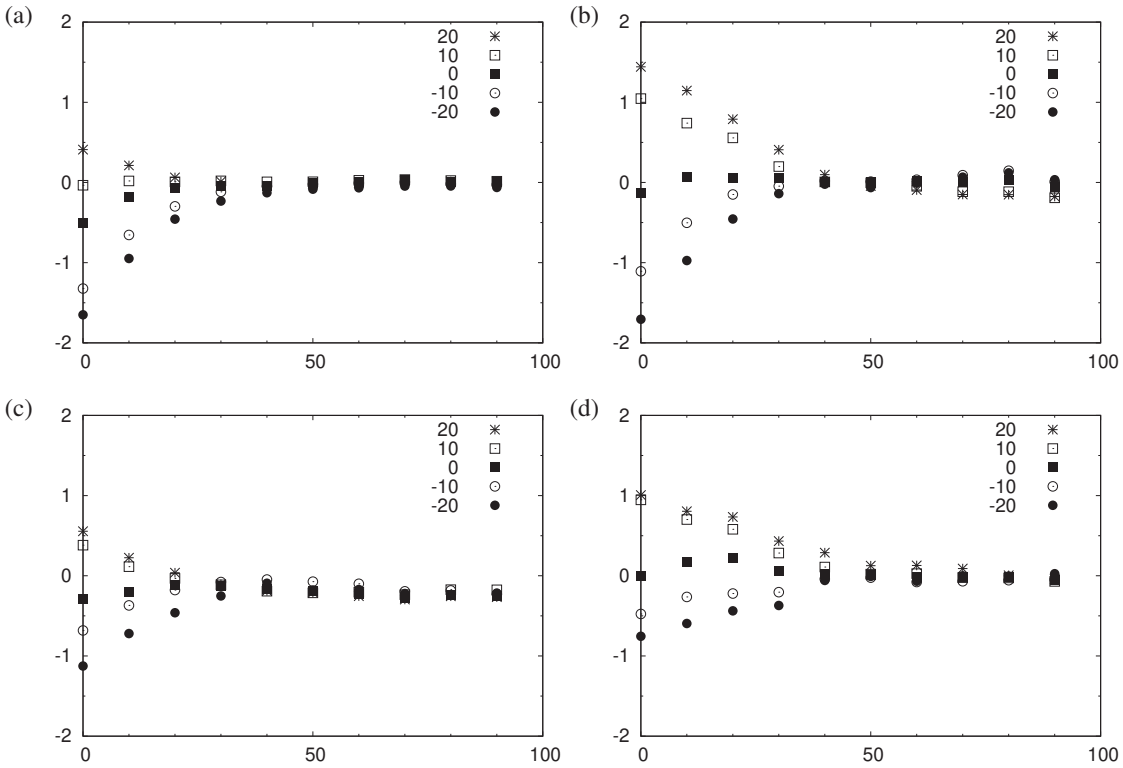

Figure 4.20: Average opening profiles (the part which is ahead of the crack tip) obtained by averaging the profiles shown on Fig. 4.16 and Fig. 4.17. It is shown respectively the average on B2, B3 and B5, on D5, D6 and D7 (Group 2) on Ia2, Ia3 and Ia6 and finally on H13, H14 and H15 (Group 3) on figures a, b, c and d.

4.3 Summary

Micro tensile samples were successfully electrochemically charged with hydrogen and the internal hydrogen cracking phenomenon was studied. The imposed cathodic potential (E_c) is the parameter which has the strongest impact on the intensity of the H-embrittlement. The charging time seems to play a secondary role. The samples were divided in three groups according to the cathodic potential used, which also corresponds to their level of H-embrittlement. The embrittlement is defined by macroscopic indicators such as the average crack propagation velocity, the deformation of the notch tip at initiation and the range of the stress intensity factor K during the test. Group 3 (E_c= -1600 mV/SCE) contains the samples that suffer more embrittlement. Group 1 (E_c= -1300 mV/SCE) and 2 (E_c= -1500 mV/SCE and -1400mV/SCE) are less embrittled. The initiation from the U-notch requires a high deformation of the notch tip which can easily achieve 30% with two intense deformation bands, inclined with respect to the notch plane.

The hydrogen charging procedure, when the potential is low enough (Group 2 and 3), dissolves the surface. It produces a pattern that enables performing digital image correlation (DIC). This technique, applied to sequences of images obtained by optical microscopy, gives the displacement fields at several magnifications and times. From this, the time evolution of the position of the tip is determined and the local velocities are calculated. The best pattern and planarity conditions give access to the displacement field with a resolution of about 1 micron. The strain is computed from its gradient. Plasticity is quantified by integrating the Von Mises strain over the appropriate region around the crack tip. This integral defines the "plastic deformation rate" (PDR) which gives the amount of plasticity injected in the system due to a crack advance. By analyzing the strain maps, two different kinds of plasticity are identified. The primary plasticity is in the form of intense, inclined, deformation bands. The secondary plasticity is located ahead of crack tip along the future crack path and expands over only a few microns. On one hand, the PDR is used for quantifying primary plasticity. On the other hand, for estimating the secondary plasticity, the strain value at the crack tip and the extension of the deformation (Λ) are used. It is observed that the magnitude of the PDR is very different between Group 2 and Group 3, but that a large difference in PDR does not necessarily mean a large difference in secondary plasticity. Crack propagation is seen as continuous at the micron scale (no intermittency was detected). The less embrittled samples (Group 2) crack with significantly higher plastic deformation rate and with lower velocities than those of Group 3. The velocity range is 20 – 500 $\mu m/h$.

It was attempted to correlate local velocity with PDR, but a range of PDR exists for every velocity. High velocities always occur with low levels of plastic deformation rate. However, for slow velocities a large range of PDR values is observed, from low to high values.

Three different H related fractures morphologies were found by inspecting the fracture surfaces in SEM. They are: intergranular rough, intergranular smooth and transgranular. Group 3 presents only intergranular smooth and transgranular fracture mechanisms. Group 2 presents only intergranular rough and intergranular smooth fractures. Intergranular rough has a tendency to develop more plasticity than intergranular smooth, but, in Group 3, the transgranular fracture has the same plasticity level than the intergranular smooth one. Transgranular fracture velocities tends to be slower than the intergranular

smooth ones.

The stress intensity factor K could not be directly related to the fracture morphology, or the local values of velocity. It seems to be a value representative of the necessary mechanical load over the full sample section.

Incremental crack opening displacement profiles were measured from DIC. The plasticity emitted from the crack tip was estimated from the shape of this profile and characterized by the "opening displacement rate" (ODR). The ODR as a function of the local velocity has a clear hyperbolic shape, with the same tendencies as the PDR (Fig. 4.14 and 4.19a). It helped discarding some velocity measurements and then it appears more clearly that transgranular fracture is slower than intergranular smooth fracture (no TG crack velocities were found beyond 250 μm/h). Besides, transgranular fracture seems to be associated with an asymmetry in the opening profile, maybe because it runs close and parallel to grain boundaries which block plasticity on one side of the crack tip.

The secondary plasticity is also evaluated from the opening displacement profile ahead of the crack tip. Regardless of the asymmetry at the back of the tip, it remains symmetric and is not significantly dependent on velocity. However, the corresponding tensile deformation is higher in Group 2 ($\epsilon_{yy} \approx 10\%$ in the first micron) than in Group 3 ($\epsilon_{yy} \approx 5\%$ in the first micron), as can be expected from a lower H-damage in Group 2. The length of this plastic zone is about 4μm.

The sample thickness, in the range studied (0.2 mm – 1.0 mm), has no evident impact on the values of K, local velocities, PDR and ODR.

Chapter 5

Stress Corrosion Cracking

In the previous chapter, a micro-tensile machine was used to create hydrogen assisted cracks in an aluminum alloy containing hydrogen obtained by an electrochemical procedure. The test was done under an optical microscope. The pictures taken enabled to measure the deformation around the crack tip with a sub-grain scale resolution, quantifying the plasticity and determining local crack propagation velocities. The same approach is used in this chapter in the case of Stress Corrosion Cracking (SCC). The experimental setup was adapted to perform tests in saline water. We will see that SCC cracks were successfully produced but that some issues appear that decreased the resolution of the digital image correlation (DIC) measurements drastically. This motivates the search for new surface patterns. This topic will be discussed in the next chapter as a part of the "perspectives".

The outline of this chapter is the following. The state of the art of the SCC of AlZnMg alloys is briefly presented. It shows that these alloys are sensitive to SCC even in air, which is our reference for SCC tests in saline water and internal hydrogen embrittlement. Therefore a first result section concerns the tests in laboratory air and the effect of a neutral dry gas. Then, SCC tests results in saline water are presented from a macroscopic viewpoint (tests conditions, average velocities, deformation at initiation, stress intensity factor). Finally, the analysis is performed at the local scale, using DIC. Plastic deformation at the crack tip (primary and secondary) and around it is quantified. The local velocities are measured at a sub-grain scale. In particular, a case of intermittent fracture is analyzed and reveals the limitations of the current surface preparation concerning DIC. The chapter ends with a summary.

5.1 The sensitivity of AlZnMg alloys to stress corrosion cracking

The Literature Review chapter presented a bibliography oriented towards hydrogen effect in metallic alloys. Here, a specific bibliography addressing the issue of SCC of AlZnMg alloys is given. Several review papers [92, 26] critically analyze the results accumulated in the literature over the years. In particular, Holroyd points at the difficulty to relate the SCC sensitivity to one particular feature of the microstructure (thickness of the precipitate free zone (PFZ), localized slip in the PFZ, size and density of intergranular precipitates,

segregation, intragranular precipitation, characteristics of intragranular plasticity like the degree of slip localization). On the one hand, this comes from the difficulty to decouple in SCC the local anodic dissolution of the alloy (electrochemical oxidation of the metal resulting in the liberation of cations into the electrolyte, it is actively involved in localized corrosion processes like pitting or crevices) and the hydrogen effects to analyze the effect of microstructure on each aspect. Indeed, they are both coupled via the electrochemical reactions within the crack, which leads to hydrogen production. On the other hand, it is difficult to design heat treatments where the different components of the microstructure vary independently. Nevertheless, a schematic diagram was drawn by Speidel [92] (Fig. 5.1a) which correlates the heat treatment and the sensitivity to SCC. The under-aged heat treatments (those for which the precipitation stage has not yet produced the maximum of hardness, for example, the T4 state, which is used in our study) give a reduced sensitivity compared to the peak aged alloys.However, over-aging also reduces the sensitivity to SCC (Fig. 5.1a) . When a flat surface is exposed to the medium, the initiation of a crack occurs at a region where corrosion is localized (a pit, the emergence of a slip band on the surface, a grain boundary triple junction, etc.). SCC is often intergranular in these alloys, involving the heterogeneity of the composition in the grain boundary region (intergranular precipitates and precipitate free zones). The "macroscopic" influence of these differences of composition is known by measuring the corrosion potential on macroscopic samples where the solutes are in solid solution at different compositions or where the phase composing the precipitates can be synthesized with a larger size.

The addition of Mg and Zn decreases the corrosion potential (with respect to the potential of pure Al), and the addition of Cu increases it. So a region enriched in Mg and Zn (respectively Cu) is anodic (resp. cathodic) with respect to a homogeneous solid solution. This was shown for model compounds like Mg_2Si and $MgZn_2$ (which is the major intergranular precipitate in our study) grown with sizes in the micrometer range in a AA7075 matrix. Only with this enlarged size were they suitable for local electrochemical measurements [93, 94, 95]. It is seen that Mg_2Si and $MgZn_2$ are dissolved (preferential corrosion of the precipitates respect to the matrix) within a crack, along a grain boundary in the T6 metallurgical state. Consequently, there will be η precipitates (of composition $MgZn_2$) and the PFZ (Precipitate Free Zone, depleted in Mg and Zn) in contact with the corrosive medium. It is concluded by extrapolation from the micron-scale experiments, η should dissolve. Moreover, Marlaud [96] has performed transmission electron microscopy observations of thin samples after immersion that confirm that the precipitates dissolve, even at the nano-scale. Furthermore, the addition of Cu in the system reduces the sensitivity to SCC. The current belief is that Cu is present in the composition of the intergranular precipitates and decreases the difference in corrosion potential between the intergranular precipitates and the PFZ, therefore slowing down the anodic dissolution (decreasing the corrosion rate). In our case, the material is alloy 7108, which has low Cu content. It is, therefore, sensitive. In the past, there have been studies on the alloy 7079, which is another industrial alloy of the same family, with a low Cu content [36]. It was spectacularly sensitive, with crack propagation velocities two orders of magnitude higher than alloy 7075 (an alloy with a higher Cu content) (see the curves in saturated NaCl on Fig. 5.1b). Modern studies [36] have shown a peculiar case where low Cu alloys can be less sensitive if the quench rate allows Cu to be incorporated into the intergranular precipitates. Figure

5.1b gives examples of propagation velocities as a function of the stress intensity factor K. For alloy 7075, the threshold K is about 7 MPam$\sqrt{m}$ and the plateau velocity is about 10^{-8}m/s (36 μm/h). The same velocity is obtained for the low Cu 7020 alloy by Knight (table 2 of the reference [36]). These reported values are average values, obtained on large Compact Test samples and they are a reference for our study.

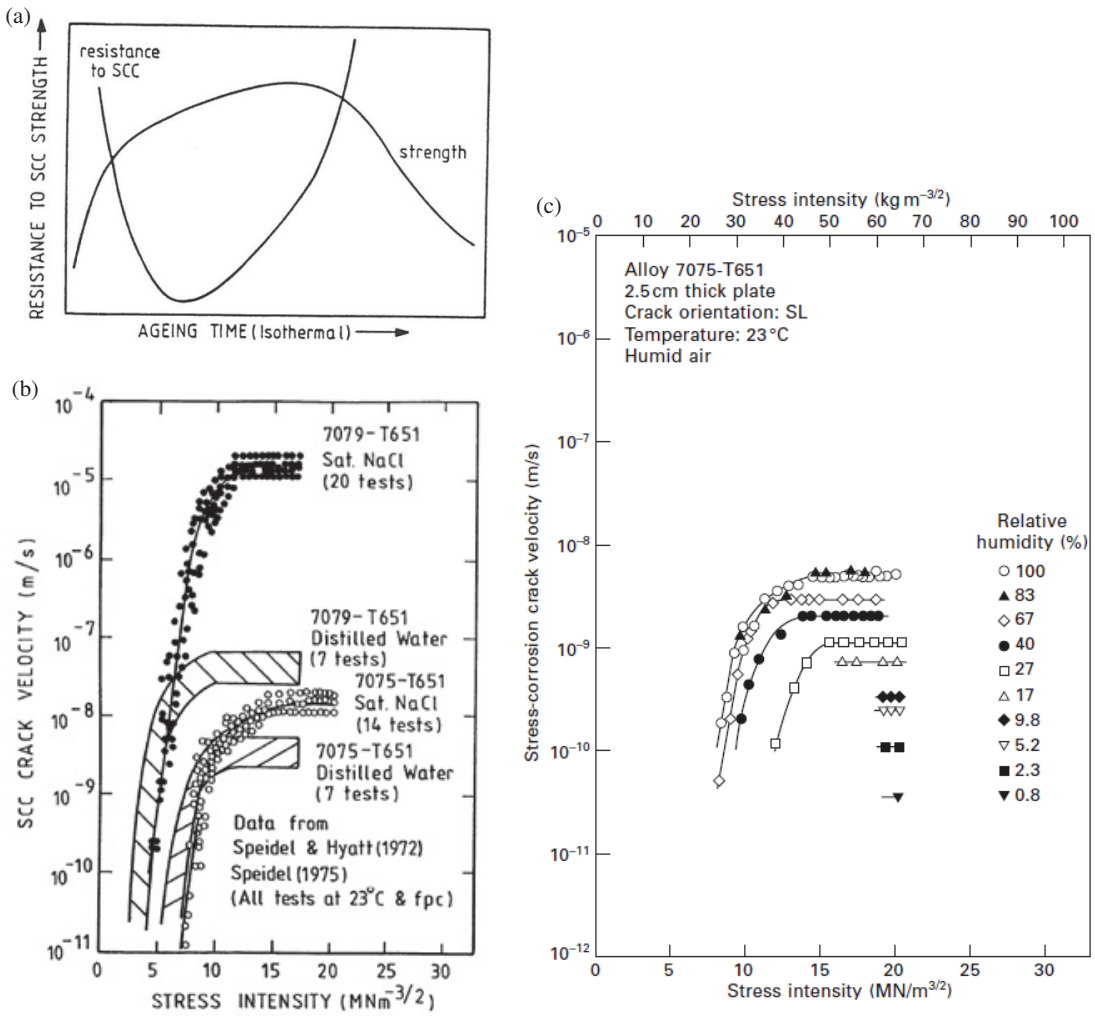

Figure 5.1: (a) SCC resistence as a function of the aging time for AlZnMgCu alloys [92] (b) SCC crack propagation velocity as a function of the stress intensity factor for 7079 and 7075 alloys tested in saline water and distilled water[92] (c) SCC crack velocity as a function of the stress intensity factor for a 7075 alloy tested at different levels of relative humidity [7] (10^{-8} m/s = 36 μm/h).

Moreover, Fig. 5.1c shows that these alloys also develop cracks in humid air [97]. The plateau (stage II) velocity continuously decreases with decreasing relative humidity (see also [36]). Dry molecular gases such as hydrogen (H_2) and dry air do not induce crack propagation [7]. It is worth noting that SCC cracks do not appear instantaneously. There is an incubation time that depends on many variables such as the aggressiveness of the environment, the microstructure, or the temperature.

SCC in saline water and in water vapor presence are connected. The electrochemical half-reactions involved in the latter are better understood [7]. First, Al is oxidized in water vapor to form an oxide:

$$2Al + 3H_2O \rightarrow Al_2O_3 + 6H^+ + 6e^- \tag{5.1}$$

The cathodic half-reaction is the reduction of H^+:

$$H^+ + e^- \rightarrow H_{ads}(c) \tag{5.2}$$

which produces chemisorbed hydrogen $H_{ads}(c)$. It is this reaction (which directly produces chemisorbed hydrogen without the need to overcome the barrier to dissociate a H_2 molecule) which is at the origin of the hydrogen penetration in the material (interstitial site). This hydrogen will eventually lead to the embrittlement of the material. Most of the chemisorbed hydrogen recombines on the surface in H_2 gas, which bubbles off and is harmless to the material. In saline solution, in the confined medium inside the crack, there is a more complex situation. The oxidation of Al leads to the formation of a porous, non-protective film composed of aluminum hydroxychlorides. However, essentially, anodic dissolution of the alloy and hydrogen reduction exist, similar to the reactions in water vapor.

Historically, SCC was thought to be produced because of stress assisted anodic dissolution, where the metal along the grain boundaries was dissolved in the corrosive medium. In the AlMgZn alloys, the crack velocities are not compatible with the known anodic dissolution rates. Consequently, anodic dissolution is now regarded as the necessary driving force for the hydrogen production at the surface, and this hydrogen after penetration in the material is considered the reason for embrittlement and fracture. A proof that hydrogen generated by corrosion is sufficient to induce fracture, on its own, is the hollow tube experiment by Gruhl [98] where corrosion occurs on one side of an AlZnMg sample and fracture occurs on the other side (notched). As a consequence, the mechanisms of SCC in aqueous media encompass those of the embrittlement due to internal hydrogen with additional ingredients and differences:

1. the hydrogen source is situated at the crack tip or behind it along the crack flanks

2. the hydrogen concentrations might be extremely large (see Scully in [1] p. 713 and 737), beyond 10% atomic concentration. However, this measurements seemed difficult to interpret, and the concentrations announced should not be taken literally.

3. the anodic dissolution of the alloy and the non protective film growth process in the exposed surface might produce vacancies which trap hydrogen and if they are mobile could be involved in fracture.

4. anodic dissolution, and therefore H production, are coupled to the plastic deformation in the vicinity of the crack tip because dislocations emerge on the surface, breaking the oxide film and therefore stimulate anodic dissolution (repassivation).

In this context, it seems interesting to study the internal hydrogen embrittlement and stress corrosion cracking in saline water, in the same material, with the same approach, to observe the similarities and the differences between the two, with sub-grain scale resolution.

5.2 SCC test in humid air

In this chapter, unless stated, the metallurgical state is T4, as presented in the Methods section, and the samples are always notched. First, the sensitivity of the material to laboratory air is tested. A previous experiment where the sample was loaded below the elastic limit did not lead to any crack initiation. So the load was raised above the elastic limit (150 MPa), up to 175 MPa, which corresponds to the beginning of a visible blunting of the notch. Going beyond this load would mean large damage made to the sample. After a period where the force was controlled to compensate for the relaxation of the setup, the displacement of the grips are set fixed, and the force decay in time is recorded, as shown in Fig. 5.2. A long period of 18 days, called "incubation," was observed with a low rate of force drop ($\dot{F} = dF/dt$). The average $\dot{F}$ during this incubation is -0.04 N/h. After that incubation time, a change in slope occurred, and a crack of 3 μm was detected on the surface at the notch tip. A more detailed recording of the force values during this sequence is shown in Fig. 5.3 where the inflection point corresponding to initiation can be seen with more details. The force recorded at initiation is 157 N. During propagation, $\dot{F}$ is constant at -1.2 N/h. The stress intensity factor at initiation is 11 MPa$\sqrt{m}$ and the deformation of the notch is $\epsilon_{notch} \approx 65\%$.

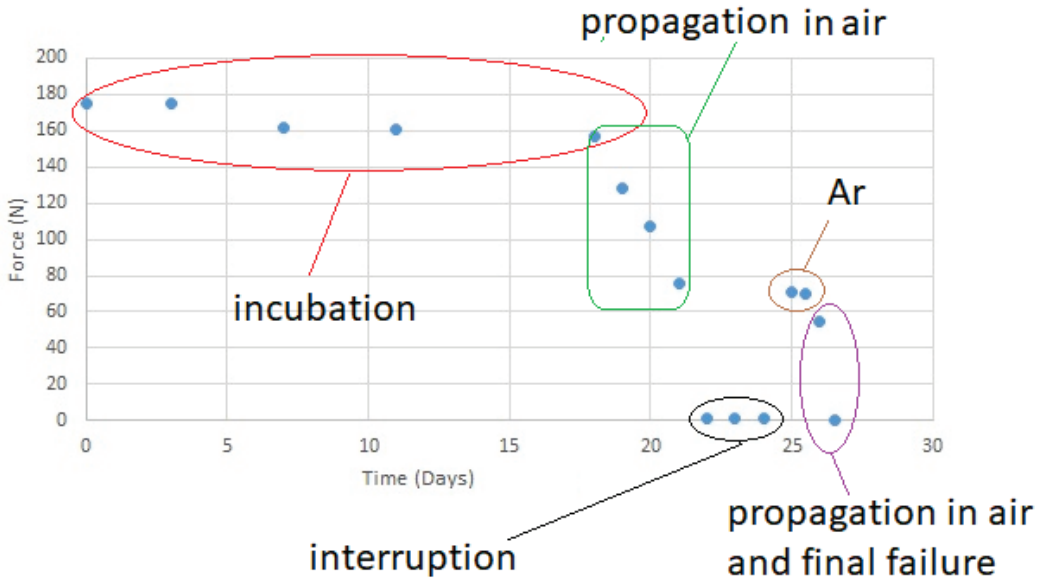

Figure 5.2: Force as a function of time (days) for SCC test in humid air. During days 22, 23, and 24 the force is set to zero because the test was interrupted. The test was restarted on day 25 and propagation started again at a very similar force and falling rate.

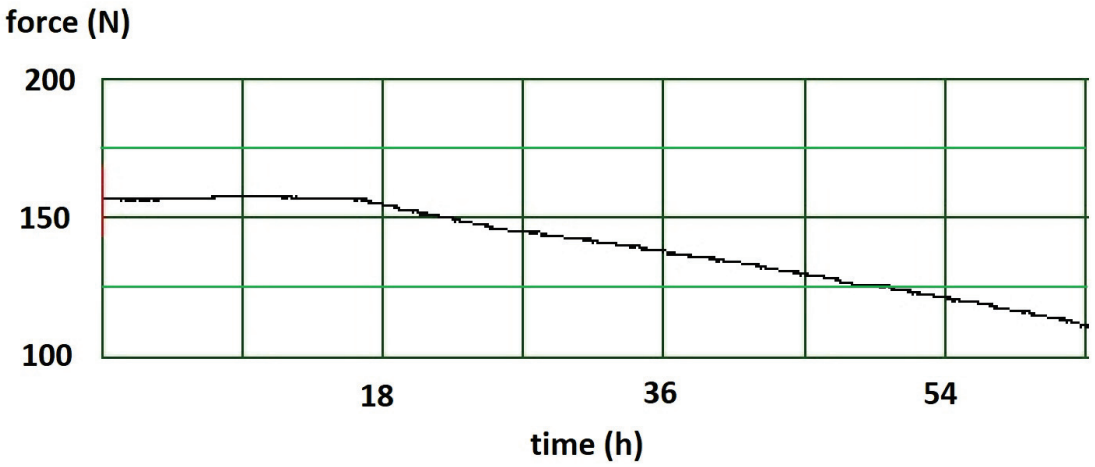

Figure 5.3: Force registered as a function of time for SCC test in humid air during crack initiation and the following crack propagation. (Days 18, 19 and 20)

Forty-eight hours after initiation (day 20), the crack has reached a length of 150 microns. A picture is shown in Fig. 5.4. The average crack propagation velocity measured from the images of the side surface is estimated as 3 μm/h. It is consistent with the plateau velocity of the SCC tests reported by Scully [7] for a 7075 T651 alloy in humid air at 67% relative humidity (Fig. 5.1c). The alloy is from the same AlZnMg family as ours but with a higher Cu content, and the average relative humidity is similar to the one found in June in Lyon, France. The same result is found for alloy 7022 (low Cu) in [36].

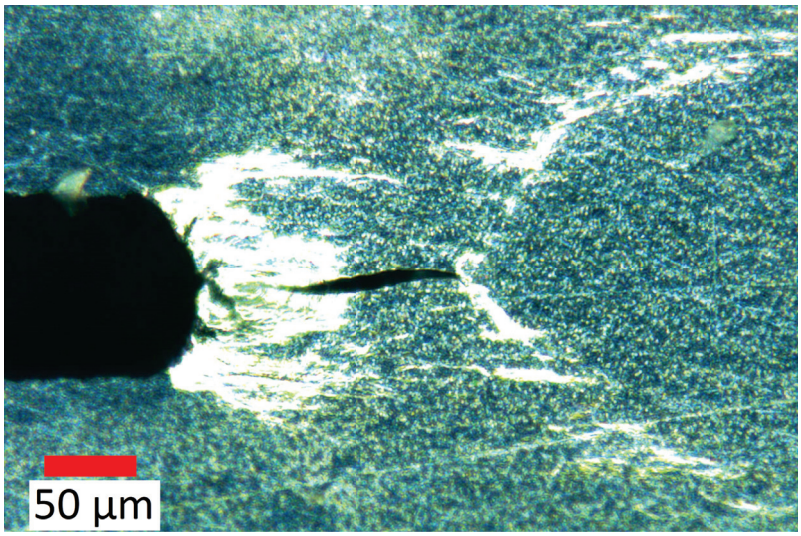

Figure 5.4: Day 20. The SCC crack initiated from the notch tip viewed with a Steroscopic Microscope at x112 with annular light. The bright contrast is a sign of plasticity created during initiation near the notch and during crack propagation. Note the two bands that emerge from the crack tip.

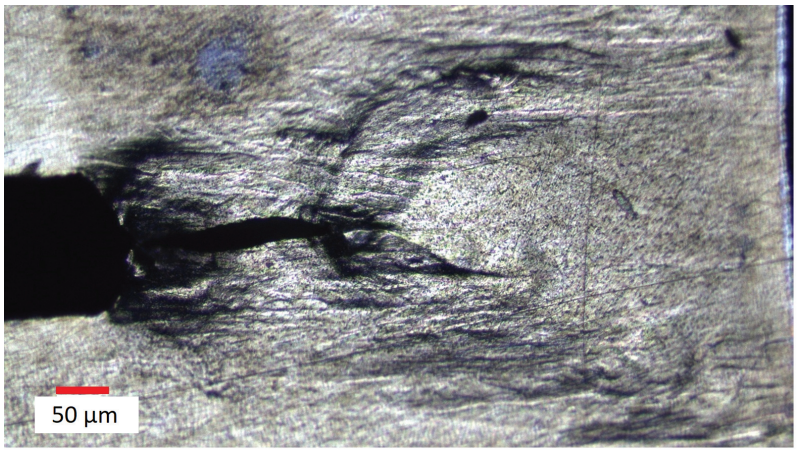

Figure 5.5: Further SCC crack propagation in humid air, after Fig. 5.4 imaged with an optical microscope with coaxial light. Plasticity can be inferred from the light scattering due to notch deformation during initiation and during the crack propagation. The effect of the slip bands can be noticed.

Once a steady propagation was established, the corrosive effect of the humid air was demonstrated by placing the sample in a dry environment and recording the effect on the force drop. This kind of experiment was used for other AlZnMg alloys in the literature (see [7] p. 744). Several attempts were not successful: silica gel bags around the sample or placing the micro-tensile machine in a desiccator with a primary vacuum pump did not change the slope of $F(t)$. Only when the entire machine was immersed in a dry argon flow did the force drop stopped immediately (Fig. 5.6). When the tensile machine was replaced back in room conditions after two hours of Ar exposure, the force remained constant for 12 more hours in the presence of humid air, but finally, the crack propagation restarted at the same rate as before and continued until the end of the test. The whole sequence is schematically illustrated in (Fig. 5.2). The final part of the fracture was done raising the force at maximum jaws' speed (0.1 mm/min) with a fracture morphology typical of a shear lip, indicating no environment effect.

Plasticity can be visually observed from the contrast on figures 5.4 and 5.5, showing the two slip bands emanating from the crack tip. However, these images were not suitable for DIC because the deformation is too high for the pattern's quality, which is simply the optical contrast of the surface particles after polishing. Only a single pair of images could be analyzed by DIC with a coarse grid size of 20 px per step that corresponds to about 5 μm length at this magnification (x200). The result is the Von Mises strain, which is overlapped on the crack image on Fig. 5.7 and an estimate of the local velocity for a crack advance of about 20 μm. This velocity is approximately 2μm/h, which is already close to the average velocity of 3 μm/h measured macroscopically. Like in the previous chapter, the integral of the Von Mises strain gives the "plastic deformation rate" (PDR), here with a value of about 4000. The plasticity at the crack tip position is 1% (approx), within a step of 5μm. The secondary plasticity extension (Λ) is roughly 14 μm. These values are for comparison with the values for SCC in saline water that are given below.

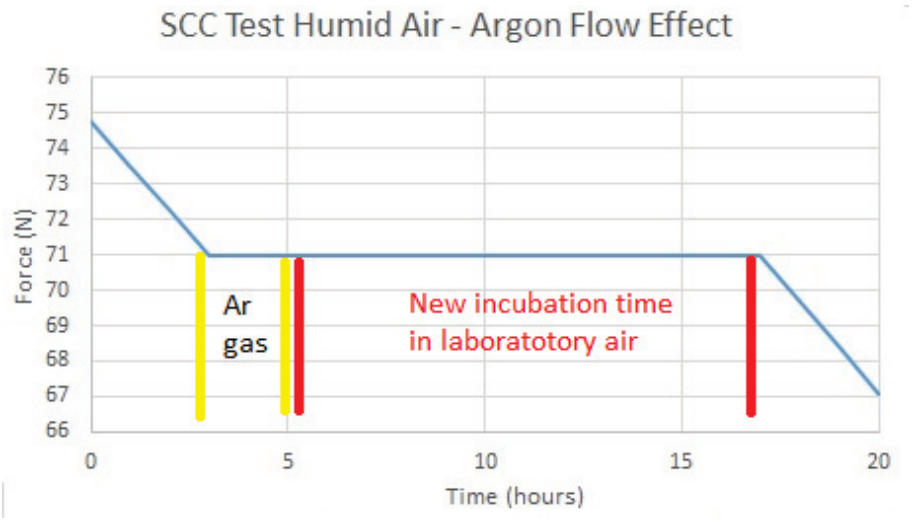

Figure 5.6: Force as a function of time. The sample was exposed to an argon flow for 2 hours (from 3 to 5 hours). Crack growth restarted after 12 hours after the sample was placed back in humid air (from 5 to 17 h). The two similar rate of force decay indicate crack propagation with a similar velocity.

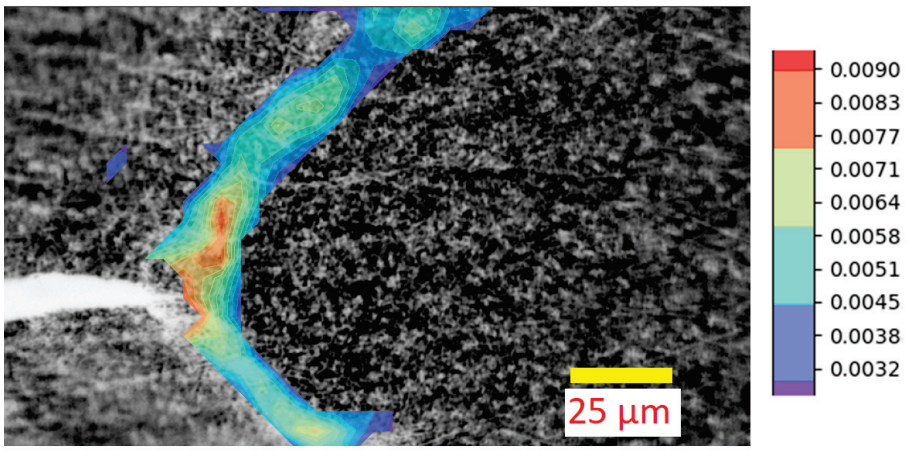

Figure 5.7: SCC crack propagation in humid air. Optical Microscope. The colormap illustrates the Von Mises strain in a range from 0.3% to 0.9%.

5.2.1 Fractography analysis

Figure 5.8 is an SEM image of the fracture surface. The final (fast) fracture is easily identified as well as the shear lip at the sample's edge (right side of the image) which represents only a small fraction of the fracture surface. Everywhere else, the fracture morphology is transgranular. It could be classified as a quasi-cleavage fracture mode with a small number of tear ridges, suggesting plastic deformation is involved in the fracture process itself (not only in the wake), but no dimples (an example of fast fracture with dimples, on our material, is shown later).

It is worth mentioning that cleavage is a low-energy fracture that propagates along well-defined low-index crystallographic planes known as cleavage planes. Theoretically, a cleavage fracture should have perfectly matching faces and should be completely flat and featureless. However, engineering alloys are polycrystalline and contain grain and subgrain boundaries, inclusions, dislocations, and other imperfections that affect a propagating cleavage fracture. Consequently, a featureless cleavage is difficult to observe. These imperfections and crystal lattice orientation changes, such as possible mismatch of the low index planes across grain or subgrain boundaries, produce distinct cleavage fracture surface features, such as cleavage steps. Quasi-cleavage is usually used to describe failure on non-cleavage planes (it is not physically cleavage), and sometimes decorated with fine lines, as it is shown in Fig. 5.8 and 5.9. Regarding our case in Fig. 5.8 and Fig. 5.9, some plasticity features are also present as a ductile tearing of some ligaments (especially near the notch and at the center of the fracture surface). Figure 5.9 might be interpreted as a quasi-cleavage fracture morphology.

In addition, the plasticity involved in the fracture process is also confirmed during the crack propagation on the side surface, as a change in the contrast in Fig.5.4, Fig. 5.5, and Fig. 5.7 near the crack tip region.

5.3 Macroscopic results of SCC tests in saline water

5.3.1 A typical SSC crack test in saline water

Some modifications to the procedure for the IHE test were performed to adapt it to SCC. Figure 5.10a shows a low magnification image of the SCC test. The sample is in contact with the saline water in the bottom part and at the sides. Only the upper part is left free of water for the optical microscope observation. Figure 5.10b shows an empty 3D-printed micro-cell with the tensile sample before being placed on the micro tensile machine.

Figure 5.11 shows the stress as a function of time in an SCC test in saline water. The tensile test starts by increasing the force slowly, below the elastic limit. When the stress of approximately 100 MPa is reached, the displacement of the jaws is imposed for at least one hour, and the time variation of the force is recorded. If no change in the force or the notch tip (microscopy observation) is found, the force is raised again by steps of 10 - 15 N with a minimum waiting time of 20 minutes. This time is a compromise between the minimum time for crack initiation obtained at high force and the maximum time the sample can be held in saline water without massive multiple cracking on all surfaces exposed (around 6 hours). The procedure is repeated until crack initiation is achieved, as shown in the last part of Fig 5.11. The incubation time is the time required to reach crack propagation

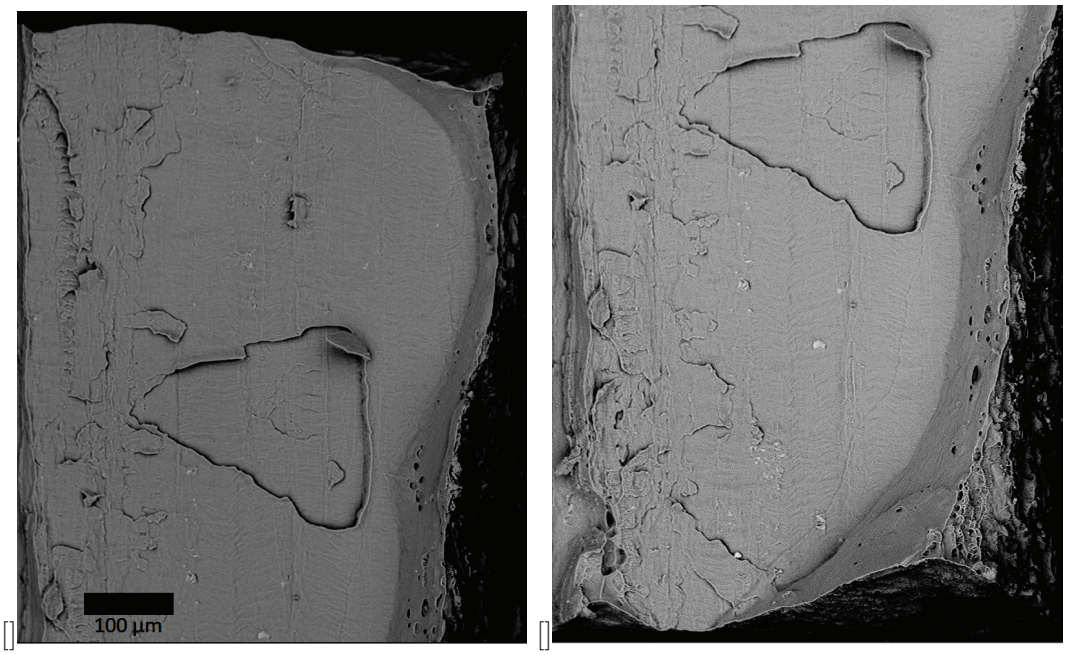

Figure 5.8: SEM images of the fracture surface of an SCC test in humid air. The transgranular fracture and the final ductile shear lip (right side) are clearly visible

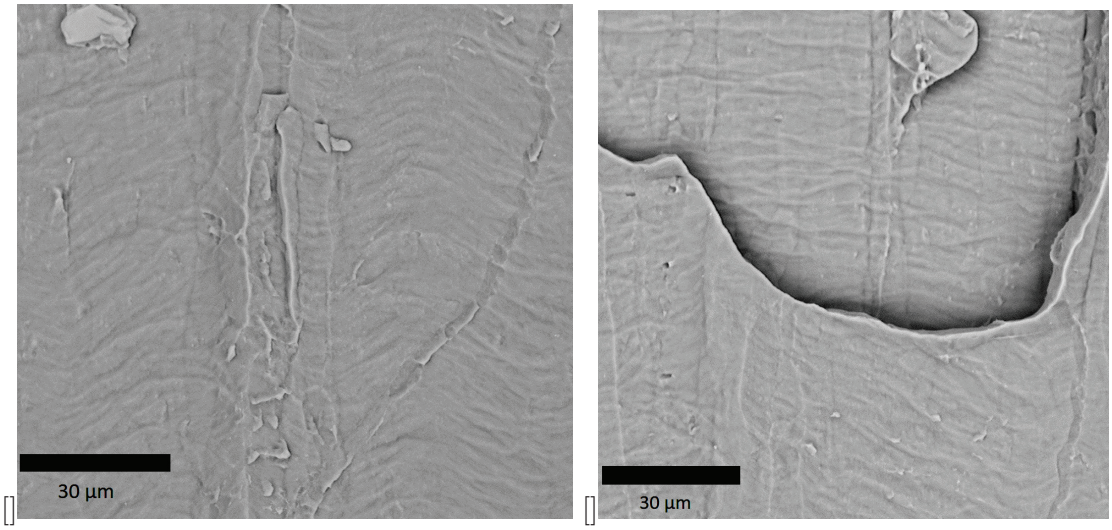

Figure 5.9: SEM images of the fracture surface of SCC test in humid air showing a transgranular fracture with fine lines.

from the notch. The final result is a single crack such as the one shown in Fig. 5.12.

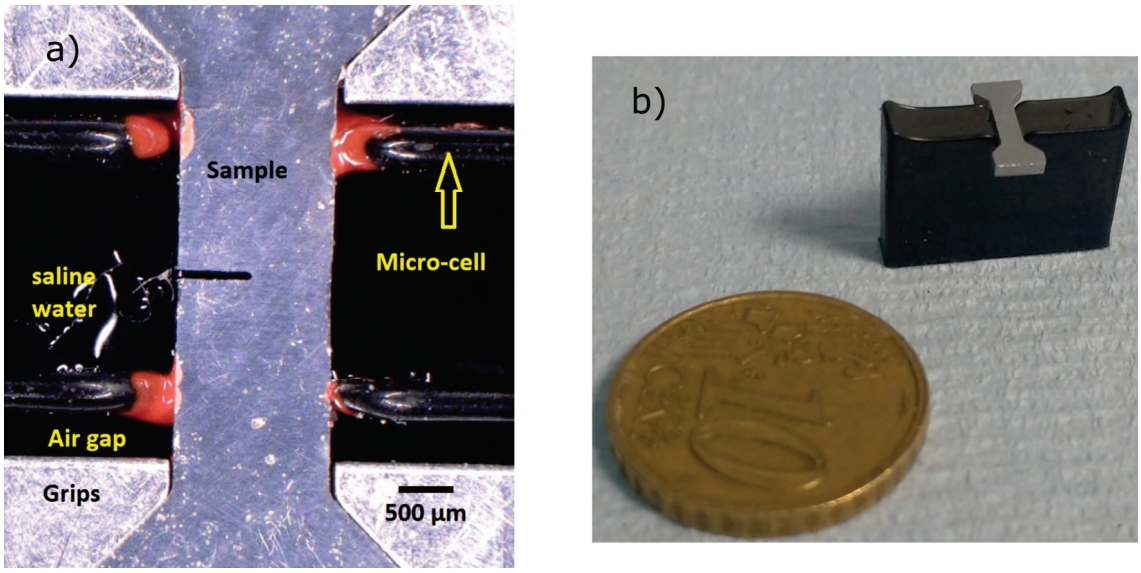

Figure 5.10: Sample A in table 5.1. (a) Top view of the SCC set up obtained with an optical microscope using an annular light. The sample is in contact with the saline water (bottom part and both lateral sides) contained in the micro-cell. The force is applied using the grips. The micro-cell is glued to the sample with red glue. (b) Tensile sample and the micro-cell with a 10 cent euro coin as a size reference.

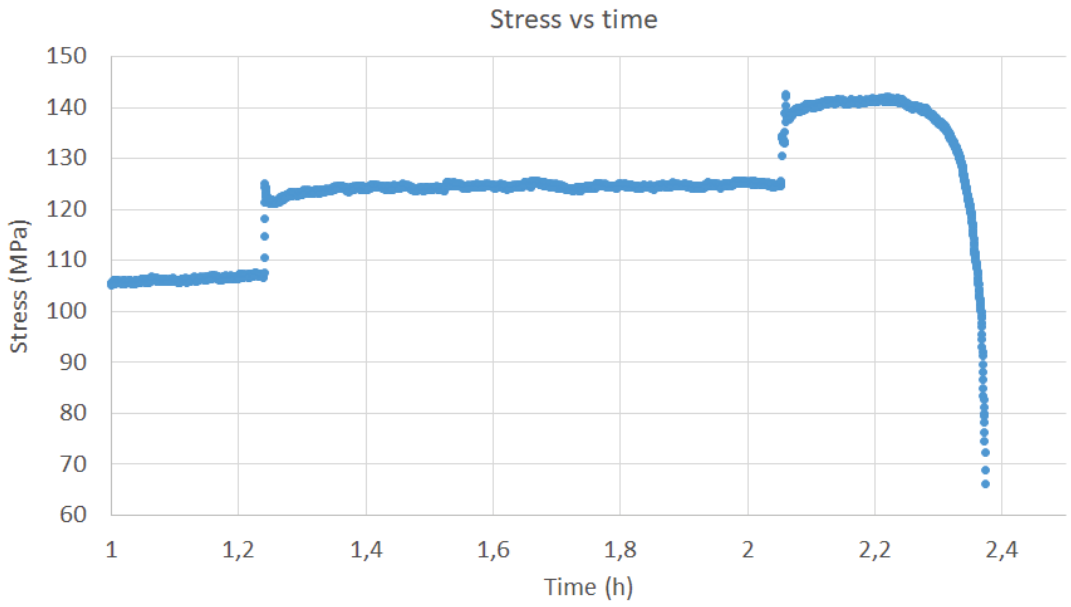

Figure 5.11: Sample 2 in table 5.1. Stress evolution as a function of time. The rapid fall in the stress is due to a fast crack propagation of the order of 4000 μm/h.

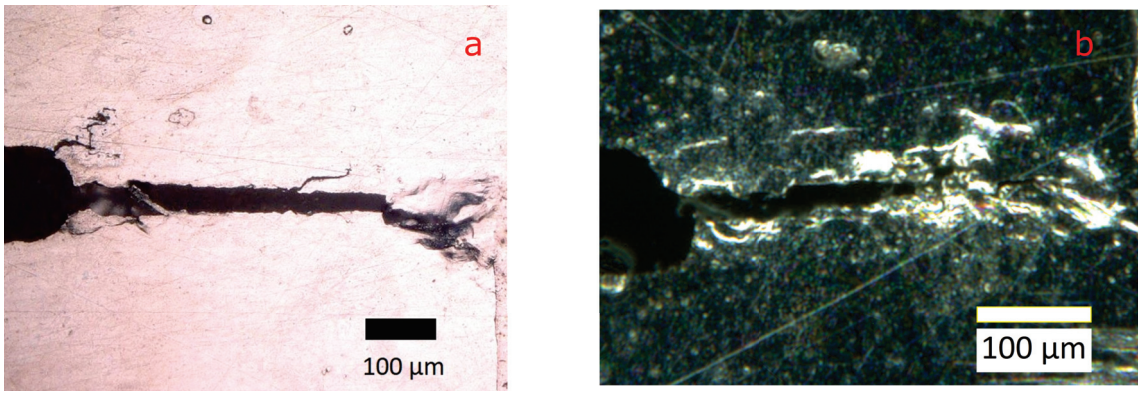

Figure 5.12: Examples of SCC cracks obtained in saline water (Tab. 5.1). (a) Sample A under optical microscope with a full coaxial light. (b) Sample 8 viewed from a stereoscopic microscope with an annular light.

Table 5.1: Characteristics of the tests done: sample name, incubation time (t_{inc}), maximum applied stress (σ_{max}: force divided by the initial section not taking into account the notch), global notch deformation (ϵ_{notch}), applied stress intensity factor (K) for initiation, average crack velocity ($\overline{v}$), sample thickness (B), notch length (a_{notch}). The * for sample 10 means that it is an average for the samples 1 to 9 as it is indicated in the main text. The yield stress is 150 MPa.

Sample	t_{inc} h	σ_{max} MPa	ϵ_{notch} %	K MPa$\sqrt{m}$	$\overline{v}$ μm/h	B mm	a_{notch} mm
1	3	130	16	11.7	4000	0.8	0.4
2	2	140	15	12.6	4000	0.7	0.4
3	4	140	16	12.6	4000	0.8	0.4
4	4	110	15	9.9	4000	0.8	0.4
5	2	125	15	11.3	6000	0.8	0.4
6	2	125	13	11.3	6000	0.8	0.4
7	3	120	13	10.8	6000	0.7	0.4
8	2	120	12	10.8	8000	0.7	0.4
9	2	120	12	8.3	9000	0.9	0.4
10*	3*	125*	14*	11.0*	6000*	-	-
A	2	95	15	11.3	1200	0.7	0.7
B	4	98	40	11.7	300	0.5	0.7
C	4	150	28	6.8	200	0.3	0.3
AIR	430	162	65	11.3	3	1.0	0.4

5.3.2 Analysis of the macroscopic behavior

Table 5.1 presents, from a macroscopic viewpoint, the results of the successful SCC tests. The first column is the sample name. The samples named with numbers (from 1 to 9) were machined using a micro-milling cutter. On the other hand, samples named with letters (A, B, and C) were machined by EDM (electrical-discharge machining). The samples machined by milling are probably pre-strained because their dimension is small compared to the influence size of the tool used to machine them. EDM does not have this drawback. Furthermore, with EDM the dimensions are more accurate, allowing to obtain straight samples that were well aligned in the tensile grips and produced the desired stress state (mode I). The incubation time is displayed in the second column, and the stress required for initiation is in the third one. The notch deformation and the stress intensity factor for crack initiation are in the fourth and fifth columns, respectively. The average crack propagation velocity is estimated using the force-time curve, from the time onset of crack propagation to the complete sample failure (crack length divided the propagation time). The geometrical parameters (thickness and notch length) are displayed in the last two columns. The tested sample in humid air is added at the end of table 5.1. Two different sample groups are created based on their SCC susceptibility. Group 1 (samples from 1 to 9, machined by micro-milling) is more susceptible to SCC than group 2 (A, B, C), machined by EDM. In addition, the samples of group 2 were analyzed at a local scale in the optical microscope. This will be presented in the next section. The average crack propagation velocity for the group 2 samples in table 5.1 are averages of the local velocities obtained from DIC.

Group 1 has a global deformation of the notch for crack initiation (notch diameter for crack initiation compared to initial notch diameter) between 12% and 16%, and the stress intensity factor for crack initiation is from 8.3 to 12.6 MPa$\sqrt{m}$. The stress required for crack initiation is in a range from 110 to 140 MPa. The incubation time is from 2 to 4 hours. No influence of the thickness (between 0.7 mm and 0.9 mm) is observed. Velocities are higher than 4000 and up to 9000 μm/h. In order to facilitate the comparison of this group with other groups of samples, the values corresponding to samples from 1 to 9 are averaged and displayed as sample 10* in table 5.1. Consequently, sample 10* is not a real sample, but it represents a micro-tensile sample machined using the milling procedure. Sample 10* has an incubation time of 3 hours, and the stress value for initiation is 125 MPa. The notch deformation is 14% with a stress intensity factor of 11.0 MPa $\sqrt{m}$, and an average crack propagation velocity of the order of 6000 μm/h.

In addition, a preliminary test was performed with a sample in the as-received state (AS). The sample is denoted as Sample 0. Sample 0 was tested in saline water for 9 hours with a 150 MPa applied stress (13.5 MPa$\sqrt{m}$). No signs of SCC sensitivity were observed. The sample was finally broken using a high strain rate, and an SEM image of the fracture surface is shown in Fig. 5.13a. The fracture morphology is completely ductile with dimples, proving no susceptibility to SCC. On the contrary, the fracture surface of sample 7 (Tab. 5.1) is intergranular smooth (Fig. 5.13b). This sample's increased susceptibility is produced by the T4 heat treatment. The T4 heat treatment increases the susceptibility of our alloys, as expected from the literature. The SCC fracture surface is mostly IG brittle, with a shear lip in the last part of the crack propagation. Minority parts of the fracture surface can be classified as transgranular (similar to Group 3, the

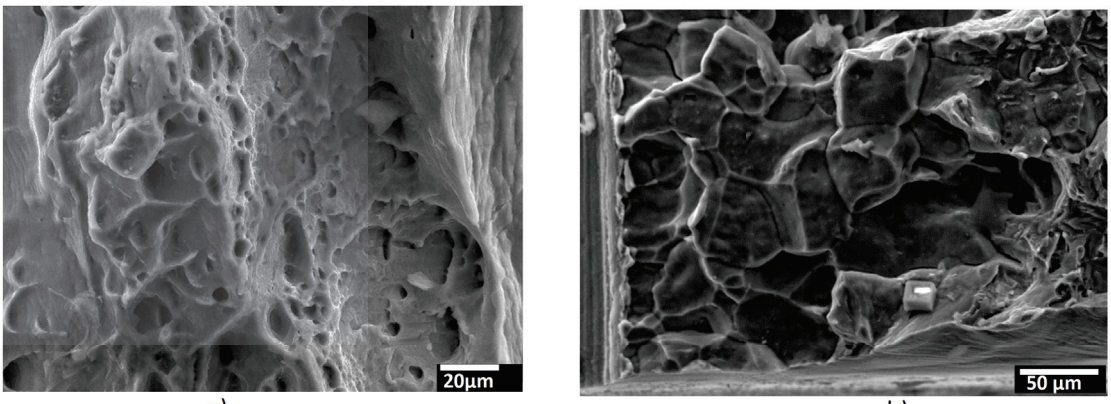

Figure 5.13: SEM images fracture surfaces: (a) As received state (sample 0). Not sensitive to SCC in saline water after 9 hours. The morphology is ductile with dimples. (b) T4 state (sample 7), it reveals a predominant intergranular brittle fracture surface morphology coherent with a susceptibility to SCC in saline water.

one with more H-embrittlement level, in the IHE Chapter), as it is shown in Fig 5.14 for sample 8.

Group 2 has different testing conditions among its samples. Samples B and C were protected with lacquer on all the surfaces, except for the notch and the top part reserved for microscope examination. On the contrary, sample A has no protection, similar to the tests in group 1. Sample A has an average crack propagation velocity of 1200 μm/h, and at the local scale, a maximum local velocity of 2970 μm/h as shown in Tab.5.3. This average velocity for sample A is five times slower than the average velocity of sample 10* representing group 1. Even at the local scale, the maximum local velocity (v_{max} = 2970 μm/h) is still 30% lower than the lowest velocity found in group 1 (4000 μm/h). Nevertheless, the notch tip's deformation is 15% with a K for crack initiation of 11.3 MPa $\sqrt{m}$, similar to group 1. The maximum stress is 95 MPa. This low value in the stress is attributed to a longer initial notch length. The incubation time is 2 hours, which is lower than the average incubation time for Sample 10*.

The conditions for testing B and C differ from those for A by adding a protective layer on the surface, exposing only the notch to saline water. It causes longer incubation times than for sample A. The samples B and C show average propagation velocities around 200 and 300 μm/h. The notch deformation at initiation (ϵ_{notch}) is significantly higher (40% and 28% for samples B and C, respectively versus 14% and 15% for samples 10* and A, respectively). The maximum local velocity in sample B is 1360 μm/h in table 5.3, and it is achieved towards the end of the test. This maximum velocity is still low in comparison with sample A or sample 10*. The maximum stress of sample B is similar to the one of sample A. However, sample C has a high maximum stress level (150 MPa), likely because of the short notch length. The low thickness (0.3mm) of sample C might also affect the test results.

In addition, the morphology of the fracture surfaces was analyzed. The "intergranular

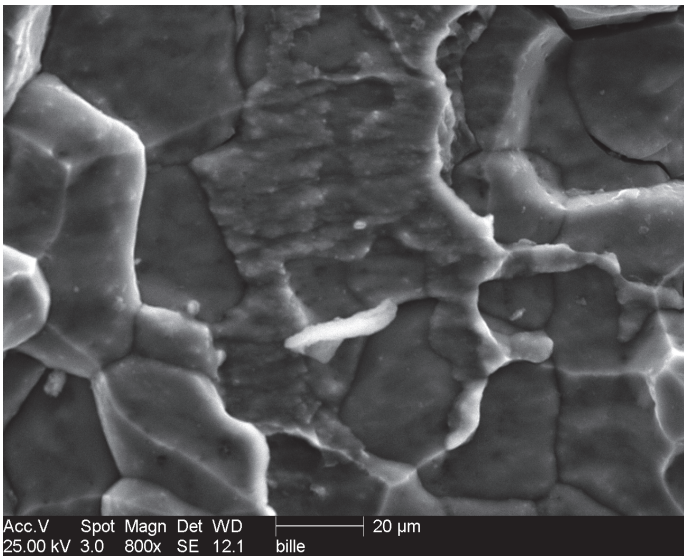

Figure 5.14: SEM image of the fracture surface of sample 8. The transgranular morphology is similar to the one found in group 3 of IHE

smooth" morphology is predominant for A and B, covering more than 50% of the surface. Other fracture morphologies were found and are labeled "TG or IG rough," meaning "transgranular or intergranular rough." There is an extra difficulty for classifying the morphology because the sample exposure to saline water during the test corrodes the surface, erasing the details. An SEM image of the Sample B fracture surface is shown in Fig.5.15. The percentage of "TG or IG rough" is 35% (Tab. 5.2). It is a high percentage compared with group 1, where TG morphology was only occasionally found covering a small surface as seen in Fig. 5.14. The fracture morphology percentages in table 5.2 are similar to those found in group 3 of the IHE chapter.

Table 5.2: Percentage of the fracture surface morphology area for SCC samples A and B in the full fracture surface. Measured by Image J. There are three different morphologies: "IG smooth" (intergranular brittle with no, or few, plastic features on the fracture surface), "TG or IG rough" (transgranular or intergranular failure with roughness on the fracture surface), and "ductile" (ductile failure, dimples and shear lip).

Sample	% IG smooth	% TG or IG rough	% ductile
A	61	36	3
B	55	35	10

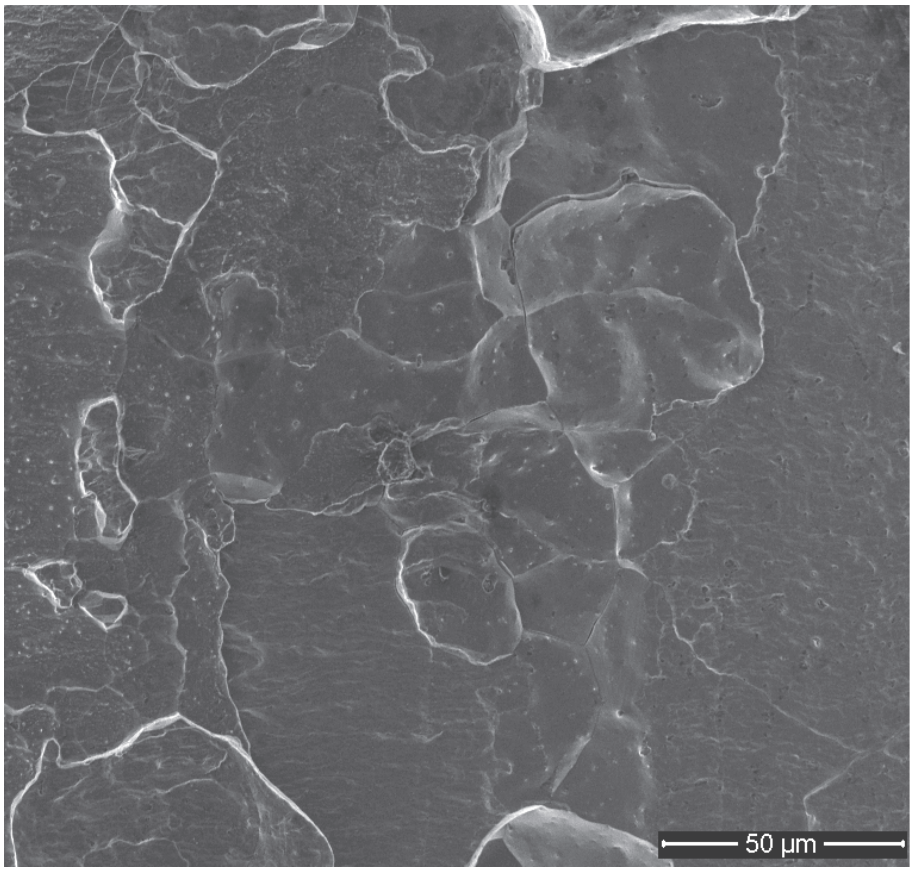

Figure 5.15: SEM image of the fracture surface of sample B. Different fracture morphology are observed. The fracture surface is similar to the ones found in the IHE chapter.

Summary of the macroscopic behavior

As a recap, the samples are split into two groups: group 1 and group 2. Samples machined by a milling cutting belongs to group 1. This group showed the highest SCC susceptibility, with much higher average propagation velocity and less deformation at the notch tip. Initiation from the notch requires a considerable strain of at least 12%. However, it is half of the necessary deformation at the notch tip for an IHE of Group 3. Moreover, the SCC crack initiates propagation at a relatively high mechanical load K $\approx$ 11 MPa$\sqrt{m}$ compared to the IHE Group 3 (between 5 and 8 MPa$\sqrt{m}$). The velocities are also much higher, with an average of 250μm/h for IHE (group 3) and 6000 μm/h for SCC group 1.

Group 2, with samples machined by EDM, showed less SCC susceptibility than group 1. Also, two testing conditions were used in group 2. The first testing condition is "without protection" for sample A (tested in the same conditions as group 1). The second testing condition is "protected." Samples B and C were protected with lacquer, reducing the surface in contact with saline water: only the notch was exposed. Lower velocities and higher deformation at the notch tip than sample A (no protection) were obtained. For these two samples, velocities and notch deformations are similar to what was found for IHE (in group 3), and sample A was intermediate between SCC group 1 and the samples B and C.

5.4 Local results of SCC tests in saline water

In this section, the same methodology as in the internal hydrogen embrittlement chapter is used. New issues appeared because of the different sample surface preparation. First, the samples of SCC group 1 were not analyzed at the local scale because the tests were performed with a "macroscope" with an annular light that had both a magnification limited to about x150 and the surface contrast was not appropriate. Therefore, the rest of the chapter deals with only the samples A, B, and C (group 2). However, several fracture sequences could be analyzed, so even with this small number of samples, we could establish that fracture is very similar to the IHE case. In sample A, the DIC measurements cover three sequences (Aa, Ab, and Ac in table 5.3) and in sample B a numerous points where analysed in the same sequence. Moreover, SCC is performed on samples not pre-exposed to any chemical attack, so the observable surface is produced by polishing. On the contrary, the IHE required a hydrogen pre-charging in an acid solution that attacked the sample and produced a surface state that was well adapted for DIC under an optical microscope. The pattern obtained after polishing comes from the emergence of dispersoids on the surface, which appear as colored features on a white matrix. When slip bands appear on the surface, the contrast is drastically changed by forming dark lines. The correlation becomes impossible in these regions if the new contrast hides the dispersoids. Therefore, the DIC points close to the crack tip are less reliable, and only information coming from points that are further away can be used. This problem can be mitigated by reducing the magnification of the observations or using a coarse step size in DIC, but then, the spatial resolution is diminished.

Despite these new difficulties, the plasticity, the position of the crack tip, and the velocity are quantified at the sub-grain scale by the usual variables: v, the plastic deformation rate (PDR), the opening displacement rate (ODR), the length of the fracture process zone (Λ), the deformation at the crack tip (ϵ_{tip}). The section presents sequentially: an example of DIC, the list of all the DIC results (all the local measures that were made), the matching of the local velocity with the details of the fracture morphology, the velocity/plasticity correlation, the velocity as a function of the stress intensity factor (K) and typical crack opening profiles. Finally, an intermittent crack could be observed, and the attempt to measure the variation of the velocity at the appropriate scale is presented.

5.4.1 Local plasticity

A representative example of the plastic zone in the case of SCC (sample Ac4) is given in Fig. 5.16a. The displacement field was obtained by DIC, and the von Mises strain was calculated from the displacement. It is overlapped with the deformed image (i.e., the second of the pair used for DIC). Only the strain values between 1% and 10% are displayed. Similar to the IHE, two forms of plasticity can be distinguished. The primary plasticity with two large deformation bands leaving the crack tip and the secondary plasticity present ahead of the crack tip along the future crack path. DIC was performed on the SCC samples with the same precision as IHE (magnification x2000 and a grid of 10 px, i.e., a spatial resolution for the displacement filled of 1 μm). A detail of the displacement field (arrows) is shown in Fig. 5.16b. The crack propagation velocity, the extension of the secondary plasticity (Λ), and the PDR are determined using the same methods applied before. The local results are shown in Tab. 5.3. The PDR values found for SCC are similar to ones found for IHE (Tab. 4.3 in IHE chapter).

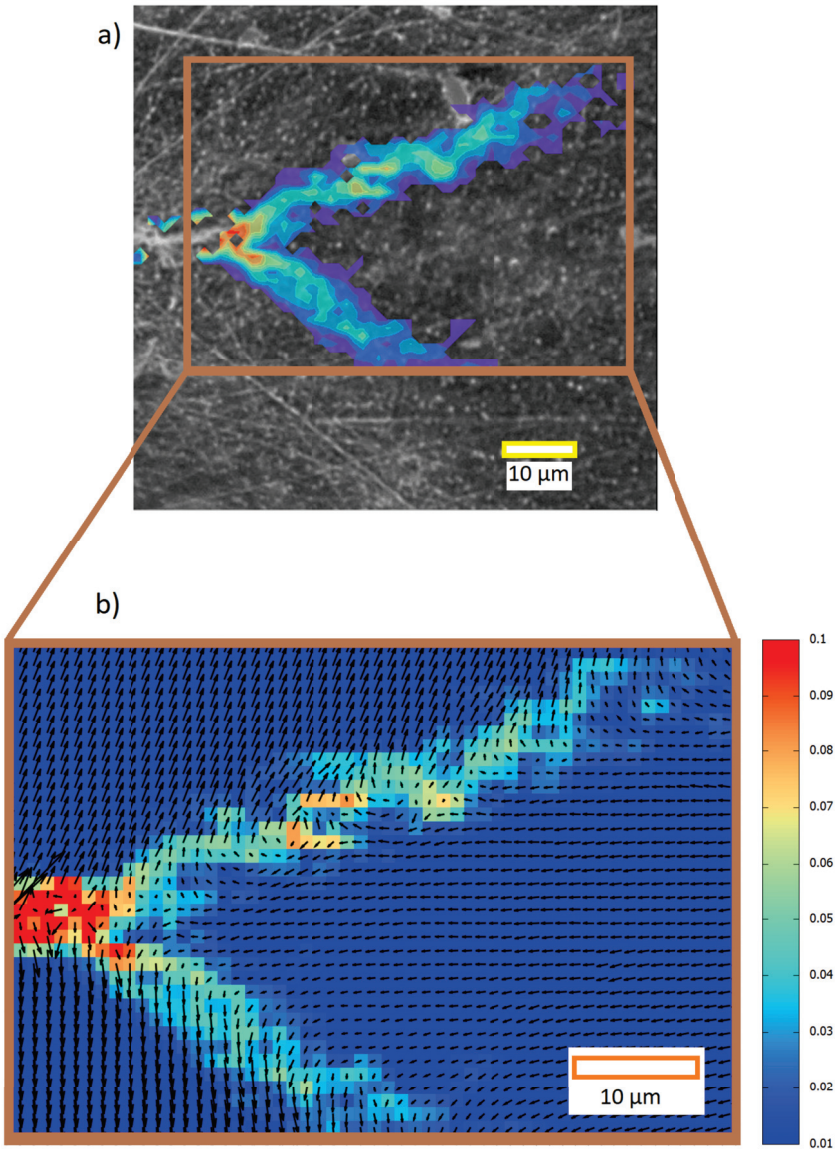

Figure 5.16: Sample Ac4 DIC in table 5.3. (a) The Von Mises strain field (between 1% and 10%) was calculated from the DIC displacement field. It is overlapped with the deformed image after the SCC crack advance. The sample is A, and the final crack position is Ac4 in Tab. 5.3, i.e., the crack advance is from the configuration Ac3 to configuration Ac4, and the characteristics of the plasticity increment during this increment of the crack extension are reported in Tab. 5.3. Figure (b) shows Von Mises strain map for the region marked in (a). The vectors represent the displacement field magnified by a factor 5. The resolution is 110 nm/px and the grid size is 10 px.

The secondary plasticity, characterized by the fracture process zone (FPZ) extension (Λ) for sample A, is estimated between 2 and 8 μm, with an average of 4 μm. Regarding segment Ac, where the magnification used was the highest available (x2000), the average extension of the plasticity ahead of the crack tip (Λ) is also 4 μm. This average Λ of 4μm coincides with the peak of the Λ distribution for IHE in Fig. 4.9 in the previous chapter. Moreover, the average deformation percentage at the crack tip location (ϵ_{tip}) is 6%. This value also matches the peak of the distribution of ϵ_{tip} in Fig.4.9 for IHE.

Regarding sample B, it has a lower average crack tip deformation of approximately 4% and a higher average Λ of 8 μm than sample A. These values are in the range found in the IHE. Also, sample B was tested with a protective paint, and only the notch is in contact with the solution. Less contact surface with the saline solution implies less hydrogen production, less general corrosion, less pitting corrosion (that could lead to micro-cracks), and less secondary cracks, so the sample is probably less embrittled than sample A. The values related to the secondary plasticity for sample B (Λ and ϵ_{tip}) are similar to those in the Aa segment. This similarity may be explained as follows: Aa is the closest segment of sample A to the crack initiation from the notch, it has been less time in contact with the aggressive medium, so the influence of hydrogen production, general corrosion, or secondary cracking is lower than the rest of sample A.

Table 5.3: Crack length (a), local velocity (v), force (F), stress intensity factor (K), Von Mises deformation measured at the crack tip location (ϵ_{tip}), length of the FPZ (Λ), and the PDR ($\Delta L_d/\Delta a$). Similar to the IHE chapter, some measurements were estimated directly on the image (Image J) because of lack of DIC condition. These points are indicated with a star *.

Image	a μm	v μm/h	F N	K MPa$\sqrt{m}$	ϵ_{tip} %	Λ μm	$\Delta L_d/\Delta a$
Aa							
1	802*	-	81.6	14.7	-	-	-
2	810	720*	79.5	14.7	4	8	1767*
3	822	1081	77.6	14.9	3	3	2237
4	834	720	74.7	14.9	4	8	3598
Ab							
1	960*	-	63.0	18.8	-	-	-
2	966	541*	62.1	18.9	3	2	634*
3	976	901	61.2	19.3	2	2	207
4	976	360	59.8	19.1	1	2	282
5	980	180	58.8	19.9	1	2	321
Ac							
1	1117*	-	51	25.6	-	-	-
2	1130	2376	47.6	24.9	11	4	1482
3	1141	1982	44.7	24.3	10	3	1293
4	1157	2772	42.2	24.2	8	6	575
5	1179	1982	37.7	23.2	11	6	658
6	1195	2970	34.3	22.2	12	3	357

Image	a μm	v μm/h	F N	K MPa$\sqrt{m}$	ϵ_{tip} %	Λ μm	$\Delta L_d/\Delta a$
B							
1	980*	-	54.0	22.4	-	-	-
2	1004	240*	53.1	23.9	3	8	1031*
3	1048	293	50.1	26.0	4	8	3867
4	1064	320	48.7	26.7	3	8	1864
5	1084	133	45.2	26.4	3	8	3508
6	1096	80	42.9	26.1	5	8	5484
7	1112	53	38.7	24.8	4	16	14987*
8	1188	507	34.4	28.3	-	-	-
9	1220	640	32.6	29.8	-	-	-
10	1280	1200	30.8	34.1	-	-	-
11	1348	1360	28.5	39.1	-	-	-
C							
1	350*	-	67.0	7.5	-	-	-
2	580*	276*	57.5	11.8	-	-	-
3	660	253*	46.9	12.0	4	12	723*
4	700	100	30.7	8.8	2	12	4964
AIR							
1	530*	2*	98.0*	13.0*	1*	14*	4000*

Matching local crack velocities with the fracture surface morphology

The fracture morphologies were classified into two categories: "intergranular smooth" and "transgranular or intergranular rough." For simplification purposes, they will be called "smooth" and "rough" morphologies. Like the previous chapter, the local velocity is confronted with the fracture surface details seen in SEM pictures. The velocity as a function of the crack tip position plot is superimposed to the fracture surface. Figure 5.17 shows this superposition for sample B. All the points of measurement in Fig. 5.17 correspond to a rough morphology (transgranular or intergranular rough). Moreover, some small areas present ridges and plastic tearing that might be classified merely as "ductile."

Sample A is different. The case is detailed in Fig. 5.18. The DIC measurements cover three sequences (Aa, Ab, and Ac in Tab. 5.3) which correspond to three zones on the fracture surface. The fracture morphology of the first sequence (Aa) is transgranular or intergranular rough. In the last sequence (Ac), the morphology is intergranular smooth. Ab is located in a transition zone with points that exhibit a smooth or a rough morphology. The segments Aa and Ab have velocities around or less than 1000 μm/h, and Ac has velocities of the order or higher to 2000 μm/h. It seems to be a clear tendency. The rough morphology is related to lower velocities than 1500 μm/h, and the IG smooth is mostly related to velocities similar to or higher than 2000 μm/h.

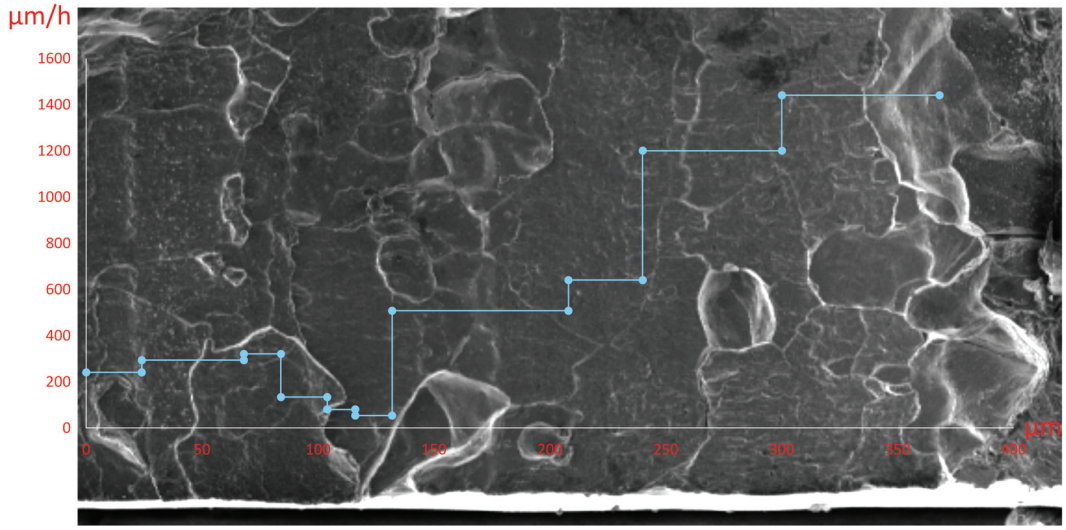

Figure 5.17: Crack velocity plot superimposed on the fracture surface of the SCC sample B.

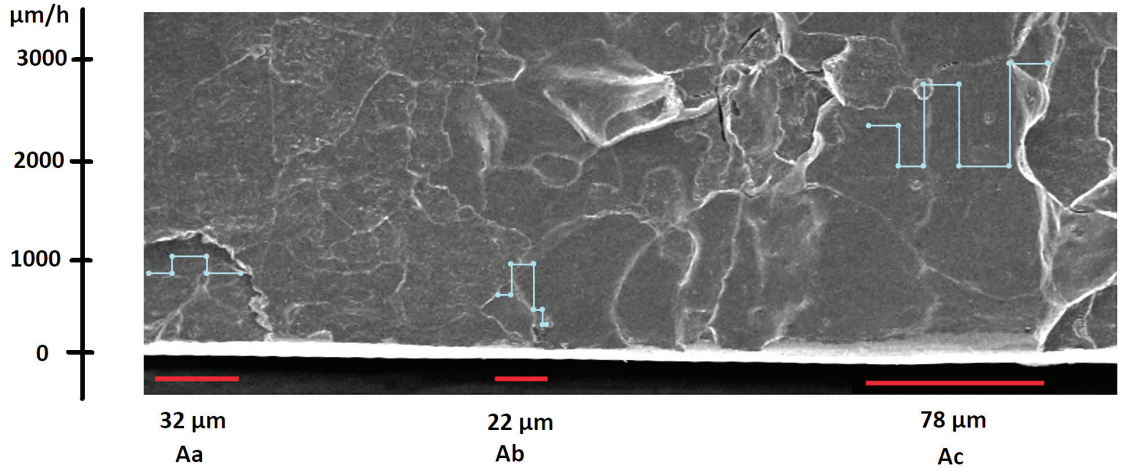

Figure 5.18: Crack velocity plots superimposed on the fracture surface of the SCC sample A for the three sequences (Aa, Ab, and Ac).

Local propagation velocity and plasticity correlation

The correlation of local velocity and plasticity is investigated via the PDR. As in the IHE Chapter, it could be expected that high plastic deformation will shield the applied mechanical load so that the fracture process zone (FPZ) will experience lower tensile stress and, therefore, would have a slower crack propagation velocity. The local velocity (v) and the plastic deformation rate (PDR) are plotted in Fig. 5.19 from the data in table 5.3. Some points were rejected, for example, B7, where the DIC conditions were far from optimal. In Fig. 5.19, the PDR axis is limited to 8000. Besides, in the horizontal axis, the local velocities for every sample are represented with different icons. A filled icon represents roughness in the fracture surface, and an empty icon represents an intergranular smooth fracture surface.

Figure 5.19 reaffirms the already mentioned tendency. The rough morphology is only present when velocities are below 1500 μm/h. The IG smooth is mostly present (except 1 point) for velocities similar or higher than 2000 μm/h. All the IG smooth points have low plasticity (lower than 2000). The points with a rough morphology are present in a wide range of plasticity, from low PDR values (lower than 300) to high PDR values (higher than 5000). The three analyzed segments in sample A show a progression with time towards a more brittle system. At the beginning of the test, Aa presents a low velocity and high plasticity, with a rough fracture morphology at every location where the velocity was measured the points. Further in time, and in crack extension, the segment Ab also has a low velocity but now with low plasticity. Besides, Ab includes a point with an IG smooth morphology. Finally, Ac has high velocities, and the plasticity is low with a smooth morphology.

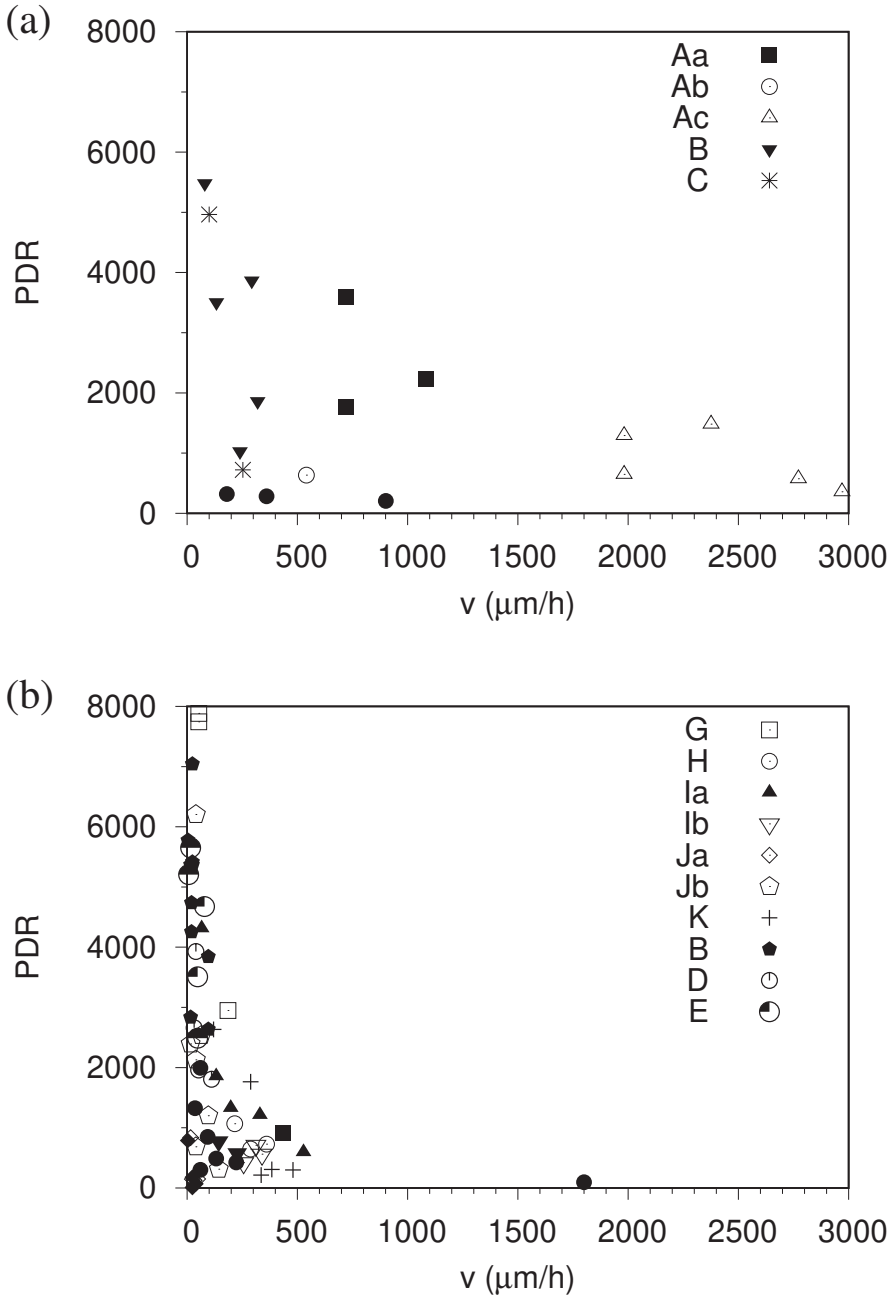

Figure 5.19: Plastic deformation rate (PDR) as a function of the local crack velocity: (a) for SCC in group 2, (b) for comparison the IHE data is also given. The filled icons (and the stars) indicate "TG or IG rough" points and the empty icons indicate "IG smooth" points.

It is interesting to compare the data in Fig. 5.19a with the IHE in the previous chapter and recalled on Fig. 5.19b. The PDR range in the SCC tests is similar to IHE Group 3 in Fig 4.14b, displaying low plasticity points below 2000 and high plasticity up to 8000. In both cases, the trend is the same: the faster the crack, the lower the plasticity. Nevertheless, fracture in IHE occurs with less plasticity for the same velocity. Moreover, it is common to both SCC and IHE that a smooth fracture morphology is faster than a rough morphology. Velocities are usually higher in SCC, regardless of the morphology. This velocity difference is more important for the smooth morphology, where SCC local velocity points can be easily one order of magnitude higher than IHE velocities. The isolated point on the IHE graph corresponds to the merging of the main crack with a secondary crack ahead of it.

The velocities measured on samples B and C are low compared to sample A, with velocities below 500 μm/h. They are similar to the ones obtained in IHE, in group 3 (large embrittlement). The difference is in the fracture surface morphology: fracture is purely rough during SCC (Sample B) while it is a mixture of transgranular (roughness) and intergranular smooth during IHE. In addition, the local velocity increases during the test. This acceleration might be related to the fact that the sample spends hours exposed to the saline solution. Because this exposure is limited to the surfaces not protected by lacquer, the acceleration in Sample B and other changes towards a more brittle behavior are less important than in sample A, where there is no protective lacquer. Conversely, in some IHE cases, the crack can be completely arrested without a complete failure, with a progression in time towards a less brittle behavior, likely because of hydrogen desorption.

Finally, the SCC crack in humid air has an extremely low local velocity (2 μm/h). It is the lowest local crack velocity for a propagating crack in SCC or IHE tests. The plasticity involved is high (PDR around 4000), but it remains in the range of values found for SCC and IHE cracking.

Local propagation velocity and stress intensity factor

Figure 5.20 shows the local crack velocity as a function of the applied stress intensity factor (SIF) for SCC tests. No correlation is found. The SIFs measured at a local scale during crack propagation have not a clear effect on the velocity. Like for the IHE results, the SIF is not adequate to evaluate local effects, but it remains useful in the macroscopic analysis for crack initiation.

In Fig. 5.20, the SIFs are in a range between 9 and 26 MPa $\sqrt{m}$. The velocities are approximately in a range between $2x10^{-8}$ and $8x10^{-7}$ m/s. All the values are in the range of results reported in the literature for the same family of aluminum alloys for SCC in saline water (Fig.5.1a). [36][7]

In Fig. 5.20, most of the values are higher than 15 MPa$\sqrt{m}$. These SCC values are higher than those observed in the IHE group 3 (group large embrittlement), where SIF is 14 MPa$\sqrt{m}$ at maximum (see Fig. 4.15a of the IHE chapter). Instead, the SIFs for SCC in figure 5.20 are similar to the ones in IHE group 2 (group low embrittlement), as it is displayed in Fig. 4.15b of the IHE chapter.

However, there is an important difference in the magnitude of the crack velocities. The crack velocities for IHE group 2 are usually much lower than the ones in SCC (for the same range of SIFs). For example, the maximum crack velocity achieved for SCC is

around 3000 μm/h at 22 MPa$\sqrt{m}$. Conversely, the maximum velocity for IHE group 2 is around 100 μm/h at 24 MPa$\sqrt{m}$. In other words, very high velocities are present with a high K applied but for the IHE samples only slow velocities are observed with a high K applied. This might be interpreted as if a mechanical overload could not stop stress corrosion cracking: in IHE if K is increased, the crack blunts and stops.

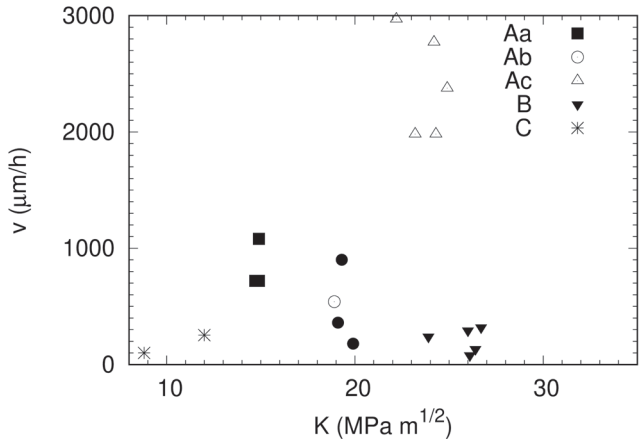

Figure 5.20: Local propagation velocity (v) for SCC as a function of the stress intensity factor (K). Empty symbols, represent intergranular smooth fracture advances, filled symbols (and stars), represent a rough fracture.

Incremental crack opening profiles

The incremental crack opening displacement (ICOD) profiles were obtained, as described in the IHE chapter. Every profile displayed comes from the correlation between two images during propagation. As mentioned before, the SCC pattern might not be stable in the crack tip's surrounding area, especially during heavy plastic deformation, generating some artifacts in the DIC analysis and in the ICOD profiles.

The figures 5.21 and 5.22 show representative ICOD profiles. The empty icons indicate a displacement that takes place at the back of the crack tip. Conversely, the filled dark icons indicate a displacement at the front of the crack tip (fracture process zone). The ICOD profiles in figures 5.21 and 5.22 have a similar shape to the ones introduced in the IHE chapter in figures 4.16, 4.17 and 4.18. The shape is either triangular, which means a constant rate of dislocation emission during propagation (Fig. 5.22 b third and fourth one) or rounded shape (Fig. 5.22 b second one) which means either an abrupt slowing down of the crack at constant dislocation emission rate or an increase of the dislocation emission rate. This is evaluated by measuring the ODR.

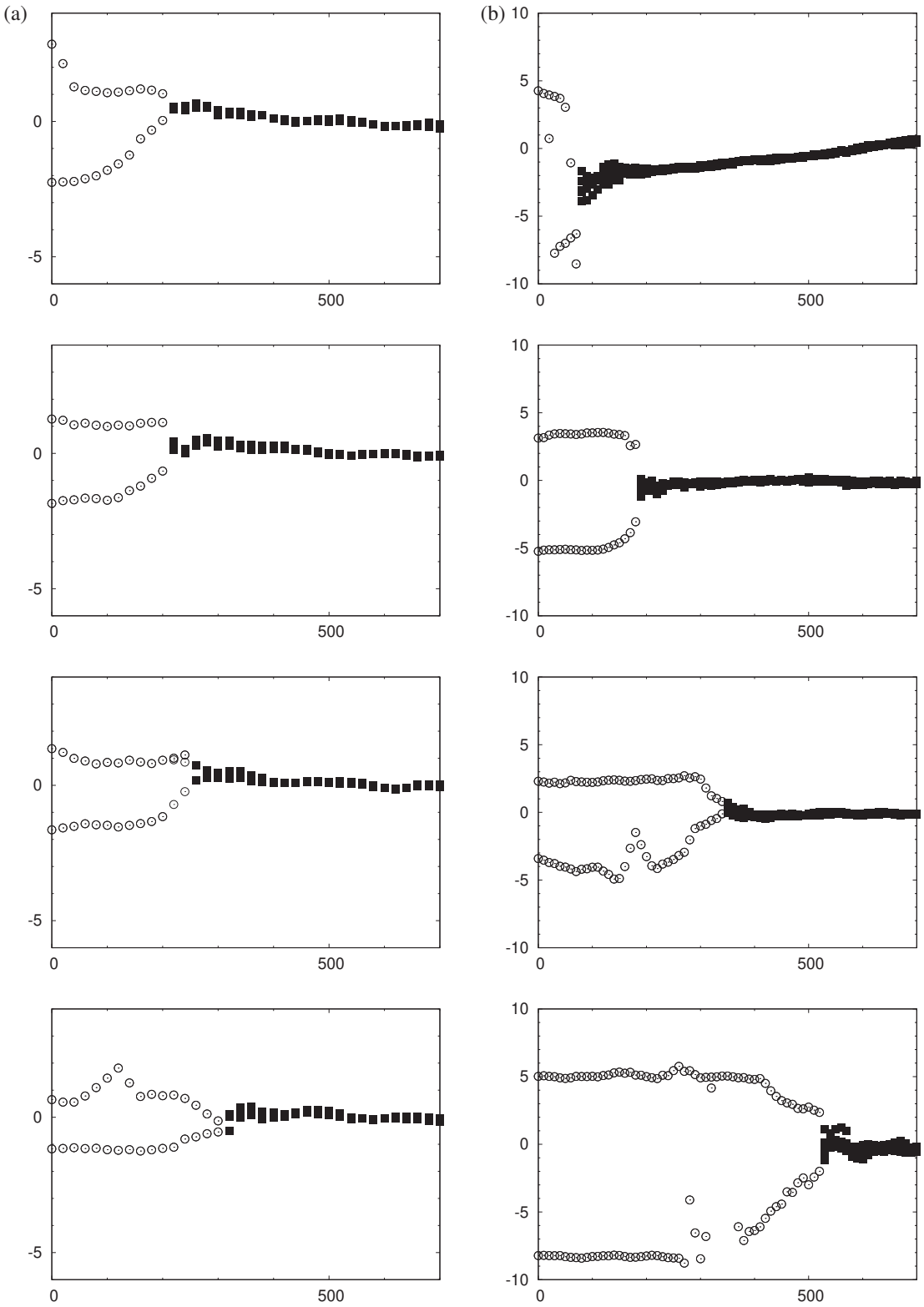

Figure 5.21: Crack opening profiles obtained from DIC: (a) configurations Ab2, Ab3, Ab4, Ab5 and (b) configurations Ac2, Ac3, Ac4 and Ac5 (see table 5.3). The magnifications were respectively x1000 and x2000. The scale compensates these differences and 10 px= 1 μm in both cases but the resolution is not the same. It is 1 displacement measurement every 2μm in (a) and one measurement every μm in (b). So, the precision on the profile within the FPZ is not the same, especially the distance between the points and the crack plane is higher in (a).

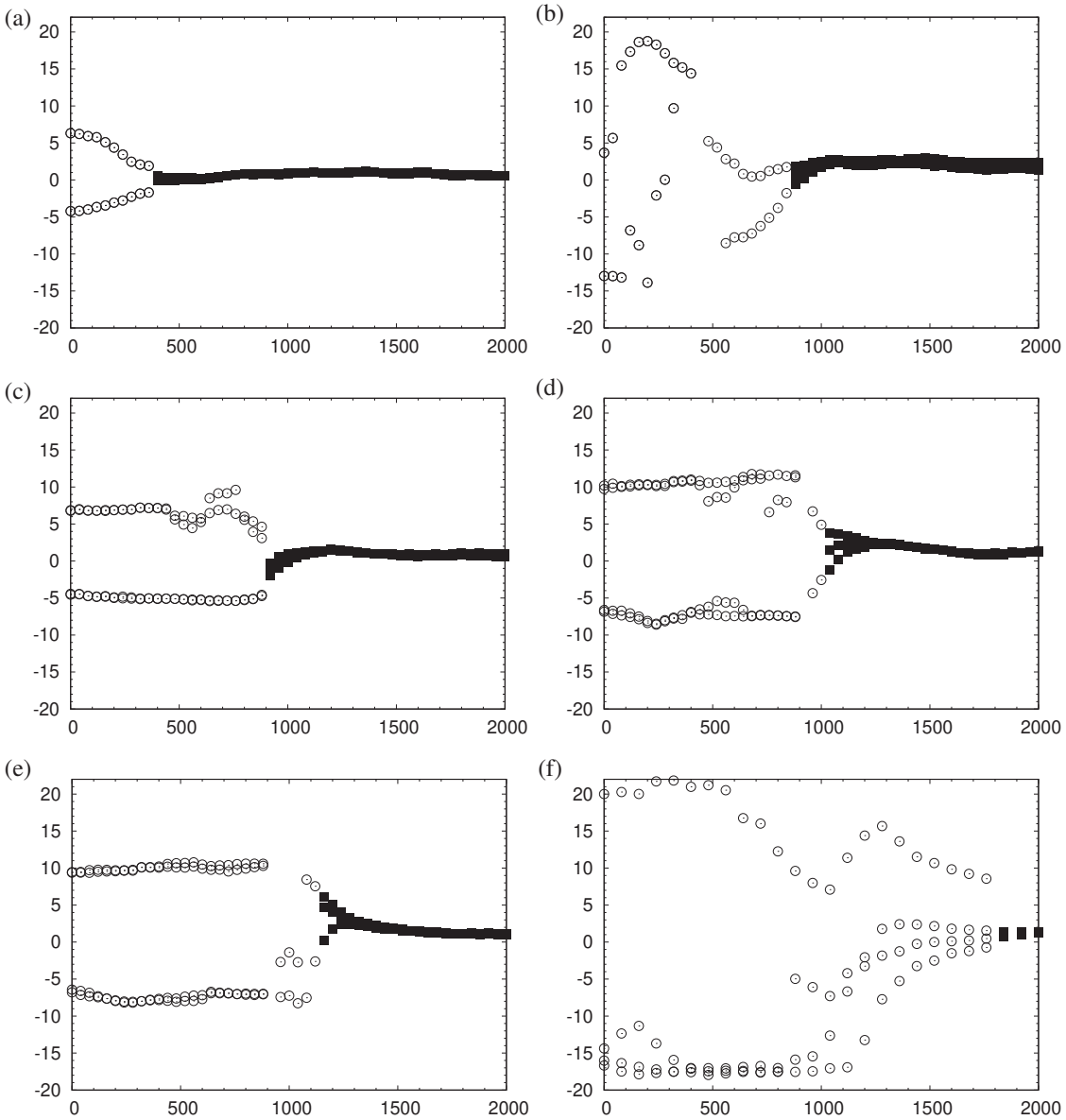

Figure 5.22: Crack opening profiles obtained from DIC: from (a) to (f) are shown the profiles corresponding to configurations B2 to B7 (see table 5.3). The magnification is x500. The scale of the figure compensates this low magnification and 10 px= 1 μm, but the resolution is low: one measurement every 4 μm. The resolution is divided by two in (f) because the surface was deformed and DIC difficult to perform.

In order to calculate the ODR, the magnitude of the displacement plateau $\Delta u_y c$ is determined from the ICOD profiles. The ratio between $\Delta u_y c$ and the crack advance Δa gives the ODR (Opening Displacement Rate, $\Delta u_y c/\Delta a$). Figure 5.23a is a plot of the ODR as a function of the local velocity. The filled symbols represent the "rough" fracture morphology, and the empty ones the "smooth" fracture morphology. The ODR range for SCC is similar to the one of IHE (Fig. 5.23b). In both cases, the ODR decreases with velocity and falls below 0.1 for the fastest cracks, similar to the PDR analysis (ODR and PDR are related, see Fig. 5.24). The fact that the velocities are so different while the amount of plasticity produced at the tip remains similar indicates that when the ODR falls below 0.1, neither the shielding nor the blunting limit the crack velocity. In this state, the rate-limiting process is not the plasticity and might be searched elsewhere, maybe in the concentration of hydrogen or its diffusion. These questions will be addressed in the next chapter.

Despite the perturbations in the DIC measurements caused by pattern quality, the ICOD profiles in Fig. 5.21 seems to be symmetric in most cases. Figure 5.21a is less precise than 5.21b because of the lower magnification during the observation (x1000). This loss of resolution might be why the opening located just in front of the crack tip (dark dots) falls drastically to almost zero. On the contrary, when using the highest magnification (x2000), the existence of the secondary plasticity becomes more clear. An example is the profile corresponding to Ac2 in Fig. 5.25. It is representative of the fracture process zone (FPZ) for the Ac segment. The fracture process zone length (Fig. 5.25) is about 40 px (approximately 4.4 microns), ending where the opening is negligible. This length is coherent with the reported value of Λ for Ac2, reported in Tab. 5.3 (4 microns), based on the magnitude of the Von Mises strain, and it also matches with the average Λ for the sample A. Besides, Fig 5.25 shows an approximate difference of 0.5 px in the displacement from the baseline is found in the first micron ahead of the crack tip. Consequently, an average deformation of 5% is estimated in the tensile direction, in the first micron from the crack plane.

In addition, Ac2 and Ac3 (Fig? 5.21b) present a rounded shape profile at the back of the crack tip. This round shape matches with higher ODR and PDR values and might be related to blunting. Besides, the triangular shape profile at the back of the crack tip is found in a wide range of ODR and PDR values. The triangular shape and the rounded shape are also found in the ICOD profiles for IHE in Figures 4.16, 4.17, and 4.18 from the previous chapter. In Fig 5.22 the precision is even lower (10 px = 4 microns). The lack of precision due to the low magnification, combined with the difficulties in the DIC pattern, result in some heavy distortions in the shape of the profiles in Fig 5.22b and d. However, in most other cases, the shape of the profile is obtained accurately.

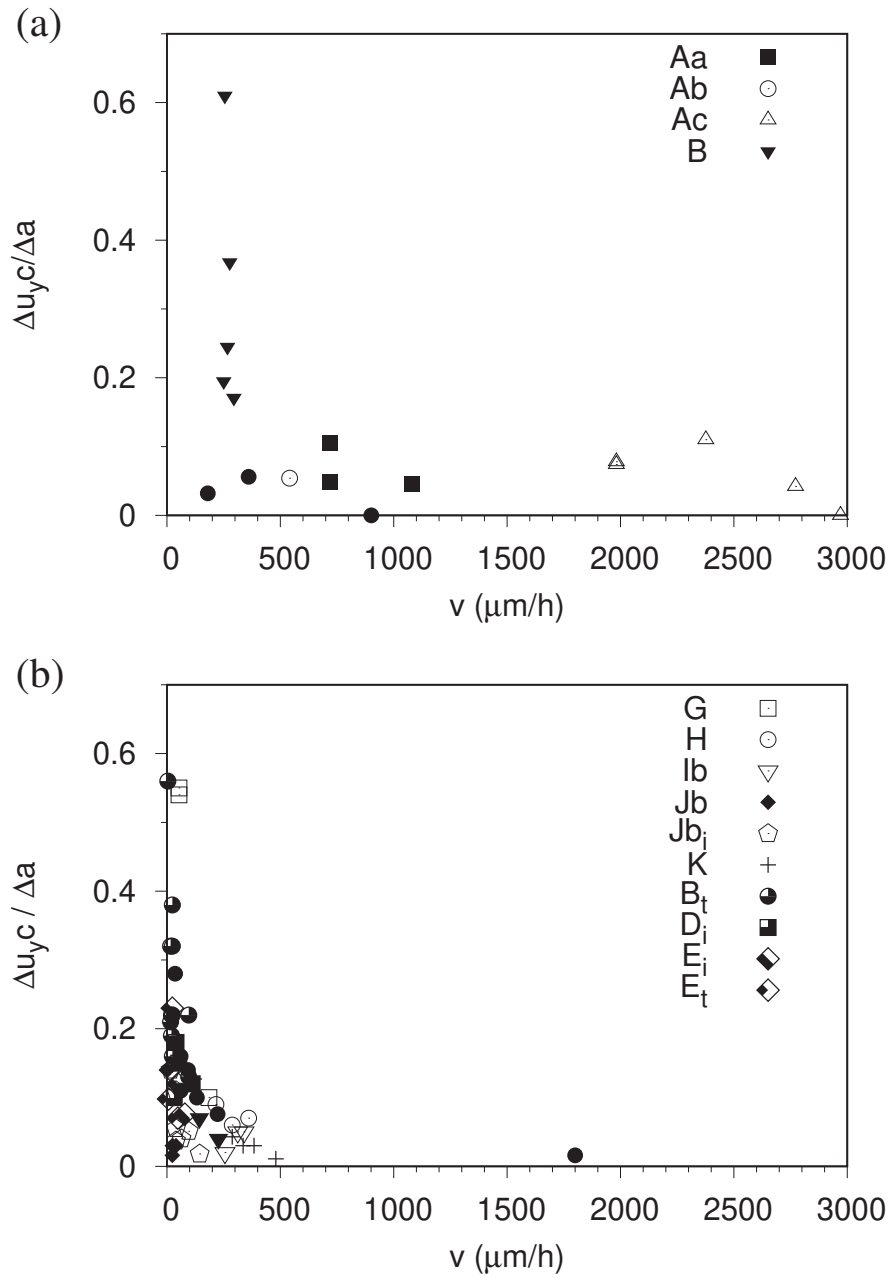

Figure 5.23: (a) Ratio $\Delta u_y c/\Delta a$, where $\Delta u_y c$ is the opening of the crack obtained during the crack advance of Δa, as a function of the local velocity for SCC. This quantity is called "opening displacement rate" (ODR) in the text. Empty symbols, represent intergranular smooth fracture advances, filled symbols, represent a rough fracture. (b) The same data in the case of IHE. The range of ODR values is similar but the velocities are faster in the SCC samples.

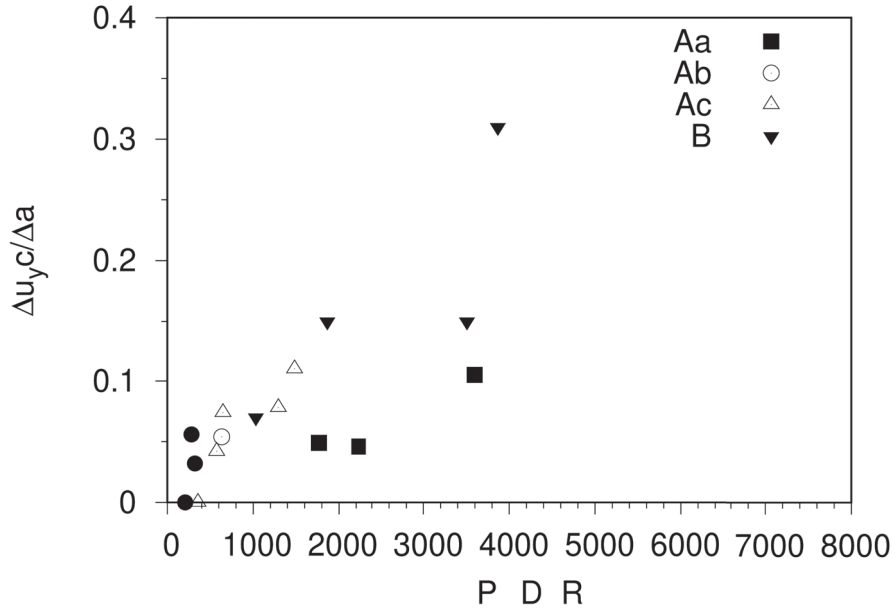

Figure 5.24: (a) Ratio $\Delta u_y c/\Delta a$ (ODR) as a function of the PDR. Empty symbols, represent intergranular smooth fracture advances, filled symbols represent a rough fracture.

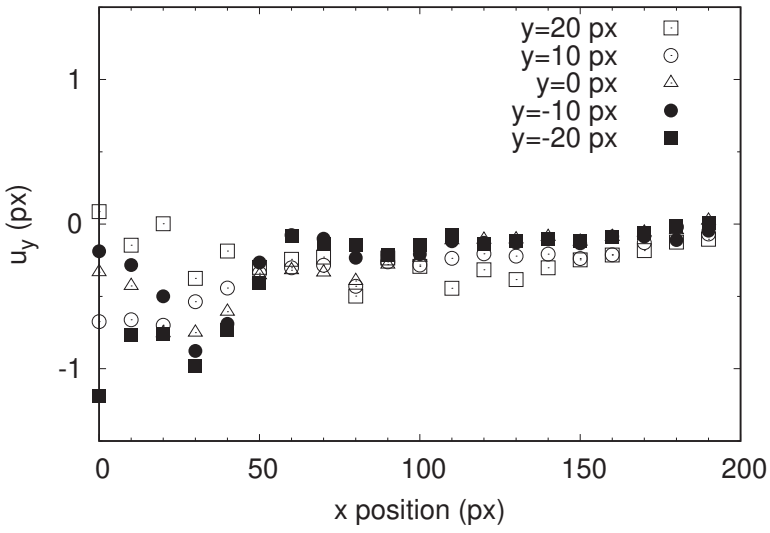

Figure 5.25: Opening profile (the part which is ahead of the crack tip) for the point Ac2. The fracture process zone is located in the first 40 px approximately

5.4.2 Intermittent transgranular fracture

An interesting phenomenon was observed in sample B: a transgranular crack propagation with the emergence of slip bands observable on the side surface with the optical microscope (Fig. 5.26). The slip bands appear on both sides of the crack, at a different angle with respect to the crack plane. They are marked with black arrows (resp. white arrows) in the lower (resp. upper) part of the crystal. The angles are approximately respectively -50 degrees and 15 degrees (the angles are orientated the usual way, i.e., anticlockwise within a reference frame with x in the propagation direction and y pointing upwards in the figure). The figures 5.26a,d, and g correspond to the points B4, B5, and B6 in table 5.3, respectively. Fig. 5.26b, c, e, and f correspond to intermediate DIC measurements.

From the perspective of modeling SCC, it is interesting to know if these slip bands correspond to crack arrests. For this, the crack position is determined with the following constraints: the time interval between two images is 3 minutes, the magnification is reduced to x500 in order to have a large field of view, which enables following the crack at night, in the absence of the operator. The lower magnification is also useful because the image conserves a focus that is acceptable during propagation. The slip bands appear on the side surface (the surface observed in the microscope) because they substantially modify the contrast. In particular, some pixels turn black. Therefore DIC becomes impossible in this region, precisely the interesting region to measure the blunting of the crack tip. Fortunately, there is a process zone that spreads ahead of the crack tip over several microns. It could be extrapolated to determine the crack tip position, but behind it, DIC could not be performed in all the areas affected by the slip bands. Finally, the grid size was decreased from 10 to 5 pixels to mitigate spatial resolution loss due to magnification reduction. The resolution is 2 μm. With a time step of 3 min, the local velocity's uncertainty is 44 μm/h.

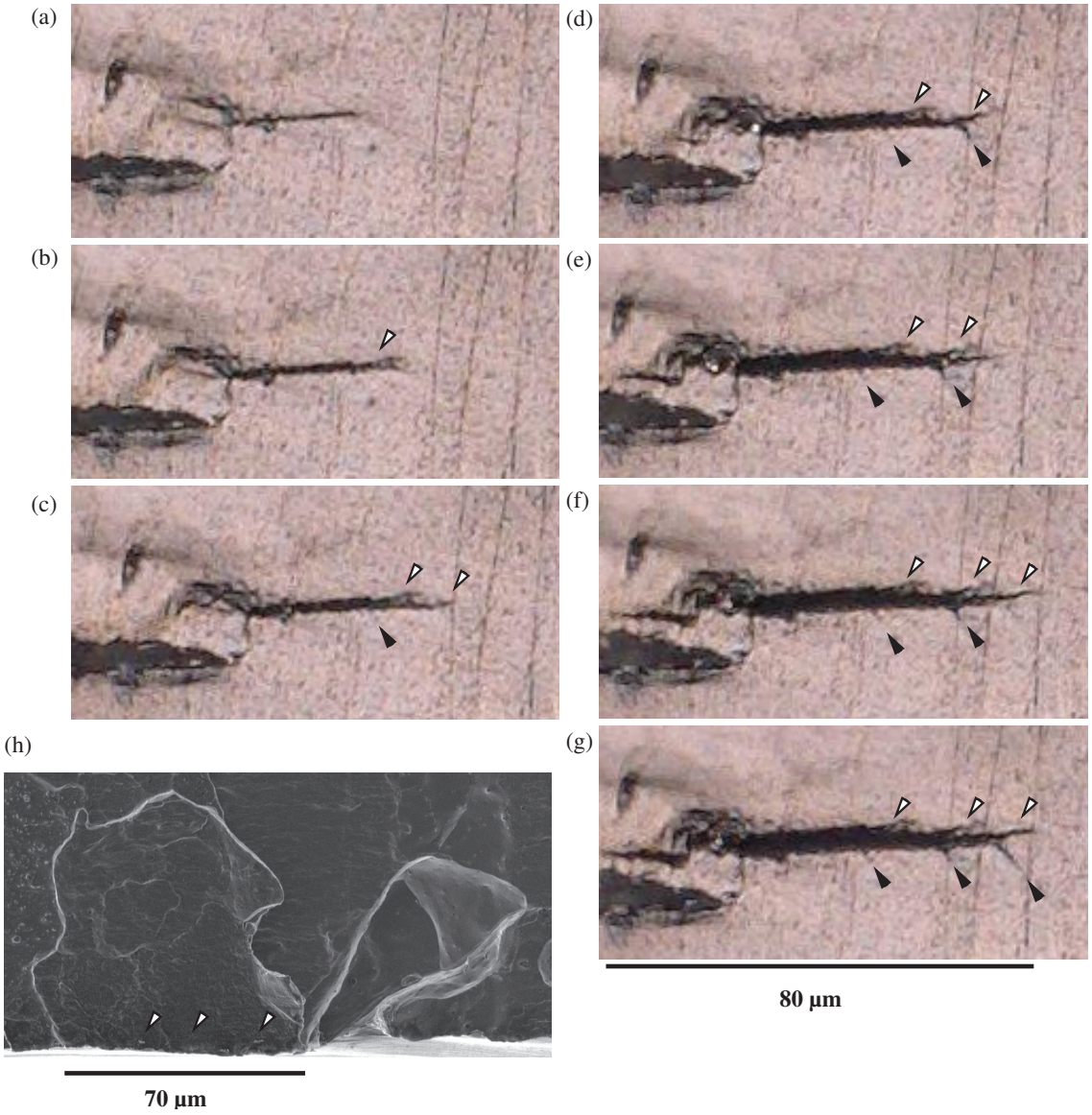

Figure 5.26: Sequence of pictures showing the details of the transgranular propagation of a crack in sample B. In (b) appears the first slip band (white arrow above the crack plane), the second appears in (c), and the third one in (f). The slip bands seem to be grouped in pairs (one above and one below the crack plane, the latter being represented by a black arrow). (h) Corresponding fracture surface, with crack tip positions (a), (d), and (f) represented by white arrows. The crack is stopped in (g), and the fracture surface shows that propagation continues to the right along an inclined grain boundary.

Despite these difficulties, the crack tip position, local velocity, and ODR were measured and are displayed in Fig. 5.27. It is difficult to establish a connection between the average velocities and the slip bands' apparition because the crack and the slip bands have the same contrast. DIC provides information concerning the crack tip position, and it is always backward from the end of the black line on the image. Therefore, the end of the black line is the trace of the upper slip band (the one which is almost parallel to the crack plane) and not the crack's end. There is also a lack of time resolution.

The average velocity captures a slow down between images (b) and (c), but the images already show a slip band in (b) and the apparition of two others in between (b) and (c). A fourth appears on image (d). We assume that the bottom and the upper slip bands are created simultaneously because the dislocations are emitted from the tip and are no longer emitted when the crack has moved away. Nevertheless, the slip band appears first in the upper part and later on in the lower part. We assume that the dislocation emission process is not instantaneous, and the intensity of the upper slip band reaches a value where it can be detected before the bottom one. Therefore, the blunting sequence has already started between the time of images (b) and (c) and finishes between (c) and (d), and when it finishes, the crack moves forward. The slowdown and the blunting (ODR goes up in Fig.5.27c) appear in between (b) and (c) in the figure 5.27b. In (f), the new slip band appears, and the crack is stopped and blunts (ODR goes up) between (f) and (g) where the last slip band is shown. Later on, the crack continues propagating after a massive plastic deformation (not shown). The fracture surface (h) shows that it is transgranular from (a) to (g) and then runs along an inclined grain boundary (which explains why it stopped in (g)). The analysis clearly shows that the time resolution is not enough to measure the crack arrest time, only its signature on the average velocity.

Nevertheless, these observations are interesting because they provide the crack opening displacement during a blunting / crack restart sequence. This information could be used within simulations to analyze the local stress ahead of the blunted tip to study how cracks restart. In the next chapter, this point is discussed, together with the time and spatial resolution issues about the design of surface patterns for DIC.

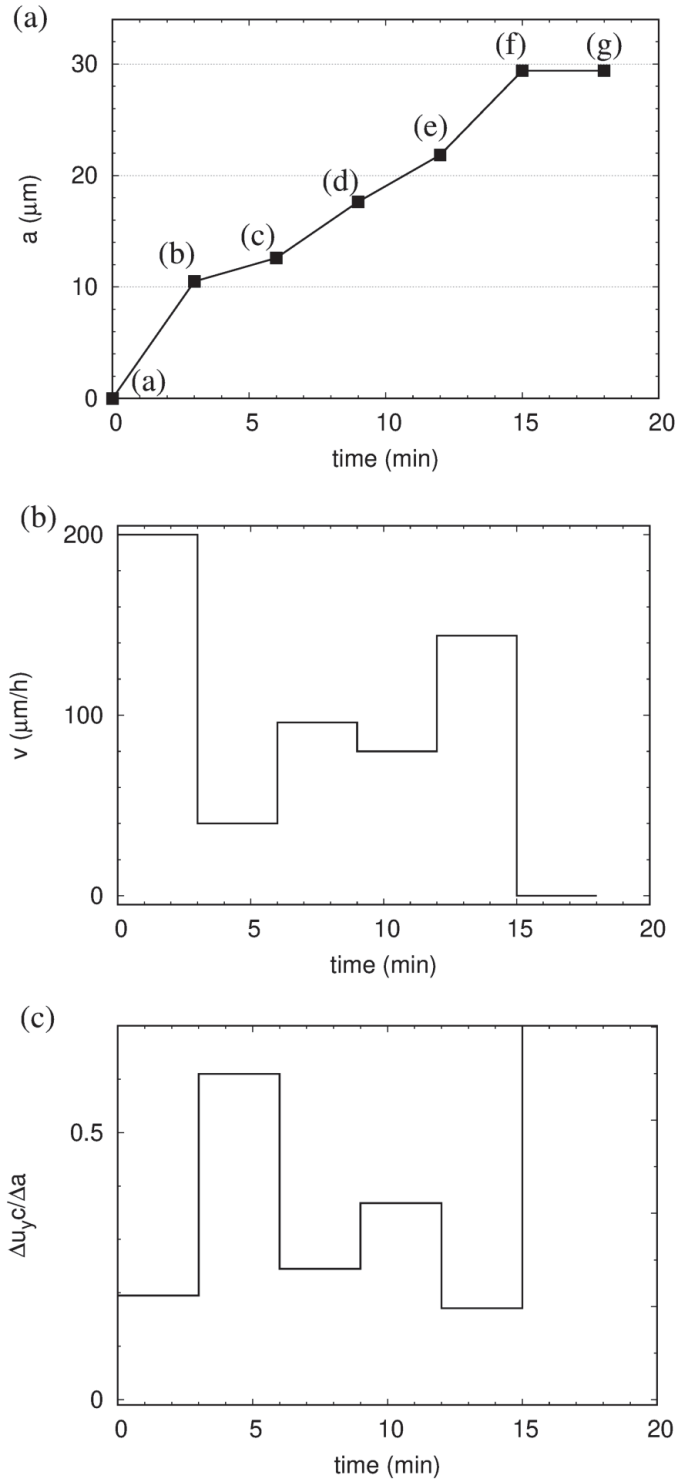

Figure 5.27: (a) Crack tip position as a function of time, (b) crack velocity as a function of time and (c) opening displacement rate, ODR ($\Delta u_y c/\Delta a$), as a function of time.

5.5 Summary

A SCC test in humid air was observed with a sample in T4 state. The susceptibility of the sample to humid air produces a crack propagation velocity that is extremely low (3 microns per hour). The crack propagation stops in the presence of argon (Ar) flow. The fracture surface is transgranular with evidence of plastic activity. Slip bands and plasticity ahead of the crack tip were found using DIC analysis at a local scale (Fig.5.7). Sample 0 has shown that a sample in AS state (as-received state, only sample not tested in T4 state) is not susceptible to SCC in saline water. The fracture surface of sample 0 is completely ductile, and covered with dimples (Fig. 5.13).

The SCC samples tested in saline water are split into two groups: group 1 and group 2. Samples machined by a milling cutting belong to group 1, and they are more sensitive than group 2 machined by EDM. The main results of the macroscopic analysis were summarized in the last part of the section 5.3.2 of this chapter.

An analysis at the local scale was performed in SCC group 2. Like the SCC in air and the IHE, two different kinds of plasticity were found, the primary plasticity in the form of two deformation bands, and the secondary plasticity that is confined just ahead of crack. The secondary plasticity for SCC (Λ and ϵ_{tip}) is similar to the IHE tests.

Crack propagation with low accompanying plasticity is found in an extensive range of velocities, from 50 to almost 3000 μm/h. The highest velocities always occur with low levels of plastic deformation rate. However, the slowest velocities can be developed also with low plasticity values. The smooth morphology is mainly associated to a fast rupture than the rough one. The PDR range coincides with the IHE tests, but the crack velocities are much faster when the SCC sample is not protected with lacquer from massive contact with the saline solution. A hyperbolic shape is seen in the graph of local velocity vs. PDR.

The calculated K is not directly related to the local values of plasticity or velocity. Very high velocities can be achieved with a high K applied. In the IHE cases only slow velocities are observed with a high K applied.

ICOD profiles were obtained despite the difficulties with the DIC pattern. The fracture process zone found in the ICOD is consistent with secondary plasticity observations in the DIC strain map. The tendencies stated with the PDR are confirmed using the ODR.

Finally, an intermittent transgranular fracture phenomenon was presented. A deacceleration with blunting followed by re-sharpening and with an increment of the velocity is produced. The emission of slip bands is assumed to occur during blunting, and the crack advance during sharpening. An improved spatial and time resolution is necessary to analyze in detail and confirmed this tendency.

Chapter 6

Discussion, conclusions and perspectives

In this final chapter, two aspects of the HE mechanisms are discussed: the hydrogen diffusion during crack propagation and the role played by plasticity in hydrogen embrittlement. In addition, a more technological aspect is also considered: the creation of an optimal surface pattern for DIC. But first, a recapitulation of the main results is made and confronted to the initial goal of the thesis.

The initial goal was to set up a micro-tensile test which allows the measurement of the crack tip position and plasticity at a scale lower than the grain size. The interest was to generate data that could be useful for developing a physically based model of crack propagation, i.e. based on the interaction of hydrogen with crystalline defects (grain boundaries and dislocations).

This goal was only partially achieved. In particular, the value of the stress intensity factor necessary for crack propagation is still completely in the range of the macroscopic tests ($K \approx 8$ MPa $m^{1/2}$), even when the thickness of the sample is reduced down to 200μm. Several attempts were made to unload the crack after propagation initiation and then reload it to find a new threshold, specific of the tip location. They failed: the critical mechanical load was always the same, independent of the grain boundary or the grain broken. Apparently, the thickness of the samples is still too large in comparison to the grain size to see the influence of the crystallography on fracture.

Furthermore, the results show that there is not a unique relation between the local velocity and the amount of plasticity generated at the crack tip (a crack can emit few dislocations and still move forward at a low velocity). Intuitively, at least in the intergranular case, it is expected that cohesion goes down, dislocation emission from the tip goes down and crack velocity goes up with an increase of H embrittlement. Atomistic simulations[91] have shown that, if the cohesive stress is not decreased enough, dislocation emission is massive and the crack stops. Therefore, it is not easy to understand, at this point, that a crack that moves forward with a low level of plastic emission and a high K, i.e. a crack which evolves in conditions where cohesion has been significantly lowered, can have a range of velocity between 50 and 500 μm/h. Maybe it is an indication that the polycrystalline nature of the sample involves a large heterogeneity of the mechanical load along the crack front. This aspect would be interesting to evaluate by decreasing

further the thickness of the samples. Another reason could also be that crack propagation is limited by very slow hydrogen diffusion. This point is addressed in the next section.

Finally, concerning the correlation between the fracture morphology and the velocity, it seems that transgranular fracture is slower than intergranular brittle fracture, but again slow intergranular cracks were also found.

So, it is difficult for the moment to interpret the data. Nevertheless, it is agreed that fracture occurs due to the contribution of three effects: (1) the external load (K), (2) shielded by the primary plasticity and (3) some time dependent phenomena responsible for fracture at the nano scale (fracture morphology is strain rate dependant, i.e. when the force is raised too fast propagation stops and the crack blunts). Time dependent effects may include (i) the dynamics of the formation of the plastic zone (that we divide in two contributions, primary and secondary, based on our results) [99, 64], (ii) hydrogen diffusion towards the fracture process zone and the redistribution between traps [65] and (iii) maybe other phenomena that are still under discussion (like H enhanced local creep[100], vacancy-hydrogen cluster formation and ordering [54], disconnections (GB steps with a Burgers vector) [101] or dislocation substructures [33]). Among these, the intense plastic activity in the secondary plastic zone has been intensively characterized by post mortem TEM [46]. In our experiments, no major difference was observed in the characteristics (deformation or length) of this zone in between slow and fast propagation. So, at the moment, there is no element to state that the secondary plasticity plays a major role in the determination of the velocity. Nevertheless, it is always present, so it could be a necessary condition to obtain fracture.

In spite of the complexity of the problems mentioned above, we can attempt to discuss the role of H diffusion and plasticity-grain boundary interactions from the bibliography and the results obtained. In the perspectives, some improvements of the set up, new experiments and simulations are proposed.

6.1 Hydrogen diffusion

In this section, hydrogen diffusion is discussed at two different scales. First, at the scale of the whole sample, the distribution of H after cathodic charging and also during the fracture test is evaluated by macroscopic diffusion calculations using effective diffusion coefficients and Fick's law. The hydrogen effective diffusion coefficient D_{eff} describes the diffusion of H as an interstitial atom in the lattice taking into account the trapping/detrapping from crystalline defects, precipitates... Therefore, it depends on the alloy and its metallurgical state. Young and Scully [102] have measured diffusion coefficients by isothermal desorption at moderate temperature and extrapolated the data to 25 °C. They obtained $D_{eff} = 10^{-11} m^2 s^{-1}$ for the alloy 7050 in the underaged state, a material which is similar to ours. However, it was recently demonstrated that the apparent diffusion coefficient is quite strongly influenced by the initial state of the system. For pure Al, $D_{eff} = 10^{-14} m^2 s^{-1}$ if the sample is free of hydrogen initially and increases to $10^{-12} m^2 s^{-1}$ when the sample already contains H[103]. This is interpreted as a concentration dependence, with a faster apparent diffusion when the traps are filled (i.e. when the average concentration is high). Note that in a previous study [74], in the same material as ours, H embrittlement was found to be coherent with $D_{eff} = 2 \times 10^{-12} m^2 s^{-1}$ and not with the slower effective diffusion

coefficients. The diffusion coefficient from Ai et al.[103] is the most reliable because it was determined at room temperature and not extrapolated from high temperatures. It has also been found independently by Hebert[103]. Therefore, we take $D_{eff} = 10^{-12} m^2 s^{-1}$ as a diffusion coefficient after the H uptake from the cathodic charging (assuming the traps are filled). This is a strong statement. We could consider the effective diffusion coefficient is $10^{-14} m^2 s^{-1}$, but then the uptake by diffusion would be limited to the first 100μm below the surface (Fig. 6.1, 6.2 and 6.3). It would not be coherent with the hydrogen affected depth which extends over the whole sample thickness, even when the thickness is 1 mm long. An argument sometimes found in the literature is that "dislocation transport" is the reason why H affects fracture deep in the material. In our case, the primary plastic bands are orthogonal to the side surfaces where H was generated and furthermore, they would transport H away from the crack propagation plane.

6.1.1 Hydrogen diffusion and crack propagation velocity

In a previous study, Ben Ali [77] measured the macroscopic propagation velocity during slow strain rate tests in the same material as the one studied here and in the same metallurgical state, but with different H charging conditions. He showed that the velocity depends on the strain rate. Strain rates of 1×10^{-5}, 1×10^{-6} and $5 \times 10^{-7} s^{-1}$, gave velocities of 45, 57, and 171 μm/h respectively, for intergranular brittle cracking. Our local crack propagation velocities are in the same range despite the different mechanical testing conditions. Dynamic fracture was simulated by Ben Ali [77] with a cohesive zone model coupled to elastic stress dependant diffusion. The initial conditions were a uniform concentration in the sample, and no desorption was allowed. First the crack was immobile and loaded just below the initiation of crack propagation. H diffuses and reaches an equilibrium where the neighborhood of the tip is enriched with H. Then the crack was overloaded at different values of K which produced different propagation velocities. The repartitioning of H was simulated. At low velocities, the hydrogen distribution is stationary and moves with the crack tip. At high velocities the hydrogen maximum concentration cannot follow the crack. Therefore, a critical velocity v_c could be estimated numerically beyond which hydrogen cannot follow the tip motion. For the two diffusion coefficient mentioned above for pure Al, Ben Ali found v_c was in between 5.4 and 180 μm/h for $D_{eff} = 10^{-14} m^2 s^{-1}$ and above 5400 μm/h for $D_{eff} = 10^{-12} m^2 s^{-1}$. Our local velocities are below 500 μm/h for internal hydrogen embrittlement. These values are all largely below the critical velocity for $D_{eff} = 10^{-12} m^2 s^{-1}$, and therefore fracture dynamics is not limited by diffusion.

This diffusion model does not take into account the trapping in the plastic zone. However, the primary slip bands do not affect much the material ahead of the crack tip (there is a large angular sector which is essentially free of dislocations), so the reasoning should be correct for internal hydrogen. On the contrary, in the stress corrosion cracking case, hydrogen comes from the crack surfaces behind the crack tip and therefore should diffuse to the crack tip through the primary slip bands. So, in this case, we cannot conclude without more elaborate simulations which would explicitly take into account the trapping by dislocations[14, 104].

6.1.2 Absorption and desorption of hydrogen

In both internal hydrogen embrittlement (IHE) and stress corrosion cracking (SCC) experiments, the duration of the exposure of the samples to the hydrogen producing environment is an issue. In IHE experiments, several charging times were used, all beyond 24h, with no clear influence on the embrittlement (table 4.1). The hydrogen concentration profile indicates the degree of homogeneity of the distribution of hydrogen in the sample, before crack propagation starts (see numerical estimations in Fig. 6.2). In SCC experiments, the sample is exposed to the corrosive medium all along the test, so there is a constant hydrogen production and uptake. The evolution of the global hydrogen content as a function of the exposure time, for the same class of alloy and the same medium (NaCl 30g/l) as ours, is given in [105] and shown in Fig. 6.4. It is interesting to see that the concentration increases fast during the first three hours of exposure which closely match the incubation time measured in our SCC tests (table 5.1). Indeed, in sample A, with a bottom side surface exposed to corrosion, an average propagation velocity markedly higher than in samples B and C was obtained. B and C were protected from corrosion, except for the notch. Furthermore, the crack velocity strongly increases with time in sample A. This is coherent with a continuous H uptake from the side surface, in addition to the uptake from the crack flanks themselves.

Finite elements analysis (FEA) were performed to estimate the H diffusion profiles using Fick's law and the two effective diffusion coefficients mentioned previously. The hydrogen concentration profiles were computed for the positions along the red line in a 2D model shown in Fig. 6.1a and in a 3D model shown in Fig. 6.1b.

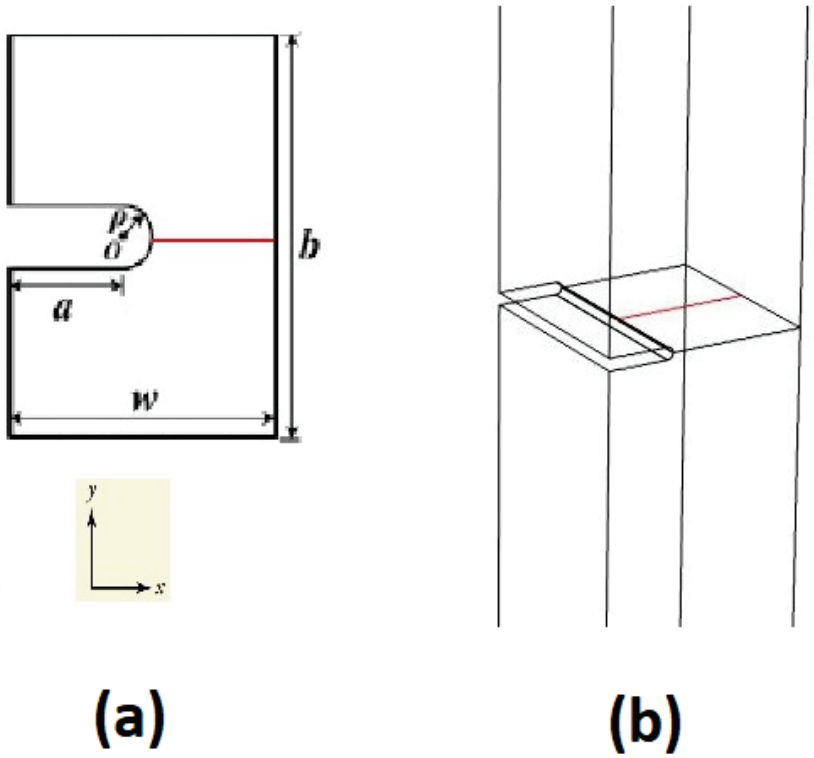

Figure 6.1: (a) 2D model and (b) 3D model of the sample showing the red line where the hydrogen profile is computed by finite elements.

Constant concentration boundary conditions are imposed on the surface of the sample. The hydrogen concentration at the surfaces is Cs=1 for simulating hydrogen uptake. It can be estimated that the concentration reaches 35% of Cs at the center of the sample after 12h of charging (Fig. 6.2), calculated by applying the moderate effective diffusion coefficient (D_{eff}) of 10^{-12} m^2/s. The hydrogen concentration increases sharply close to the surface where the hydrogen is produced. Therefore, a sample should be reasonably charged even at the center part of the sample before the tensile test starts (the minimum charging time used in our IHE tests is 24h). In our experiments, a typical stress corrosion crack has an incubation time of 3h and crosses the sample in less than an hour. The simulated profiles show that passed the center of the sample, the concentration increases, which might explain why the crack accelerates at the end of test. In addition, when a really conservative $D_{eff} = 10^{-14}$ m^2/s is used, the penetration is much lower, being 10% of Cs in the last 50 μm (Fig. 6.3). So, the acceleration of crack velocity is more unlikely in this scenario (this is another argument in favor of a relatively fast diffusion in our alloy since we do observe crack acceleration).

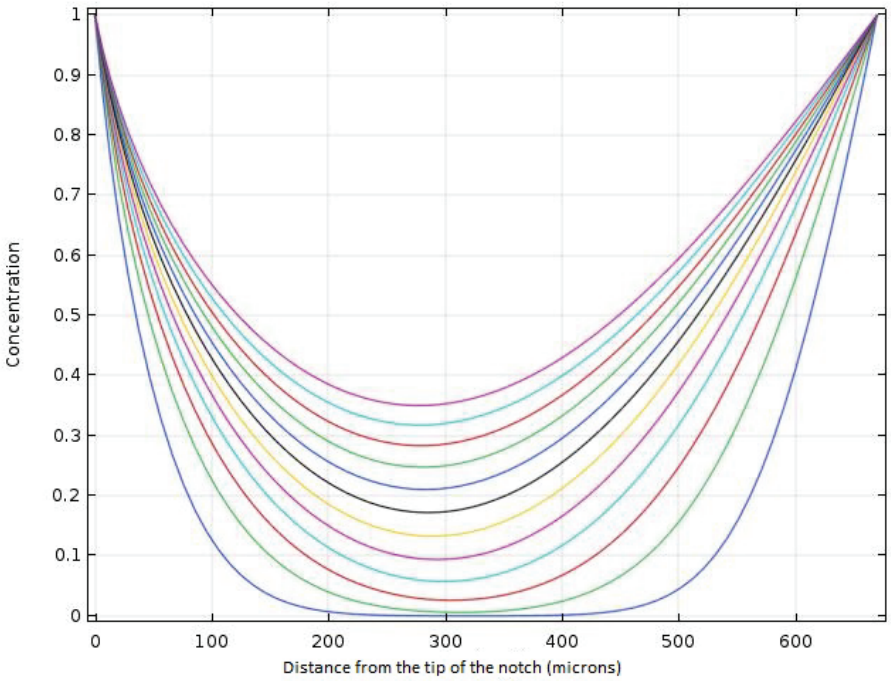

Figure 6.2: Hydrogen concentration profile along the red line in Fig.6.1. 2D model for H charging. Position zero is the notch tip location (30 μm radius). Moderate D_{eff} of 10^{-12} m^2/s. The blue line is the profile after 1-hour charging (Ci=0 at time zero). The concentration in the surface (Cs) is constant and equal to 1. The green line is after 2 hours of charging. The time step is 1 hour, and the upper purple line represents the profile after 12 hours of charging.

Conversely, in the IHE case, the samples suffer hydrogen desorption during the test. It could be a possible explanation of why towards the end of the test when the crack moves

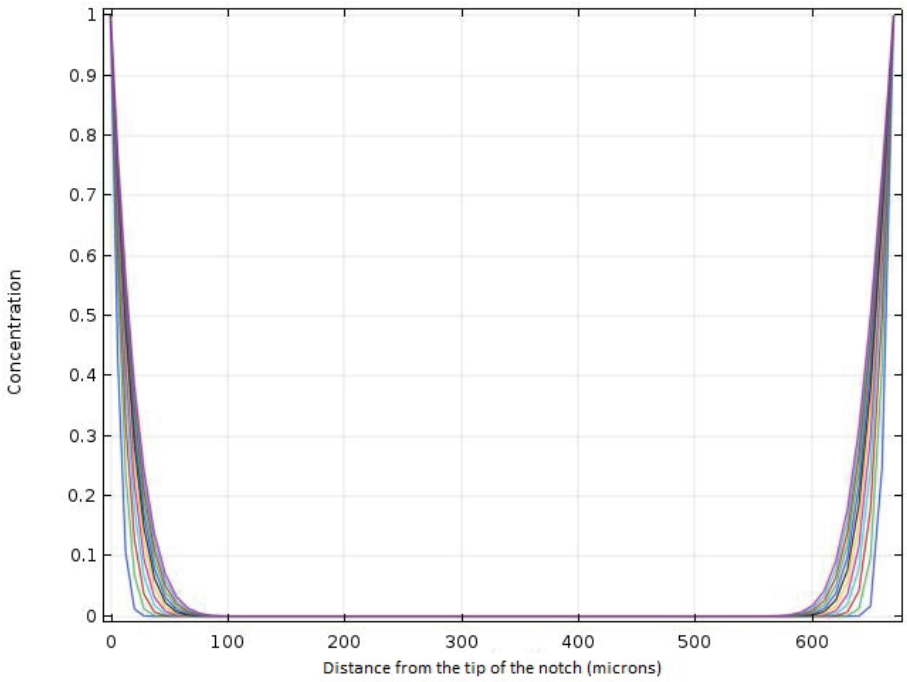

Figure 6.3: Hydrogen concentration profile along the red line in Fig.6.1. 2D model for H charging. Position zero is the notch tip location (30 μm radius). Slow D_{eff} of 10^{-14} m^2/s. The blue line is the profile after 1-hour charging (Ci=0 at time zero). The concentration in the surface (Cs) is constant and equal to 1. The green line is after 2 hours of charging. The time step is 1 hour, and the purple line represents the profile after 12 hours of charging.

closer to the end surface, the crack is often arrested or deflected, or excessive plasticity is created with secondary cracks. Samples of IHE Group 3 have the fastest propagation velocities among the IHE samples. In this group, the total duration of the test is 4 hours on average. FEA indicates that after this time, half of the hydrogen could be desorbed, and the profiles show a strong falling of hydrogen concentration close to the free surface (Fig. 6.5).

An interesting phenomenon was observed in the IHE Group 2, where average velocities are of the order of 25 μm/h. The crack is still propagating 10 hours after the beginning of the test. According to our calculations, approximately 15% of the initial hydrogen concentration remains at the sample center (Fig. 6.5). Hydrogen is depleted further in the vicinity of the free surfaces. However, after 16 hours of desorption, crack propagation is still observed while all the hydrogen should be almost entirely desorbed. This seems to indicate that there are traps which are still filled (irreversible traps) with hydrogen. Su et al. have proposed that plasticity could empty these traps (for example, we can imagine H is trapped into a shearable precipitate that is put back in solution by intense dislocations flow, therefore releasing the hydrogen it was storing). Su's theory is briefly summarized in the next paragraph.

Su and others claim ([68][64] [65] [70] [67] and Chap. 2) that under IHE in 7XXX

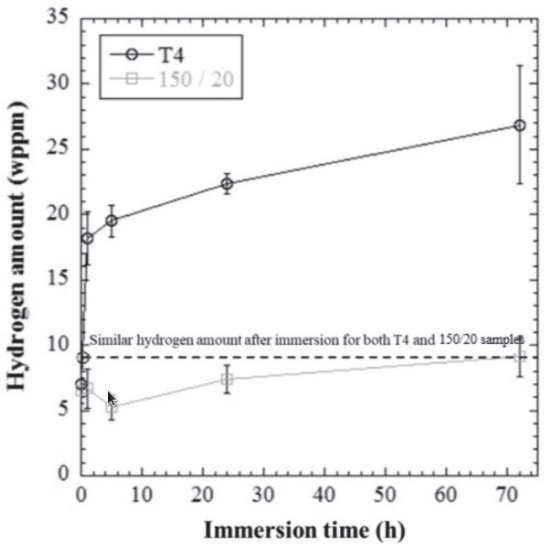

Figure 6.4: Time evolution of the hydrogen concentration after exposure to NaCl 30g/l of a 2 mm thick sample of alloy 7046[105]

alloys, the hydrogen can be partitioned among traps. Hydrogen can diffuse to the crack tip because of the hydrostatic strain gradient. Moreover, accompanying plasticity during propagation, especially in the crack tip region, promotes this repartition of hydrogen in grain boundaries and other traps and induces crack growth. This can explain propagation after a major desorption of the "free hydrogen". Shimizu [68] could not accurately determine the accompanying plasticity due to DIC resolution problems in the strain measurements. Shimizu[68] suggested (from "crack opening displacement" analysis) that strain needs to be localized to initiate crack propagation and that sharp cracks grow along the strain-localized region.

We confirmed the speculation of Shimizu[68] by overcoming his spatial resolution issue, and we clearly showed the presence of accompanying plasticity (the one we call "secondary plasticity") with a crack propagating in a pathway that is previously deformed. We have been also able to quantify this plasticity ahead of the crack tip using the DIC analysis.

In addition, we have made experiments that prove that H can be deeply trapped in our material, but still cause embrittlement. Two samples where cathodically charged and then heat treated at 400°C for one our. After this heat treatment, the samples where broken in traction at $\dot{\epsilon}_0 = 2 \times 10^{-5} s^{-1}$ in air. The fracture surface was more than 50% brittle. Our results are also consistent with the data reported by Bhuiyan and others [62] of 7XXX samples exposed to heat treatments to promote desorption after H charging, but the hydrogen remains in the sample causing degradation of the mechanical properties.

Hydrogen desorption is a major concern when designing experiments with reduced thickness. It seems that the electrochemical charging procedure used is capable to produce deeply trapped hydrogen that can embrittle the material. This opens us the possibility to perform internal hydrogen embrittlement experiments on samples thinner than 200μm.

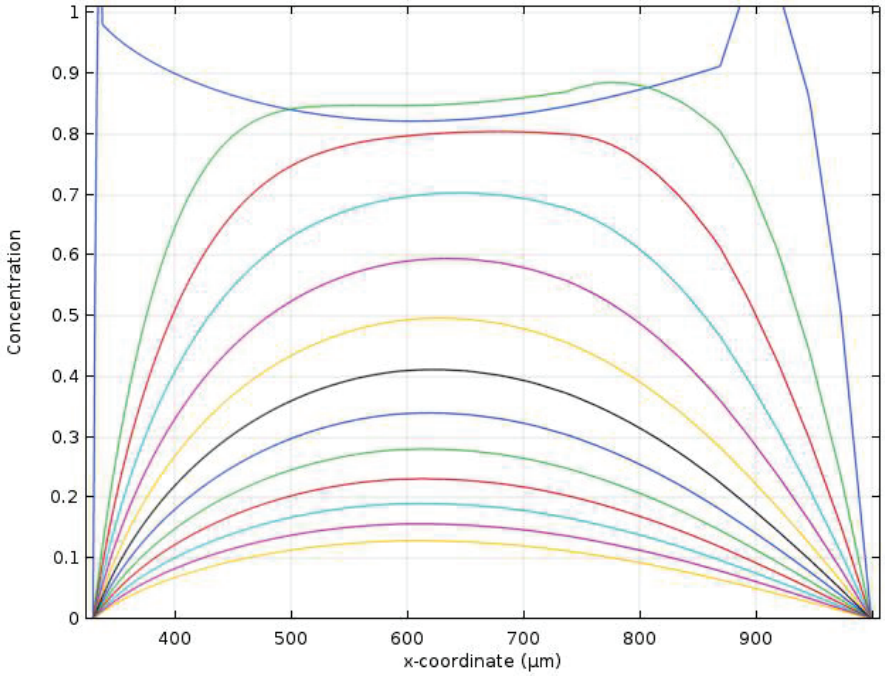

Figure 6.5: Hydrogen concentration profile along the red line in Fig.6.1, using a 3D model for desorption under 100 MPa (elasto-diffusive model) from "full charged" (Ci=1). The position x=300μm is the notch tip (30 μm radius). D_{eff} of 10^{-12} m^2/s and 0.5 mm thickness is chosen. The concentration in the surface (Cs) is constant and equal to 0. The blue line is after 15 minutes of desorption. The green line is after 1 hour, the red line after 2 hours, and it continues with a time step of one hour until the golden line that is 12 hours after desorption.

6.2 Plasticity - grain boundary interactions

In this section some additional mechanisms involving the contribution of plasticity to the embrittlement of the grain boundaries are discussed. There is an interaction between the dislocations and grain boundaries (GBs). This interaction might diminish the GB strength, and it can play an important role in intergranular failure in the presence of hydrogen. According to the HELP mechanism (Chap. 2), the presence of hydrogen enhances dislocation mobility and slip localization. Our experiments show regions of localized plasticity thanks to the DIC analysis. Intense slip bands are observed during crack propagation in SCC and IHE. Different possible interactions between the localized deformation and the grain boundaries were reported in the literature [33][52] [51][42], and mentioned in Chap.2. We will use the following three classifications strain transmission ("transmission"), strain blockage ("blockage"), and strain transfer along the grain boundary ("along GB"). The transmission is when the deformation band changes its direction and angle when it crosses a GB (a new slip system is activated). The second classification is "blockage". The deformation band is stopped at a GB (or it crosses the GB with important loss of intensity). It might involve an accommodation of the dislocations in the GB. The third classification is "along GB". The strain can be transferred along the grain boundary (maybe producing cross-slip onto the grain boundary plane). The strain can also be transmitted again after being transferred along the grain boundary. All these interactions in the presence of hydrogen can produce a combination of HELP and HEDE mechanisms, causing an important loss in the cohesive strength of the GBs (H could be accumulated in the GBs) and producing hydrogen embrittlement [33].

The strain "transmission", "blockage" and "along GB" interactions were observed in our DIC analysis in IHE. Many more interactions between localized deformation and GBs could also occur on a lower scale, beyond our resolution. Figure 6.6 shows a crack propagation sequence (Jb2 Fig. 6.6 a and Jb3 Fig.6.6 b) in the IHE Group 3 (table 4.3). The images in Fig. 6.6 are in greyscale due to the DIC analysis. The von Mises strain is overlapped with the pictures. Some grain boundary locations are revealed during the chemical attack in the H charging procedure. The events of "blockage", "transmission", and "along GB" are indicated with red arrows in Fig. 6.6.

In addition, a colored picture of the final fracture at the end of the Jb sequence (after Jb8) is shown in Fig. 6.7 a. Also, an EBSD map of the region was performed before, and is included in Fig. 6.7b. It can be seen that after the two marked "along GB" interaction in Fig. 6.6 b, a failure is produced later Fig. 6.7a, a secondary crack in the bottom part (where "along GB 1" took place) and in the upper part the failure (when it took place "along GB 2") is part of the main crack, even when it concerns a grain boundary not completely favorably oriented (i.e. not perpendicular to the tensile force).

All these evidences support a HELP contribution in our fracture process, not only in the intergranular failure but maybe also in the transgranular (TG) failure. A fracture along the slip bands parallel to GB is a possible explanation for our TG fracture mode. A systematic study with a high-resolution EBSD, and full characterization of the grain boundary, using a stable and high-quality DIC pattern, could help elucidating this question. Moreover, with the appropriate surface pattern, a similar study could be performed in SCC.

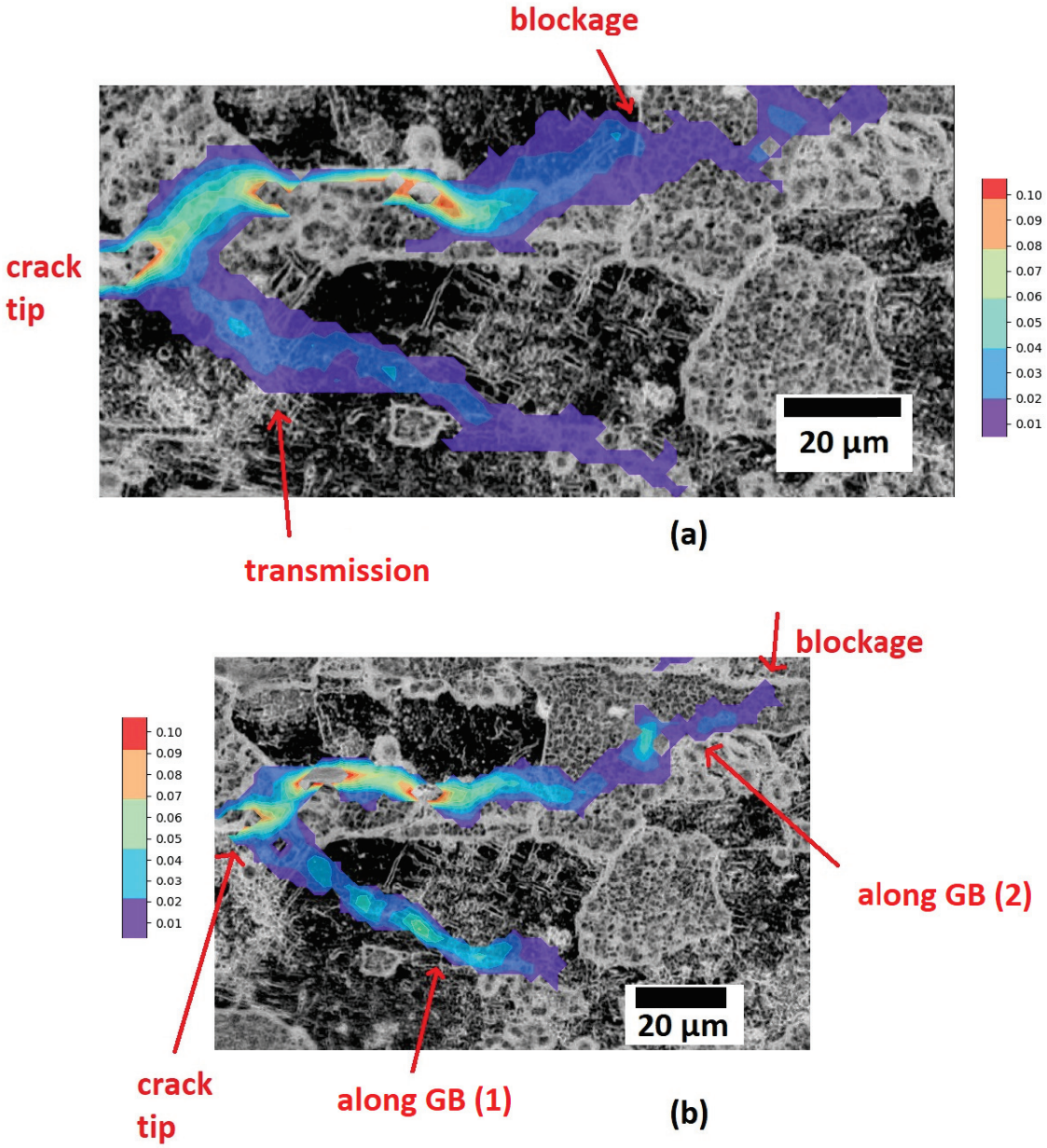

Figure 6.6: The Von Mises strain field calculated from the DIC displacement field is shown. It is overlapped with the deformed image after the crack advance (a) Jb2 and (b)Jb 3 in table 4.3. The interactions of the localized strain with the GBs are signaled with red arrows.

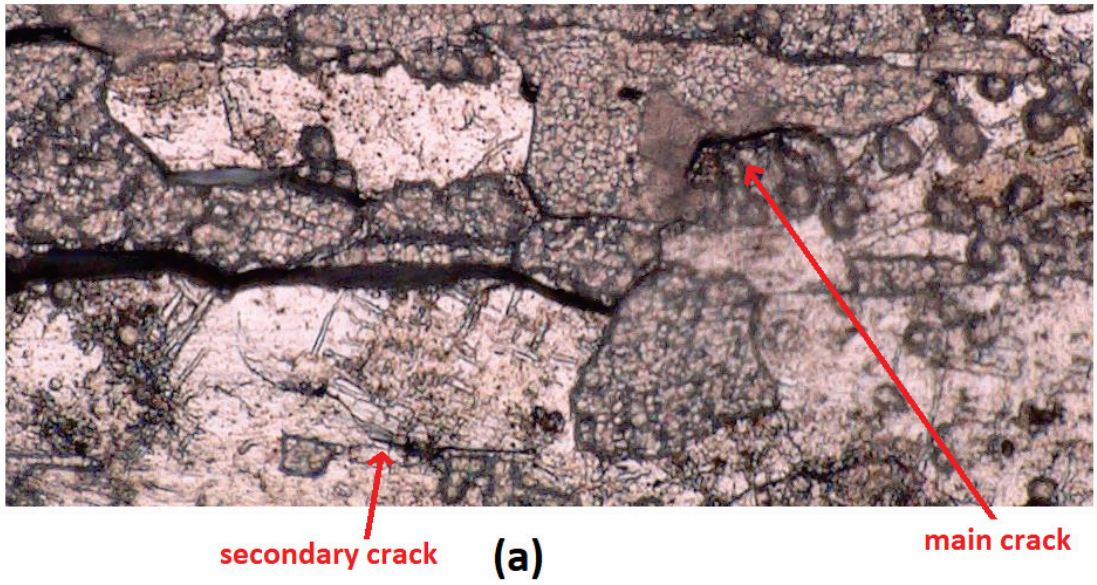

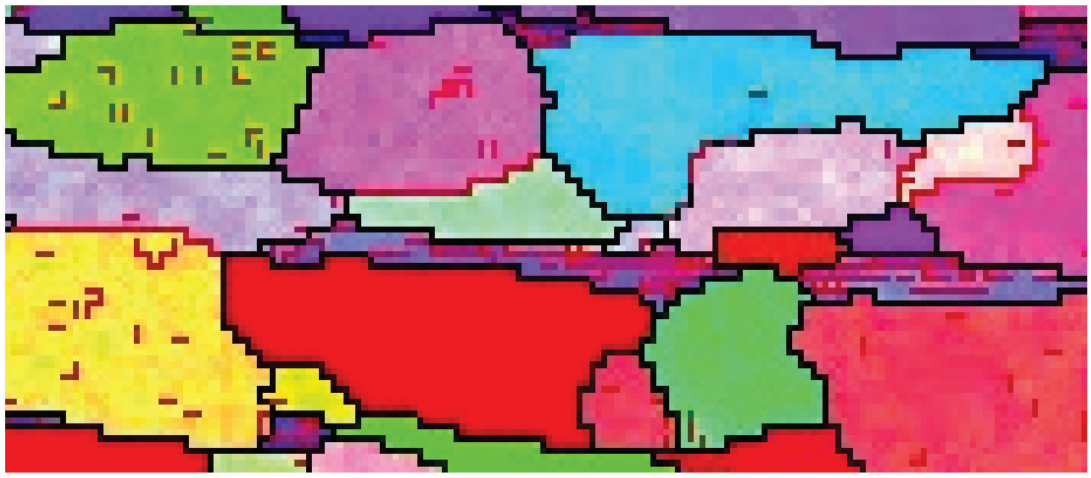

Figure 6.7: (a) Optical microscope image (×1000) of the final fracture after completed the sequence Jb. (b) EBSD map (produced before H-charging) of the the region where cracking was produced in (a)

6.3 Optimizing the surface pattern for DIC

The goal of this section is to discuss how to obtain surface patterns that could be used to perform DIC under an optical microscope at the maximum magnification of $\times 2000$ and within an SEM at higher magnifications.

Three patterns were tested. Pattern 1 is obtained by polishing the surface. The contrast comes from different phases in the aluminium matrix which appear colored on a white background in the optical microscope (in light transmission mode). Pattern 2 is obtained by exposing the sample to a cathodic potential in H_2SO_4, during the hydrogen charging process. Pattern 3 is obtained from nanoparticles. Pattern 1 showed its limitations during the SCC tests. Essentially, the density of particles is too low for a magnification of $\times 2000$ and the emergence of slip bands on the surface creates a shadow which does not allowed the images to be used for DIC. Furthermore this phenomenon is very intense in the vicinity of the crack tip where the determination of the displacement field is the most interesting. Finally, there is almost no contrast in SEM.

The contrast in pattern 2 comes from the dissolution of the surface (Fig. 6.8) during the cathodic polarisation. There is a strong tendency to pitting corrosion during this process. When it was used for the internal hydrogen embrittlement study, most of the images where not appropriate for DIC when the crack entered regions that were too pitted. As a consequence a lot of information from the experiments were lost simply because full portions of the crack propagation coud not be exploited. For the same reason, the time resolution was not very good. Duration and polarization were optimized to reach a good compromise between the contrast, the size of the corrosion features and the pits. The result is shown in Fig. 6.9. The optimum is $E_c = -1500\text{mV/SCE}$ for 17 hours. The pattern obtained was used to image strain localization in a tensile test, without notch. The sample was heat treated again (400°C for 1 hour and water quenched) after the pattern was created to desorb the hydrogen introduced. A typical strain map is shown in Fig. 6.10. It corresponds to an average deformation of 8%. The deformation is heterogeneous with some grains more deformed than others. The red regions correspond to glide at the level of the grain boundaries. The resolution for the displacement field is 2μm for this image. Very fine details, like slip bands, that could be useful to understand hydrogen damage are not resolved. A drawback of this procedure is that hydrogen cannot be fully removed. Indeed when the samples were strained to complete fracture, the elongation was reduced from 30% (the elongation in the absence of H pre-charging) to 20% and the fracture surface showed that more than 50% of it was affected by hydrogen. Some regions were intergranular brittle.

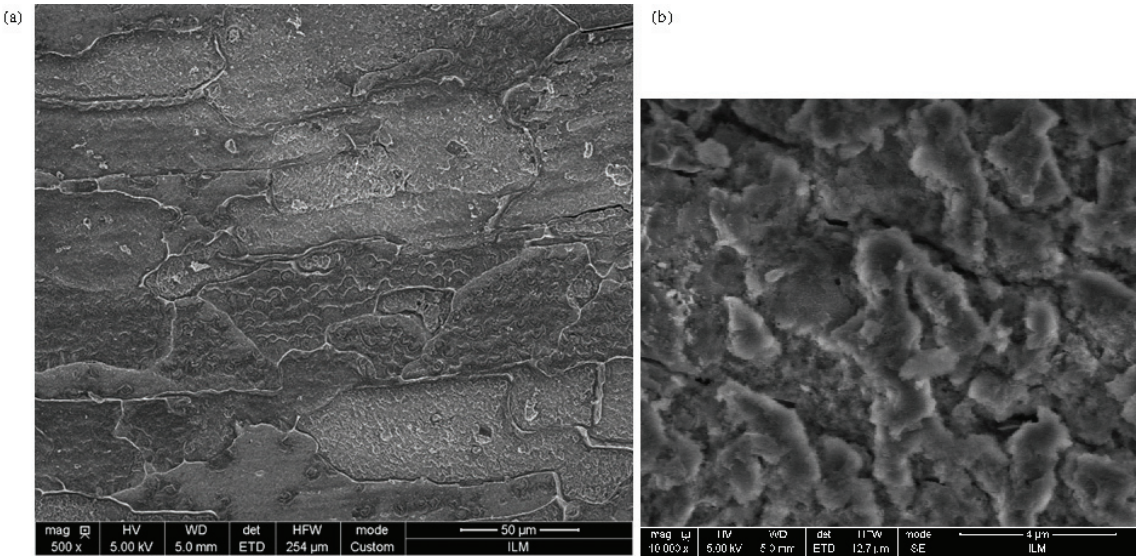

Figure 6.8: Pattern created by the H charging procedure (-1500 mV/SCE for 72h in H_2SO_4) viewed in the SEM. (a) and (b) are two different magnifications.

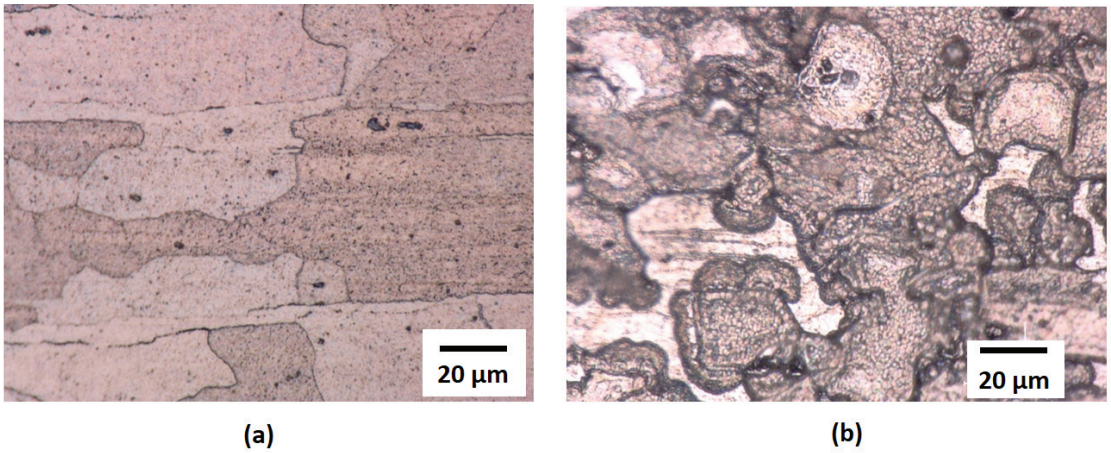

Figure 6.9: Optical microscope images (×2000) (a) State surface after 1500 mV/SCE for 17h and (b) 1500 mV/SCE for 48h

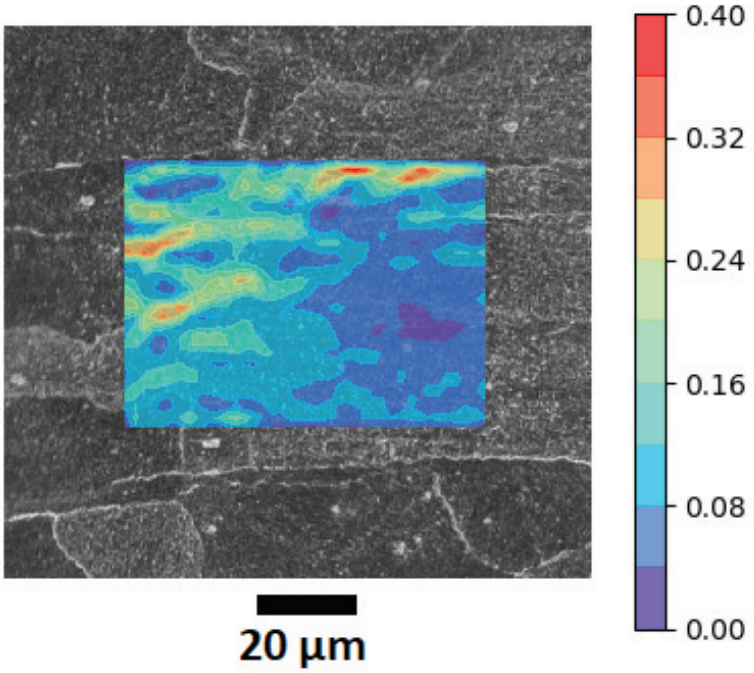

Figure 6.10: Von Mises strain obtained by DIC during a tensile test overlapped in the deformed image (elongation 8%). The image is in gray scale ×1000 (10 px step size = 2 μm). Several regions of the sample were also mapped at different magnifications.

A third method was tested with the goal to: not deteriorate the sample, have a high enough resolution, be efficient within an SEM and under the optical microscope (especially to perform SCC). Gold nanoparticles were chosen because they are produced at the iLM by different techniques. "Pulsed laser deposition" followed by laser induced dewetting was used because it offers a wide choice of particles sizes (from a few nanometers up to several hundreds of nanometers). There are multiple parameters to optimize during the deposition part and the dewetting part to obtain gold nanoparticles of the right size, shape, dispersion, and density. The parameters scanned are the thickness of the initial deposit layer, the energy of the laser shot for the dewetting and the number of shots. Dewetting depends on the substrate, it means that the nano particle size and distribution are materials dependent. An example of the distribution of sizes obtained is shown on Fig. 6.11. In this case, the size distribution is bimodal which could be interesting for performing DIC at two different magnifications. Another example is shown of Fig. 6.12 and 6.13 where the same sample was imaged under the optical microscope at $\times 2000$ and in the SEM at the same magnification for comparison. The nanoparticles produced seem to be appropriate but have not been tested with an applied strain under the optical microscope yet. First tensile tests under SEM (Fig. 6.14) with non-embrittled samples without notch were performed.

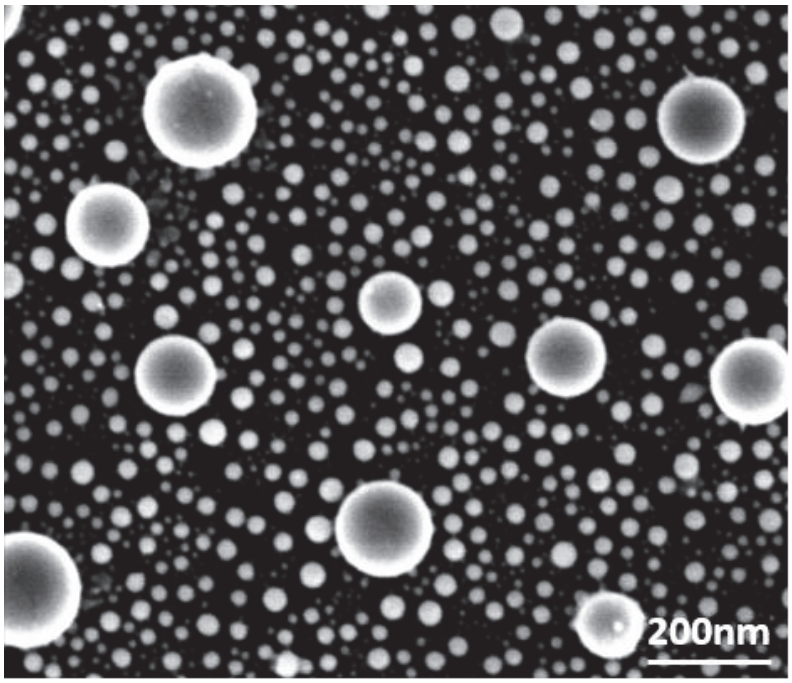

Figure 6.11: SEM imange of gold nanoparticles obtained by laser induced dewetting on the surface of AA7108 alloy.

The gold nanoparticles pattern under SEM observation at x5000 is shown in Fig. 6.15a (bright circles). The sample was not H charged. A DIC analysis during the tensile test is also displayed in Fig. 6.15b. The average elongation in the tensile direction measured by

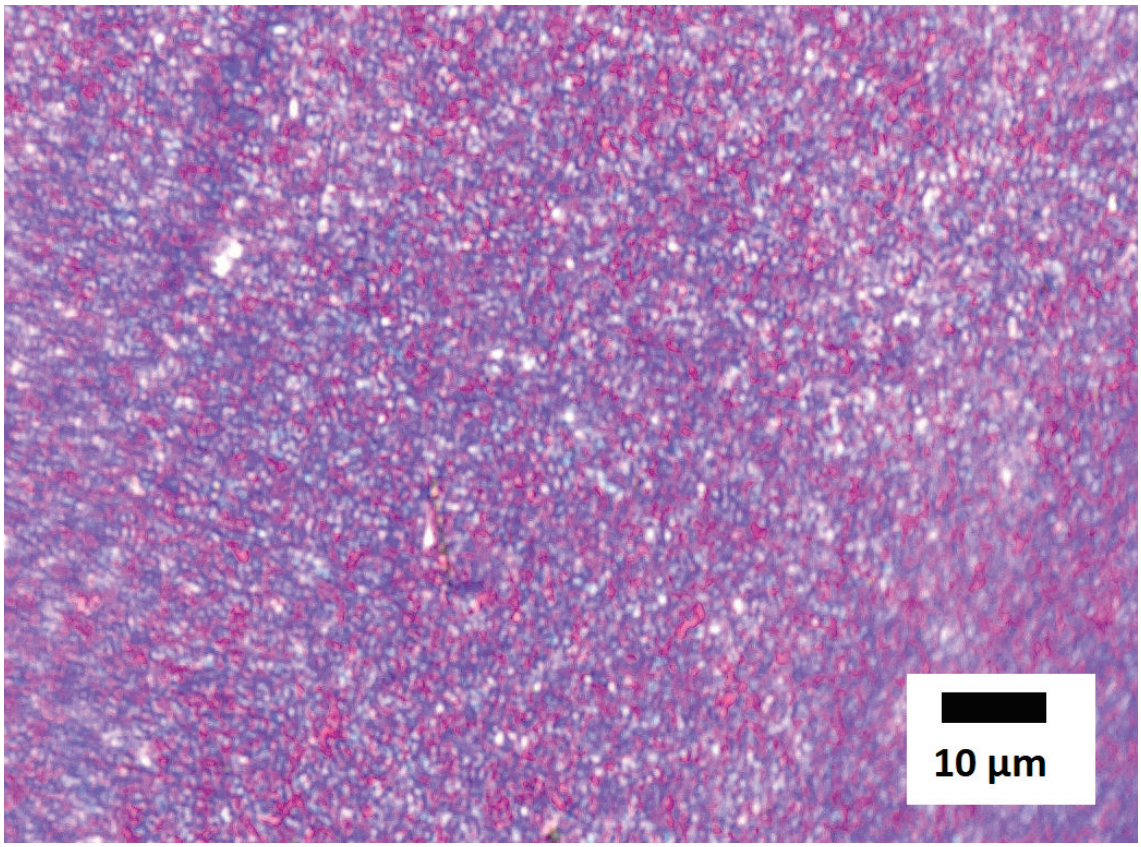

Figure 6.12: Gold nanoparticles pattern in an optical microscope (×2000)

DIC is in agreement with the elongation measured with the extensometer (1.5%) of the tensile machine, confirming the efficacy of the pattern. However, more local details, such as local deformation bands, could not be observed. Further work needs to be done. Our main concern are the distortions of the images which come from the SEM itself and are currently under study.

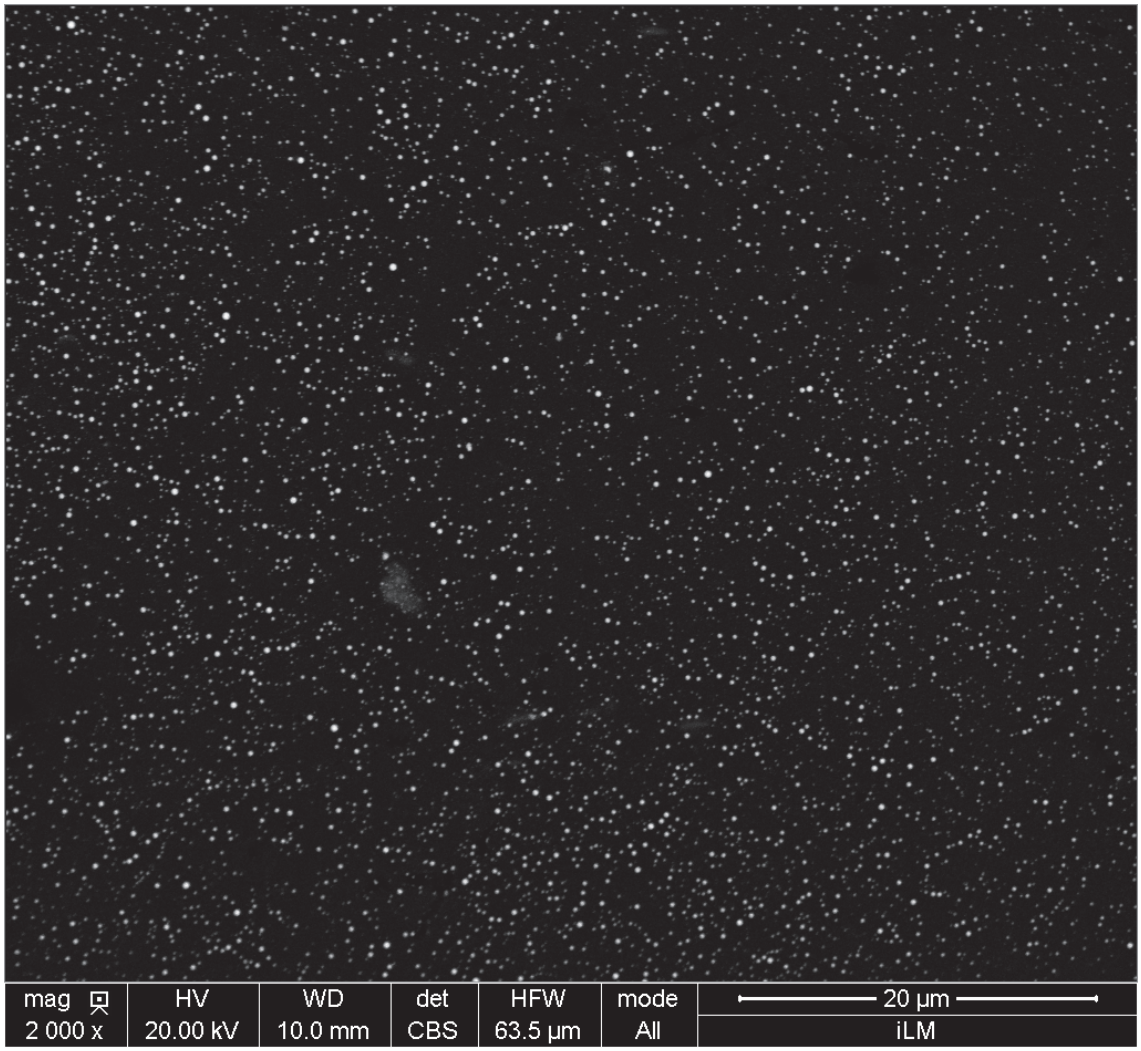

Figure 6.13: SEM image of the gold nanoparticles pattern (×2000)

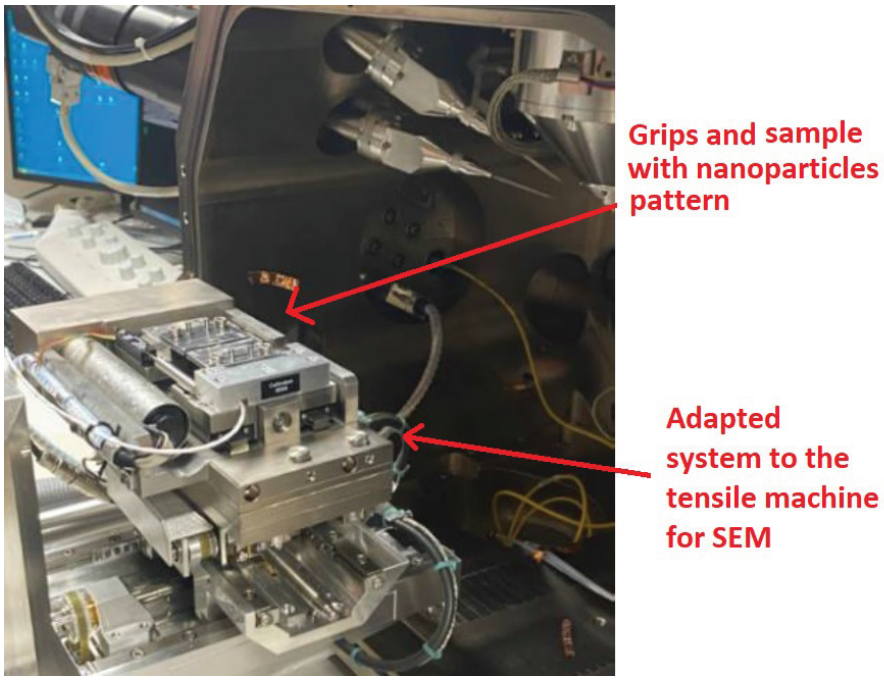

Figure 6.14: Microtensile machine being placed in the SEM at iLM.

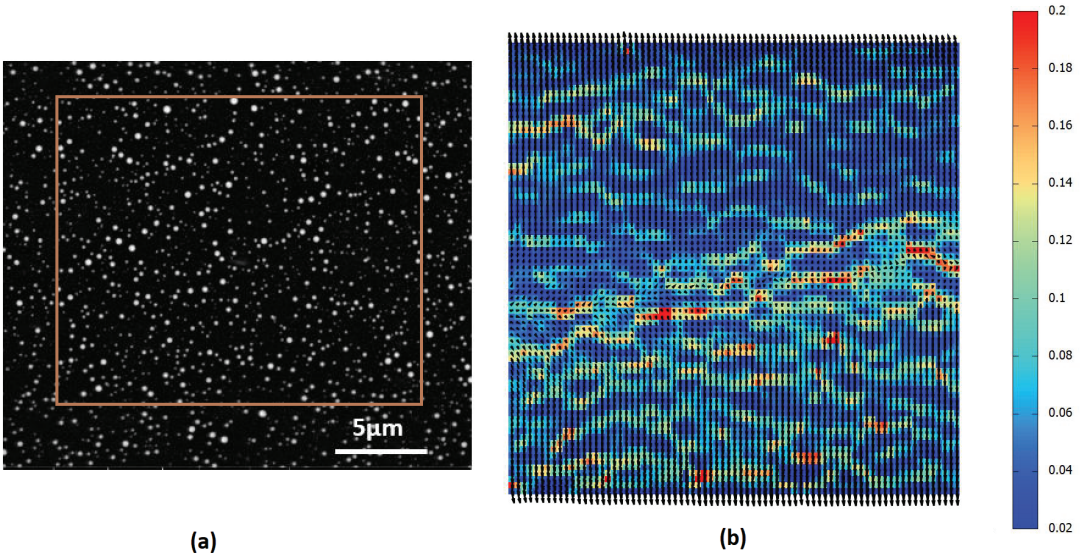

Figure 6.15: Non hydrogen charged tensile sample (a) Gold nanoparticles pattern in a SEM (b) Strain map of the marked region in (a), elongation 1.5%, 10 x 10 step size (10 px = 0.25 micron), the black arrows are the displacement field, the arrows points up in the upper part of the image and points down in the bottom part of the image (typical tensile test).

6.4 Conclusions and perspectives

The literature review has shown that there is a rich phenomenology concerning hydrogen embrittlement of metallic alloys and stress corrosion cracking. The "mechanistic models" (HELP, AIDE, HEDE) are good guides to review the possible interactions between hydrogen and the crystalline defects that might be at the origin of fracture. The main ingredients are: the loss of cohesion related to the segregation of hydrogen along the fracture path, for example along grain boundaries (or slip bands); the hydrogen-dislocation interaction which localizes and intensifies slip (HELP model) and leads to the formation of a very refined dislocation substructure in the vicinity of the crack tip; the nano ductile fracture occurring by the coalescence of nano-cavities formed by intersection and recombination of dislocations ahead of the crack tip; the void nucleation and growth in the HELP zone ahead of the crack tip by the formation of vacancies stabilized by hydrogen. These mechanisms are widely used to interpret macroscopic fracture experiments with more or less convincing successes. Post mortem TEM, from FIB sliced samples, has been intensively used to characterize the plastic wake and the cavities along slip bands in Ni based alloys. The progress made in the understanding of embrittlement is important but there is a lack of in situ observation of cracks at low scale. The goal of this thesis was to try to set up one of these experiments by taking advantage of the well established technique of Digital Image Correlation (DIC).

Samples were cut in the "short direction" of an 8 mm thick AlZnMg plate to take advantage of a morphological texture where the grains are more orientated perpendicular to the tensile direction. The alloy chosen is known for being sensitive to stress corrosion cracking and internal hydrogen embrittlement. A micro-tensile machine was used to perform constant displacement tests on these samples after they have been notched. A pattern on the surface, either from the dissolution of the surface during hydrogen charging or directly from the polishing, enabled performing DIC from images taken with an optical microscope. Magnifications up to $\times 2000$ were reached which gave a final resolution of 1μm for the displacement field obtained by DIC. Single cracks were studied both in internal hydrogen conditions or when the sample was exposed to saline water.

These experiments gave access to the velocity of the cracks, followed on the surface, and to the strain field, with sub-grain size resolution. The local velocities are in between 25 and 500 μm/h in the case of internal hydrogen embrittlement (IHE) and 50 to 3000 μm/h in the case of stress corrosion cracking (SCC). The plastic deformation was measured in a region about $80 \times 80\ \mu\text{m}^2$ around the crack tip. The plasticity accompanying the crack advance was characterized together with the local velocity. Despite the large difference in the velocity range between IHE and SCC, the plastic deformation range is the same. It was also found that there is systematically a plastically deformed zone ahead of the tip which characteristics only marginally change between IHE and SCC and between slow and fast cracks. The tensile deformation in the first micron ahead of the tip is in between 5 and 10% and the length of this plastic zone is about 4 μm. We named "primary plastic zone", the much larger zone affected by the slips bands which emerge from the tip itself and which expands over tens of microns and "secondary plastic zone", the micron size zone ahead of the crack tip. It shows that the crack path is plastically prestrained, like what Robertson et al. [46] have shown recently with post mortem TEM. Other direct observations are scarce [106] and obtained in other conditions. The pre-straining of the

crack path seems obvious to people who refer to the continuum plasticity model of cracks (Irwin, von Mises yield criterion, HRR model), but the ductile to brittle transition in Fe is well described by a discrete dislocation dynamics model which contains only a pair of slip bands, intersecting the crack tip (i.e. no plastic activity exists along the future crack path) and a decohesion condition at the tip [99]. Early models of IHE also do not take into account this prestraining [32], but only the shielding effect from the "primary plastic zone".

The local velocities were correlated to the fracture morphology. It appeared that transgranular fracture was, on average, slower than intergranular fracture (although slow intergranular cracks were observed).

One puzzling aspect of the results is that there is no unique relation between the local velocity and the emission of dislocation from the crack tip. It is expected that a loss of cohesion involves a decrease of the dislocation emission because the stresses are released. However, even if the stress intensity factor is high, some "brittle cracks" (i.e. cracks which do not emit much dislocations) move forward with a low velocity. The hypothesis of a hydrogen diffusion control has been ruled out in the case of internal hydrogen because the velocities are too small in comparison to the diffusion coefficient. One possibility is that the spreading of the velocities stems from the polycrystalline nature of the sample and a heterogeneous distribution of the stress along the crack front. This gives a motivation to try to modify the set up to adapt to thinner samples (below 200μm thick). The link between the crystallography (in particular the grain boundary crystallography) and the critical mechanical load for crack propagation is one of the experimental goals in the future. The DIC pattern is also expected to be much more efficient with nanoparticles.

From the simulation perspective, there are already a number of generic features of fracture, like the characteristics of the "secondary plastic zone" and the incremental crack opening profiles, which are well adapted to discrete dislocation dynamics simulations, in 2D. Now, efforts are being made to improve the efficiency of the in-house code [107] allowing to increase the number of dislocations and reach an applied stress intensity of 8 MPa$\sqrt{m}$ for a better comparison to the experiments. It is also planned to analyze in detail the intermittent SCC crack sequence observed, in particular we want to evaluate the stress at the crack tip at the re-initiation after blunting by combining finite elements calculations and discrete dislocation dynamics.

Bibliography

[1] R. P. Gangloff and B. P. Somerday, "Gaseous hydrogen embrittlement of materials in energy technologies: mechanisms, modelling and future developments, vol. 1," pp. 707–768, Woodhead Publishing Limited, 2012. 1, 100

[2] D. M. Symons, "A comparison of internal hydrogen embrittlement and hydrogen environment embrittlement of X-750," *Engineering Fracture Mechanics*, vol. 68, no. 6, pp. 751–771, 2001. 1, 3

[3] B. N. Popov, J.-W. Lee, and M. B. Djukic, "Hydrogen permeation and hydrogen-induced cracking," in *Handbook of environmental degradation of materials*, pp. 133–162, Elsevier, 2018. 1

[4] European Commission, "A hydrogen strategy for a climate-neutral europe," *Brussels, 8.7.2020 COM 301 final*, 2020. 1

[5] K. Sasaki, H.-W. Li, A. Hayashi, J. Yamabe, T. Ogura, and S. M. Lyth, *Hydrogen Energy Engineering*. Springer, 2016. 1

[6] R. Ambat and E. Dwarakadasa, "Effect of hydrogen in aluminium and aluminium alloys: A review," *Bulletin of Materials Science*, vol. 19, no. 1, pp. 103–114, 1996. 1

[7] J. Scully, G. Young Jr, and S. Smith, "Hydrogen embrittlement of aluminum and aluminum-based alloys," in *Gaseous hydrogen embrittlement of materials in energy technologies*, pp. 707–768, Elsevier, 2012. 1, 99, 100, 103, 104, 122

[8] S. K. Das and W. Yin, "The worldwide aluminum economy: The current state of the industry," *Jom*, vol. 59, no. 11, pp. 57–63, 2007. 1

[9] H. Wang, D. Y. Leung, M. Leung, and M. Ni, "A review on hydrogen production using aluminum and aluminum alloys," *Renewable and sustainable energy reviews*, vol. 13, no. 4, pp. 845–853, 2009. 2

[10] J. K. Norskov and F. Besenbacher, "Theory of hydrogen interaction with metals," *Journal of the less-common metals*, vol. 130, pp. 475–490, 1987. 3

[11] Y. Fukai, *The Metal-Hydrogen System: Basic Bulk Properties*. Springer-Verlag Berlin and Heidelberg GmbH & Co. K; 2nd edition, 2003. 3

[12] A. Van der Ven and G. Ceder, "The thermodynamics of decohesion," *acta mater.*, vol. 52, pp. 1223–1235, 2004. 3, 10

[13] H. Mehrer, *Diffusion in solids: fundamentals, methods, materials, diffusion-controlled processes*, vol. 155. Springer Science & Business Media, 2007. 4

[14] P. Sofronis and R. McMeeking, "Numerical analysis of hydrogen transport near a blunting crack tip," *Journal of the Mechanics and Physics of Solids*, vol. 37, no. 3, pp. 317–350, 1989. 4, 14, 137

[15] A. H. Krom, R. W. Koers, and A. Bakker, "Hydrogen transport near a blunting crack tip," *Journal of the Mechanics and Physics of Solids*, vol. 47, no. 4, pp. 971–992, 1999. 4

[16] S. I. Hong and C. Laird, "Mechanisms of slip mode modification in fcc solid solutions," *Acta metallurgica et materialia*, vol. 38, no. 8, pp. 1581–1594, 1990. 5

[17] G. Girardin, C. Huvier, D. Delafosse, and X. Feaugas, "Correlation between dislocation organization and slip bands: TEM and AFM investigations in hydrogen-containing nickel and nickel-chromium," *acta mater.*, vol. 91, pp. 141–151, 2015. 5, 14

[18] I. Aubert, N. Saintier, J.-M. Olive, and F. Plessier, "A methodology to obtain data at the slip-band scale from atomic force microscopy observations and crystal plasticity simulations. application to hydrogen-induced slip localization on AISI 316L stainless steel," *Acta Materialia*, vol. 104, pp. 9–17, 2016. 5, 14

[19] H. Vehoff and P. Neumann, "Crack propagation and cleavage initiation in Fe-2.6%-Si single crystals under controlled plastic crack tip opening rate in various gaseous environments," *Acta Metallurgica*, vol. 28, no. 3, pp. 265–272, 1980. 6, 7

[20] Q. Bai and Y. Bai, *Subsea pipeline design, analysis, and installation*. Gulf Professional Publishing, 2014. 6

[21] H. Toda, S. Yamamoto, M. Kobayashi, K. Uesugi, and H. Zhang, "Direct measurement procedure for three-dimensional local crack driving force using synchrotron X-ray microtomography," *Acta Materialia*, vol. 56, no. 20, pp. 6027–6039, 2008. 6, 7

[22] E. R. Cahn and P. Haasen, "Physical metallurgy 4th edition," ch. 26, Fracture by Thomson, Vol III, Elsevier Inc, 1996. 7

[23] S. Lynch, "Hydrogen embrittlement phenomena and mechanisms," *Corrosion Reviews*, vol. 30, no. 3-4, pp. 105–123, 2012. 8, 9

[24] R. P. Gangloff and B. P. Somerday, "Gaseous hydrogen embrittlement of materials in energy technologies: the problem, its characterisation and effects on particular alloy classes," ch. 9 by Lynch, Vol I, McGraw-Hill book company, The United States of America, 2012. 8, 10

[25] S. Lynch, "Discussion of some recent literature on hydrogen-embrittlement mechanisms: addressing common misunderstandings," *Corrosion Reviews*, vol. 37, no. 5, pp. 377–395, 2019. 8, 9

[26] R. P. Gangloff, "Hydrogen assisted cracking of high strength alloys," tech. rep., Aluminum Co of America Alcoa Center Pa Alcoa Technical Center, 2003. 10, 11, 60, 97

[27] Y. A. Du, L. Ismer, J. Rogal, T. Hickel, J. Neugebauer, and R. Drautz, "First-principles study on the interaction of H interstitials with grain boundaries in α-and γ-Fe," *Physical Review B*, vol. 84, no. 14, p. 144121, 2011. 10

[28] H. Vehoff and W. Rothe, "Gaseous hydrogen embrittlement in FeSi-and Ni-single crystals," in *Perspectives in Hydrogen in Metals*, pp. 647–659, Elsevier, 1986. 10

[29] O. Barrera, D. Bombac, Y. Chen, T. Daff, E. Galindo-Nava, P. Gong, D. Haley, R. Horton, I. Katzarov, J. Kermode, *et al.*, "Understanding and mitigating hydrogen embrittlement of steels: a review of experimental, modelling and design progress from atomistic to continuum," *Journal of materials science*, vol. 53, no. 9, pp. 6251–6290, 2018. 10, 14

[30] O. Barrera, D. Bombac, Y. Chen, T. Daff, E. Galindo-Nava, P. Gong, D. Haley, R. Horton, I. Katzarov, J. Kermode, *et al.*, "Correction to: Understanding and mitigating hydrogen embrittlement of steels: a review of experimental, modelling and design progress from atomistic to continuum," *Journal of Materials Science*, vol. 53, no. 14, pp. 10593–10594, 2018. 10

[31] E. Martínez-Pañeda, C. F. Niordson, and R. P. Gangloff, "Strain gradient plasticity-based modeling of hydrogen environment assisted cracking," *Acta Materialia*, vol. 117, pp. 321–332, 2016. 10, 13

[32] Y. Katz, N. Tymiak, and W. W. Gerberich, "Nanomechanical probes as new approaches to hydrogen/deformation interaction studies," *Engineering Fracture Mechanics*, vol. 68, no. 6, pp. 619–646, 2001. 11, 155

[33] I. M. Robertson, P. Sofronis, A. Nagao, M. Martin, S. Wang, D. Gross, and K. Nygren, "Hydrogen embrittlement understood," *Metallurgical and Materials Transactions A*, vol. 46, no. 6, pp. 2323–2341, 2015. 11, 16, 17, 18, 19, 22, 136, 144

[34] R. Gangloff, "H-enhanced deformation and fracture in the crack tip process zone," in *Materials Performance in Hydrogen Environments: Proceedings of the 2016 International Hydrogen Conference*, pp. 1–35, 2017. 11, 12

[35] R. P. Gangloff, "Critical issues in hydrogen assisted cracking of structural alloys," in *Environment-induced cracking of materials*, pp. 141–165, Elsevier, 2008. 11

[36] S. Knight, K. Pohl, N. Holroyd, N. Birbilis, P. Rometsch, B. Muddle, R. Goswami, and S. Lynch, "Some effects of alloy composition on stress corrosion cracking in Al–Zn–Mg–Cu alloys," *Corrosion Science*, vol. 98, pp. 50–62, 2015. 12, 98, 99, 100, 103, 122

[37] N. Fleck and J. W. Hutchinson, "A reformulation of strain gradient plasticity," *Journal of the Mechanics and Physics of Solids*, vol. 49, no. 10, pp. 2245–2271, 2001. 12

[38] E. Martínez-Pañeda and C. Betegón, "Modeling damage and fracture within strain-gradient plasticity," *International Journal of Solids and Structures*, vol. 59, pp. 208–215, 2015. 12

[39] E. Martínez-Pañeda and C. F. Niordson, "On fracture in finite strain gradient plasticity," *International Journal of Plasticity*, vol. 80, pp. 154–167, 2016. 13

[40] I. Robertson, "The effect of hydrogen on dislocation dynamics," *Engineering fracture mechanics*, vol. 68, no. 6, pp. 671–692, 2001. 14

[41] Jagodzinski, Hanninen, Tarasenko and Smuk, "Interaction of hydrogen with dislocation pile-ups and hydrogen induced softening of pure iron," *Scripta mater*, vol. 43, pp. 245–251, 2000. 15

[42] M. L. Martin, M. Dadfarnia, A. Nagao, S. Wang, and P. Sofronis, "Enumeration of the hydrogen-enhanced localized plasticity mechanism for hydrogen embrittlement in structural materials," *Acta Materialia*, vol. 165, pp. 734–750, 2019. 14, 18, 144

[43] P. Sofronis, Y. Liang, and N. Aravas, "Hydrogen induced shear localization of the plastic flow in metals and alloys," *European Journal of Mechanics-A/Solids*, vol. 20, no. 6, pp. 857–872, 2001. 15

[44] Y. Liang, P. Sofronis, and N. Aravas, "On the effect of hydrogen on plastic instabilities in metals," *Acta Materialia*, vol. 51, no. 9, pp. 2717–2730, 2003. 15

[45] D. Ahn, P. Sofronis, and R. Dodds Jr, "On hydrogen-induced plastic flow localization during void growth and coalescence," *International Journal of Hydrogen Energy*, vol. 32, no. 16, pp. 3734–3742, 2007. 15

[46] M. Martin, B. Somerday, R. Ritchie, P. Sofronis, and I. Robertson, "Hydrogen-induced intergranular failure in nickel revisited," *Acta Materialia*, vol. 60, no. 6-7, pp. 2739–2745, 2012. 16, 136, 154

[47] S. Wang, M. L. Martin, P. Sofronis, S. Ohnuki, N. Hashimoto, and I. M. Robertson, "Hydrogen-induced intergranular failure of iron," *Acta materialia*, vol. 69, pp. 275–282, 2014. 16, 17

[48] M. Martin, I. Robertson, and P. Sofronis, "Interpreting hydrogen-induced fracture surfaces in terms of deformation processes: a new approach," *Acta Materialia*, vol. 59, no. 9, pp. 3680–3687, 2011. 16

[49] M. L. Martin, J. A. Fenske, G. S. Liu, P. Sofronis, and I. M. Robertson, "On the formation and nature of quasi-cleavage fracture surfaces in hydrogen embrittled steels," *Acta Materialia*, vol. 59, no. 4, pp. 1601–1606, 2011. 16

[50] J. Kacher, B. Eftink, B. Cui, and I. Robertson, "Dislocation interactions with grain boundaries," *Current Opinion in Solid State and Materials Science*, vol. 18, no. 4, pp. 227–243, 2014. 18, 19

[51] M. McMurtrey, G. Was, B. Cui, I. Robertson, L. Smith, and D. Farkas, "Strain localization at dislocation channel–grain boundary intersections in irradiated stainless steel," *International Journal of Plasticity*, vol. 56, pp. 219–231, 2014. 18, 20, 144

[52] B. Cui, J. Kacher, M. McMurtrey, G. Was, and I. Robertson, "Influence of irradiation damage on slip transfer across grain boundaries," *Acta materialia*, vol. 65, pp. 150–160, 2014. 18, 19, 144

[53] M. Nagumo and K. Takai, "The predominant role of strain-induced vacancies in hydrogen embrittlement of steels: overview," *Acta Materialia*, vol. 165, pp. 722–733, 2019. 21

[54] M. Nagumo, "Hydrogen related failure of steels–a new aspect," *Materials Science and Technology*, vol. 20, no. 8, pp. 940–950, 2004. 21, 136

[55] K. Takai, H. Shoda, H. Suzuki, and M. Nagumo, "Lattice defects dominating hydrogen-related failure of metals," *Acta Materialia*, vol. 56, no. 18, pp. 5158–5167, 2008. 21

[56] M. Nagumo, "Conformity between mechanics and microscopic functions of hydrogen in failure," *ISIJ international*, vol. 52, no. 2, pp. 168–173, 2012. 21

[57] T. Neeraj, R. Srinivasan, and J. Li, "Hydrogen embrittlement of ferritic steels: observations on deformation microstructure, nanoscale dimples and failure by nanovoiding," *Acta Materialia*, vol. 60, no. 13-14, pp. 5160–5171, 2012. 21

[58] Z. Zhang, G. Obasi, R. Morana, and M. Preuss, "Hydrogen assisted crack initiation and propagation in a nickel-based superalloy," *Acta Materialia*, vol. 113, pp. 272–283, 2016. 22, 23

[59] M. Koyama, H. Springer, S. V. Merzlikin, K. Tsuzaki, E. Akiyama, and D. Raabe, "Hydrogen embrittlement associated with strain localization in a precipitation-hardened Fe–Mn–Al–C light weight austenitic steel," *International Journal of Hydrogen Energy*, vol. 39, no. 9, pp. 4634–4646, 2014. 22

[60] S. Li, Y. Li, Y.-C. Lo, T. Neeraj, R. Srinivasan, X. Ding, J. Sun, L. Qi, P. Gumbsch, and J. Li, "The interaction of dislocations and hydrogen-vacancy complexes and its importance for deformation-induced proto nano-voids formation in α-Fe," *International Journal of Plasticity*, vol. 74, pp. 175–191, 2015. 24

[61] A. Tehranchi, X. Zhang, G. Lu, and W. Curtin, "Hydrogen–vacancy–dislocation interactions in α-Fe," *Modelling and Simulation in Materials Science and Engineering*, vol. 25, no. 2, p. 025001, 2016. 24

[62] M. S. Bhuiyan, H. Toda, K. Shimizu, H. Su, K. Uesugi, A. Takeuchi, and Y. Watanabe, "The role of hydrogen on the local fracture toughness properties of 7XXX aluminum alloys," *Metallurgical and Materials Transactions A*, vol. 49, no. 11, pp. 5368–5381, 2018. 25, 26, 27, 28, 43, 142

[63] M. S. Bhuiyan, Y. Tada, H. Toda, S. Hang, K. Uesugi, A. Takeuchi, N. Sakaguchi, and Y. Watanabe, "Influences of hydrogen on deformation and fracture behaviors of high Zn 7XXX aluminum alloys," *International Journal of Fracture*, vol. 200, no. 1-2, pp. 13–29, 2016. 25, 43

[64] H. Su, H. Toda, R. Masunaga, K. Shimizu, H. Gao, K. Sasaki, M. S. Bhuiyan, K. Uesugi, A. Takeuchi, and Y. Watanabe, "Influence of hydrogen on strain localization and fracture behavior in AlZnMgCu aluminum alloys," *Acta Materialia*, vol. 159, pp. 332–343, 2018. 25, 28, 29, 30, 35, 36, 37, 43, 136, 141

[65] H. Su, H. Toda, K. Shimizu, K. Uesugi, A. Takeuchi, and Y. Watanabe, "Assessment of hydrogen embrittlement via image-based techniques in Al–Zn–Mg–Cu aluminum alloys," *Acta Materialia*, vol. 176, pp. 96–108, 2019. 25, 29, 35, 37, 43, 136, 141

[66] K. Shimizu, H. Toda, C. Kadogawa, H. Fujihara, and A. Takeuchi, "Influence of nanovoids in the hydrogen embrittlement fracture of Al-Zn-Mg-Cu alloys," *Materialia*, p. 100667, 2020. 25

[67] K. Shimizu, H. Toda, H. Fujihara, K. Hirayama, K. Uesugi, and A. Takeuchi, "Hydrogen partitioning behavior and related hydrogen embrittlement in Al-Zn-Mg alloys," *Engineering Fracture Mechanics*, vol. 216, p. 106503, 2019. 25, 28, 35, 141

[68] K. Shimizu, H. Toda, K. Uesugi, and A. Takeuchi, "Local deformation and fracture behavior of high-strength aluminum alloys under hydrogen influence," *Metallurgical and Materials Transactions A*, vol. 51, no. 1, pp. 1–19, 2020. 25, 27, 29, 30, 31, 32, 33, 34, 35, 141, 142

[69] H. Gao, H. Su, K. Shimizu, C. Kadokawa, H. Toda, Y. Terada, K. Uesugi, and A. Takeuchi, "Evolution behavior of hydrogen-induced nano voids in Al–Zn–Mg–Cu aluminum alloys under loading," *Materials Transactions*, vol. 59, no. 9, pp. 1532–1535, 2018. 25

[70] T. Tsuru, K. Shimizu, M. Yamaguchi, M. Itakura, K. Ebihara, A. Bendo, K. Matsuda, and H. Toda, "Hydrogen-accelerated spontaneous microcracking in high-strength aluminium alloys," *Scientific reports*, vol. 10, no. 1, pp. 1–8, 2020. 25, 35, 141

[71] J. Adams *et al.*, "ASM metals handbook vol. 2: Properties and selection: Nonferrous alloys and special-purpose materials," *ASM International*, 1990. 39

[72] B. Dubost and P. Sainfort, "Durcissement par précipitation des alliages d'aluminium," *Techniques de l'ingénieur. Matériaux métalliques*, no. M240, pp. M240–1, 1991. 41

[73] W. Wunderlich and H.-J. Gudladt, "TEM-studies of grain boundaries in cyclically deformed AlZnMg-bicrystals," *Acta Metallurgica et Materialia*, vol. 40, no. 9, pp. 2123–2129, 1992. 41

[74] N. Ben Ali, D. Tanguy, and R. Estevez, "Effects of microstructure on hydrogen-induced cracking in aluminum alloys," *Scripta Materialia*, vol. 65, no. 3, pp. 210–213, 2011. 41, 136

[75] M. Dumont, W. Lefebvre, B. Doisneau-Cottignies, and A. Deschamps, "Characterisation of the composition and volume fraction of η' and η precipitates in an Al–Zn–Mg alloy by a combination of atom probe, small-angle X-ray scattering and transmission electron microscopy," *Acta Materialia*, vol. 53, no. 10, pp. 2881–2892, 2005. 42

[76] J. K. Park and A. Ardell, "Precipitation at grain boundaries in the commercial alloy al 7075," *Acta Metallurgica*, vol. 34, no. 12, pp. 2399–2409, 1986. 42

[77] N. Ben Ali, *Caractérisation et modélisation micromécanique de la propagation de fissures fragiles par effet de l'hydrogène dans les alliages AA7xxx*. PhD thesis, École Nationale Supérieure des Mines des Saint Etienne, 2011. 42, 43, 137

[78] W. Lepage, *A practical guide to DIC*. www.digitalimagecorrelation.org/, 2019. 47, 48

[79] M. A. Sutton, J. J. Orteu, and H. Schreier, *Image correlation for shape, motion and deformation measurements: basic concepts, theory and applications*. Springer Science & Business Media, 2009. 49

[80] E. M. Jones, M. A. Iadicola, *et al.*, "A good practices guide for digital image correlation," *International Digital Image Correlation Society*, 2018. 49

[81] Correlated Solutions Inc., *DIC support*. www.correlatedsolutions.com, 2019. 49

[82] B. Wang and B. Pan, "Subset-based local vs. finite element-based global digital image correlation: A comparison study," *Theoretical and Applied Mechanics Letters*, vol. 6, no. 5, pp. 200–208, 2016. 49, 50

[83] J. Yang, *Fast Adaptive Augmented Lagrangian Digital Image Correlation*. PhD thesis, California Institute of Technology, 2019. 49, 50

[84] D. André, *Pydic*. www.unilim.fr - Université de Limoges, 2019. 51

[85] J.-Y. Bouguet *et al.*, "Pyramidal implementation of the affine Lucas Kanade feature tracker description of the algorithm," *Intel corporation*, vol. 5, no. 1-10, p. 4, 2001. 51

[86] J. Zhao, Y. Sang, and F. Duan, "The state of the art of two-dimensional digital image correlation computational method," *Engineering Reports*, vol. 1, no. 2, p. e12038, 2019. 51

[87] J. Stinville, M. Echlin, D. Texier, F. Bridier, P. Bocher, and T. Pollock, "Sub-grain scale digital image correlation by electron microscopy for polycrystalline materials during elastic and plastic deformation," *Experimental mechanics*, vol. 56, no. 2, pp. 197–216, 2016. 52

[88] H. Tada, P. C. Paris, and G. R. Irwin, "The stress analysis of cracks," *Handbook, Del Research Corporation*, vol. 34, 1973. 52

[89] Pilkey, *Formulas for Stress, Strain, and Structural Matrices*. John Wiley Sons, Inc, 2005. 52

[90] COMSOL Inc., "Comsol multiphysics reference manual," 2007. 53

[91] D. Tanguy, "Cohesive stress heterogeneities and the transition from intrinsic ductility to brittleness," *Physical Review B*, vol. 96, no. 17, p. 174115, 2017. 66, 135

[92] N. Holroyd, "Environment-induced cracking of high-strength aluminum alloys," *Environment-induced cracking of metals*, p. 311, 1990. 97, 98, 99

[93] F. Andreatta, H. Terryn, and J. De Wit, "Effect of solution heat treatment on galvanic coupling between intermetallics and matrix in AA7075-T6," *Corrosion Science*, vol. 45, no. 8, pp. 1733–1746, 2003. 98

[94] N. Birbilis and R. G. Buchheit, "Electrochemical characteristics of intermetallic phases in aluminum alloys: an experimental survey and discussion," *Journal of the Electrochemical Society*, vol. 152, no. 4, p. B140, 2005. 98

[95] J. Wloka and S. Virtanen, "Detection of nanoscale η-$MgZn_2$ phase dissolution from an Al-Zn-Mg-Cu alloy by electrochemical microtransients," *Surface and Interface Analysis: An International Journal devoted to the development and application of techniques for the analysis of surfaces, interfaces and thin films*, vol. 40, no. 8, pp. 1219–1225, 2008. 98

[96] T. Marlaud, *Microstructures de précipitation et mécanismes de corrosion feuilletante dans les alliages d'aluminium de la série 7000 à très hautes caractéristiques mécaniques*. PhD thesis, Grenoble INPG, 2008. 98

[97] U. De Francisco, N. O. Larrosa, and M. J. Peel, "Hydrogen environmentally assisted cracking during static loading of AA7075 and AA7449," *Materials Science and Engineering: A*, vol. 772, p. 138662, 2020. 100

[98] W. Gruhl, "Stress corrosion cracking of high strength aluminum alloys," *Zeitschrift fuer Metallkunde*, vol. 75, pp. 819–826, 1984. 100

[99] M. Tanaka, E. Tarleton, and S. Roberts, "The brittle–ductile transition in single-crystal iron," *Acta Materialia*, vol. 56, no. 18, pp. 5123–5129, 2008. 136, 155

[100] K. Arioka, "Change in bonding strength at grain boundaries before long-term SCC initiation," *Corrosion*, vol. 71, no. 4, pp. 403–419, 2015. 136

[101] A. Rajabzadeh, F. Mompiou, S. Lartigue-Korinek, N. Combe, M. Legros, and D. Molodov, "The role of disconnections in deformation-coupled grain boundary migration," *Acta Materialia*, vol. 77, pp. 223–235, 2014. 136

[102] G. A. Young and J. R. Scully, "Hydrogen production, absorption and transport during environment assisted cracking of an Al-Zn-Mg-(Cu) alloy in humid air," in *International Conference on Hydrogen Effects on Material Behavior and Corrosion Deformation Interactions, Moran, WY*, pp. 22–26, 2002. 136

[103] J.-H. Ai, M. L. C. Lim, and J. R. Scully, "Effective hydrogen diffusion in aluminum alloy 5083-H131 as a function of orientation and degree of sensitization," *Corrosion*, vol. 69, no. 12, pp. 1225–1239, 2013. 136, 137

[104] Y. Charles, H. T. Nguyen, and M. Gaspérini, "Comparison of hydrogen transport through pre-deformed synthetic polycrystals and homogeneous samples by finite element analysis," *International Journal of Hydrogen Energy*, vol. 42, no. 31, pp. 20336–20350, 2017. 137

[105] L. Oger, E. Andrieu, G. Odemer, L. Peguet, and C. Blanc, "Hydrogen-dislocation interactions in a low-copper 7xxx aluminium alloy: About the analysis of interrupted stress corrosion cracking tests," *Materials Science and Engineering: A*, vol. 790, p. 139654, 2020. 138, 142

[106] Y. Deng and A. Barnoush, "Hydrogen embrittlement revealed via novel in situ fracture experiments using notched micro-cantilever specimens," *Acta Materialia*, vol. 142, pp. 236–247, 2018. 154

[107] D. Tanguy, D. Delafosse, and M. Razafindrazaka, "Plasticity localization ahead of a crack tip modeled by 2D discrete dislocation dynamics," *Philosophical Magazine*, vol. 90, no. 11, pp. 1415–1434, 2010. 155